INAUGURAL – DISSERTATION

zur

Erlangung der Doktorwürde

der

Naturwissenschaftlich – Mathematischen

Gesamtfakultät

der

Ruprecht – Karls – Universität
Heidelberg

vorgelegt von

Dipl.–Phys. Thomas Gäng
aus Oberhausen/Baden-Württemberg

Tag der mündlichen Prüfung: 16. Februar 2000

Dynamic and Static Conditions in the Atmospheres of Luminous Blue Variables

———

A Study of High-Resolution Spectra
in the Optical Wavelength Range

Gutachter: Herr Prof. Dr. Bernhard Wolf

Herr Prof. Dr. Rainer Wehrse

Dissertation
submitted to the
Combined Faculties for the Natural Sciences and for Mathematics
of the Rupertus Carola University of
Heidelberg, Germany
for the degree of
Doctor of Natural Sciences

Dynamic and Static Conditions in the Atmospheres of Luminous Blue Variables

——

A Study of High-Resolution Spectra in the Optical Wavelength Range

presented by

Diplom-Physicist: Thomas Gäng
born in: Oberhausen/Baden-Württemberg

Heidelberg, February 16, 2000

Referees: Prof. Dr. Bernhard Wolf
Prof. Dr. Rainer Wehrse

Dynamische und Statische Bedingungen in den Atmosphären von Leuchtkräftigen Blauen Veränderlichen

ZUSAMMENFASSUNG

Um die spektrale Variabilität von Leuchtkräftigen Blauen Veränderlichen (LBVs) zu untersuchen wurde der galaktische BA-Hyperriesenstern HD 160529 von 1992 bis 1995 über jeweils $2-4$ Monate beobachtet. Der umfaßte Wellenlängenbereich betrug $3450\,\text{Å} \lesssim \lambda \lesssim 8630\,\text{Å}$ mit einer spektralen Auflösung von $R = \lambda/\Delta\lambda \approx 20\,000$ ($\approx 15\,\text{km s}^{-1}$). Zeitserienanalysen der Spektren ergeben dominante Perioden von 92.5 ± 1 Tage für photosphärische Linienprofilvariationen (LPVs) und $114-127$ Tage für Wind–LPVs; die Werte liegen im Bereich der beobachteten photometrischen Zeitskalen. Zeitliche Varianz Spektren und LPVs deuten auf die Existenz von radialen (RP) und nicht-radialen (NRP) Pulsationen niedriger Ordnung ($|m| \lesssim 2$) hin; z.B. die gegen die Rotationsrichtung laufenden Variationen der He I λ5876-Linie werden sehr gut von NRPs mit $l = +m = 1$ reproduziert. TLUSTY 194–Modelle der temperaturempfindlichen Ti II λ4468 Linie lassen auf eine variable Temperatur–Schichtung der Photosphäre von etwa $T_{\text{eff}} \approx 10\,000-11\,500\,\text{K}$ schliessen. Temperatur–Variationen in diesem Bereich ergeben sich auch aus RPs und NRPs mit $l \lesssim 2$ (Guzik, private Mitteilung) und können die Kontinuums–Strahlung ausreichend beeinflussen um die beobachteten Variationen der Sternwindlinien zu erklären. Dynamische Wind–Modelle des SEIDYNAMIC–Programmes bestätigen diese Ergebnisse und demonstrieren daß selbst beträchtliche Dichteschwankungen des stellaren Ausflusses nicht Hauptursache der Windveränderlichkeit sein können.

Zur Untersuchung der LBV-Windstruktur wurden sehr hoch aufgelöste Spektren ($R \approx 50\,000-100\,000$) von 20 Sternen gesammelt. *Alle* Objekte zeigen Inhomogenitäten in ihren Spektrallinien–Profilen, die darauf hinweisen, daß "Verklumpung" (engl: "clumping") eine allgemeine Eigenschaft der LBV-Sternwinde sein könnte. Die Inhomogenitäten werden ausgeprägter und häufiger bei Spektrallinien die weiter außen in der Sternatmosphäre geformt werden. Es entsteht ein Bild eines zunächst homogenen Windes, der auf dem Weg von der Sternoberfläche in das interstellare Medium gestört wird und Klumpen oder Schalen bildet.

Dynamic and Static Conditions in the Atmospheres of Luminous Blue Variables

ABSTRACT

We have observed the galactic BA-type hypergiant HD 160529 from 1992 to 1995 over $2-4$ months per year to study the spectral variability of Luminous Blue Variables (LBVs). The covered spectral wavelength range was $3450\,\text{Å} \lesssim \lambda \lesssim 8630\,\text{Å}$ with a spectral resolution of $R = \lambda/\Delta\lambda \approx 20\,000$ (i.e. $\approx 15\,\text{km s}^{-1}$). Time-series analyses of the spectra result in dominant periods of 92.5 ± 1 days for photospheric line profile variations (LPVs) and $114-127$ days for wind LPVs, which are in a range similar to observed photometric variation time scales. Temporal variance spectra and LPVs indicate radial (RP) and low-order ($|m| \lesssim 2$) non-radial (NRP) pulsations, e.g. retrograde moving variation features of the photospheric He I λ5876 line are well reproduced by NRPs with $l = +m = 1$. TLUSTY 194 models of the temperature sensitive Ti II λ4468 line indicate a variable temperature structure of the photosphere in the range of $T_{\text{eff}} \approx 10\,000-11\,500\,\text{K}$. Temperature variations of this order are expected in RPs and NRPs with $l \lesssim 2$ (Guzik, private communication) and can change the continuum radiation sufficiently to explain the observed variations of the wind lines. Dynamical wind models using the SEIDYNAMIC code confirm these results and demonstrate that even substantial density variations in the stellar outflow cannot be the main cause of the wind variability.

We have obtained very high resolution spectra ($R \approx 50\,000-100\,000$) of 20 LBVs to study their wind structure. *All* objects show inhomogeneities in their line profiles indicating that clumping might be a common feature in LBV-winds. The inhomogeneities get more pronounced and more frequent in spectral lines that are formed further out in the atmosphere. The resulting picture is that of an initially "smooth" wind that gets disturbed and forms clumps or shells as it travels away from the star into the interstellar medium.
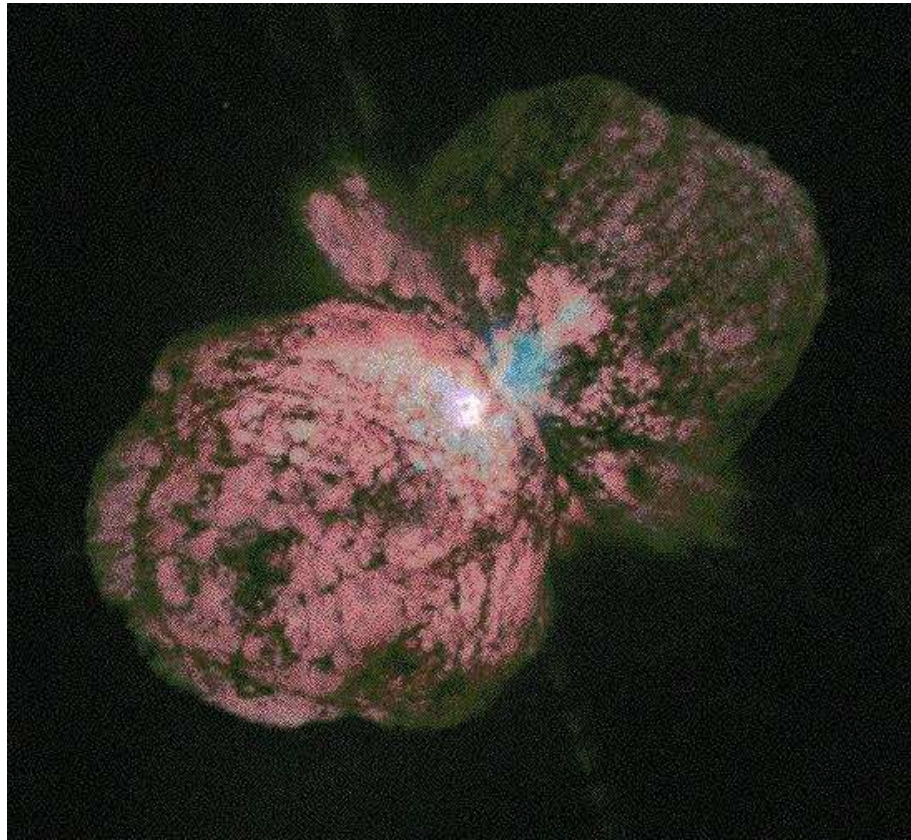
Image of the Luminous Blue Variable (LBV) Eta Carinae (η Car) taken with the Wide Field Planetary Camera 2 on board the Hubble Space Telescope in September 1995. Images taken through red and near-ultraviolet filters were subsequently combined to produce the color image shown.

The huge, billowing pair of gas and dust clouds probably originate from super-outbursts and strong, dense stellar winds which are characteristic features of LBVs and possible interaction with one or more companion stars. The study of the spectroscopic signatures of LBV-outflows and their underlying extended stellar atmospheres is subject of this thesis.

Photo Credit: Jon Morse (University of Colorado), and NASA

Technical Data

This thesis has been created with TEX (C Version 6.1) and LATEX2ϵ (PL 3) using a modified version of the `report`–style (LaTeX3 Project, 1997). The postscript file for the final printing has been formatted with `dvips` (dvipsk–version 5.58, Radical Eye Software, 1994).

The data reductions and analyses have been carried out mainly on the HP–Apollo–Serie–700–Cluster of the Landessternwarte Heidelberg running under HP–UX and various Sun–workstations (SPARC 5–20) under SunOS and Solaris at the Space Telescope Science Institute. The software packages MIDAS Release 92NOV–98NOV of ESO and IRAF Revision 2.10–2.11 of NOAO have been used for data reduction and analysis. Multiple small programs have been written for the analysis and graphical representation of the results, mostly using PERL (Version 5.002), UNIX-sh/csh, sed/awk, SUPERMONGO (Version SM2_3_23) and IDL (Version 4.0.1c).

Contents

Chapter 1:   Introduction

In this chapter we highlight the astrophysical significance of massive stars, and in particular Luminous Blue Variables (LBVs), summarize the observational characteristics of LBVs and then present the current state of research in this area. The following section describes unsolved problem areas and how this thesis contributes to their solution. Finally we add some notes about spectral line accuracies in general and how we resolved problematic issues for this work.

1.1   Motivation: The Importance of Massive Star Research

Massive stars with Zero-Age-Main-Sequence (ZAMS) masses of $M_{ZAMS} \gtrsim 10\,M_\odot$ have surface temperatures of over $\sim 10\,000$ K, high luminosities ($10^4 - 10^6\,L_\odot$) and relatively short lifetimes ($\sim 10^7$ yrs). Their strong radiation fields can ionize large volumes (up to 10 parsecs for H II regions) of the surrounding interstellar medium (ISM). Also strong mass loss driven by radiation pressure is a characteristic feature of hot luminous stars (Kudritzki & Hummer 1990). Although these objects constitute only a small fraction ($\sim 10^{-7}$) of the total stellar population, their radiation and mass-loss properties dominate the power and momentum input into the ISM.

From an evolutionary point of view, mass loss is of minor importance on the main sequence but it is the single most important parameter governing stellar evolution in the H-shell- and core-He-burning and in later stellar phases (Chiosi & Maeder 1986). Observationally, these phases are associated with Of stars, LBVs, and Wolf-Rayet (W-R) stars. Understanding the mass-loss properties of these stars is crucial for modeling the final evolutionary stages of massive stars and the relationships with their predecessors.

LBVs have recently been recognized as keys to the evolution of massive stars. *Every* massive star with $M \gtrsim 40\,M_\odot$ passes through the LBV phase, where it may lose more than 50% of its initial mass by dense winds, multiple eruptions and occasional large outbursts (see e.g. the evolution summary in the introduction of Langer et al. 1999). Thus LBVs deposit large amounts of mainly unprocessed material back into the ISM before nuclear synthesis by a supernova explosion can occur. Therefore these objects are not only important for *stellar* evolution but for the chemical evolution of *galaxies* as well.

The LBVs are ideally suited to probing the stellar wind at various distances from the photosphere using spectral lines: unlike strong-lined Wolf-Rayet stars, their wind densities are low enough that regions with $v \approx v_{\mathrm{sound}}$ can still be directly observed; and unlike normal O stars, densities are high enough that a large number of lines in the visual spectral range are formed up to distances from the photosphere where the terminal velocity of the outflow is reached.

Given this unique observational possibility, the density structure of the wind can be determined empirically. Comparison with predictions of the theory of radiatively driven winds can then reveal important information on the mass-loss mechanism.

The extreme brightness and irregular spectrophotometric variability of the LBVs makes them easily detectable even in extragalactic systems. They are thus particularly interesting as potential indicators for the cosmological distance scale. If it can be shown that LBV outflows are purely driven by radiation pressure they can be analyzed with the empirical relation between the wind momentum and the luminosity (WLR) published by Kudritzki (1995): $\dot{M}v_\infty R_\star^{1/2} \sim L$.
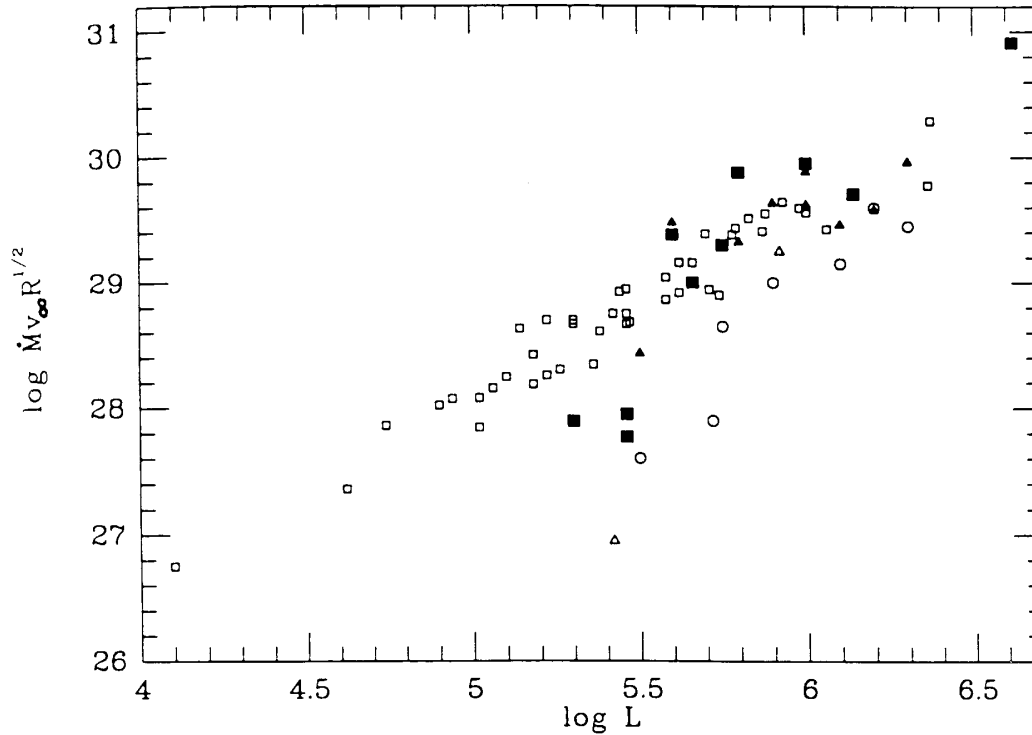
Figure 1.1: $\dot{M}v_\infty R_*^{1/2}$ (in $M_\odot yr^{-1}$, $km\,s^{-1}$, and $R_\odot$) versus L (in $L_\odot$). Full squares: LBVs of Leitherer (1997); full triangles: Ofps/WN9 stars of Pasquali et al. (1997), and HD 80077 and HD 152236; open squares: Galactic OBA stars of Kudritzki et al. (1996); open circles/triangles: SMC/M33 stars of Kudritzki et al. (1996). This plot is reproduced from Leitherer (1997).

For normal O supergiants this relation is very tight and theoretical models based on spherically symmetric, radiation driven winds can explain the hydrodynamic processes in these objects very well. However, the mass-loss mechanism in LBVs with their very massive winds and irregular spectrophotometric variability is still uncertain. In Figure 1.1 this is illustrated in the much larger scatter of LBVs around the general trend. For the most recent results on WLR for galactic BA supergiants see Kudritzki et al. (1999).

Using a core-halo approximation for photosphere and stellar wind, the theory of hydrodynamics shows that $\dot{M}$ is determined by the forces existing in the region below a critical point (which is usually close to the sonic point). Additional forces to the radiation pressure in the supersonic region may change the wind velocity structure (in particular v_∞) but do not influence the mass-loss rate. In general more refined models are necessary when the above assumption is not valid (see Lamers & Cassinelli 1999).

Processes like pulsations and local magnetic fields together with rotation have been proposed to explain the atmospheric variabilities. These forces act at the base of the wind, i.e. in subsonic regions, and thus influence $\dot{M}$.

Furthermore, even small density or velocity perturbations can quickly grow into shocks which would change the density, velocity and temperature structure of the stellar winds. In the case of inhomogeneities in the wind of LBVs, current mass-loss rates could be drastically overestimated (Barlow & Cohen 1977). Schmid-Burgk (1982) showed that narrow streaming outflow cones mimic high mass-loss rates as well while the effects of non-spherical wind geometries overestimate $\dot{M}$ only by a relatively small amount (typically less than a factor two).

Continuous high resolution spectroscopic observations are needed to investigate the underlying physical mechanisms of LBV-variabilities and to study their effects on mass-loss rates.

Until recently the required high-resolution spectrographs were only available at large telescopes (i.e. diameters $\gtrsim 1$ m). The time-allocation pressure factor on these telescopes is generally too high to carry out dedicated monitoring programs to study the observed variabilities over the relevant time scales (on the order of weeks to months). However, the development of a fiber-linked echelle spectrograph with an efficient CCD detector at the observatory of Heidelberg permitted a spectroscopic monitoring program of bright stars on sub-meter class telescopes. These observations provide for the first time the required time resolution for a detailed scrutiny of the spectroscopic variability of LBVs, which is presented here.

As seen in W-R stars, inhomogeneities in the outflows would manifest themselves in faint narrow substructures in the spectral lines. Because the wind velocities in the LBV phase are an order of magnitude smaller than in W-R stars, a corresponding higher resolution is necessary to detect narrow line features in LBV spectra. Consequently we have obtained ultra-high resolution spectra ($R \gtrsim 50\,000$) with high S/N ratios which are presented in the second part of the thesis.

1.2   General Characteristics of LBVs

The term "Luminous Blue Variables", introduced by Conti (1984), combines stars identified as S Dor and Hubble-Sandage variables and as P Cygni-like stars into one unique class. These objects are (apart from supernovae) visually the most luminous stars in the universe ($M_v = -8$ to -11) and exhibit irregular photometric and spectroscopic variations over several distinct time scales, ranging from weeks to decades. In particular they are characterized by three photometric variability stages:

1. Sporadic *giant eruptions* with changes in V magnitude by more than 3 mag.

2. *Moderate variability* or *S Dor eruptions* at optical and IR wavelengths with amplitudes of $1 - 2$ mag on time scales of years to decades at constant bolometric brightness (i.e. luminosity).

3. *Microvariations* of up to a few tenths of a magnitude on time scales of weeks to months.

The defining characteristic is showing variations of type 1 and/or 2 – whereas the third type is common for many luminous stars.

Together with the photometric changes we observe spectroscopic variations: at quiescence (optical minimum), LBV stars show early-type spectra (OB to early-A), while during an outburst (optical maximum) they typically exhibit mid-A to early-F spectra. Mass loss rates of the order of 10^{-5} to $10^{-4}\,\mathrm{M_\odot yr^{-1}}$ are usually derived by fitting the emission lines of the optical spectrum (in particular Hα) which often have P Cygni profiles. The wind velocities are usually measured from the UV or optical spectral lines and range typically from ~ 100 to $\sim 200\,\mathrm{km\,s^{-1}}$ (see e.g. Wolf 1992).

The outbursts and dense winds result in extended nebular shells. Studies of the dynamics of these envelopes yield a typical kinematic time scale of approximately $10^4 - 10^5$ yrs (see e.g. Leitherer et al. (1994) for AG Car). Most LBV nebulae exhibit axisymmetric morphologies (Nota et al. (1995); see also previous image of η Car).

LBVs represent an episode in the evolution of high mass OB stars to Wolf-Rayet stars: e.g. Langer (1994) proposed the following evolutionary sequence stars with $M_{ZAMS} \gtrsim 40\,\mathrm{M_\odot}$:

$$O \to Of \to \text{H-rich WN} \to \text{LBV} \to \text{H-poor WN} \to \text{H-free WN} \to WC \to SN.$$

Bohannan (1997) estimated the LBV lifetime from the relative numbers of W-R stars and LBVs in the Large Magellanic Cloud (LMC) to $\sim 40\,000$ yrs using a W-R lifetime of 5×10^5 yrs and 115 W-R stars and 10 LBVs[1]. This corresponds to about 1 % of the main sequence lifetime of a $40\,M_\odot$ precursor (de Koter 1993).

A more detailed discussion of the properties of LBVs can be found in the comprehensive review of Humphreys & Davidson (1994).

1.3   Current State of Research

In recent years significant progress has been made in the theoretical interpretation of LBV phenomena.

The observed moderate photometric variations which are found to occur at almost constant luminosity (Wolf et al. 1981, Lamers 1989) are explained as a change in bolometric correction due to a variation of the photospheric radius and temperature: during minimum, when the star is hottest, it is smallest in radius and vice versa. That is, on its way from the minimum to the maximum phase the star is expanding and its temperature is cooling proportionally to the square root of the radius. This behavior can be explained by two mechanisms:

1. The variations are due to a drastic, but unexplained, increase in mass loss which makes the wind optically thick in the continuum. This would form a "pseudo-photosphere" which would mimic an increase of the photospheric radius (Lamers 1987).

2. The variations are due to a drastic, but unexplained, increase in *real* stellar radius (Leitherer et al. 1989).

Lamers (1995) reports that in the analysis of S Dor a true radius change between 100 and $380\,R_\odot$ is required and that the changes in luminosity suggest that about 10^{-3} to $10^{-2}\,M_\star$ participate in the expansion of the star. De Koter (1997) showed with detailed calculations that a change of mass loss is generally insufficient to explain the required change in radius. This led to the important implication that the responsible mechanism for the radius change *must* act in subphotospheric/interior layers of the star.

One of the possible causes for the LBV variability phenomena is the close vicinity to their respective Eddington limit as represented by the location of many LBVs in the Hertzsprung-Russell-diagram (HRD) around the Humphreys-Davidson limit. Langer (1997) has shown that if the evolution of massive stars toward the Eddington limit is responsible for the giant eruptions, then the stellar rotation defines the critical hydrostatic stability limit. This Ω-limit can naturally explain the highly bipolar nebulae that are seen around LBVs. Hydrodynamical simulations of the giant eruption of η Car by García-Segura et al. (1996) illustrate this behavior. Lamers (1997) calculated the location of the *atmospheric* Eddington limit (AEL) in the HRD and showed that LBVs are close to the AEL with $\Gamma \simeq 0.95$. Thus changes of the stellar interior will result in drastic variations of the overlaying atmosphere.

Pulsations (radial and non-radial, normal and strange modes) occur naturally during the evolution of massive stars with high mass-loss rates when the luminosity-to-mass ratio is high as it is the case for LBVs (calculations of Glatzel 1997). In particular, strange mode instabilities (SMIs) can be associated with the opacity bumps of Fe, He and He/H and coincide with the observed location of LBVs in the HRD around the Humphreys-Davidson limit. Cox et al. (1997) and Guzik et al. (1997) found that outbursts require pulsations to be triggered in their models and that SMIs are controlled by the surface He content.

---

[1] There are currently only six confirmed LBVs known in the LMC; Bohannan used the number 10 in his estimation to account for possible unknown objects.

Stothers & Chin (1993, 1996) have suggested adiabatic instabilities as the cause for minor and major LBV outbursts. However, the reported instabilities could not be reproduced by models calculated by Glatzel & Kiriakis (1996).

Davidson (1989) and Maeder (1992) proposed a "Geyser mechanism" to explain the LBV outbursts: here a density inversion layer is found in the models where the thermal time scale is shorter than the dynamical time scale in large regions.

Recent theoretical models show that density irregularities can form within a few stellar radii due to shocks from line-driven instabilities (Feldmeier 1995, 1998) and/or in corotating interactive regions (see recent 2D-CIR models of Owocki 1999). At larger distances "ram-ram" pressure mechanisms and fast/slow wind models can create inhomogeneities that reproduce observed LBV nebulae structures very well (García-Segura et al. 1996).

Fullerton (1990) conducted a large spectroscopic survey of O stars in his PhD thesis and found absorption line profile variations (LPVs) that could be attributed to pulsations, rotational modulations or evolving substructures in the stellar wind. Similar LPVs, although on different times scales and also affecting emission lines, have been observed in BA supergiants (Kaufer 1996), B hypergiants (Rivinius et al. 1997), W-R stars (see e.g. the relevant sections in: Nonisotropic and Variable Outflows from Stars, ASP Conference Series Vol. 22) and LBVs (see e.g. Wolf & Kaufer (1997), Stahl (1997) and this study). Hydrodynamical codes have been developed to model these observations, e.g.:

- Simulations of Corotating Interaction Regions (CIRs) and Discrete Absorption Components (DACs) in rotating OB-Star Winds including the effects on limb darkening have been carried out by Cranmer (1996), Cranmer & Owocki (1996) and Owocki et al. (1996).

- Lepine et al. (1996) modeled the profile variations of emission lines in W-R winds by clumps propagating in the wind direction and causing large turbulent motions and shock waves.

- Rivinius et al. (1997) incorporated density irregularities in their code (SEIDYNAMIC) to model P Cygni-type line variations in B hypergiants.

- Non-radial pulsation codes have been developed and applied to model the spectral variations of rotating early-type stars (e.g. Townsend 1997, Schrijvers et al. 1997).

To summarize we find that the above mentioned theoretical models can explain the characteristic variations of LBVs: the S Dor variability may be modeled by pulsations and adiabatic instabilities and giant outbursts from crossing the Eddington-limit or via the "Geyser mechanism". Nevertheless to decide which mechanisms really exist or dominate, continuous spectroscopic observations of LBVs are necessary. In particular the pulsation models need accurate radial velocity measurements of photospheric lines over a long time period to confirm their results.

Spectroscopic observations of early-type stars have been carried out by the Heidelberg research group of Wolf, Stahl and Mandel and have been presented by Gäng (1993; A hypergiants), Kaufer (1996; BA supergiants) and Rivinius et al. (1997; B hypergiants). The tools developed for these studies provide the basic analysis methods for the studies of LBV variabilities as carried out in this thesis.

The studies of "ordinary" super- and hypergiants from the above long-term spectroscopic monitoring programs revealed that a variety of effects might be responsible for the observed line variations: Kaufer et al. (1996) explains the observed variability of BA-type supergiants with rotational modulation due to weak magnetic surface structures and instabilities of the ionization structure of the wind. In the early B hypergiants of the sample, propagating discrete absorption components (DACs) could be seen directly

and were modeled with a dynamical wind code assuming density perturbations of ca. 10% at the base of the wind (Rivinius et al. 1997).

It has been known for some time that W-R stars exhibit narrow-line features (seen in both emission and absorption (Brown & Richardson 1994)) and that O stars show discrete absorption components (DACs) in their spectral lines (Prinja 1992 for O stars). Narrow-line features have also been detected in the IUE spectra of late B-type supergiants (Bates & Gilheany 1990). These features are ascribed to regions of locally enhanced densities, indicating clumping and/or asymmetries in the wind structure, and have dramatic consequences on the observed wind structure (see IAU Symp. No. 163 about W-R star properties). The DACs are excellent probes of the varying mass-loss features which may occur in the winds of LBVs: they reflect changes in the column densities and the distribution of absorbing matter in the wind, thus delivering information on the line formation depth (Willis et al. 1989).

Several factors indicate that LBV stars may have irregular or clumpy winds. The LBV stars are known to have variable mass-loss rates and/or to shift in and out of the W-R phase (e.g. AG Car, see Leitherer et al. (1994) and possibly HD 5980, a WN eclipsing binary system that has experienced an LBV-like eruption (Barbá et al. 1995)). The existence of inhomogeneities in the circumstellar envelope of the LBV prototype P Cygni is also supported by recently obtained infrared observations with ISO (Lamers et al. 1996). Finally, coronographic images exhibit clumpy substructures in LBV nebulae (Nota et al. 1995).

It is plausible why such line structures have not yet been detected in LBVs – as opposed to W-R or O stars: since the wind velocities in the LBV phase are an order of magnitude smaller than in W-R and O stars, a correspondingly higher resolution is necessary to detect narrow line features in LBV spectra. The spectra observed for the ultra-high resolution project provide for the first time sufficient high spectral resolution *and* high S/N to check for spectroscopic evidence of inhomogeneities in LBV winds.

The most up-to-date progress reports in the field of LBV research can be found in the proceedings of the LBV-workshop "Luminous Blue Variables: Massive Stars in Transition", ASP Conference Series, Vol. 120, eds. A. Nota & H.J.G.L.M. Lamers, 1997 and the IAU Colloquium 169 "Variable and Non-spherical Stellar Winds in Luminous Hot Stars", eds. B. Wolf, O. Stahl & A.W. Fullerton, 1999.

1.4   Outline of this Work

From the previous overview of the current state of LBV-research we can summarize the following open questions:

- The time development of wind and photospheric spectral lines is poorly studied. The causes for the variability on all time scales is unknown.

- The influence of suggested existing processes like radial or non-radial pulsations and rotational modulated magnetic fields on the photospheric variability is unknown.

- The role of possible shocks in the stellar outflows is unclear.

- The contributions of the previously described processes to the derived mass-loss rate is completely uncertain.

- The interaction between photospheric and wind variability has been poorly investigated. Previous core-halo approximations are too inaccurate to describe the velocity and density structure of LBV atmospheres if photospheric processes influence the supersonic regions and possibly drive the wind and determine the mass-loss rates.

- The question of why most LBV's, the descendants of O stars, are surrounded by bipolar outflows, whereas O star winds are spherically symmetric, is open.

- Is our mass-loss calibration at the high-mass end systematically wrong due to inhomogeneities and clumps in the winds?

The main goal of this work is to deliver the material necessary to tackle the previously described research areas and make initial approaches to solve the open questions with basic analyses.

To address the variability issues, spectral observations with high resolution in time and spectral wavelength over a sufficiently long time period have been carried out. Because of the enormous observational expense of this program we concentrated on one object – HD 160529 – for this monitoring program. The analyses and discussion of these data are presented in chapter 3 and constitute the main part of this thesis.

To study the question of inhomogeneities in the stellar wind we have observed 20 LBVs and LBV candidates[2] in the Galaxy and the Magellanic Clouds with a spectral resolving power of $R = 50\,000 - 100\,000$. We have tried to achieve the highest possible S/N ratios with the available observing time to resolve and detect the expected faint narrow substructures in the spectral lines. These observations are discussed in chapter 4. The mean profiles of the obtained spectra are presented in the appendix together with a summary of the relevant observational informations for quick reference.

In chapter 2 we outline the main theoretical points of stellar astrophysics and pulsation; the collected formulae serve as references in the respective analyses. In chapter 5 we summarize our results and draft future prospects.

1.4.1 Selection of Program Stars

Currently only telescopes of the sub-meter class have low enough observing time pressure factors to allow monitoring programs over time spans of months, which are typical time scales for the observed LBV microvariations. The European Southern Observatory (ESO) generously allocated us sufficient time on its 50-cm telescope in La Silla/Chile to observe stars in the southern hemisphere, where most confirmed LBVs are located. Previous observations at a 70-cm telescope with the echelle spectrograph of the Landessternwarte Heidelberg, which was planned to be used for the spectroscopic monitoring, revealed that stars with visual brightness of $V \lesssim 7$ are bright enough to achieve the desired high S/N ratio (~ 100) in a reasonable exposure time (i.e. under two hours per exposure).

With $V \approx 6.5$ to 6.9 the established LBV HD 160529 fulfills this requirement. Additionally it has been one of the initial stars observed in the "Long-term Photometry of Variables (LTPV)" program at ESO (Sterken 1983). Thus a large database of its photometric variability was already available and has been analyzed by various authors.

A comparison of the photometric and spectroscopic variability to check for correlations made this object particularly desirable for the proposed research project. Quasi-periods on the order of weeks to months have been observed in the photometric variability of HD 160529. Consequently the initiated spectroscopic monitoring project covered similar durations.

For our proposed ultra-high resolution study of LBV atmospheres we were granted observing time at three different observing sites. We selected the program stars to be LBVs or LBV-candidates with visual

---

[2]Due to a software error during the observations at the AAT on January 1996 the data of 4 stars were not usable and are thus not included in the discussion of this project.

brightness high enough to achieve a typical S/N ratio of around 100 while covering the whole optical wavelength range with a resolving power of at least 50 000.

This allowed us to observe most confirmed LBVs brighter than $V \lesssim 11.0$ in the Galaxy and the Large and Small Magellanic Clouds. The achieved high resolution corresponds to a velocity resolution of $\lesssim 6 \, \mathrm{km \, s^{-1}}$ which is sufficient to observe narrow line features in the slow moving outflows which have a typical sound velocity of $\gtrsim 10 \, \mathrm{km \, s^{-1}}$.

Table 1.1 lists all objects that were observed for this thesis project with their visual brightness and co-ordinates for epoch 2000. The noted observing time, instrument and approximate spectral resolution ($\sim \lambda/\Delta\lambda$) correspond to observations for the ultra-high resolution project (see chapter 4).

Table 1.1: Observed Program Stars (sorted by right ascension, i.e. α_{2000}).

Object	V [mag]	α_{2000} [h,m]	δ_{2000} [° ′]	Observing run	Instrument [$]	$\sim \lambda/\Delta\lambda$
HD 5980 [†]	9.3	00 59	−72 10	Oct 1995	UCLES/AAT	50 000
R 40	10.7	01 07	−72 28	Oct 1995	UCLES/AAT	50 000
R 71	9.8	05 02	−71 20	Oct 1995	UCLES/AAT	50 000
R 81	10.4	05 10	−68 46	Oct 1995	UCLES/AAT	50 000
S Dor	10.0	05 18	−69 14	Oct 1995	UCLES/AAT	50 000
HDE 269582 [‡]	11.3	05 27	−68 59	Jan 1996	UCLES/AAT	50 000
R 110 [‡]	10.3	05 30	−69 03	Jan 1996	UCLES/AAT	50 000
R 127 [‡]	11.1	05 36	−69 30	Jan 1996	UCLES/AAT	50 000
R 143 [‡]	12.2	05 39	−69 08	Jan 1996	UCLES/AAT	50 000
HD 80077 [†]	7.6	09 15	−49 58	Apr 1996	CES/CAT	60 000
HR Car	8.6	10 22	−59 37	Apr 1996	CES/CAT	60 000
η Car	6.2	10 45	−59 41	Apr 1996	CES/CAT	60 000
AG Car	6.9	10 56	−60 27	Apr 1996	CES/CAT	60 000
HD 326823 [†]	9.0	11 09	−60 43	Apr 1996	CES/CAT	60 000
HD 160529	6.7	17 41	−33 30	Oct 1995	UCLES/AAT	50 000
HD 316285 [†]	9.1	17 48	−28 00	Apr 1996	CES/CAT	60 000
HD 168607	8.3	18 21	−16 22	Oct 1995	UCLES/AAT	50 000
HD 168625	8.4	18 21	−16 22	Oct 1995	UCLES/AAT	50 000
HD 169454 [†]	6.6	18 25	−13 58	Apr 1996	CES/CAT	60 000
P Cyg	4.8	20 18	+38 02	May 1996	CFS/CFT	100 000

[†] LBV-candidate
[‡] Observations not usable
[$] UCLES: University College London Echelle Spectrograph, AAT: Anglo-Australian Telescope,
   CES: Coudé Echelle Spectrometer, CAT: Coudé Auxiliary Telescope,
   CFS: Coudé Feed Spectrograph, CFT: Coudé Feed Telescope

1.5   Notes about Spectral Line Accuracies

We point out that there are considerable differences in the literature about the laboratory rest wavelengths (λ_{lab}) of specific spectral lines. For example the He I $\lambda5876$ line is formed from multiplet 11 with at least 6 different contributions with $\lambda_{lab} = 5875.599 - 5875.966$ Å (Kurucz & Bell 1995).

Many authors still use the old Moore tables or just pick the wavelength with the highest oscillator strengths ($\log gf$) as λ_{lab}. Typical differences in the various line lists of $\Delta\lambda \approx 0.1$ Å correspond to a Δv of $\sim 5\,\mathrm{km\,s^{-1}}$ at 5876 Å. In high-resolution spectra such as ours (dispersion of wavelength calibration less than $1\,\mathrm{km\,s^{-1}}$) this introduces a significant error in the absolute v_{rad} measurements. Calculating the mean value, weighted with the given oscillator strengths or intensities from the respective λ_{lab}-tables, improves these values but still leaves inaccuracies (in the case of He I λ5876 the error is of the order of 0.01 Å or $\sim 0.5\,\mathrm{km\,s^{-1}}$). The more recent wavelength tables of Kurucz & Bell (1995) and Hubeny (1996) contain very similar values and yield the same results for the weighted averages.

A more accurate procedure is to let the synthetic codes handle the convolution of the various line contributions but then fitting these spectral lines to get λ_{lab} values (e.g. using the line center of Gaussian fits) introduces errors (in our tests with TLUSTY 194/SYNSPEC 41 and ATLAS 9 models the fitting errors were of the order of $\lesssim 0.03$ Å). In this thesis we use the published values of Hubeny (1996) when there is only one unique transition in the line list and otherwise use the line centers of single Gaussian fits to appropriate synthetic spectra calculated with TLUSTY 194/SYNSPEC 41 as λ_{lab} values. Table 1.2 lists the λ_{lab} values used, except for the analyses and plots of the forbidden iron lines in P Cygni where we took the λ_{lab} values from Coluzzi (1993).

Fortunately this λ_{lab} problem only causes a shift in the *absolute* velocity determination (which influences e.g. the derived value of v_{sys}); the amplitude of the radial velocity variations are independent of λ_{lab} and have the same *differential* value.

In Table 1.3 we list the values for the He I λ5876 and He I λ4471 lines from the literature and our measurements of the calculated synthetic spectrum to illustrate the differences in the atomic data of published line lists. In column 3 we have listed the oscillator strengths ($\log gf$) as given in the line lists of Hubeny (1996) and Kurucz & Bell (1995) or the intensities (INT) from the tables of Moore 1972.

Table 1.2: λ_{lab} values [in Å] of selected spectral lines as used in this thesis. The values are taken from line lists of Hubeny (1996) or from single Gaussian fits to the TLUSTY 194/SYNSPEC 41 spectra. The list is sorted by rising λ_{lab} value within each element group. Line-ID: element, ionization stage, rounded rest wavelength (well-known diagnostic lines like Balmer lines, Na D lines, ... are listed with their common names (e.g.: H 9, H 8, Hε, Na D1, Ca K, ...) and thus deviate from the usual line-ID specifications).

Line-ID	λ_{lab}	Line-ID	λ_{lab}	Line-ID	λ_{lab}
H 11 3771	3770.632	He I 4922	4921.931	Mg II 4481	4481.201
H 10 3798	3797.900	He I 5015	5015.678	Si II 4553	4552.640
H 9 3835	3835.386	He I 5876	5875.668	Si III 4568	4567.840
H 8 3889	3889.051	He I 6678	6678.154	Si III 4575	4574.757
Hε 3970	3970.074	Ca K 3934	3933.664	Si III 5978	5978.930
Hδ 4102	4101.737	Ca H 3968	3968.469	Si II 6347	6347.110
Hγ 4340	4340.468	Na D2 5890	5889.951	Si II 6371	6371.371
Hβ 4861	4861.332	Na D1 5896	5895.924	Fe II 5074	5073.903
Hα 6562	6562.817	Ti II 4469	4468.510	Fe II 5087	5086.701
He I 4026	4026.190	Ti II 4780	4779.985	Fe II 5243	5243.306
He I 4388	4387.929	N II 5667	5666.629	Fe II 5387	5387.136
He I 4471	4471.499	N II 5711	5710.766	Fe II 6248	6247.541

Table 1.3: Comparison of atomic line data. Line-ID: element, ion-
ization stage, multiplet-number, WAVE = Weighted AVErage (with
$\log gf$ or intensity). The entry in *Synthetic spectrum* is the line cen-
ter value of a single Gaussian fit to the TLUSTY 194/SYNSPEC 41
spectrum of Figure 3.21).

Line-ID	λ_{lab}	$\log gf$, (INT)	Source
He I 14	4471.477	(6)	Moore 1972
He I 14	4471.688	(1)	Moore 1972
He I 14	4471.507		WAVE–Moore
He I 14	4471.469	–2.198	Kurucz & Bell 1995
He I 14	4471.473	–1.028	Kurucz & Bell 1995
He I 14	4471.473	–0.278	Kurucz & Bell 1995
He I 14	4471.485	–1.028	Kurucz & Bell 1995
He I 14	4471.488	–0.548	Kurucz & Bell 1995
He I 14	4471.682	–0.898	Kurucz & Bell 1995
He I 14	4471.501		WAVE–Kurucz & Bell
He I 14	4471.469	–2.200	Hubeny 1996
He I 14	4471.473	–1.030	Hubeny 1996
He I 14	4471.473	–0.280	Hubeny 1996
He I 14	4471.485	–1.030	Hubeny 1996
He I 14	4471.488	–0.550	Hubeny 1996
He I 14	4471.682	–0.900	Hubeny 1996
He I 14	4471.501		WAVE–Hubeny
He I 14	4471.499		Synthetic spectrum
He I 11	5875.618	(10)	Moore 1972
He I 11	5875.650	(10)	Moore 1972
He I 11	5875.989	(1)	Moore 1972
He I 11	5875.651		WAVE–Moore
He I 11	5875.599	–1.511	Kurucz & Bell 1995
He I 11	5875.614	–0.341	Kurucz & Bell 1995
He I 11	5875.615	+0.409	Kurucz & Bell 1995
He I 11	5875.625	–0.341	Kurucz & Bell 1995
He I 11	5875.640	+0.139	Kurucz & Bell 1995
He I 11	5875.966	–0.211	Kurucz & Bell 1995
He I 11	5875.661		WAVE–Kurucz & Bell
He I 11	5875.599	–1.510	Hubeny 1996
He I 11	5875.614	–0.340	Hubeny 1996
He I 11	5875.615	+0.410	Hubeny 1996
He I 11	5875.625	–0.340	Hubeny 1996
He I 11	5875.640	+0.140	Hubeny 1996
He I 11	5875.966	–0.210	Hubeny 1996
He I 11	5875.661		WAVE–Hubeny
He I 11	5875.668		Synthetic spectrum

Chapter 2: Theory

Considerable progress has been made in recent years in modeling the spectra of hot star atmospheres. Particularly impressive results have been achieved by Najarro (1995) in modeling the spectra of the LBV P Cygni. However, the inclusion of many important mechanisms (NLTE, line blanketing, expanding atmosphere, electron scattering, rotation, ...) make these codes very complex and require long computation times even on current high-speed supercomputers.

It is thus often necessary to select specific codes that model only the particular features one wants to study (e.g. photosphere, wind, variability), while ideally the effects of neglected parameters should also be estimated (e.g. with another code) in order to determine the validity of the obtained results.

In this chapter we outline the theoretical framework of modeling stellar atmospheres and summarize the basics of pulsation theory. For detailed explanations of the underlying concepts we refer to the standard textbooks and review articles on stellar atmospheres (in particular Lamers & Cassinelli 1999, Mihalas 1978, Kudritzki 1988) and on pulsations (e.g. Cox 1980, Unno et al. 1989). We refer to these sections later when we analyze the corresponding items.

2.1 Stellar Photospheres

Here, a photosphere is considered to be a plane-parallel, horizontally homogeneous atmosphere in radiative and hydrostatic equilibrium. This approximation is valid when the thickness of the atmosphere is small compared with the stellar radius and effects of wind, pulsation, magnetic fields, etc. are negligible.

The simplest atmospheric models can be constructed assuming local thermodynamic equilibrium (LTE). In these calculations we have a Maxwellian velocity distribution of particles with a local kinetic temperature T, which can be used to compute the excitation and ionization conditions by means of the simple equations of *Boltzmann*:

$$\frac{N_s}{N_0} = \frac{g_s}{g_0} e^{-\chi_{e,s}/kT} \tag{2.1}$$

and *Saha*:

$$\frac{N_{i,0}}{N_{0,0}} = \frac{g_{i,0}}{g_{0,0}} 2 \frac{(2\pi m_e kT)^{3/2}}{h^3 N_e} e^{\chi_{i,0}/kT} \tag{2.2}$$

where k is the Boltzmann constant, h the Planck constant, N_0 the number of atoms in the ground level 0 with statistical weight g_0, N_s the number of atoms in the excitation state s with statistical weight g_s and excitation potential $\chi_{e,s}$, $N_{i,0}$ the number of atoms in ionization state i and ground level 0 with ionization potential $\chi_{i,0}$, $N_{0,0}$ the number of neutral atoms in the ground level 0, N_e the number of free electrons, m_e the electron mass; the term before the exponent in the Saha equation is the statistical weight of the ionized atom in the ground level plus one free electron divided by the statistical weight of the neutral atoms in the ground level.

Under the assumption that the absorption coefficient is independent of the frequency we can construct a mean opacity. Together with the distribution of atoms and ions described by Equations 2.1 and 2.2 we can then calculate a *grey* atmosphere to get a continuum spectrum.

The next important step is to include line blanketing (i.e. the influence of spectral lines on the resulting atmospheric structure and predicted emergent spectrum) in the calculations. In LTE the total line opacity is a function only of temperature and electron density and therefore determined locally. Dealing with millions of lines still makes this a nontrivial problem that requires some kind of statistical approach. A solution was provided with the introduction of opacity distribution functions (ODF) which resample the total opacities in given frequency intervals. In particular Kurucz (1979, 1992) has calculated widely used grids of LTE line-blanketed model atmospheres that consider more than 10^8 spectral lines for a model construction.

In non-LTE (NLTE) calculations the number densities of selected energy levels and elements are allowed to depart from their LTE values. The influence of NLTE effects can be expressed directly by means of "departure coefficients" which are defined as the ratio of the NLTE to LTE occupation numbers: $b_i = n_i(\text{NLTE})/n_i(\text{LTE})$. The individual spectral lines contribute in non-LTE not only to the total opacity but also to the global statistical equilibrium and so influence the radiative rates, and therefore the level populations, of other elements. This affects the conditions of different layers in the atmosphere and makes the calculations inherently nonlocal and highly nonlinear.

Is it really necessary to spend so much efforts in understanding the conditions of stellar atmospheres? For stars in a certain range of stellar parameters the answer is definitely yes.

The LTE-assumption is valid at high densities when collisional processes of particles ensure a detailed balance of the relevant energy levels. In stellar atmospheres of early-type supergiants where $\log g$ (and thus the density) is low and radiation rather than collision dominates the population of energy levels (i.e. at high temperatures) this condition is violated. The experience from more than two decades of computing non-LTE model atmospheres (summarized e.g. by Kudritzki & Hummer 1990) has demonstrated that non-LTE effects play a crucial role in atmospheres of virtually all types of hot stars (effective temperature larger than $\sim 10\,000$ K).

Yet, neglecting line blanketing introduces an uncertainty, which sometimes outweighs the correct non-LTE calculations. The only reliable solution is to calculate non-LTE model atmospheres with full line blanketing.

In the 1970s it became clear that the basic physical ingredient to understanding a stellar atmosphere is the nonlocal *coupling* of physical quantities (level population, radiation field, temperature). The tool which allowed an explicit and fully consistent treatment of such a coupling was the complete linearization (CL) method as introduced by Auer & Mihalas (1969). However it was soon realized that only a very limited number of atomic levels and opacity sources could be treated within this framework due to limitations of computer resources (e.g. the CPU runtime increases as the cube of the total number of unknowns). With millions of lines to consider this would be beyond the capacity of even the most powerful computer.

A solution was found by realizing that not all possibilities of couplings are equally important: that only the essential parts have to be treated explicitly; the rest can be done by iterations.

The accelerated lambda iteration (ALI) method (for a review see e.g. Hubeny 1992) utilized this idea by expressing the radiation intensity through an approximate lambda operator acting on the source function plus a correction term from the previous iteration.

This method still treated all energy levels separately and was thus limited to treating only $\sim 100 - 1000$

lines of mostly light elements (like C, N, O). To solve this problem Anderson (1989) introduced a statistical method where many energy levels were grouped together in a small number of "superlevels" which makes it possible to calculate also atoms with very complex energy levels such as the iron-peak elements.

The incorporation of the above mentioned methods led to numerical codes that are able to calculate truly line-blanketed non-LTE atmospheres. In particular TLUSTY 194 and SYNSPEC 41, the codes we used for our analyses of the photospheric lines, are state-of-the-art programs to calculate NLTE atmospheres and synthetic spectra.

2.2 Stellar Winds

Many hot stars and particularly all LBVs have extended atmospheres where the above plane-parallel approximation is not valid but a spherical geometry has to be used in the calculations. Furthermore most spectral lines show a definite influence of stellar outflow (indicated by asymmetric line profiles, sometimes of the P Cygni type) and thus the static assumption has to be given up and hydrodynamic codes are necessary to model the observed spectra.

To model expanding atmospheres it is commonly assumed that the stellar outflow is in a steady state (i.e. time-independent) and that it is radially and spherically symmetric. In the polar coordinate system (r, Θ, Φ) these assumptions significantly simplify the calculation of the relevant equations since the velocity, density and temperature distribution depend only on the radial distance r and have no angular components in Θ or Φ.

For early-type stars the dominant outward force driving the stellar winds is the strong radiation field of the star: photons from the photosphere transfer momentum to ions via scattering and absorption processes. This results in a net outward force mainly on ions with high absorption coefficients like C, N, O, Fe. Through Coulomb-interaction these particles drag the surrounding ions and electrons with them and form the total stellar outflow.

These conditions lead to wind velocity profiles where the speed of the expanding material increases in the outward direction and reaches a terminal velocity, v_∞, at a large distance from the star. Such wind velocity fields are well described with functions of the beta-law type and an initial velocity, v_0:

$$v(r) = v_0 + (v_\infty - v_0) \left(1 - \frac{R_\star}{r}\right)^\beta \tag{2.3}$$

The stellar wind is then described by the equations of mass, momentum and energy conservation. The equation of *mass conservation* is:

$$\frac{1}{r^2} \frac{\partial}{\partial r} (\rho v r^2) = 0 \tag{2.4}$$

where ρ is the mass density and its product with the velocity, ρv, the mass flux per unit area of a spherical surface around the star. Integrating equation 2.4 provides the total outward mass flux with $\dot{M}$ as the *mass-loss rate*[1]:

$$\dot{M} \equiv -\frac{dM}{dt} = 4\pi \rho v r^2 = constant \tag{2.5}$$

The acceleration of the outflowing material is given by the *wind momentum equation* which is formed by the combination of radiative acceleration (g_{rad}) and pressure gradient (dP/dr) counteracting the

---

[1] We adopt the conventional use of the mass-loss rate $\dot{M}$ as a positive number although we can see in Equation 2.5 that $\dot{M}$ is negative for stellar winds.

gravitational forces (where G is the gravitational constant) of the star:

$$\frac{dv}{dt} \equiv v\frac{dv}{dr} = -\frac{1}{\rho}\frac{dP}{dr} - G\frac{M}{r^2} + g_{rad}. \tag{2.6}$$

The gas pressure P is related to the temperature T by the *equation of state* for a perfect gas:

$$P = \frac{\rho kT}{\mu m_H} = \frac{\rho RT}{\mu} = \rho v_s^2, \tag{2.7}$$

where k is the Boltzmann constant, μm_H the mean particle mass, $R = k/m_H$ the gas constant and v_s the isothermal speed of sound.

Provided that all energy is transported by photons and no sources or sinks of energy exist in the stellar atmosphere then the *equation of radiative equilibrium* describes the energy state:

$$L = 4\pi r^2 H = constant \tag{2.8}$$

Equation 2.8 implies that that the stellar luminosity L is independent of the distance r. H is the integrated radiative flux, i.e. the total amount of energy integrated over all frequencies. For black-body radiation this corresponds to the *Stefan-Boltzmann law*:

$$H = \sigma T_{\text{eff}}{}^4. \tag{2.9}$$

An equivalent formulation is that locally the absorbed amount of energy is equal to the amount that is emitted. With ϵ_ν and κ_ν the absorption and emission coefficients and J_ν the mean intensity, we get:

$$\int_0^\infty (\kappa_\nu J_\nu - \epsilon_\nu)d\nu = 0. \tag{2.10}$$

Similar to H, J_ν is the total intensity integrated over all frequencies. These angle-averaged quantities describe the radiation field and are given by:

$$J_\nu = \frac{1}{2}\int_{-1}^{1} I_\nu(r,\mu)\,d\mu, \tag{2.11}$$

$$H = \int_0^\infty H_\nu\,d\nu, \tag{2.12}$$

with the flux per frequency (also called *Eddington flux*):

$$H_\nu = \frac{1}{2}\int_{-1}^{1} \mu\, I_\nu(r,\mu)\,d\mu = \frac{1}{4\pi}F_\nu(r), \tag{2.13}$$

where $F_\nu(r)$ is the radial flux component and $\mu = \cos\Theta$ is the cosine of the angle between a beam of radiation and the outward normal on a spherical surface element.

The specific intensity I_ν along a distance $ds = dr/\cos\Theta$ is given by the *equation of transfer*:

$$\frac{dI_\nu}{ds} = \mu\frac{\partial I_\nu}{\partial r} + \frac{1-\mu^2}{r}\frac{\partial I_\nu}{\partial \mu} = \epsilon_\nu - \kappa_\nu I_\nu. \tag{2.14}$$

The intensity after crossing a volume element I_ν is connected with the entering intensity $I_{\nu,0}$ via:

$$I_\nu = I_{\nu,0}\, e^{-\tau_\nu}. \tag{2.15}$$

The dimensionless variable τ_ν is called *optical depth*:

$$\tau_\nu = \int_0^s \kappa_\nu\, ds. \tag{2.16}$$

The ratio of emission and absorption coefficients is called the source function: $S_\nu = \epsilon_\nu/\kappa_\nu$ which becomes the *Planck function* B_ν for black-body radiation in thermodynamic equilibrium:

$$B_\nu(T) = \frac{2h\nu^3}{c^2}\frac{1}{e^{hc/kT}-1}. \tag{2.17}$$

The radiative acceleration in Equation 2.6, i.e. the amount of absorbed radiative momentum per time and mass, is given by:

$$g_{rad} = \frac{4\pi}{c}\frac{1}{\rho}\frac{1}{2}\int_0^\infty \int_{-1}^1 \kappa_\nu\, I_\nu\, \mu\, d\mu\, d\nu \tag{2.18}$$

The absorption coefficient κ_ν consists of three principal contributions: the Thomson scattering (mainly on electrons) κ_{Th}, the continuum absorption (i.e. bound-free and free-free absorption) κ_ν^c and the sum of all line absorption κ_ν^l:

$$\kappa_\nu = \kappa_{Th} + \kappa_\nu^c + \kappa_\nu^l. \tag{2.19}$$

Accordingly the radiative acceleration can be split into:

$$g_{rad} = g_{rad}^{Th} + g_{rad}^c + g_{rad}^l. \tag{2.20}$$

The line absorption coefficient is given by:

$$\kappa_\nu^l = \kappa\,\rho\,\phi, \tag{2.21}$$

with the line strength $\kappa \sim 1/\rho \sim 1/\Delta\nu_D$. The profile of an absorption line ϕ is determined by the intrinsic line width, the damping broadening, the thermal motions and the microturbulence (i.e. small scale turbulent motions). In stellar winds the density is usually low enough that damping can be neglected. The remaining line broadening mechanisms lead to a profile function that can be expressed as a normalized Gaussian. With the Doppler effect due to the expanding atmosphere ϕ becomes:

$$\phi(x) = \frac{1}{\sqrt{\pi}}e^{(-x-\mu v_{out})^2}, \tag{2.22}$$

with x the frequency displacement from the line center ν_0 measured in Doppler units:

$$x = \frac{\nu-\nu_0}{\Delta\nu_D} \tag{2.23}$$

and v_{out} the outflow velocity in units of the thermal velocity of the ion:

$$v_{out} = \frac{v(r)}{v_{th}}. \tag{2.24}$$

The characteristic length of flow, l_c, along which the density or ionization changes significantly, can be expressed by:

$$\frac{1}{l_c} = \frac{d\,ln\,\rho}{dr}.$$ (2.25)

The existence of $v(r)$ in the profile function results in a strongly anisotropic absorption coefficient: κ_ν^l is peaked at $x = \mu\,v_{out}$ and drops quickly outside this "interaction region" where the line is formed. The width of this zone Δs becomes small when $d(\mu\,v_{out})/ds$ becomes large. In the presence of a large velocity gradient, ϕ behaves like a δ-function and the optical depth shows the behavior of a step function (zero before and constant after $x = \mu\,v_{out}$). Sobolev (1957) first applied this approximation which significantly simplifies the calculations of radiative transfer equations. The location where $x = \mu\,v_{out}$ is called the *Sobolev point* and the limit where the δ-function approximation of ϕ is applicable is called the *Sobolev approximation* (hereafter SA). The SA is valid when $\Delta s \ll l_c$ which is a typical condition found in the supersonic velocity fields around stellar winds of early type stars.

With the SA it is possible to calculate the radiative acceleration due to many lines (of order 10^6). In contrast the physically exact treatment of the radiative transfer in the *co-moving frame* (hereafter CMF) is limited to several hundreds of lines because of the computational expense of this method.

Based on the previously described formulae, a self-consistent theory can be developed to derive the relevant stellar parameters. For example one can use the stellar luminosity L, mass M and radius R as free parameters and derive the density, velocity and temperature distribution together with the mass-loss rate and the emergent energy spectrum. Comparison with the observed spectra allows an iterative process to determine all parameters consistently. Figure 2.1 shows the scheme[2] for self-consistent modeling of stellar spectra used by Pauldrach et al. (1994). Note that the authors also solved the rate equations to derive the occupation numbers for an accurate NLTE treatment.

In a pioneering paper Castor, Abbott & Klein (1975, hereafter CAK) laid the groundwork for a self-consistent theory of radiation driven winds. The authors found that the force on the stellar material due to radiation in a large number of subordinate lines can be very large and is a function of the local velocity gradient in an expanding atmosphere. Further studies show that the dominant term in Equation 2.20 is indeed g_{rad}^l: the large number of absorption lines in hot stars, especially in the UV region, drives the wind. To simplify the radiative transfer equations CAK applied the Sobolev approximation and assumed radially streaming photons in their calculations.

Pauldrach, Puls & Kudritzki (1986, hereafter PPK) compared the CAK theory using the improved force multipliers of Abbott (1982) with exact calculations of the radiative transfer in the CMF. They found that the SA is a good description of hot star wind dynamics but that the "radial streaming" approximation leads to completely unrealistic results.

In cases where the turbulent velocities are not negligible ($v_{\text{turb}} \gtrsim 0.02\,v_\infty$) the SA calculated profiles do not agree well with observed line profiles. To solve these problems Lamers et al. (1987) developed the SEI method: **S**obolev approximation with **E**xact **I**ntegration. Here the source function is calculated using the escape probability method, whereas the transfer function is solved exactly. Their results agree very well with with synthetic profiles calculated with the CMF method but require very little CPU time so that interactive analyses of line profiles are still possible.

State-of-the-art synthetic hydrodynamic codes now include the effects of NLTE, electron-scattering, line-blanketing, Auger ionization, level dissolution and more (see e.g. Hillier & Miller 1998). Successful

---

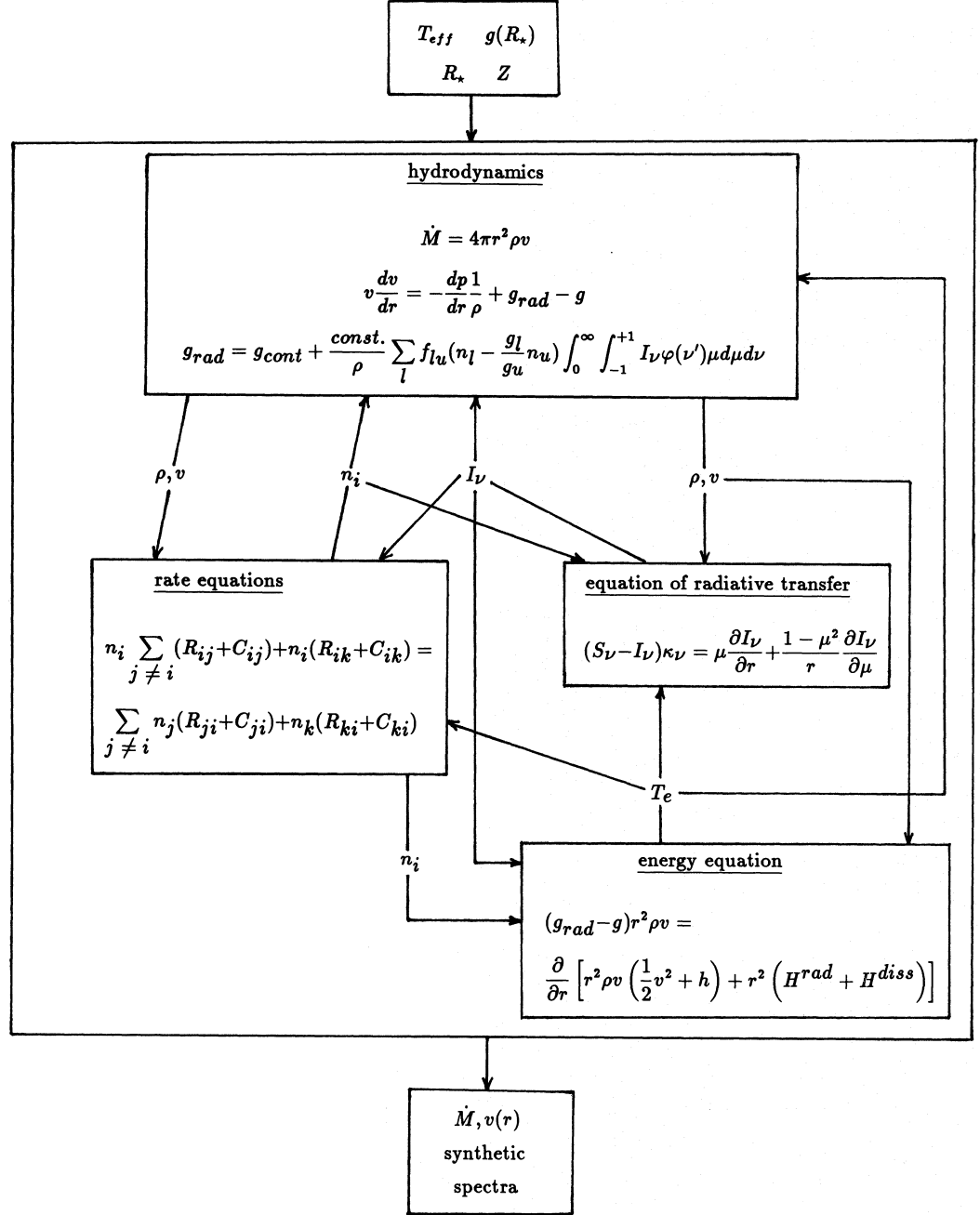[2]For a detailed description of this figure and the used notation we refer to their article.

$T_{eff} \quad g(R_*)$

$R_* \quad Z$

hydrodynamics

$$\dot{M} = 4\pi r^2 \rho v$$

$$v\frac{dv}{dr} = -\frac{dp}{dr}\frac{1}{\rho} + g_{rad} - g$$

$$g_{rad} = g_{cont} + \frac{const.}{\rho}\sum_l f_{lu}\left(n_l - \frac{g_l}{g_u}n_u\right)\int_0^\infty \int_{-1}^{+1} I_\nu \varphi(\nu')\mu d\mu d\nu$$

ρ, v $\quad n_i$ $\quad I_\nu$ $\quad \rho, v$

rate equations

$$n_i \sum_{j \neq i}(R_{ij}+C_{ij})+n_i(R_{ik}+C_{ik}) =$$

$$\sum_{j \neq i} n_j(R_{ji}+C_{ji})+n_k(R_{ki}+C_{ki})$$

equation of radiative transfer

$$(S_\nu - I_\nu)\kappa_\nu = \mu\frac{\partial I_\nu}{\partial r} + \frac{1-\mu^2}{r}\frac{\partial I_\nu}{\partial \mu}$$

T_e

n_i

energy equation

$$(g_{rad}-g)r^2\rho v =$$

$$\frac{\partial}{\partial r}\left[r^2\rho v\left(\frac{1}{2}v^2 + h\right) + r^2\left(H^{rad} + H^{diss}\right)\right]$$

$\dot{M}, v(r)$
synthetic
spectra

Figure 2.1: Scheme of self-consistent atmospheric modeling (reproduced from Pauldrach et al. 1994).

examples of their applications for hot stars are the studies of Pauldrach et al. (1994), and in particular in the case of Luminous Blue Variables, the work of de Koter et al. (1996) and Najarro et al. (1997).

2.3 Stellar Pulsations

Intrinsically variable stars are usually divided into pulsating and eruptive variables. Luminous Blue Variables present a somewhat special case in the sense that they show cyclic as well as eruptive variability patterns and thus can be associated with both classes. However the LBV eruptions might be caused by pulsational instabilities as well and thus it is worthwhile to discuss the basic theoretical framework of the pulsation theory in this section.

Up until the middle of this century observed periodic brightness variability was thought to arise from *radial* pulsations (RP). The developed RP theory is very successful in explaining the classical (δ) cepheids and the derived period-luminosity relation is one of the best tools for the measurement of the galactic distant scale. However the simple RP theory implies that a given star can only oscillate in a definite "harmonic" frequency or one of its discrete overtones, which provides a maximum allowed period P_{max}.

Ledoux (1951) was the first who suggested that for stars whose brightness changes occur at periods greater than P_{max} a *non-radial* pulsation (NRP) theory must be applied. In particular he showed that the long period of β CMa could be explained by a beating mechanism between two pulsation modes of similar frequencies.

In recent years pulsation-related phenomena have been discovered in many stars that were previously regarded as non-variable. The best example here is our Sun itself where the field of "helioseismology" has brought many fruitful insights of its internal structure. Other objects include early-type stars with luminosity classes V to I which can be classified into β Cephei Variables with times scales of ~hours and rather large variations in brightness and radial velocity, the 53 Persei Variables (slow rotational velocity: $v \sin i \lesssim 170 \,\mathrm{km\,s^{-1}}$) and the ζ Ophiuchi Variables ($v \sin i \gtrsim 170 \,\mathrm{km\,s^{-1}}$) which exhibit small v_{rad} variations and periods that are not stable over a long time. The most important characteristic of these stars are that their non-radial pulsations are multi-periodic with several modes of oscillations (see e.g. the study of α Cygni by Lucy 1976).

The two fundamental types of stabilities which characterize stars are:

- *Dynamical stability* where the stellar gravitation acts against the outward pressure gradient to restore the equilibrium structure. A star spends most of its life in this state. However, this condition might be violated locally, e.g. a star is dynamically unstable against non-radial perturbations in a convection zone.

- *Thermal stability* where an excess of thermal energy causes the gas to expand which in turn decreases the temperature. An example of thermal instability is found in the degenerate helium core at the beginning of the helium burning (visible as the helium flash).

Each stability state has an associated time scale. The *dynamical* or *free-fall* time scale, τ_{dyn}, is the characteristic time for a star to adjust a significant departure from hydrostatic equilibrium. It can be estimated via:

$$\tau_{dyn} \approx \frac{1}{\sqrt{G\bar{\rho}}} \approx \sqrt{\frac{R_\star{}^3}{G\,M_\star}} \qquad (2.26)$$

where $\bar{\rho} \approx M_\star/R_\star{}^3$ is the average density.

The *Kelvin-Helmholtz* time, τ_{KH}, is essentially the relaxation time for departures of a star from thermal equilibrium which is the balance between the energy generated by the thermonuclear reactions in the stellar interior and the energy lost by radiation:

$$\tau_{KH} \approx \frac{G\,M_\star{}^2}{R_\star\,L_\star}. \qquad (2.27)$$

Cox (1980) estimated the ratios of the time scales as:

$$\frac{\tau_{dyn}}{\tau_{KH}} \sim 10^{-12}\frac{L_\star\,R_\star{}^{5/2}}{M_\star{}^{5/2}}, \qquad (2.28)$$

with $L_\star$, $R_\star$ and $M_\star$ in solar units.

We can see from Equation 2.28 that τ_{dyn} is much shorter than τ_{KH}. Thus, apart from degenerate thermonuclear ignitions (e.g. nova-like outbursts, helium flash) after which thermal stability is restored quickly, longer-term thermal instabilities are usually not relevant to non-radial pulsations.

The fact that $\tau_{dyn} \ll \tau_{KH}$ forms the basis of the *adiabatic* approximation for the study of stellar pulsation (i.e. *all* heat exchange mechanisms may be ignored). Again neglecting effects due to rotation or magnetic fields, this approximation reduces the problem to a purely mechanical system and is analogous to the study of sound waves confined in a box.

The relevant hydrodynamical equations are thus only the conservation of mass and momentum while the equation of energy conservation can be dropped in the adiabatic approximation. Using the gravitational potential Ω we can express the mass and momentum equations by:

$$\frac{\partial \rho}{\partial t} + \nabla(\rho \mathbf{v}) = 0 \tag{2.29}$$

and

$$\rho \left(\frac{\partial}{\partial t} + \mathbf{v}\,\nabla \right) \mathbf{v} = -\nabla p - \rho \nabla \Omega. \tag{2.30}$$

To complete the description of this system we need a third equation, namely the *Poisson equation*:

$$\nabla^2 \Omega = 4\,\pi\,G\,\rho. \tag{2.31}$$

In the above equations $\mathbf{v}$ denotes the fluid velocity, ∇ the gradient operator and ∇^2 the Laplacian operator; the other symbols have their previously defined meanings.

To obtain the equations describing the non-radial pulsations in stars the above equations are subjected to perturbations which are usually described using the *spherical harmonics*:

$$Y_l^m(\Theta, \Phi) = \sqrt{\frac{(2l+1)}{4\pi}\frac{(l-m)!}{(l+m)!}}\ P_l^m(\cos \Theta)e^{im\Phi}, \tag{2.32}$$

where the $P_l^m(\cos \Theta)$ are the associated Legendre polynomials. Using $x = \cos \Theta$ we get:

$$P_l^m(x) = \frac{(-1)^m}{2^l\,l!}(1-x^2)^{m/2}\frac{d^{l+m}}{d\,x^{l+m}}(x^2-1)^l. \tag{2.33}$$

Normal modes are eigenfunctions of $Y_l^m(\Theta, \Phi)$ with $l = 0, 1, 2, \ldots$ and $|m| \leq l$. We see that we can also describe the purely radial modes with this system when we set $l = 0$. Each normal mode with index l has a number of nodes n which describe the radial component of displacement from the equilibrium (i.e. the stellar surface). The node values are: $n = 0, 1, 2, \ldots$ with $n = 0$ as fundamental node, $n = 1$ as first overtone, etc.

The two dominant restoring forces in stellar pulsations are pressure, which causes acoustic waves called p-modes, and gravity, which leads to g-modes. The spectrum of radial pulsations is restricted to p-modes while NRP includes the g-modes as well. P-modes usually have higher frequencies than g-modes. The pressure and gravity modes without nodes are called fundamental or f-modes and have frequencies that lie in between the p-mode and g-mode spectrum. G-modes are preferably excited in convection-free regions; for high-mass stars these are in the outer region and atmospheres and are thus observable in optical stellar spectra.

Additionally to the standard modes so-called "strange modes (SM)" can be found that do not fit in nor follow the above described frequency spectrum. In general they are connected with instabilities having growth rates in the dynamical range and occur only in non-adiabatic RP and NRP calculations. It is found that the classical κ and ϵ mechanisms (see below) cannot be responsible for the SM instabilities; however, the SMIs can be of nonthermal origin and might be interpreted fully in mechanical quantities. For massive stars (in particular LBVs) the strange modes are related to the three opacity maxima of the iron-peak elements ("Fe"), helium ("He") and the helium-hydrogen balance ("He/H"). Here the observed frequencies are closely related to the inverse sound travel time between the photosphere and the outermost opacity maximum which indicates that they are acoustic modes for these objects. For a discussion on strange mode instabilities see Glatzel (1997, 1998).

To maintain stellar pulsations for an extended time a periodic energy input (e.g. in the form of entropy or heat) is necessary to overcome the oscillation damping resulting from energy loss by radiation. Some important excitation mechanisms (additionally to the nonthermal, acoustic origins of SMIs) are:

- The κ *mechanism* which works in the outer layers of stellar atmospheres, i.e. the hydrogen and helium ionization zones. Here ionization prevents the temperature from rising very much upon compression and the density variation dominates the opacity variation of the respective volume element: the increasing density increases the opacity and "dams up" the radiation thus driving the pulsations. This mechanism is responsible for the regular oscillations of the classical cepheids.

- The nuclear energy generation in the stellar core always has a destabilizing effect and is called the ϵ *mechanism*. This effect may be important in very massive stars: e.g. it might drive the fundamental radial modes of W-R stars (Unno et al. 1989).

- Rotation and semi-convection zones might affect the pulsations in massive stars. Calculations show that preferably prograde (i.e. oscillations in direction of rotation) NRP are excited which may coincide with the stellar eigenfrequencies and could be visible at the stellar surface as g-modes.

Several observational methods exists to distinguish between radial and non-radial pulsations:

- Direct observations of resolved stellar images (only possible for the Sun or nearby stars).

- Phase shifts of pulsations during stellar eclipses in binary systems indicate NRP (note that these observations can also be explained by other traveling features around the equator).

- The observed period is longer than the fundamental period of the RP theory.

- The "beating" phenomenon: two simultaneous oscillations with nearly equal frequencies can modulate the amplitude of the observed oscillation and result in a longer period. This effect can easily be caused by stellar rotation.

- *Baade's pulsation test*: the luminosity variation due to radial pulsation can be expressed by: $L(t) = 4\pi R^2(t)\,\sigma\,T_{\mathrm{eff}}^{4}(t)$. If we estimate the temperature variation from the color and measure the luminosity we get the radius variations from this equation. In case of radial pulsations $R(t)$ is correlated with the phase of the v_{rad} variations while for NRP $R(t)$ is anticorrelated.

- NRPs divide the stellar surface into regions with different velocity fields, which, in the presence of rotation, redistribute the flux over the line profiles and create moving patterns of peaks and troughs. Smith (1977) has observed such line-profile variations (LPVs) in early- to mid-B stars and modeled them successfully using non-radial pulsations. In particular LPVs with v_{rad}-variations but constant equivalent widths cannot be explained by radial oscillations.

In recent years the numerical modeling of LPVs due to non-radial pulsations in rotating stars (Townsend 1997, Telting & Schrijvers 1997) has progressed a lot. Most NRP codes use the previously described linear adiabatic approximation and achieve very good results in fitting observed line profiles. An example of the effects of NRP on the line profiles of a rotating star is given in Figure 2.2. We use these theoretical models in comparison with our observed LPVs and calculate simple numerical models to support our discussion.
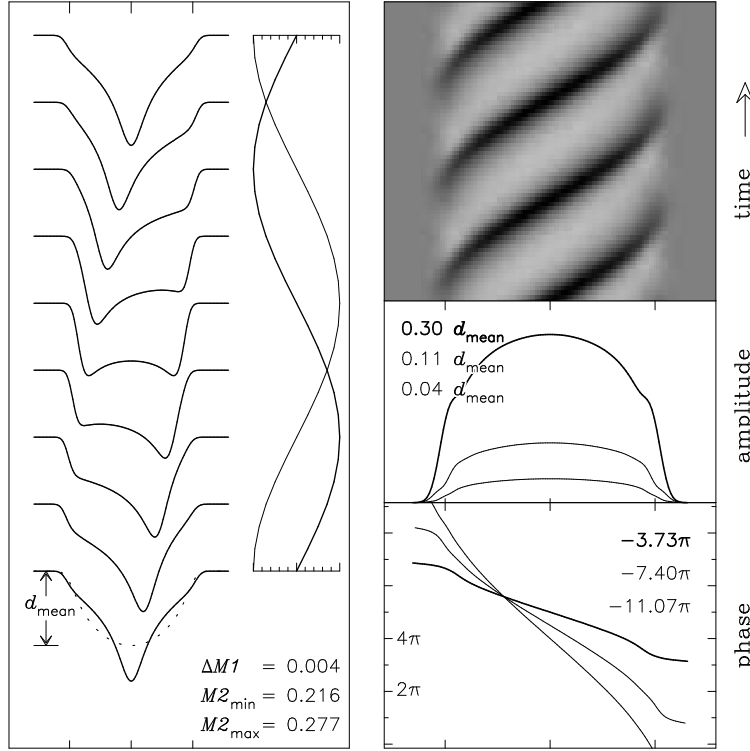
Figure 2.2: Example of line profile variations caused by non-radial pulsations (reproduced from Schrijvers et al. 1997). The main input parameters for this model are: $l = 4, m = -4, v_{max} = 0.15\,v\sin i$ and an inclination angle of $i = 90°$. *Left*: line profiles and first (thick line, $M1$) and second (thin line, $M2$) velocity moments during the pulsation cycle. The tick marks at the velocity axis (x-axis) indicate $v\sin i$. *Right*: Top: three pulsation cycles of residual line profile (mean subtracted) shown as grey-scale image. Intensities less than average are dark. Middle and bottom: amplitude distribution and phase diagram of LPVs (thick to thin lines: input, first harmonic and second harmonic frequency).

Non-radial pulsations do not necessarily affect the photometric brightness of the star. In particular, oscillations with higher harmonics may cause certain kinds of dynamical phenomena like macro- or micro-turbulence or the heating of stellar chromospheres, coronae or winds. However these issues are still subject to scientific debate. More *simultaneous* photometric and spectroscopic observations and further theoretical studies are needed to advance our knowledge in this area.

The most recent summary of stellar pulsation theories as well as their applications in modeling observations can be found in: "A Half Century of Stellar Pulsation Interpretations: A Tribute to Arthur N. Cox", ASP Conference Series, Vol. 135, eds. P.A. Bradley & J. Guzik, 1998.

Chapter 3:   Spectroscopic Variability of the LBV HD 160529

3.1   Introduction

The variability of the extreme BA-type hypergiant HD 160529 was already established $30-40$ years ago when studies of its lightcurve and spectra at different epochs resulted in different temperatures and spectral types. Table 3.1 shows the various spectral classifications of HD 160529 together with the literature references. This behavior is one of the characteristic features of Luminous Blue Variables (LBVs) when they shift between minimum and maximum state.

Table 3.1: Spectral classifications of HD 160529.

Spectral type	Reference
A3eIa–O	Bidelman, 1954, PASP 66, 249
A2Ia$^+$	Hiltner, 1954, ApJ 120, 41
A2Ia$^+$	Smith, 1956, ApJ 124, 43
A3Ia$^+$	Buscombe, 1959, MtSOM 3, 1B
A2Ia–O	Feast et al., 1961, MNRAS 122, 239
A9Ia	Houk, 1982, Michigan Spectral Survey 3
B8Ia$^+$	de Jager et al., 1984, A&A 138, 246
B8Ia	Sterken et al., 1991, A&A 247, 383
A9Ia	Sterken et al., 1991, A&A 247, 383

The spectrum of HD 160529 was studied extensively by Wolf et al. (1974) who found radial velocity variations with amplitudes of about $40\,\mathrm{km\,s^{-1}}$ and line splitting of some metallic lines. Intensity variations of absorption lines of the order of 20 % and considerable photometric variations (e.g. 0.27 mag in y) were explained as reactions of pronounced time- and depth-dependent nonthermal photospheric velocity fields. Amplitudes of 25 to $30\,\mathrm{km\,s^{-1}}$ were found for the photospheric velocity variations by measuring the radial velocities of the H_8, H_9 and H_{10} lines. On the basis of a curve-of-growth analysis and strict hydrostatic LTE-models with $\log g = 1$, they estimated the effective temperature of HD 160529 to be approximately $T_{\mathrm{eff}} = 8800\,\mathrm{K}$. Their observed variations in visual magnitude could be explained by irregular temperature variations of the order of $\Delta T = 700\,\mathrm{K}$ or continuum variations caused by the variable velocity field.

The star was classified as a new galactic LBV by Sterken et al. (1991) due to its brightness decrease of 0.5 mag from 1983 to 1991 and spectral type change from B 9 to B 8. The authors found pulsation-like variations in their photometric data with a quasi-period of 57 days with peak-to-peak amplitudes of 0.1 mag in b and y, while previous analyses suggested a possible 101.3-day period (Sterken 1981). From comparison with R 110, a close photometric and spectroscopic counterpart of HD 160529 in the Large Magellanic Cloud, they derived an absolute magnitude of $M_V = -8.9$ and a distance of 2.5 kpc. The stellar parameters characterizing the maximum state were estimated to be $T_{\mathrm{eff}} \approx 8000\,\mathrm{K}$, $\log g \approx 0.55$, $R_\star \approx 330\,\mathrm{R_\odot}$ and $M_\star \approx 13\,\mathrm{M_\odot}$. They concluded that HD 1605291 is located at the lower limit of the LBV instability strip and possibly in an evolutionary phase after the Red SuperGiant (i.e. post-RSG) state.

HD 1605291 is one of the few stellar objects with a high enough centimeter flux to be accessible with current radio telescopes. Leitherer et al. (1995) observed the star at 8.64 and 4.80 GHz and found that the measured flux is consistent with thermal emission from an optically thick expanding wind at constant velocity. The authors adopt the spectroscopic distance of $d = 2.5$ kpc from Sterken et al. (1991) with an error of 40 %, an electron temperature of $T_{electron} = 5000$ K for the radio emitting region and a terminal velocity of $v_\infty = 180$ km s^{-1} to derive a mass-loss rate of $\dot{M} = 10^{-4.87\pm0.24}$ M$_\odot$yr^{-1}.

Blomme & Runacres (1995) and Blomme et al. (1998) mentioned the possibility of clumping in the wind of HD 160529 from IRAS observations and preliminary results of far Infrared observations with the ISO satellite (60, 90 and 160 μm photometry). Because of problems with the detector response function of ISOPHOT their data could not provide definitive conclusions (private communication).

In order to study the underlying physical mechanisms of the observed variability we have monitored HD 160529 spectroscopically over a time span of $2-4$ months in four successive years, i.e. $1992-1995$.

In this thesis project we present and analyze the obtained spectroscopic data set and compare it with the observed photometric[1] variations of HD 160529:
we describe the high S/N averaged spectra and some of their characteristic features in section 3.4 and study the line variations of HD 160529 with tools developed specifically for spectroscopic time-series observations (section 3.5). The photosphere and the stellar wind are modeled with synthetic spectra in their static and dynamic states in chapters 3.6 and 3.7 respectively. In section 3.8 we summarize and discuss the results obtained.

3.2   Observations

The spectrographs which have been used for the variability study of HD 160529 are described in great detail in the dissertations of Mandel (1988) and Kaufer (1996a). The details of the data reduction procedures and the applied modifications are explained in Gäng (1993), Stahl et al. (1993) and Kaufer (1996a). Hence we describe in the following paragraphs only the essential instrumental specifications and the necessary data reduction steps and refer to the above publications for a more extensive discussion.

3.2.1   Instruments

From $1992-1994$ the observations were carried out with FLASH (*Fiber Linked Astronomical echelle Spectrograph of Heidelberg*) as described by Mandel (1988a, 1988b). It was equipped with an EEV-CCD (1252 x 770, 22 μm pixel) and an optical fiber of 100 μm core diameter. The covered spectral wavelength range was 4000 Å $< \lambda <$ 6850 Å with a pixel-to-pixel resolution of R $= \lambda/\Delta\lambda \approx$ 20 000 (corresponding to $\sim$15 km s^{-1}).

Prior to the observing period in 1995 the instrument was upgraded to enable simultaneous observations in the blue and red range of the optical spectrum, now including wavelengths beyond the Balmer jump. For this purpose a beamsplitter (dichroitic filter at 5700 Å) and an additional blue-sensitive CCD chip (1170 x 800, 22 μm pixel) were integrated in the spectrograph. The wavelength range covered with one exposure is now 3450 Å $< \lambda <$ 5550 Å and 5800 Å $< \lambda <$ 8630 Å. To distinguish the two setups, the name of the spectrograph was changed to HEROS (*Heidelberg Extended Range Optical Spectrograph*).

By using optical fibers with identical core-diameters (100 μm, corresponding to a "sky-slit" of $\sim$2.7 arcsec at the ESO 50-cm telescope) in FLASH as well as in HEROS, the resolving power was kept constant in both instruments.

---

[1]The photometric data was kindly placed at our disposal by Dr. C. Sterken.

Table 3.2: Observing campaigns of HD 160529. [†]: S/N at $\lambda = 5850\,\text{Å}$, [‡]: S/N at $\lambda = 5500\,\text{Å}$.

| Observing Season | | Spectra/ | Spectral | Instrument | Typ. |
Date	Julian Date	Nights	Range [Å]		S/N
Jun – Aug, 1992	244 8794 – 244 8849	54/55	4050 – 6760	FLASH	110[†]
Feb – Jun, 1993	244 9034 – 244 9141	71/101	4010 – 6735	FLASH	110[†]
Feb – Jul, 1994	244 9399 – 244 9534	54/129	4030 – 6735	FLASH	120[†]
Mar – May, 1995	244 9791 – 244 9864	23/72	3450 – 5550	HEROS	60[‡]
Mar – May, 1995	244 9791 – 244 9864	27/72	5840 – 8630	HEROS	120[†]

Calibration exposures with an internal flatfield lamp and a thorium-argon (ThAr) arc lamp were taken immediately before and after the exposures of HD 160529. The light of the calibration lamps is fed into the fiber and follows the same light-path as the light from the observed stars which ensures always the same illumination of the CCD pixels.

The design of the instrument together with the mechanical separation of the spectrograph from the telescope and the applied observing techniques ensure excellent stability during the night.

3.2.2 Observing Campaigns

The observations were carried out at the ESO 50-cm telescope in four observing periods in 1992 (June to August) and 1993, 1994 and 1995 (February to June). Numerous observers participated in the long-term monitoring projects (see Table 4.5 in Kaufer 1996) to collect sufficient data for a spectroscopic variability study.

A total of 226 spectra were obtained, with each spectrum averaging a S/N ≈ 100 around 5500 Å. Table 3.2 shows the observational characteristics of the individual runs. The third column gives the wavelength range that was used for the final averaging of the spectra. The typical exposure time for one observation was approximately 120 minutes. The given S/N values reflect the quality achieved for a typical spectrum of the corresponding observing run.

In the first observing run in 1992 we observed HD 160529 twice per night with short (~ 10 min) and long (~ 120 min) exposure times to make sure possible line saturation effects could be corrected for. In all following periods the star was observed once per night or every other night (weather permitting) with a typical exposure time of two hours.

3.2.3 Data Reduction

The spectra were reduced semi-automatically with a modified version of the echelle reduction package available with the ESO-MIDAS image processing system running at the Unix workstations of the Landessternwarte Heidelberg. The following outline describes the basic steps performed:

- The flatfield and wavelength calibration (ThAr) exposures are checked for possible shifts of the spectra during the night. If shifts larger than one third of a pixel are found, the night is divided into two or more sections for which the reductions are performed independently. The observed shifts during 2 hour exposures are less than 1/10 th of a pixel, reflecting the internal v_{rad} accuracy of $\lesssim 1\,\text{km}\,\text{s}^{-1}$.

- Cosmic rays hits are located and removed and the inter-order background intensity is fitted and subtracted.

- The wavelength calibration and flatfield correction are done in the two-dimensional pixel-order frame. Because the optical fiber illuminates the CCD always in the same way the flatfielding removes the existing echelle ripples with high precision.

- The orders are merged into one continuous spectrum which gets rebinned to heliocentric velocities and normalized by low-order spline fits through predefined continuum windows.

The accuracy of the wavelength calibration is of the order of $1\,\mathrm{km\,s^{-1}}$; the continuum in well-exposed parts of the spectrum is generally determined to approximately $\pm 1\,\%$. The uncertainty is mainly due to remaining echelle-ripples after the reduction.

The fully reduced spectra obtained in the years 1992 to 1994 are published in FITS format on CD ROM (Stahl et al. 1995).

3.3   Selected Diagnostic Spectral Lines

The broad range of our spectra (wavelength coverage: $3450 - 8620\,\text{Å}$) offers a huge number of spectral lines to study. Which lines can we select from this set to learn the most about the atmospheric conditions of HD 160529?

A clear distinction between *pure* photospheric and *pure* wind lines is not possible in the case of HD 160529 (and possibly for LBVs in general) because all observed spectral lines show some signs of wind influence through asymmetry in their profiles (e.g. usually the blue side of an absorption line is flatter and more extended than the red side).

Nevertheless we can sort the spectral lines according to their depth of origin in the stellar atmosphere and thus distinguish main contributions of photosphere and wind. In the atmosphere of BA supergiants strong lines with small excitation potential (χ_e) emerge generally in higher atmospheric regions than weak lines with high χ_e (see Wolf et al. 1974). This leads to the following sequence for HD 160529 in the radial direction away from the star:

- He I $\lambda 5876$ ($\chi_e = 20.87\,\mathrm{eV}$)

- Mg II $\lambda 4481$ ($\chi_e = 8.83\,\mathrm{eV}$)

- Si II $\lambda 6347$ ($\chi_e = 8.09\,\mathrm{eV}$)

- Fe II $\lambda 6248$ ($\chi_e = 3.87\,\mathrm{eV}$)

- Ti II $\lambda 4468$ ($\chi_e = 1.13\,\mathrm{eV}$)

A more accurate assignment of the location of the line forming regions using the radial velocities of the observed lines confirms the above sequence except in the case of the iron and titanium lines which exchange their order: the mean radial velocities of their absorption lines are $\sim 73\,\mathrm{km\,s^{-1}}$ and $\sim 45\,\mathrm{km\,s^{-1}}$ respectively. However, because Fe II $\lambda 6248$ has a complicated line profile (P Cygni type with time dependent multiple absorption components), comparing average radial velocities is not appropriate in this case and does not lead to reliable results. We conjecture that these two line originate at roughly the same optical depth and do not use them for direct comparisons of depth dependent examinations. Rather we use Ti II $\lambda 4468$ as a temperature indicator of the wind and scrutinize Fe II $\lambda 6248$ for its line-profile variations.

The most important diagnostic lines in the spectra of early-type supergiants are usually the Balmer lines which reach their maximum strength in stellar atmospheres with temperatures of around $\sim 10\,000$ K (i.e. spectral type A). Their line forming region extends over the whole stellar atmosphere with Hα furthest away and the higher Balmer lines closer to the photosphere (see Balmer progression, Figure 3.2 and Figure 3.20): in our spectra Hα, Hβ and Hγ exhibit strong P Cygni profiles pointing to the stellar wind as the dominant influence in their respective line forming regions. The rather symmetric line profiles and the decreasing radial velocities of the highest observed Balmer lines indicate that they are formed close to the photosphere.

The continuum around 3650 Å was badly determined because only a few spectra with very low the S/N ratio were available in 1995. Thus the Balmer jump itself could not be used in the analysis.

Because sodium is practically fully singly ionized (i.e. in the state of Na$^+$) in stellar atmospheres of $T_{\text{eff}} \gtrsim 10\,000$ K, the Na D resonance lines (excited from ground state: $\chi_e = 0.00$ eV) give information about the conditions far out in the stellar envelope where the temperature is low enough to allow for recombination of these lines. Note that the Na D and Ca K / H resonance lines are also strongly blended by interstellar lines; however we can separate the stellar contribution by studying the fast varying components in their line profiles.

The following sequence can be established through the excitation potential of the different lines, their "grade of asymmetry" and their respective radial velocities:

$$\text{He}\,\textsc{i} \;\rightarrow\; \text{Mg}\,\textsc{ii} \;\rightarrow\; \text{Si}\,\textsc{ii} \;\rightarrow\; \text{Ti}\,\textsc{ii}\,/\,\text{Fe}\,\textsc{ii} \;\rightarrow\; \text{H}\delta \;\rightarrow\; \text{H}\gamma \;\rightarrow\; \text{H}\beta \;\rightarrow\; \text{H}\alpha \quad (\;\rightarrow\; \text{Na D}\;)$$

$$\textit{photosphere} \qquad\qquad \longrightarrow \qquad\qquad \textit{wind} \qquad\qquad (\rightarrow \textit{envelope}\,)$$
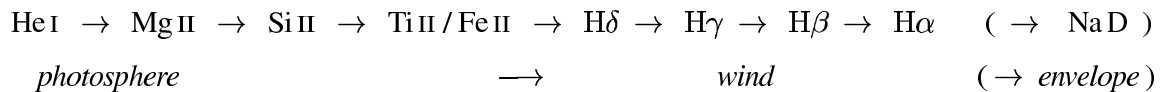
We concentrate our analysis of HD 160529 on the above mentioned spectral lines.

3.4 Spectral Characteristics of the Mean Spectra

In order to improve the S/N ratio we averaged all spectra weighted by their S/N ratio (measured around 5500 Å) and merged the different spectral ranges to one continuous mean spectrum ranging from 3450 Å to 8620 Å.

For the blue wavelength range from $3450 - 4050$ Å the automatic continuum normalization (spline fitting in preselected continuum windows; see last data reduction step in section 3.2.3) failed because of the extremely low S/N ratio of individual spectra and the high number of metallic lines in this area. Also the Balmer jump contributes to the normalization problem so that we normalized this area completely interactively for each single spectrum[2]. An overview of the resulting S/N ratio at different wavelength positions is given in Table 3.3.

Table 3.3: S/N ratio of mean spectrum at various wavelengths.

λ [Å]	3500	4000	4100	5500	5600	6700	6800	8600
S/N	10	80	120	330	490	740	1000	240

---

[2]We have used the less-interactively reduced UCLES spectrum as a reference for our interactive normalization process (see chapter 4.3 for UCLES data reduction and appendix A.2 for the UCLES spectrum of HD 160529).

The chosen wavelengths in Table 3.3 reflect positions where the various spectral ranges were merged. The S/N values were determined in areas of ± 25 Å around the given wavelengths. Note that the S/N ratio gets much lower at the blue end. This is mainly due to the poor sensitivity of the spectrograph and CCD at $3450-4050$ Å and the limited amount of spectra available in this spectral range. The given S/N value is therefore a result of instrumental constraints, the number of averaged spectra and the flux level of the star itself at the considered wavelength.

General Appearance

In this section we describe the spectral characteristics of the total mean spectrum and the yearly averaged spectra of the observing runs.

In this context it is important to point out that all spectral lines are highly variable (see section 3.5) and that even photospheric absorption lines show signs of wind influences through asymmetries in their line profiles (i.e. their blue wings are more extended and "flatter" than their red sides) and possible pulsations through radial velocity variations. Averaging the spectra smears out these features so that the resulting lines can look almost Gaussian while the individual spectra might deviate substantially from a symmetric profile (see e.g. Si II $\lambda6347$ in section 3.5.1).

However the general condition of the stellar atmosphere is well described by the averaged spectrum. Hence to examine the atmospheric conditions of HD 160529 we study the averaged spectrum first and then try to explain the variations as deviations from this mean state.

We find that the mean spectra of each year look very similar with the exception of the observing run of 1994. In this observing run the lines with a strong P Cygni profile (i.e. most notably Hα, Hβ, Hγ and some strong Fe II lines) show a distinctly lower emission with a more blue-shifted and shallower absorption component. Pure absorption lines are practically unaffected which suggests that only the wind structure has changed in this event. In section 3.7.3 we model the wind lines and discuss possible scenarios of changing wind structures to explain the observed behavior. Figures 3.1 and 3.2 show the mean plots of the yearly observing runs together with the total averaged spectrum.

Photospheric Lines

Photospheric lines with small wind influence have only absorption components and are almost symmetric; they have low radial velocities and exhibit rather regular $v_{\rm rad}$ variations. Good examples are (in order of increasing radial velocity): He I, Mg II and Si II. Weak iron lines ($W_\lambda \lesssim 250$ mÅ) have similar line profiles, variability patterns and velocities comparable with the He I and Mg II lines. The Ti II lines have higher radial velocities and exhibit irregular variations and stronger deviations from the symmetric profile. Figures 3.1a-f illustrate the conditions of the "mean" photosphere.

Wind Lines

A high degree of wind influence is obvious for all spectral lines with a P Cygni profile. In the spectra of HD 160529 these are the strong Fe II and Balmer lines.

The Fe II lines, especially those of multiplets 27, 38, 42, 43, 49, 48 and 74, typically exhibit a P Cygni profile with a weak emission and two absorption components (see Figure 3.1f).

The Balmer lines show the expected pronounced progression toward the systemic velocity for higher members of the series (see Fig. 3.2a and Fig. 3.20). Measuring the individual velocities of the higher

Balmer lines ($\lambda \lesssim 3900$ Å) did not lead to a systematic trend mainly because the quality of the few spectra from 1995 is not sufficient to derive accurate radial velocity measurements from Gaussian fits and many Balmer lines are blended by metal lines in this wavelength region. On the other hand we see radial velocity variations with amplitudes and absolute values similar to the photospheric lines when we measure isolated lines (e.g. H_{13}, H_{14}, H_{18}) which indicate that these higher Balmer lines are predominantly influenced by the variability mechanisms of the photosphere and not the wind.

The mean spectrum of the Hα line in 1994 exhibits a distinctly different line profile than in the other observing runs: the emission intensities of the normalized spectra are about $10-20\%$ lower and the blue edge of the absorption component has moved by about -15 to -40 km s^{-1}.

In Fig. 3.2b we see that Hα shows strong emission wings up to 35 % of the continuum and extending to $\sim 1300-1500$ km s^{-1}. These wings are (within the error of the continuum determination) not affected by the event of 1994. The wings are weaker but still visible in Hβ and are not detectable in the higher Balmer lines. The origin of the emission wings is discussed in section 3.7.3.
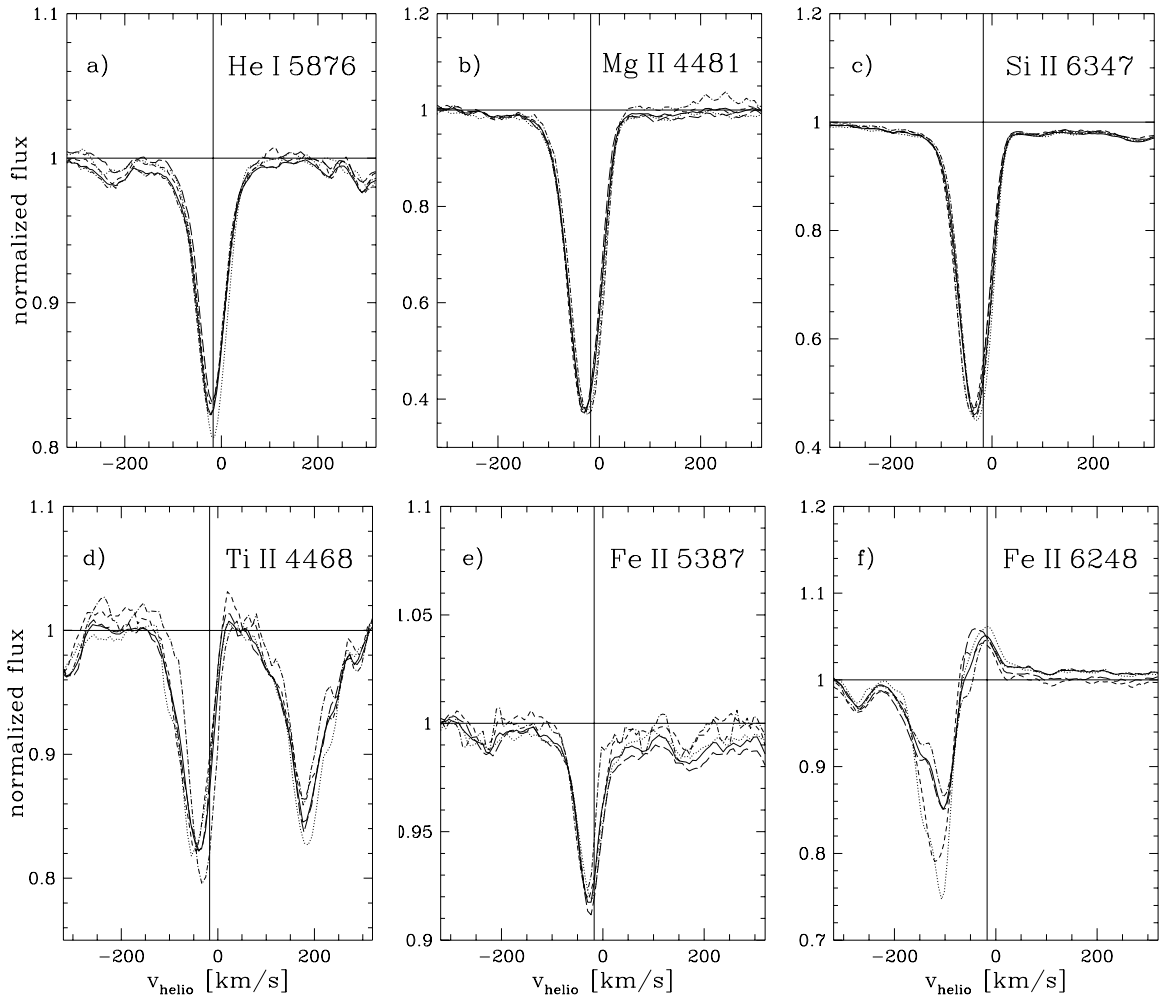
Figure 3.1: Atmospheric spectral lines in heliocentric velocity scale vs. normalized flux. The vertical and horizontal thin lines represent the adopted systemic velocity ($v_{sys} = -17$ km s^{-1}) and the normalized continuum. The solid lines are from the total averaged spectrum, the interrupted lines from the mean spectra of the respective yearly observing runs: dotted: 1992, short-dashed: 1993, long-dashed: 1994, dot-dashed: 1995.

Distant Envelope

As mentioned in the previous section we can study the Na I and Ca II lines to get information about the conditions in the extended envelope of HD 160529. Although the analysis of the Na D and Ca K / Ca H lines is hampered by the strong ISM blends, the variable line sections provide information on the stellar contributions to their line profiles: synthetic models with temperatures around 10 000 K do not show other strong lines in the close vicinity of these lines so that the line profile variations must come from Na I and Ca II. The line profiles exhibit an emission part and multiple absorption components which are highly variable from year to year (Figure 3.6, left) and even on time scales of days within one observing run of the length of a few weeks (Figure 3.6, right).

The possibility of Na D in emission was speculated for P Cyg by Beals (1951) who observed a broad emission component near Na D 1. Bernat & Lambert (1978) showed this could not be the case because there was no corresponding emission visible in Na D 2. They proposed C II and Fe III as most probable contributors to the emission because other lines of these multiplets were also present.

However this is not the case for HD 160529:
Na D 1 and Na D 2 show an almost exact agreement in their line profiles. Furthermore the Ca K and Ca H resonance lines which are also formed in a region far away from the stellar surface show a similar
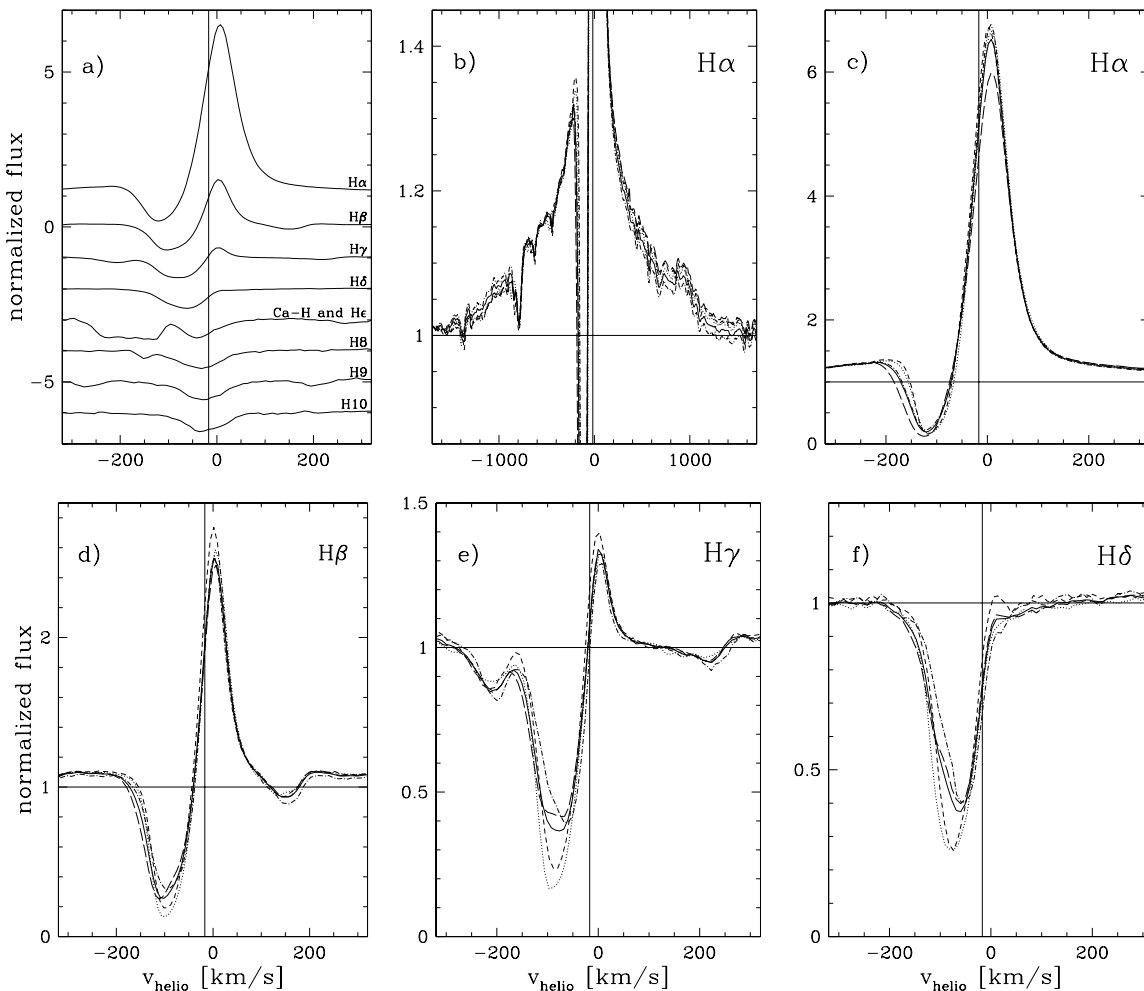
Figure 3.2: Balmer lines in heliocentric velocity scale vs. normalized flux. Same line specification as in Fig. 3.1.
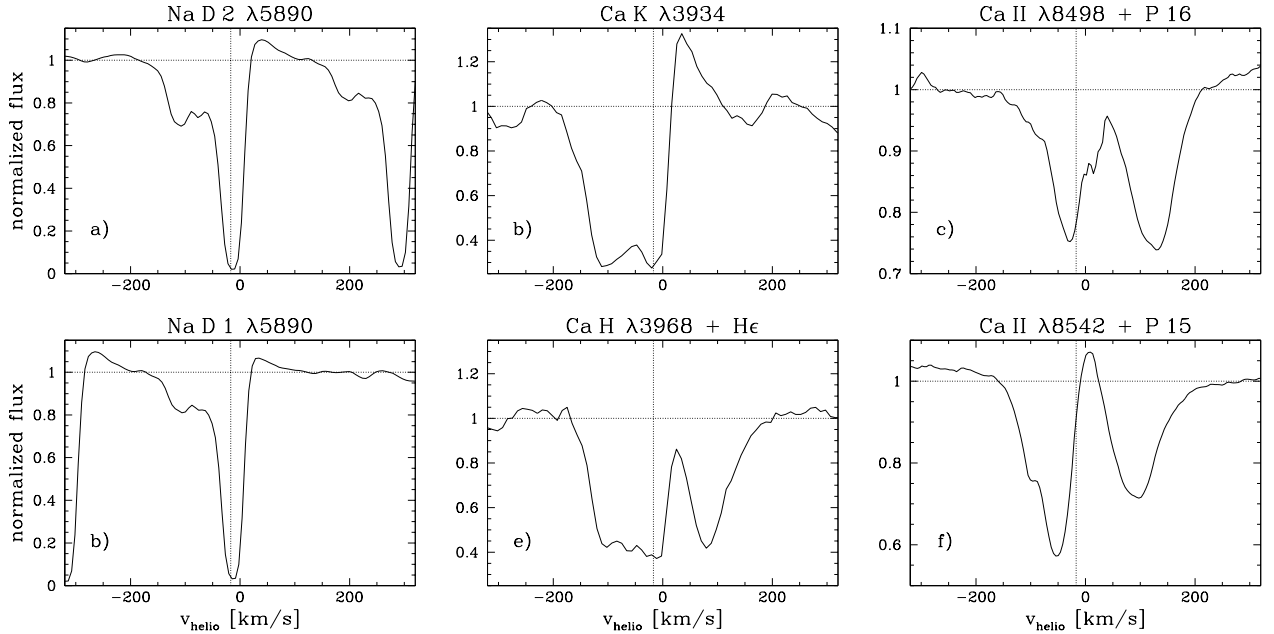
Figure 3.3: Mean line profiles of the Na I D and Ca II K, H, 8498 and 8542 lines. The emission components of Ca II H, 8498 and 8542 are suppressed by blends with hydrogen lines. The dotted horizontal and vertical lines represent the normalized continuum and the systemic velocity of $v_{sys} = -17\,\mathrm{km\,s^{-1}}$.

velocity structure in their line profiles (see Figure 3.3; note that the emission component of the Ca H line is suppressed by the blend with Hε). The simultaneous observations of the emission components in Na I and Ca II make a misidentification unlikely.

We have also detected the Ca II 8498 and Ca II 8542 lines in the spectra of 1995 (observations with HEROS = extended wavelength region). These lines are not excited from the ground state and thus have no interstellar contribution. Although they are both slightly blended by the neighboring Paschen lines P 16 λ8502 and P 15 λ8545 a weak emission component is also visible in Ca II 8542. The third component of this Ca II triplet at 8662 Å is outside our covered wavelength range.

Forbidden Emission Lines

The high signal-to-noise ratio of the mean spectrum (up to 1000) would be sufficient to detect faint forbidden lines if they existed. Contrary to other LBVs like P Cygni where flat-topped forbidden lines of the iron group were found (Stahl et al. 1993), no such lines are visible in the spectrum of HD 160529. The only nebular line visible is [N II] λ6584 in the broad red wing of Hα (see Figure 3.2b at $\sim$900 km s^{-1}). Other nebular lines like [S II] or [O III] were not detected[3].

Unidentified Weak Emission Lines

Motivated by the recent discovery of weak emission lines in the spectra of BA supergiants (Kaufer 1996) we inspected our spectra for these features.

First we examined the averaged spectrum for weak emission features. A valid detection was assigned to features where the intensity was significantly above the noise level but less than 0.2 dex above the local continuum and the emission was clearly not part of a P Cygni profile.

---

[3]On images taken with the STScI-coronograph in May 1995 no nebula could be found around HD 160529 (Nota et al. (private communication)).

Table 3.4: Weak emission lines for $\lambda < 7000$ Å. Given are the mean values and standard deviations of the averaged spectra of each yearly observing run (i.e. the year-to-year variations). Notes: P: P Cygni line profile, E/A: emission/absorption line, K: feature observed in BA supergiants (Kaufer 1996), b = blended by nearby absorption line, intensities in averaged spectrum (measured in relative continuum units): w: weak ($\leq \pm 0.05$), m: medium ($0.05 - 0.1$), s: strong ($0.1 - 0.2$).

$\overline{\lambda}$ [Å]	$\overline{W_\lambda}$ [mÅ]	$\overline{FWHM}$ [Å]	Notes
5119.87 ± 0.10	-15 ± 4	0.47 ± 0.08	wE
5132.16 ± 0.05	-25 ± 6	0.47 ± 0.05	wE
5413.56 ± 0.05	-35 ± 9	0.63 ± 0.04	mE
5424.76 ± 0.05	-24 ± 4	0.50 ± 0.09	mE, P?
5427.24 ± 0.05	-66 ± 4	0.61 ± 0.05	sE
5524.55 ± 0.11	-18 ± 4	0.65 ± 0.07	wE
5529.40 ± 0.04	-58 ± 2	0.63 ± 0.07	sE, P?
5534.50 ± 0.06	-34 ± 14	0.48 ± 0.23	mE, P?
5567.20 ± 0.08	-69 ± 4	0.72 ± 0.02	sE
5586.54 ± 0.05	-42 ± 3	0.65 ± 0.06	mE
5657.45 ± 0.08	-32 ± 5	0.66 ± 0.03	wE
5990.77 ± 0.08	-98 ± 9	0.64 ± 0.05	sE, P
6083.50 ± 0.05	-64 ± 1	0.66 ± 0.05	mE, P
6368.73 ± 0.07	-23 ± 4	0.71 ± 0.22	wE
6383.16 ± 0.10	-18 ± 5	0.55 ± 0.05	wE
6384.84 ± 0.11	-25 ± 2	0.69 ± 0.05	wE
6406.57 ± 0.13	-20 ± 1	0.66 ± 0.07	wE, P?
6432.08 ± 0.07	-109 ± 16	0.70 ± 0.09	sE, P?
6515.52 ± 0.06	-125 ± 19	0.69 ± 0.12	sE, P?
$3.76\,\mathrm{km\,s^{-1}}$	$16\,\%$	$13\,\%$	mean σ
$6.09\,\mathrm{km\,s^{-1}}$	$41\,\%$	$48\,\%$	max. σ
$2.17\,\mathrm{km\,s^{-1}}$	$2\,\%$	$3\,\%$	min. σ

We also checked the positions of the 19 emission features found by Kaufer (1996) in the spectra of BA supergiants. Most lines could not be detected in our mean spectrum but if a line feature was found at the expected position it was included in our sample (even when we observed it in absorption rather than in emission).

With this systematic search we found a total of 48 weak and so far unidentified spectral features (47 in emission, 1 in absorption) in our mean spectrum. Most weak emission lines were found in the red part of the optical spectrum but, because the S/N ratio decreases very quickly in the blue wavelength region, it cannot be excluded that there are more weak emission features existing at $\lambda < 5000$ Å which could not be detected with our method.

The wavelengths (λ) and the full width at half maximum (FWHM) of the resulting spectral features were determined by fitting Gaussians to the line profiles; the equivalent widths were integrated directly with

Table 3.5: Weak emission lines for $\lambda > 7000\,\text{Å}$. Given are the mean values and standard deviations measured in the observing run of 1995. Notes: see Table 3.4.

$\overline{\lambda}$ [Å]	$\overline{W_\lambda}$ [mÅ]	$\overline{FWHM}$ [Å]	Notes
7221.77 ± 0.05	-40 ± 20	0.71 ± 0.24	mE
7307.45 ± 0.06	-41 ± 23	0.64 ± 0.18	mE
7320.10 ± 0.10	-55 ± 30	0.95 ± 0.40	mE, P?
7448.68 ± 0.05	-37 ± 15	0.87 ± 0.28	mE, P?
7461.82 ± 0.11	-42 ± 21	0.84 ± 0.53	mE, P
7515.15 ± 0.06	-62 ± 20	0.85 ± 0.15	mE, P, K?
7532.73 ± 0.07	-31 ± 14	0.67 ± 0.23	mE, P?
7711.26 ± 0.27	-104 ± 17	1.14 ± 0.99	sE, P?
7754.99 ± 0.30	-51 ± 15	1.08 ± 0.52	wE, K
7780.01 ± 0.38	$+9 \pm 10$	0.98 ± 1.48	wA, K
7788.67 ± 0.11	-27 ± 12	1.01 ± 1.03	wE, K
7800.51 ± 0.24	-12 ± 17	0.69 ± 0.68	wE
7817.19 ± 0.22	-16 ± 12	0.74 ± 0.51	wE
7840.70 ± 0.21	-8 ± 7	0.68 ± 0.62	wE
7842.79 ± 0.20	-15 ± 9	0.99 ± 0.95	wE
7848.52 ± 0.29	-64 ± 27	2.51 ± 1.98	wE, K?
7851.29 ± 0.15	-14 ± 8	0.79 ± 0.84	wE, K?
7865.79 ± 0.11	-29 ± 10	1.05 ± 0.36	wE
8068.86 ± 0.28	-26 ± 13	1.36 ± 1.57	wE
8073.76 ± 0.30	-44 ± 18	1.05 ± 0.47	wE, P?
8100.78 ± 0.09	-63 ± 20	1.40 ± 0.75	mE, K?
8109.75 ± 0.11	-24 ± 15	0.82 ± 0.98	wE, P?
8450.29 ± 0.08	-128 ± 38	1.16 ± 0.37	sE, K?
8485.51 ± 0.20	-24 ± 16	0.91 ± 0.82	wE
8489.60 ± 0.23	-14 ± 15	0.76 ± 0.67	wE, P?, K?
8515.16 ± 0.17	-58 ± 56	1.02 ± 0.56	mE, b
8521.71 ± 0.27	-14 ± 8	0.45 ± 0.36	wE, P?
8582.06 ± 0.14	-47 ± 24	1.18 ± 0.54	wE, P?
$6.54\,\text{km}\,\text{s}^{-1}$	$58\,\%$	$69\,\%$	mean σ
$14.66\,\text{km}\,\text{s}^{-1}$	$139\,\%$	$151\,\%$	max. σ
$2.01\,\text{km}\,\text{s}^{-1}$	$30\,\%$	$32\,\%$	min. σ

the local continuum set interactively.

The mean values of the measured wavelengths ($\overline{\lambda}$), equivalent widths ($\overline{W_\lambda} < 0$: *emission*, $\overline{W_\lambda} > 0$: *absorption*) and the $\overline{FWHM}$ are listed in tables 3.4 and 3.5. The average standard deviation of each column is given at the bottom of the tables. For a better relative representation we transformed the wavelengths into velocities and gave the other values as percentages.

The given $\pm$-ranges are the standard deviations ($1\,\sigma$) of the corresponding year-to-year (y-y) variations
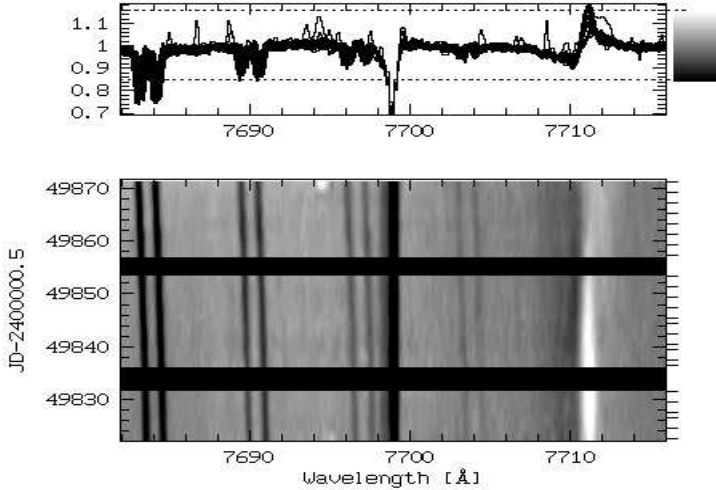
Figure 3.4: Dynamical spectrum (see section 3.5.1 for explanations) of telluric absorption lines (A-band) and the weak emission feature at 7711 Å. The line drift due to the movement of the Earth is clearly visible in our heliocentric spectra. The slightly different strength of the telluric lines is due to changing observing conditions (e.g. passing clouds, different air masses, ...). The very stable absorption feature at 7699 Å is probably an interstellar K I line.

(i.e. the σ values of the variations of the yearly mean spectra) in Table 3.4.

For wavelengths greater than 7000 Å we had only the observations of one year (i.e. 1995). The corresponding listed mean and sigma values of λ, W_λ and $FWHM$ are measured from this observing cycle only and represent the day-to-day (d-d) variations. The σ values can be used as an estimate of the degree of the line variability: by comparing the standard deviations of the values for $\lambda < 7000$ Å and $\lambda > 7000$ Å we see that the year-to-year variations are rather modest whereas the variability during an observing cycle can peak at rather high values, especially in W_λ and $FWHM$ (see also section 3.5.2 for a quantification of the amplitudes of spectral variability). The wavelength variations of the y-y variations are generally less than 6 km s^{-1} while the d-d variations peak at $\sim$14.7 km s^{-1}, which is comparable to the weak emission features in BA supergiants which have a sigma of typically $\sim$5 km s^{-1} with a maximum of $\sim$12 km s^{-1} at 8101 Å (Kaufer 1996). These values are similar to the v_{rad} variations found in some photospheric and wind lines of HD 160529 (see section 3.5.1).

An examination of the time series of the individual spectra revealed that most weak emission lines show some degree of line profile variability and sometimes even a distinct P Cygni line profile with a weak absorption component. By averaging the spectra these absorptions got "smeared out" and/or "filled in" by the local variations so that they are not visible in the averaged spectrum. None of the features show the same run of time with the telluric lines which excludes a terrestrial origin (see Figure 3.4).

This result confirms the existence of weak emission features found by Kaufer (1996) in LBV spectra; however in contrast to the non-variable features in the BA supergiant spectra we can see line profile variations of these features that are similar to observed photospheric and wind lines.

We concur with Kaufer (1996) that a detailed examination of these features is desirable to identify their origin and judge their diagnostic values. However, this is a topic for studies in atomic physics and the required research is beyond the scope of this thesis.

3.5 Time-Series Analysis (TSA)

In this section we used the following methods to visualize, quantify, analyze and discuss the observed line-profile variations (LPVs):

- two-dimensional *dynamical spectra* and their corresponding *quotient* and *difference spectra* were created to mark the location of the variability and visualize the time dependence (for the quotient / difference spectra each spectrum was divided / subtracted by the mean spectrum of the respective observing run; see Figures 3.7 – 3.12 and Figure 3.5, middle),

- *temporal variance spectra* (TVS) were used to quantify the amplitude of the observed line variations (see Figure 3.13). TVS essentially reflect the variances of the intensities for the considered wavelength bin (for details on TVS see Kaufer et al. 1996),

- *radial velocities* (v_{rad}), *relative intensities* (I) and *Full-Width-Half-Maxima* ($FWHM$) of all components of the studied spectral lines were determined by multiple Gaussian fits (the Gaussian fits of the emission and absorption components were executed separately) while the *equivalent widths* (W_λ) were derived by integrating directly over the whole line profiles. The resulting data sets were used to correlate various parameters and spectral lines originating in different atmospheric regions,

- the above measured v_{rad} and W_λ curves were then used together with the available photometric data in Fourier analyses (i.e. periodograms and power spectra applying the CLEAN-algorithm) to determine the predominant time scales.

3.5.1 Line-Profile Variations (LPVs)

Dynamical Spectra and Variation Patterns

Simple overplots of spectra and overplots of spectra with a mean spectrum divided or subtracted can mark the location of line variations very well (see e.g. Figure 3.5) but to keep the information about the time development of the LPVs a two-dimensional representation of the spectra is needed. For this purpose we use the form of *dynamical spectra* developed by Kaufer et al. (1996, 1997 b): the grey scale or color images visualize the time development in the velocity space of the respective lines. The dynamical spectrum is left with a black line if there are more than three time steps between observations and is otherwise interpolated with splines to account for the uneven time sampling. The spectra are overplotted in the wavelength space on top of the image to show the exact intensity variations. The indicated grey or color scale on the right ordinate can be used as a look-up table for intensities of the dynamical spectrum.

In Figures 3.7 to 3.12 we show the dynamical spectra and dynamical quotient spectra (not corrected for the systemic velocity) of a representative sample of our diagnostic spectral lines. Note the different lengths of the various observing runs, namely: 1992: 55 days, 1993: 101 days, 1994: 129 days, 1995: 72 days.

Studying the dynamical spectra we see that the photospheric lines (e.g. He I λ5876) show LPVs on their whole profile while lines that are dominated by the stellar wind (Fe II λ6248 Hα) have a fairly constant blue edge. The Si II λ6347 lines show a mix of both extremes: in 1992 mostly their red wing was variable and we could in fact apply double Gaussian fits to their line profiles showing a basically constant blue component with an overlying variable (in v_{rad} and I) red component (see Figure 3.5). In 1993 – 1995 we can then see both sides of the line varying. Note that in 1992 the observing run was only about half as long as in the subsequent years so that we probably did not cover the whole variation cycle at that time. The variation patterns of the Mg II λ4481 lines are very similar to those of the Si II λ6347 lines.
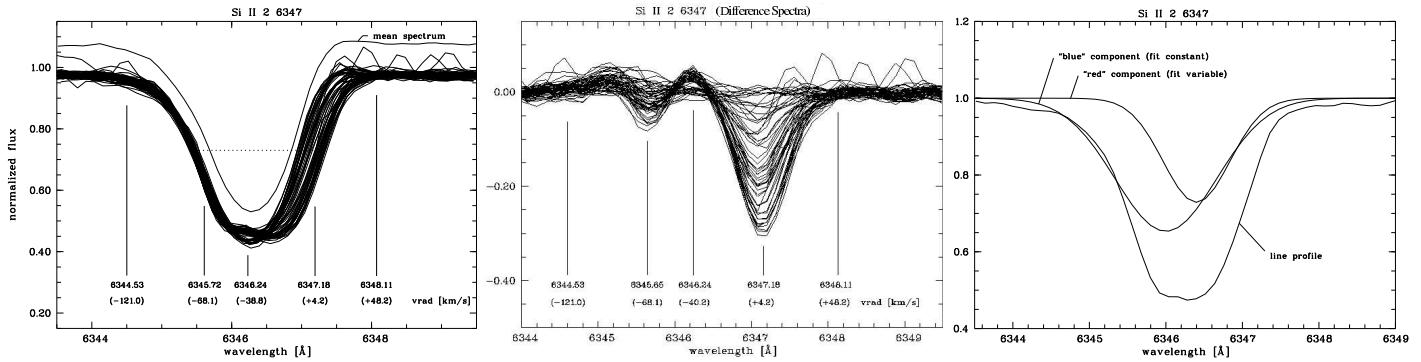
Figure 3.5: *Left*: overplot of spectra from 1992 observing run around Si II λ6347 lines and their mean spectrum shifted by +0.02 dex on the y-axis. *Middle*: overplot of spectra from 1992 observing run around Si II λ6347 lines with their mean spectrum subtracted (= difference spectra). *Right*: double Gaussian fits of one particular Si II λ6347 line with constant blue and variable red component.

The corresponding quotient spectra show that the variations occur predominantly at about $\sim 0\,\mathrm{km\,s^{-1}}$ and $-60\,\mathrm{km\,s^{-1}}$ at *all* lines. They have the form of quickly appearing and disappearing pseudo-absorptions and pseudo-emissions that are rather symmetric about the systemic velocity with mostly constant radial velocity. The variation patterns exhibit strong cyclical behavior with time scales around ~ 40 and ~ 80 days. A few times we also see cyclical prograde and retrograde moving features (see Figure 3.9 and Figure 3.26, left). In the wind and envelope lines (i.e. Fe II λ6248, Hγ, Hβ Hα, Na D) we can see additional non-cyclical blue-shifted intensity-variable but stationary features. Progressing features that move through the whole line profile to the blue edge of the wind profiles at about $-170\,\mathrm{km\,s^{-1}}$ have not been detected at any line (neither studying individual observing runs nor tracing the whole observing period). The only possible slowly outward moving non-cyclical features are found around the blue-shifted Na D absorption components: e.g. in 1993 the strongest of these weak features appears to move from about $-80\,\mathrm{km\,s^{-1}}$ to $-85\,\mathrm{km\,s^{-1}}$ in ~ 90 days (Figure 3.12) – and even in this case it seems likely that intensity-variable *stationary* features cause the apparent "moving" effect. Although no progressing features were found over the full observing cycle it is possible that they occur at other times: e.g. the stellar wind might have previously swept up density enhancements or perhaps shell ejections occurred which could produce the observed multi-component absorption line profiles.

The Fe II λ6248 lines probably show the most complex line profiles and variation patterns with multiple, variable absorption and emission components. In 1992 we can see four distinct variation features at around $v_{\mathrm{rad}} \approx -95, -65, -30$ and $0\,\mathrm{km\,s^{-1}}$. Again the features appear to vary quickly in their intensity and switch from pseudo-absorption to pseudo-emission while their radial velocity remains constant. The blue edge of the Fe II λ6248 line with a maximum velocity of about $-145\,\mathrm{km\,s^{-1}}$ is never variable. In 1993 – 1995 the Fe II λ6248 quotient spectra look similar to the Si II λ6347 variation patterns with only two or three distinct variation features that move slightly in a prograde direction (see Figure 3.9).

The Hα profiles do not show significant radial velocity variations during a given observing epoch (typical v_{rad} variations are less than $\sim 2\,\mathrm{km\,s^{-1}}$). However we note again that the absorption components of the Hα–P Cygni profiles in 1994 have higher velocities (about $15-40\,\mathrm{km\,s^{-1}}$) than during the other observing runs. The main Hα line variations during an individual observing cycle occur in the relative intensity of the emission component which can vary by $10-20\,\%$ on a time scale of a $3-4$ weeks (see Figures 3.11 and Figure 3.33, top/left). Apart from the emission component the strong variation patterns seen in the dynamical quotient spectra of Hα are not real. They occur because of the strong gradient of the P Cygni profiles at those positions (e.g. in particular the strongest emission components of the Balmer lines and the saturated absorption lines of Hα, Hβ and Na D) where even minor inaccuracies in the normalization and wavelength determination in the data reduction steps produce large differences in the quotient spectra.
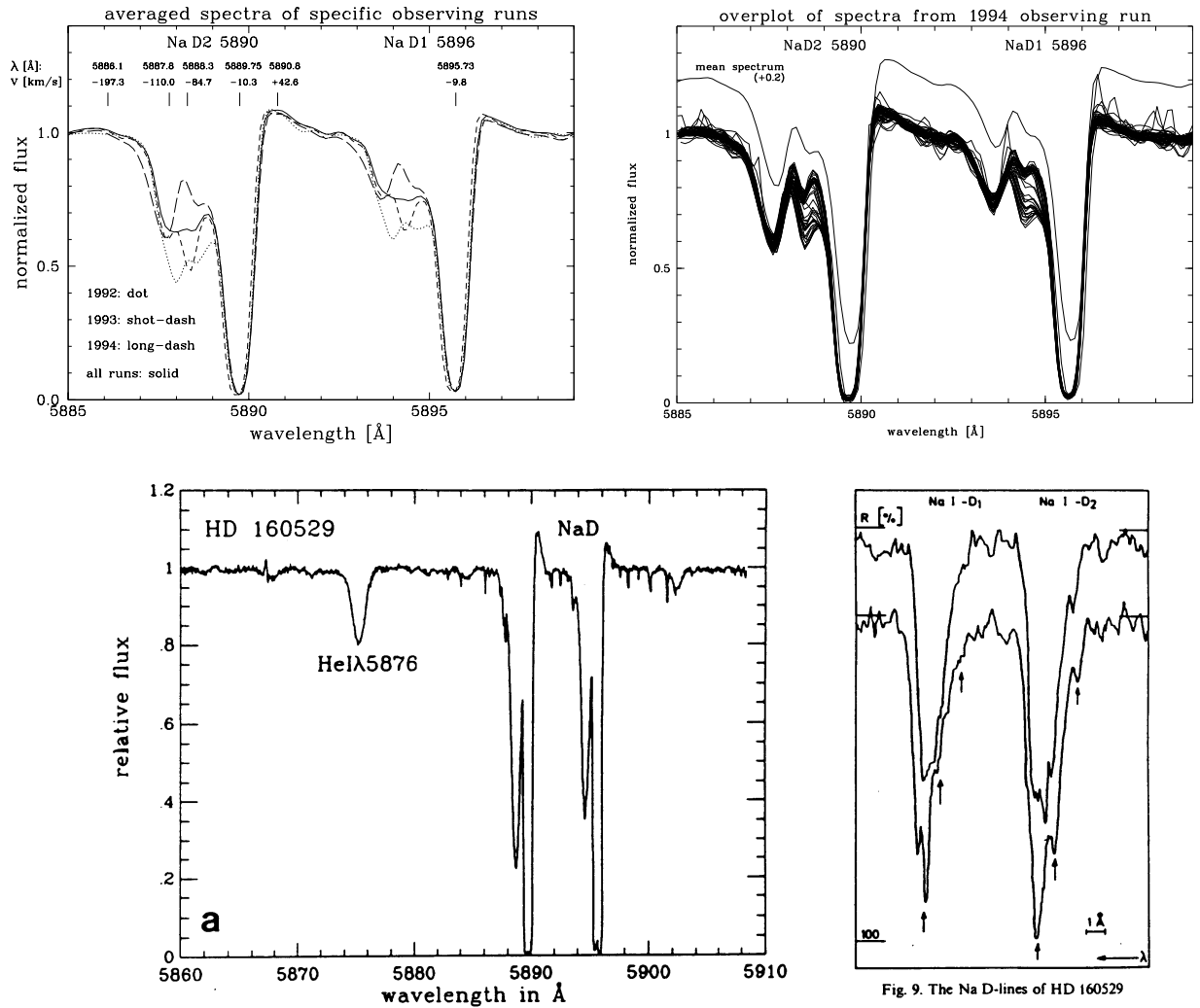
Figure 3.6: *Top/Left*: year-to-year variability of Na D lines. Marked are the blue edge and the maxima in the line profile of the mean spectrum of all observations. *Top/Right*: overplot of spectra from 1994 observing run around Na D lines and their mean spectrum shifted in y by +0.02 dex. *Bottom*: reproduced plots of Sterken et al. (1991) with observations taken in 1986 (*left*) and Wolf et al. (1974) with observations taken in 1973 (*right*).

The quotient spectra of the Na D lines suffer from the same gradient problem as the Hα lines so we dismiss the two strongest variation features around the saturated interstellar absorption component although there might be some stellar contribution to their LPVs as well. Instead we focus on the weaker variation pattern around $v_{rad} \approx -70$ to $-130\,\mathrm{km\,s^{-1}}$. Note that the observed Ca II lines show very similar line profiles and variation patterns to the Na D spectra and our discussion of the Na D lines applies for the Ca II as well. In the right plot of Figure 3.6 we show an overplot of the Na D spectra from 1994 which exhibit the strongest variations during a given observing run. Studying the line-profile variations of individual observing runs we see that particularly the absorption component around $-70\,\mathrm{km\,s^{-1}}$ is strongly variable in Ca II and Na I whereas the absorption component around $-100\,\mathrm{km\,s^{-1}}$ and the emission component at about $+35\,\mathrm{km\,s^{-1}}$ remain fairly constant. The LPVs around $-100\,\mathrm{km\,s^{-1}}$ in the year-to-year variations plot of Figure 3.6 (left) are thus only blending effects from the dominant $-70\,\mathrm{km\,s^{-1}}$ variability. Comparing the Na D lines with spectra taken by Sterken et al. (1991) and Wolf et al. (1974) we can see that the Na D line profiles are strongly variable on a time scale of years to decades: in Sterken's observations of 1986 the absorption components are quite different from our measurements while in Wolf's spectra of 1973 the emission component is different (i.e. missing) as well.
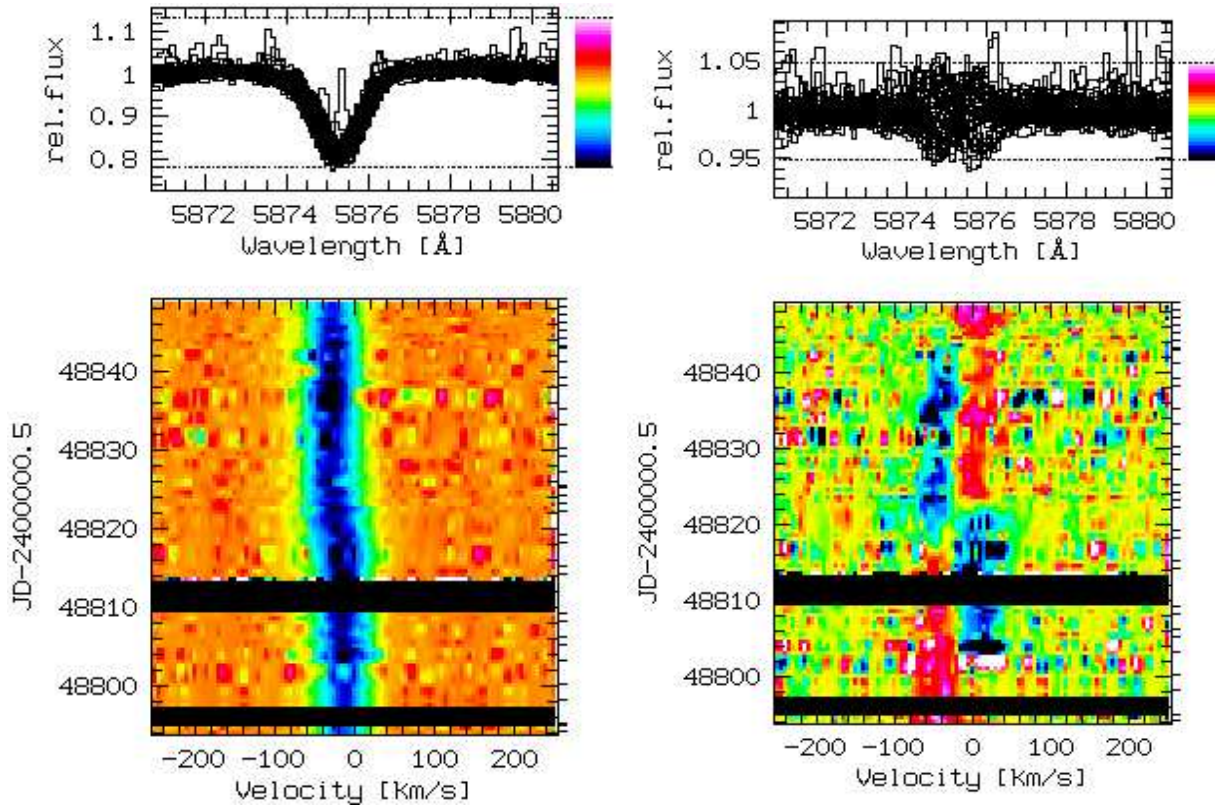
Figure 3.7: He I λ5876 line profile variations in 1992. *Left/Right*: dynamical spectrum/dynamical quotient spectrum.
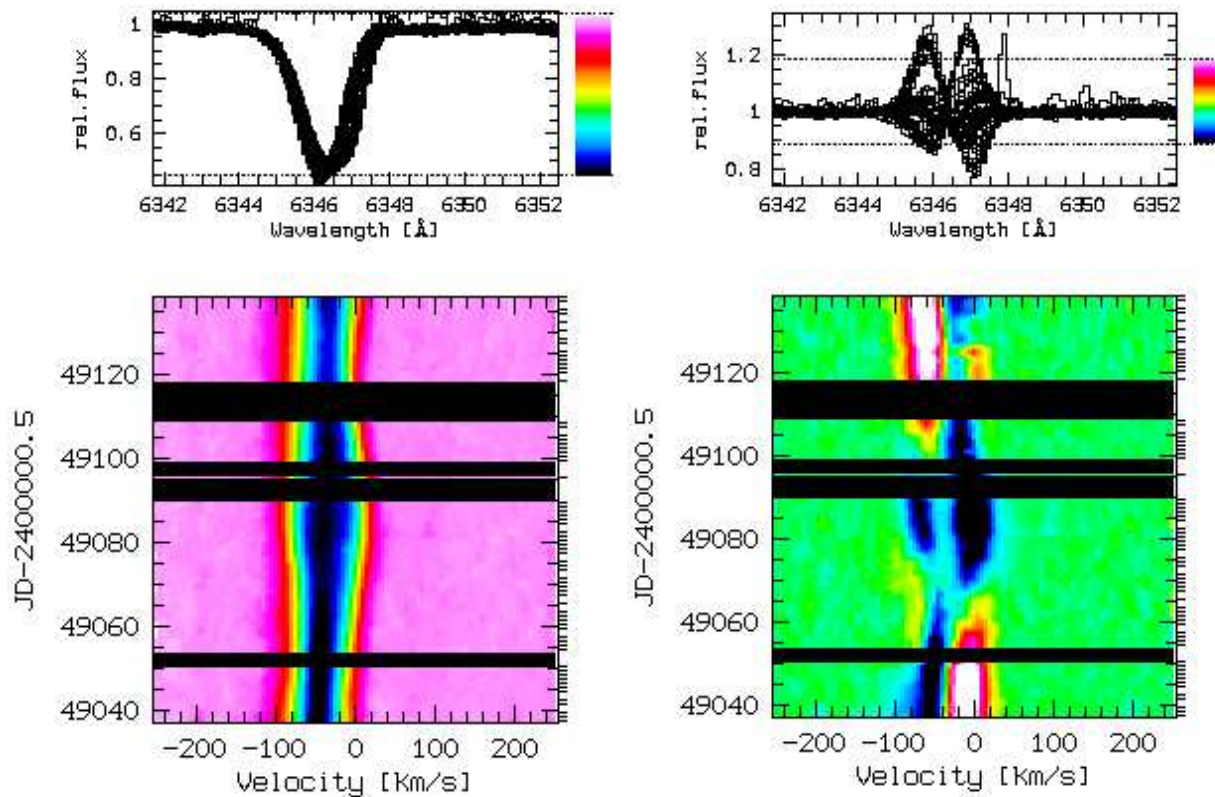
Figure 3.8: Si II λ6347 line profile variations in 1993. *Left/Right*: dynamical spectrum/dynamical quotient spectrum.
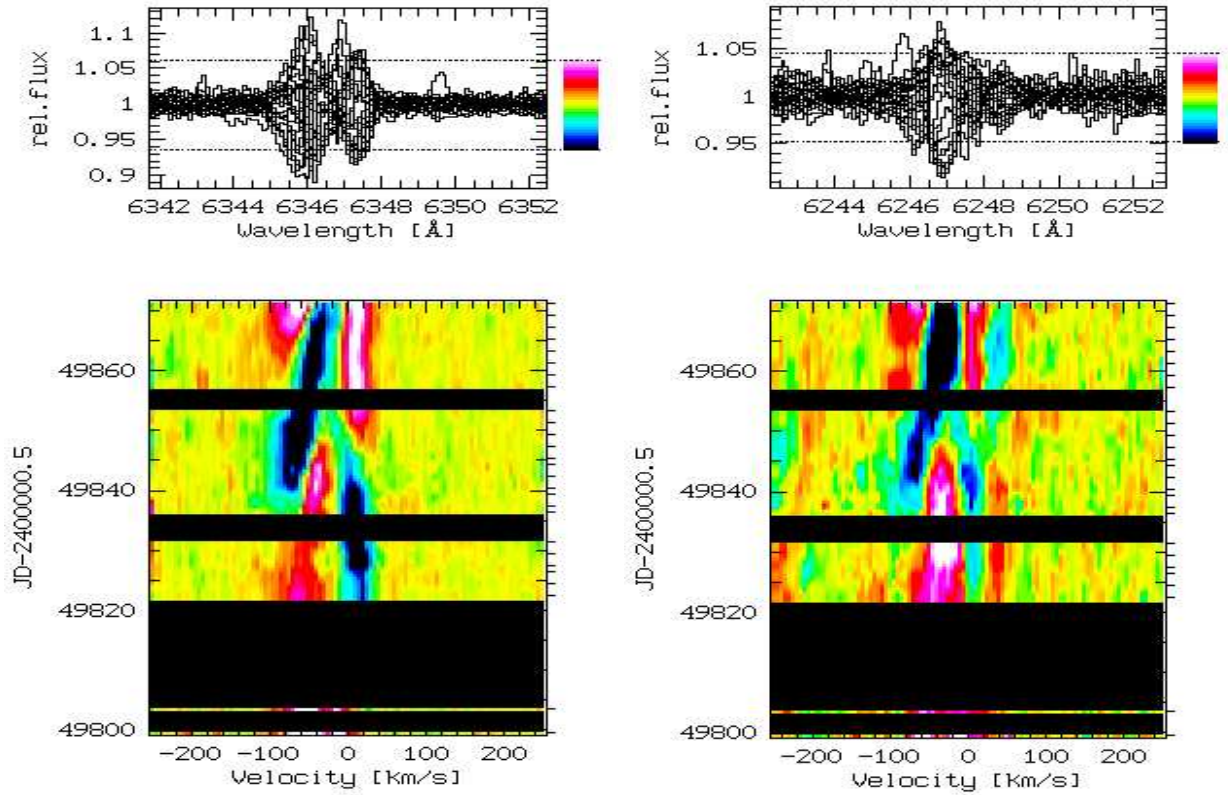
Figure 3.9: *Left*: Dynamical quotient spectra Si II λ6347 in 1995. *Right*: Dynamical quotient spectra Fe II λ6248 in 1995.
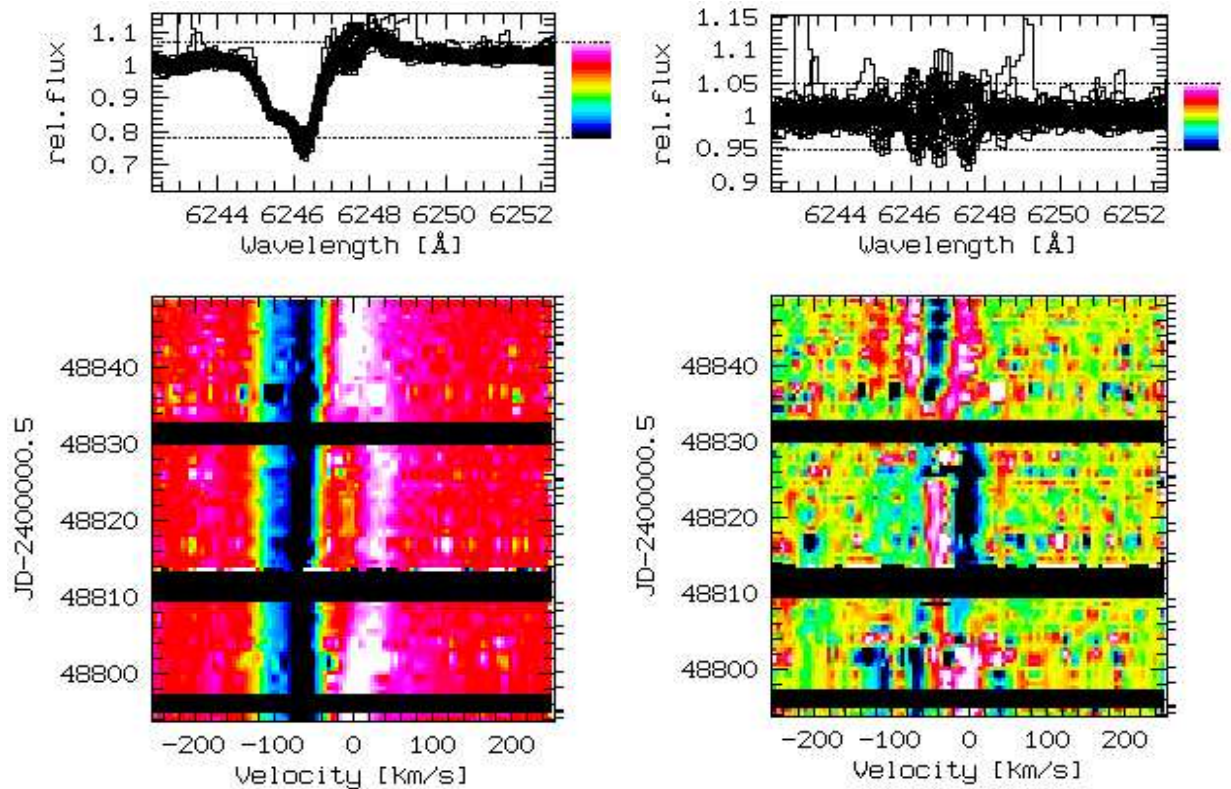
Figure 3.10: Fe II λ6248 line profile variations in 1992. *Left/Right*: dynamical spectrum/dynamical quotient spectrum.
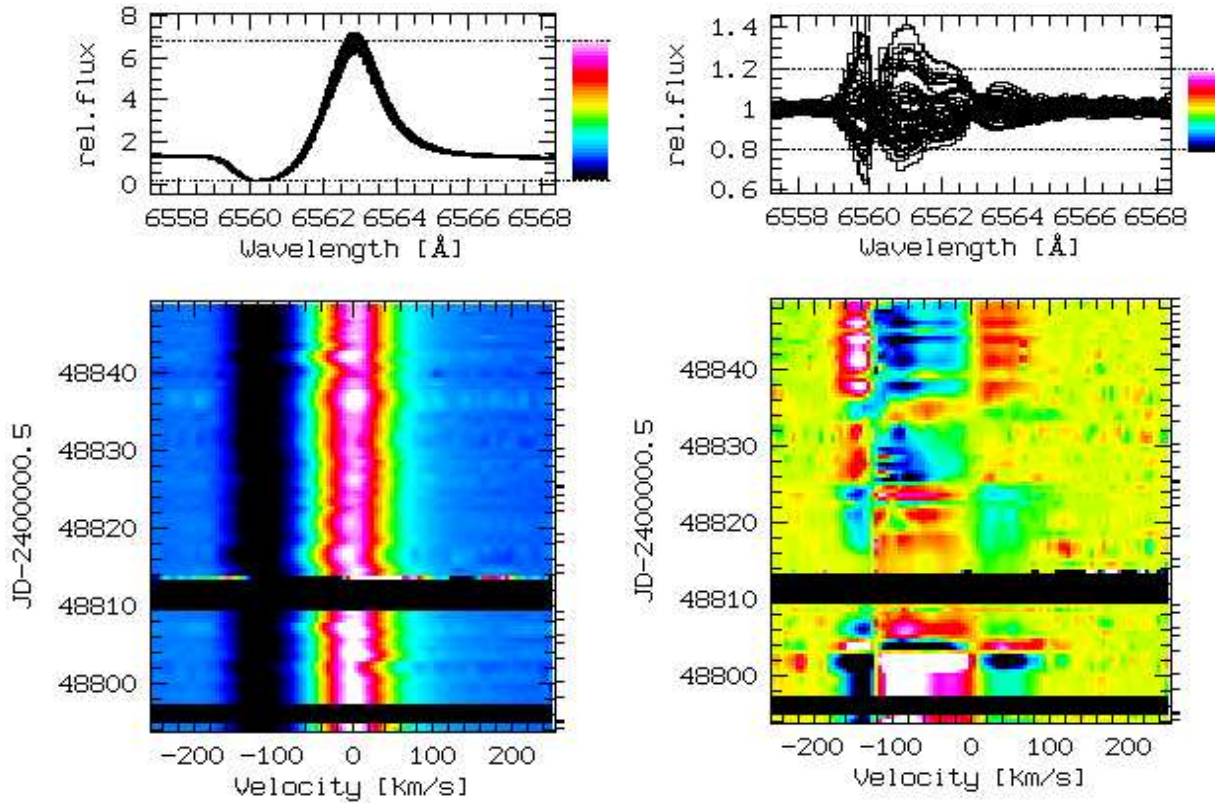
Figure 3.11: Hα line profile variations in 1992. *Left / Right*: dynamical spectrum / dynamical quotient spectrum.
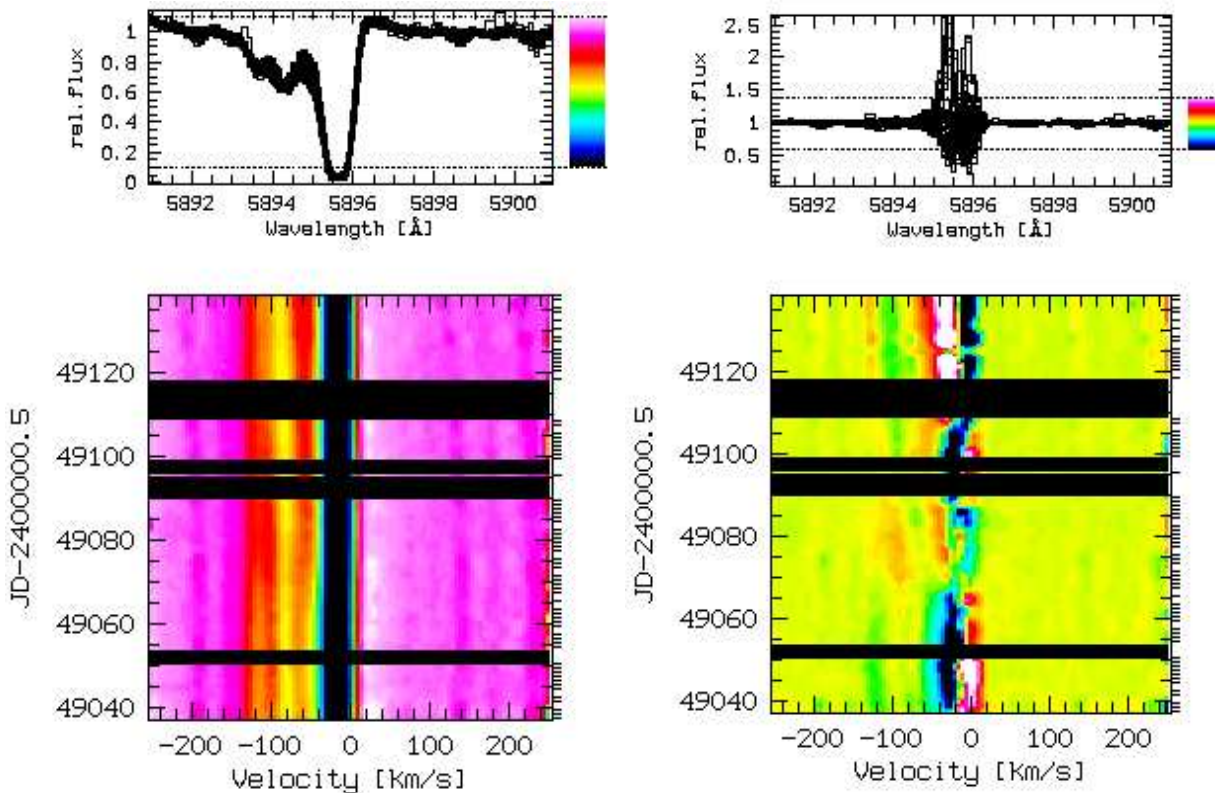
Figure 3.12: Na D 1 line profile variations in 1993. *Left / Right*: dynamical spectrum / dynamical quotient spectrum.

3.5.2 Temporal-Variance Spectra (TVS)

Fullerton (1990) developed in his dissertation the method of temporal-variance spectra (TVS) to local-ize and quantify the amplitudes of line-profile variations by comparing the LPVs with the surrounding continuum:

$$(TVS)_i = \sigma_0^2 \frac{1}{N-1} \sum_{j=1}^{N} \left(\frac{S_{ij} - \bar{S}_i}{\sigma_{jc} \sqrt{S_{ij}}} \right)^2$$

where S_{ij} is the normalized intensity of pixel i in spectrum j, $\bar{S}_i$ the weighted mean of the normalized intensity, σ_{jc} the inverse of the S/N of spectrum j measured in a continuum band, and σ_0 the inverse of the rms S/N of the time series.

In simple terms this calculation produces a one-dimensional "spectrum" of the distribution of the LPV across the line profile. A detailed description of the method can be found in Fullerton et al. (1996). For our data set we used the adapted form of the TVS analysis for CCD spectra from Kaufer (1996).

Because $(TVS)^{1/2}$ is linearly proportional to the amplitude of the variability we plotted this quantity in percent versus the rest velocity of the corresponding spectral line. Due to the statistical approach we can derive a level of significance for the probability of a variation. In our plots the level of significance for a 95% probability is at approximately 1 % $(TVS)^{1/2}$ for all lines and observing periods.

In Figure 3.13 we show the temporal-variance spectra of the individual observing periods for some diag-nostic spectral lines. The correlation between the intensity variations of the dynamical quotient spectra and the corresponding TVS is clearly visible. However the temporal-variance spectra now allow precise measurements (e.g. positions and intensities) of the previously described line profile variations:
the photospheric lines always show a double-peaked TVS profile that is quite symmetric about the sys-temic velocity (around $v_{\rm sys} \pm 20 - 40\,{\rm km\,s^{-1}}$). The separation of the peaks from $v_{\rm sys}$ is increasing with increasing radial velocity of the lines (e.g. in 1992 the peaks of the He I λ5876 line are at $v_{\rm sys} \pm 25\,{\rm km\,s^{-1}}$, while they are at $v_{\rm sys} \pm 40\,{\rm km\,s^{-1}}$ for the Si II λ6347 line). The wind lines have two additional blue-shifted peaks (around $v_{\rm sys}$–70 km s^{-1} and $v_{\rm sys}$–130 km s^{-1}) that are weaker than the $v_{\rm sys}$-centered ones. Note that the Hα peaks close to $v_{\rm sys}$ are mainly due to the steep line gradients and spectral normalization and are not reliable (see previous discussion of this effect for quotient spectra). This artifact to a lesser extent also exists in the blue-shifted peaks which is where we see the saturated absorption in Hα and Hβ. However the peaks also exist at the Hγ and Fe II λ6248 lines where the artifact should be negligible. In 1994 the Fe II λ6248 line has as an additional strong component at $v_{\rm rad} = -200\,{\rm km\,s^{-1}}$ that is not vis-ible at the other spectral lines. The envelope lines (i.e. Na D) show again the unreliable extreme double peaks close to $v_{\rm sys}$ but also have one to three weak and variable components around $v_{\rm rad} = -80, -100$ and $-130\,{\rm km\,s^{-1}}$.

The double-peaked structure of the photospheric TVS lines is very similar to those found for BA super-giants by Kaufer et al. (1997 b). The authors explain these profiles by radial and non-radial pulsations: radial pulsation modes contribute only to the line wings while non-radial modes give the main contribu-tion at the line cores due to traveling bumps crossing the complete profile. We examine this theory in section 3.6.3 by trying to model our observed photospheric LPVs with a simple pulsational code.

The far blue-shifted TVS peaks of the wind and envelope lines however are not easily explained by pulsational mechanisms. Even if we exclude all blue-shifted lines that might be contaminated by the above mentioned artifact the observed slowly moving features at the blue side of the sodium lines are definitely real. As these blue components do not have a red counterpart we can also exclude axially symmetric outflow structures (e.g. rotational modulation of wind lines and corotating magnetic fields
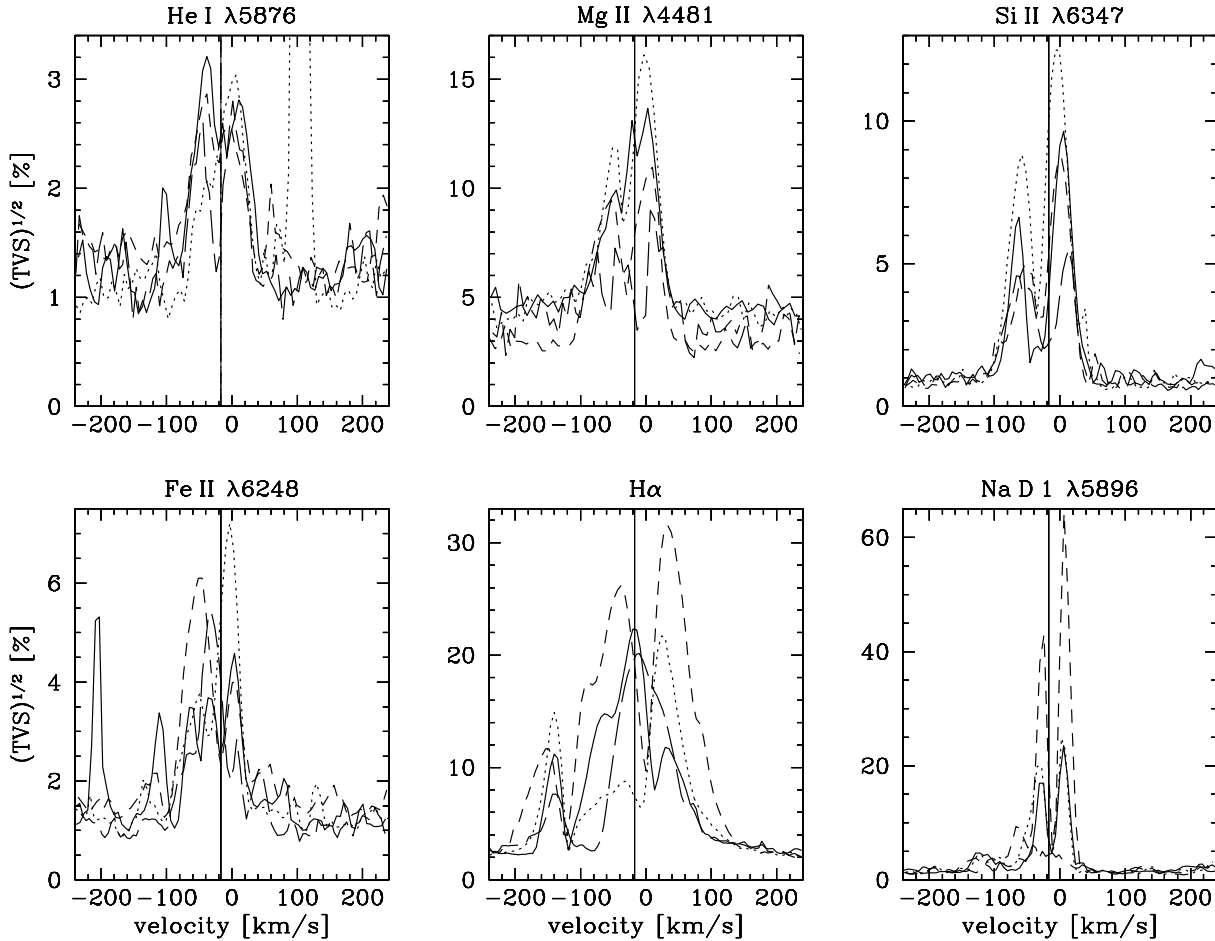
Figure 3.13: TVS of some selected lines. Solid lines: 1992, dotted lines: 1993, short-dashed lines: 1994, long-dashed lines: 1995. The peak at $+100\,\mathrm{km\,s^{-1}}$ in the He I $\lambda5876$ line of 1993 is due to a bad pixel row crossing the corresponding echelle order on the CCD. Note the different scaling of the ordinates. The level of significance for a 95% probability is approximately 1 % $(\mathrm{TVS})^{1/2}$ for all lines and observing periods. The thin vertical line indicates the systemic velocity ($v_{\mathrm{sys}} = -17\,\mathrm{km\,s^{-1}}$).

have been found in BA supergiants by Kaufer et al. 1996). One explanation might be that these peaks arise from slowly outward moving density enhancements in the wind. They might have been caused by previous eruptions through shell ejections or by wind interactions with the ambient medium moving at different speeds and thus sweeping up slowly outward moving shells.

3.5.3   Equivalent Width (W_λ), Radial Velocity (v_{rad}) and Photometric Variations

Individual examinations of the huge number of obtained spectra would be subjective and very time-consuming. Thus we used automatic procedures to objectively measure the equivalent widths (W_λ), radial velocities (v_{rad}) and intensities (I) of the spectral lines. Gaussian fits were used to derive the v_{rad}, I and $FWHM$ values with the start and end values of the Gaussian usually set to about $\pm1-2\,\text{Å}$ around the previously measured position of the line in the mean spectrum. A χ^2 value was assigned to each data point so that extreme values could be easily identified and removed from further analyses if necessary (e.g. when the line was crossed by a cosmic ray). The W_λ values were measured by integrating the line directly (with limits set to similar values as above).

This method generally leads to good results as long as the lines are not blended or distorted (e.g. by

Table 3.6: Mean values from TSA (sorted by spectral lines with increasing wind influence, i.e. increasing $v_{\rm rad}$ values). Given are the mean values and standard deviations for the individual observing runs. EM: emission component ($\overline{W_\lambda} < 0$), AB: absorption component ($\overline{W_\lambda} > 0$), −: feature not found. The equivalent width was derived by intergrating over the whole profile; for lines with P Cygni profile the dominant component determines the sign of $\overline{W_\lambda}$.

spectral line	year	$\overline{W_\lambda}$ [mÅ]	$\overline{v_{\rm rad}\,(AB)}$ [km s^{-1}]	$\overline{v_{\rm rad}\,(EM)}$ [km s^{-1}]
He I λ4471	1992	$+113 \pm 42$	-14.3 ± 12.0	−
	1993	$+91 \pm 57$	-14.1 ± 14.7	−
	1994	$+103 \pm 27$	-18.3 ± 6.9	−
	1995	$+126 \pm 56$	-20.1 ± 32.8	−
He I λ5876	1992	$+270 \pm 30$	-21.2 ± 6.6	−
	1993	$+246 \pm 77$	-23.5 ± 5.0	−
	1994	$+226 \pm 23$	-24.1 ± 4.1	−
	1995	$+237 \pm 22$	-24.2 ± 5.3	−
Mg II λ4481	1992	$+758 \pm 82$	-31.1 ± 4.6	−
	1993	$+720 \pm 88$	-33.1 ± 5.2	−
	1994	$+692 \pm 46$	-35.2 ± 5.1	−
	1995	$+772 \pm 63$	-26.2 ± 2.2	−
Si II λ6347	1992	$+946 \pm 73$	-37.1 ± 4.6	−
	1993	$+879 \pm 101$	-38.5 ± 3.4	−
	1994	$+840 \pm 35$	-41.0 ± 4.7	−
	1995	$+861 \pm 50$	-32.4 ± 1.8	−
Ti II λ4468	1992	$+194 \pm 76$	-52.9 ± 13.5	−
	1993	$+207 \pm 90$	-49.8 ± 10.4	−
	1994	$+181 \pm 57$	-44.4 ± 10.3	−
	1995	$+114 \pm 55$	-30.4 ± 5.0	−
Fe II λ6248	1992	$+280 \pm 39$	-74.8 ± 3.4	$+24.6 \pm 20.9$
	1993	$+221 \pm 67$	-75.3 ± 5.3	$+17.0 \pm 17.5$
	1994	$+139 \pm 58$	-76.5 ± 12.6	$+11.0 \pm 16.0$
	1995	$+132 \pm 46$	-60.3 ± 11.6	$+33.1 \pm 12.6$
Hδ	1992	$+1028 \pm 143$	-74.1 ± 19.4	−
	1993	$+870 \pm 184$	-73.5 ± 8.3	−
	1994	$+837 \pm 98$	-71.6 ± 4.4	−
	1995	$+833 \pm 142$	-58.8 ± 4.1	−
Hγ	1992	$+742 \pm 96$	-86.2 ± 4	$+5.9 \pm 6.7$
	1993	$+554 \pm 107$	-86.3 ± 4	$+1.3 \pm 8.1$
	1994	$+471 \pm 89$	-90.2 ± 5.9	$+4.0 \pm 8.0$
	1995	$+458 \pm 59$	-72.5 ± 4.0	$+6.0 \pm 5.0$
Hβ	1992	$+161 \pm 148$	-98.3 ± 1.9	$+4.6 \pm 1.5$
	1993	-463 ± 149	-97.6 ± 1.5	$+1.8 \pm 1.7$
	1994	$+60 \pm 150$	-108.5 ± 1.9	$+2.6 \pm 1.3$
	1995	$+284 \pm 169$	-94.0 ± 2.9	$+4.4 \pm 1.8$
Hα	1992	-8076 ± 378	-116.0 ± 0.8	$+4.2 \pm 0.9$
	1993	-8488 ± 481	-114.1 ± 0.9	$+3.6 \pm 1.0$
	1994	-6822 ± 404	-130.8 ± 2.0	$+2.8 \pm 1.1$
	1995	-8596 ± 707	-119.4 ± 0.9	$+6.9 \pm 0.9$
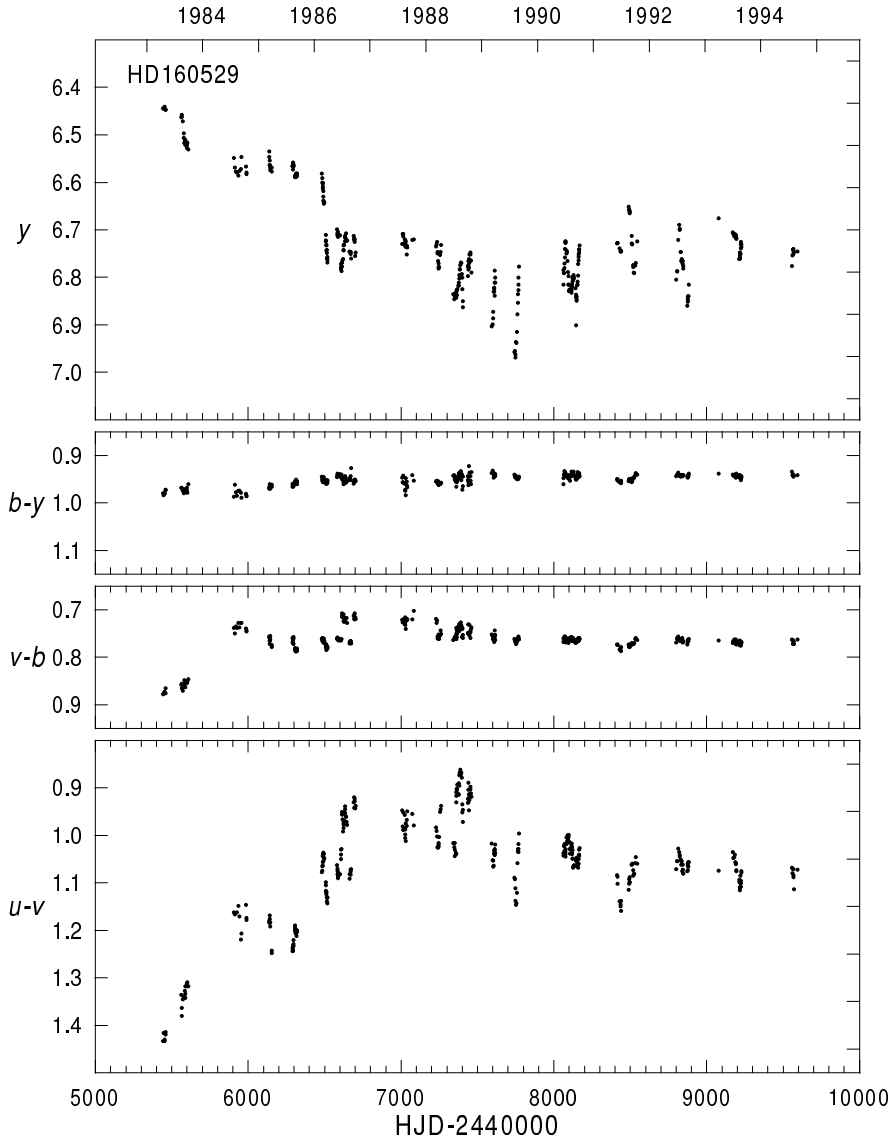
Figure 3.14:   Photometric history of HD 160529: *uvby* data obtained during the LTPV project at small telescopes on La Silla/ESO. A total of 365 datapoints (i.e. nightly averages of 1 – 3 measurements) have been collected. Plotted is the differential photometry to comparison star A5011 (HD 160461). The average values and standard deviations are:

$y = 6.758 \qquad (\sigma_y = 78)$,
$b - y = 0.946 \; (\sigma_{b-y} = 7)$,
$m_1 = -0.178 \quad (\sigma_{m_1} = 8)$,
$c_1 = 0.300 \qquad (\sigma_{c_1} = 41)$.
(*Figure 3.14 plots courtesy of Dr. C. Sterken.*)

cosmic rays or CCD defects) and the S/N ratio is above ∼30. The left plot of Figure 3.15 shows a typical result from the Gaussian fits. The error bars of the data points are derived from the fits. W_λ in this plot is derived by multiplying I and $FWHM$ so that the error bars are retained. Because of the good Gaussian fits of the He I λ5876 lines this measure of W_λ traces the directly integrated W_λ very closely but can substantially deviate for other lines (e.g. at regions with low S/N ratios).

The photometric data (*uvby*) were obtained at ESO in the framework of the "Long-Term Photometry of Variables" (LTPV) project which was initiated more than a decade ago (Sterken 1983). In Figure 3.14 we show the complete available photometric history of HD 160529 (courtesy of Dr. C. Sterken). Unfortunately only during 1992 between JD-2448795 and JD-2448848 (and on one day at JD-2449079 in 1993) are simultaneous spectroscopic and photometric observations available so that long-term (i.e. multi-year) correlations between LPVs and *uvby* data cannot be performed. Thus we concentrate on the observing run of 1992 in the discussion of correlations and photometric data.

The spectroscopic data curves reveal that *all* examined parameters (v_{rad}, W_λ, $FWHM$, I) are variable: Table 3.6 shows the mean values and standard deviations of each observing run. Looking at the values of
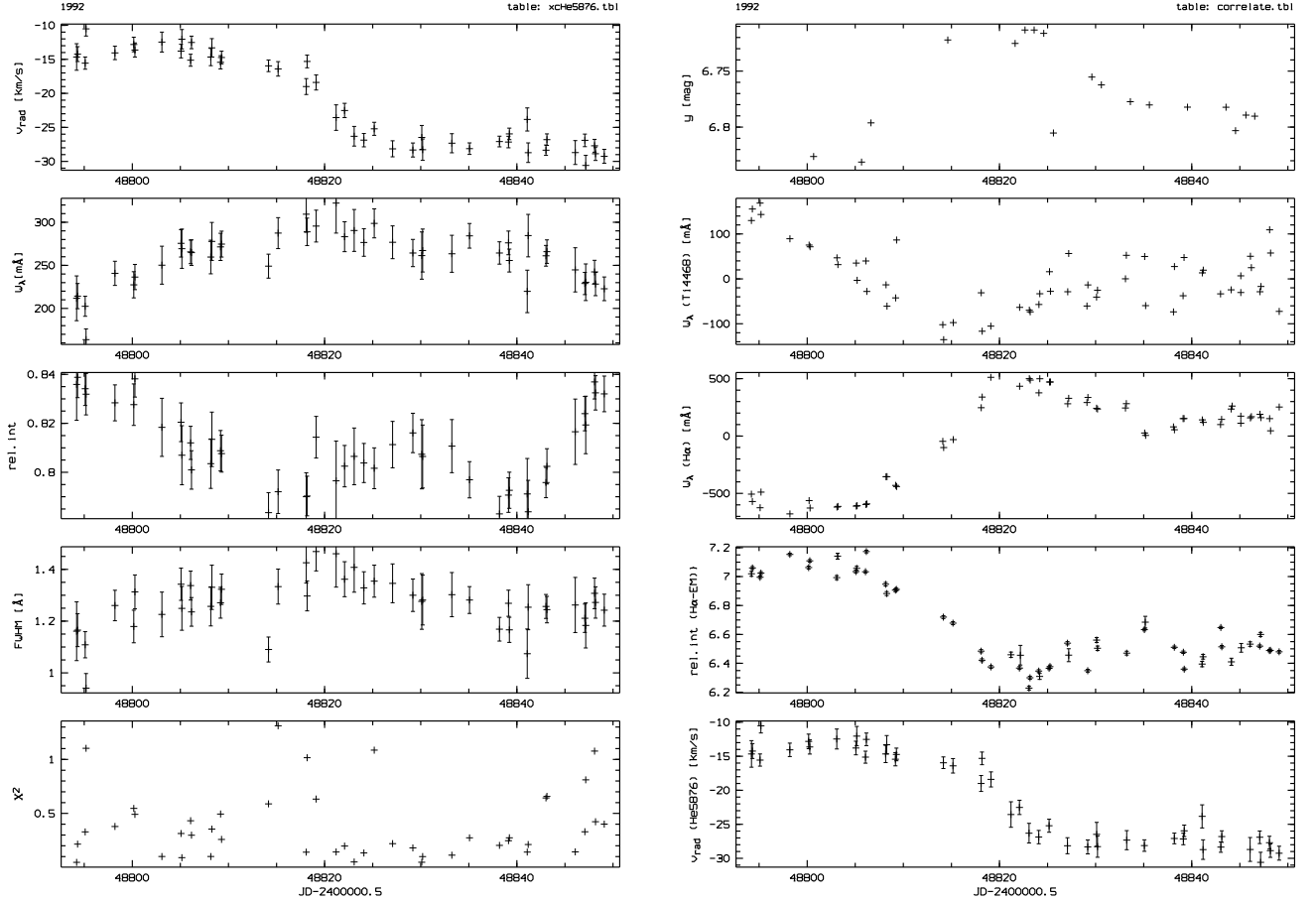
Figure 3.15: *Left*: Spectroscopic variability of He I λ5876 line in 1992 ($W_\lambda = FWHM \times I$). *Right*: Comparison of photometric and spectroscopic variability in 1992 (W_λ = directly integrated and normalized by subtracting its mean value).

the well fitting line components[4] we can see three trends:

- the *absolute* radial velocities variations decrease from the photosphere (He I λ5876, Mg II λ4481, Si II λ6347) to the wind (Hγ, Hβ, Hα),

- the *absolute* and *relative* equivalent width variations increase from photospheric to wind lines (note that for the wind lines with strong P Cygni profiles the dominating components of the W_λ variations are the emission parts of the line),

- the equivalent width variations of the wind lines are predominantly caused by variations of the line intensities while photospheric lines have about equal contributions of $FWHM$ and I to W_λ.

The next step after looking for general trends is to search for correlations between the various parameters that reflect the the physical conditions at different regions in the stellar atmosphere.

Traditionally the photometric data has been used to derive temperatures. For blue stars $c1 = (u - v) - (v - b)$ or the dereddened $c0$ and $b - y$ are good temperature indicators: when $c1$ or $b - y$ become more positive, the temperature decreases. In 1992 the $c1$ values of HD 160529 vary by $\lesssim 0.045$ dex while the $b - y$ values vary by $\lesssim 0.01$ dex. However the curves are not correlated: it looks like $b - y$ varies randomly around a constant value of 0.946 while the $c1$ curve shows a behavior that is similar to the

---

[4]He I λ4471 and Ti II λ4468 are in regions with low S/N and Fe II λ6248 and Hδ exhibit both photospheric and wind influences that are not easily separable. Thus these lines are not included in this particular analysis.
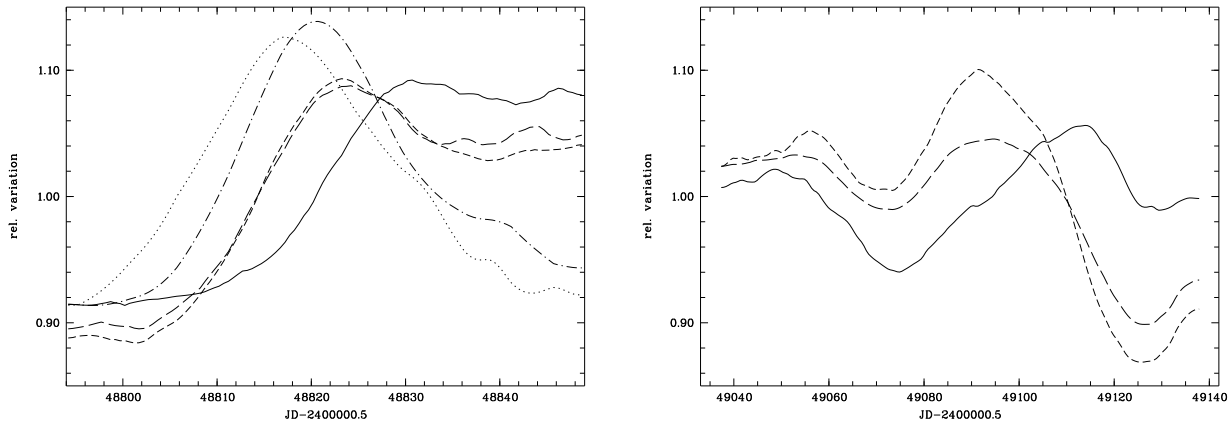
Figure 3.16: Normalized variations of y (dash-dotted), c_1 (dotted), $W_\lambda(\text{H}\alpha)$ (short dashed), $I(\text{H}\alpha)$ (long dashed) and $v_{\text{rad}}(\text{He\,I\,}\lambda5876)$ (solid). *Left*: 1992. *Right*: 1993.

observed LPVs (i.e. quasi-periodic variations with time scales of weeks to months).

We ascribe this discrepancy to the P Cygni lines with strong emission components that fall into the photometric bands: the v-band around $4100\,\text{Å}$ includes the Hδ and probably the Hγ line while the b-band around $4700\,\text{Å}$ is definitely influenced by the Hβ line and its extended electron scattering wings. Additionally the u band covers the Balmer jump region so that the only photometric parameter without hydrogen line influence is the b-band around $5500\,\text{Å}$. For HD 160529 the y behavior mirrors the $c1$ variations very closely but with much larger values: e.g. in 1992 y varied between 6.72 – 6.82 mag ($\delta y = 0.1$ mag).

Turning to our spectroscopic data set we find that for HD 160529 the Ti II $\lambda4468$ line is very temperature sensitive: comparing the observed Ti II $\lambda4468$ LPVs with calculated synthetic models we find the temperature varying from approximately $10\,000\,\text{K}$ to $11\,500\,\text{K}$ (see Figure 3.25 in section 3.6.2). To get information about the connection of photospheric and wind conditions we study the v_{rad} curve of the He I $\lambda5876$ line and the W_λ curve of Hα: if we assume that pulsations are responsible for the variations in the stellar atmosphere we can see their effect directly on the photospheric lines as radial velocity shifts and LPVs while the optically thick wind lines would reflect changes predominantly as equivalent width variations.

The easiest way to display correlations is to overplot the data points using the observing time as common abscissa. In the right plot of Figure 3.15 we show the data curves for y, the normalized[5] equivalent width values of Ti II $\lambda4468$ and Hα, the relative intensity variations of the Hα emission component and the radial velocity curve of He I $\lambda5876$. A connection between these parameters is obvious:
as the equivalent width of Ti II $\lambda4468$ decreases, the star gets brighter (y decreases), W_λ and I of Hα decrease and the radial velocity of He I $\lambda5876$ increases. The W_λ and I curves of Hα show an almost identical behavior. The W_λ (Ti II $\lambda4468$) curve peaks (i.e. has a minimum) around JD-2448815 while y and the Hα parameters reach their peak value around JD-2448820. The v_{rad} (He I $\lambda5876$) curve does not have a sharp peak but has its inflection point around JD-2448820 (assuming a sinusoidal curve). Note that the equivalent width measurements of the Ti II $\lambda4468$ lines have relatively large errors as the spectra in this blue region are already rather noisy. All other data points have very small error bars. Around their respective peaks the curves show a rather wide plateau of about 5 – 10 days. The described

---

[5]The normalized curves are obtained by subtracting the mean value of the respective parameter. The mean values can be found in Table 3.6. Note that the mean W_λ value of Hα for 1992 is $-8076\,\text{m\AA}$; adding this to the W_λ (Hα) curve shows that the *absolute* W_λ values of Hα are always negative.

behavior is even more readily discerned in Figure 3.16 where we have normalized the data curves by dividing the parameters by their mean values and fitting a spline function through those data points. The normalization and splining of the data smoothed the curves and decreased the plateau sizes. We have not plotted the W_λ (Ti II λ4468) curve in this figure because the large scatter of the original Ti II λ4468 data points (caused by the low S/N and consequently bad W_λ measurements) do not produce a reliable curve with this method.

Even considering the uncertainties and the curve shapes with their wide plateaus we can see certain time shifts between the data curves and differences in the curve shapes indicating that there might be additional mechanisms at work.

Using the W_λ (Ti II λ4468) curve as temperature indicator we can see that when the temperature increases (W_λ (Ti II λ4468) decreases) the star gets brighter (y and $c1$ decrease) so that these photometric values might be used as temperature indicator after all (e.g. when no appropriate spectroscopic data is available). At about the same time the relative intensity and equivalent width of the Hα emission decreases (note: we have already seen that the W_λ values of Hα are determined by the emission strength), however these parameters reach their peaks a few days after the Ti II λ4468 curve. This could be explained by an increase of continuum flux provoked by the temperature increase. If the Hα line profile itself did not change, the normalization of the data (i.e. division of spectra by continuum in data reduction steps) decreases the emission strength of the P Cygni line *simultaneously* to the temperature increase. The time lag of the wind variations might have been caused by mechanisms that require some travel time to affect the wind line regions (e.g. density changes that might have been triggered by radius variations).

The sinusoidal v_{rad} curve of He I λ5876 is consistent with radial and/or non-radial pulsations at the stellar surface which could trigger the observed atmospheric temperature variations and might also cause density variations in the wind that could account for the diverse time scales and curve shapes (for a discussion on pulsations see sections 2.3, 3.6.3 and 3.8).

3.5.4 Period Analysis

In the previous section we have seen that the LPVs clearly show cyclical variation patterns; however, they cannot be described with a single, simple sinusoidal function. To get an estimate of the predominant time scales and pseudo-periods we need to apply more sophisticated Fourier analysis methods.

In the following analysis we consider the v_{rad} and W_λ curves of the spectral lines and the photometric values as separate data sets and compare the individual results.

The Lomb-Scargle statistics (Lomb 1976, Scargle 1982) were used to calculate periodograms and power spectra. These methods are optimized for a non-equidistant sampling of data points and are thus ideally suited to model our data. Because the resulting spectra have a known $\chi^2(2)$ probability distribution, we can assign them levels of significance (LOS). In our period analyses we have rejected the peaks below a LOS of 99.5 %.

To examine our data sets for periodic signals we have normalized the corresponding values by subtracting their respective mean values and applied the iterative CLEAN algorithm implemented in the MIDAS TSA context (Schwarzenberg-Czerny 1993).

We tested a subsample of data sets with and without prewhitening (i.e. the removal of periods of the length of the data set) in the period search and received similar qualitative results. However because prewhitening affects the quality of the analysis (especially for long time series, see LTPV analysis) we have not used it in our final CLEAN schemes.

Table 3.7: Periodicities from CLEAN analysis. The time spans of the data sets are: spectroscopy: JD-2448795–JD-2449864, photometry: JD-2445442–JD-2449592. Ab/Em: Absorption/Emission, no notation: absorption component.

Data Set		Period (relative Power = Power/max. Power)			
photometry	dy	126.7 (1.000),	53.5 (0.308).		
	y	105.8 (1.000),	152.2 (0.632),	87.0 (0.484),	80.5 (0.155),
		45.8 (0.135),	135.9 (0.107).		
	$c1$	238.0 (1.000),	70.3 (0.250),	100.5 (0.158),	116.1 (0.150).
He I $\lambda5876$	v_{rad}	92.7 (1.000),	83.6 (0.406),	46.4 (0.197).	
	W_λ	91.6 (1.000),	29.4 (0.330).		
Mg II $\lambda4481$	v_{rad}	93.5 (1.000),	61.1 (0.128).		
	W_λ	92.6 (1.000).			
Si II $\lambda6347$	v_{rad}	93.5 (1.000),	61.7 (0.230).		
	W_λ	92.0 (1.000),	116.0 (0.289).		
Ti II $\lambda4468$	v_{rad}	101.3 (1.000),	51.7 (0.752).		
	W_λ	90.7 (1.000),	53.3 (0.346),	34.1 (0.234).	
Fe II $\lambda6248$	Ab1-v_{rad}	92.6 (1.000),	83.5 (0.875),	28.2 (0.632),	10.4 (0.244).
	Ab2-v_{rad}	114.9 (1.000),	76.1 (0.211).		
	Em-v_{rad}	94.1 (1.000).			
	W_λ	86.5 (1.000),	75.8 (0.794),	33.6 (0.484),	54.6 (0.254),
		26.3 (0.189),	51.5 (0.161).		
Hδ	v_{rad}	86.8 (1.000),	96.1 (0.836).		
	W_λ	17.2 (1.000),	12.1 (0.559),	67.0 (0.438).	
Hγ	Em-v_{rad}	126.0 (1.000),	51.2 (0.290),	69.5 (0.283).	
Hβ	Em-v_{rad}	67.6 (1.000),	44.2 (0.426),	59.5 (0.232),	60.4 (0.174),
		40.5 (0.134).			
	W_λ	127.2 (1.000),	45.3 (0.364),	64.1 (0.180),	69.8 (0.117).
Hα	Em-v_{rad}	37.9 (1.000),	20.4 (0.888),	13.3 (0.862),	17.8 (0.861),
		4.2 (0.799).			
	W_λ	114.2 (1.000),	45.1 (0.460),	36.4 (0.269),	63.3 (0.143).

The following steps are applied in this algorithm:

- calculate the level of significance for 99.5 % confidence (i.e. 3 σ probability that the detected period is significant),

- compute the power spectrum and Scargle periodogram,

- fit a sine/cosine function to the power spectrum using the frequency of the strongest peak in the periodogram,

- subtract the Fourier model from the data set and recalculate the power spectrum and periodogram for the residual,

- repeat the above steps until no more peaks are found above the LOS.

Applied on the data sets of an individual yearly observing run this algorithm produces only a few periods with rather low power. As the typical length of a variation cycle is of the order of the time of an observing run these results are rather unreliable. We have thus merged the corresponding data sets into

one combined table and used them for the following analysis.

The quantitative results of the Fourier analyses of the LPVs and some photometric parameters are shown in Table 3.7. The periods found are sorted by their relative power: we assign unity to the strongest peak in the power spectrum and normalize subsequent peaks according to this maximum value (i.e. relative power = power/maximum power). Listed are the periods with relative power greater than 0.1 and level of significance greater than 99.5 %. Note that the analyses often yield $2-5$ additional periods with rather small power (i.e. under the arbitrary 0.1 threshold that we set). The periods are measured by fitting Gaussians to the peaks in the power spectra. Periods with unrealistic fit values (e.g. standard deviation errors in the fit of the power peak greater than 1.0 dex) are not included even if their power was above the LOS threshold.

We included the differential magnitude measurements (dy) from the photometric data set in Table 3.7 to enable a direct comparison of our measurements with the photometric variability analyses of Sterken et al. (1991): those authors used some filtering techniques to remove certain trends and uniques events (e.g. a jump in the photometric data around JD-2446500) before applying the Fourier analysis which resulted in a strong period of 57 days and another possible period of about 101 days. We can see that our method (no filtering) achieves comparable results with periods of $\sim$127 days and $\sim$52 days, which strengthens our confidence in the results achieved for the spectroscopic data sets.

The extreme values of $\sim 4-20$ days and the periods in the range of $\sim 50-70$ days have rather small power values (relative as well as absolute) and mostly higher fit errors than the dominant periods so we discard them in the subsequent discussion. Note that, although our whole observing cycle covers 1069 days (JD-2448795 $-$ JD-2449864), we did not find the main $c1$ period of 238 days in our spectroscopic data so that we conclude that this value is probably not real: as we have previously discussed the $c1$ measurements are strongly affected by various Balmer lines and we suspect that this also causes the period analysis on $c1$ to be unreliable.

We can see that the dominant photospheric pulsation time scales are confined to a very narrow range of 92.5$\pm$1 days (for both the v_{rad} and the W_λ values). Note that the v_{rad} data of He I λ5876 has a secondary period (46.4 days) that is almost exactly half the dominating period (92.7 days) but that such close "integer-relations" are not found in other data sets. This might indicate the existence of beating mechanisms that only show up in the deepest photospheric regions and get quickly disturbed by wind influences. For the wind dominated lines the W_λ analyses of Hα and Hβ yield periods of $\sim$114 days and $\sim$127 days, somewhat longer than the photospheric time scales. We note that the absolute power of the equivalent width power spectra decreases strongly from Hα to Hβ (by a factor $\sim$14) and is negligible for Hγ. For the lines that originate in the regions that are influenced by the wind as well as the photosphere we find very small absolute values for the power spectra and sometimes (as in the case of W_λ (Hγ)) we cannot find any significant period at all. This indicates for that the resulting periods are most reliable for lines originating in one dominating region (i.e. either photosphere or wind).

In summary we find that the predominant time scales of the photometric and spectroscopic variabilities are within a similar range around $92-127$ days. Whereas the photospheric periods are very closely defined (92.5$\pm$1 days), the wind lines show a larger spread of time scales (about $114-127$ days). The larger periods and time scale range found for the winds lines are consistent with the previous argument that pulsations might cause temperature variations which would be immediately visible in all spectral lines through the changing continuum flux and that wind lines could be additionally influenced by density variations in the outer atmosphere that can also be triggered by the pulsations but do not affect the photospheric spectral lines.
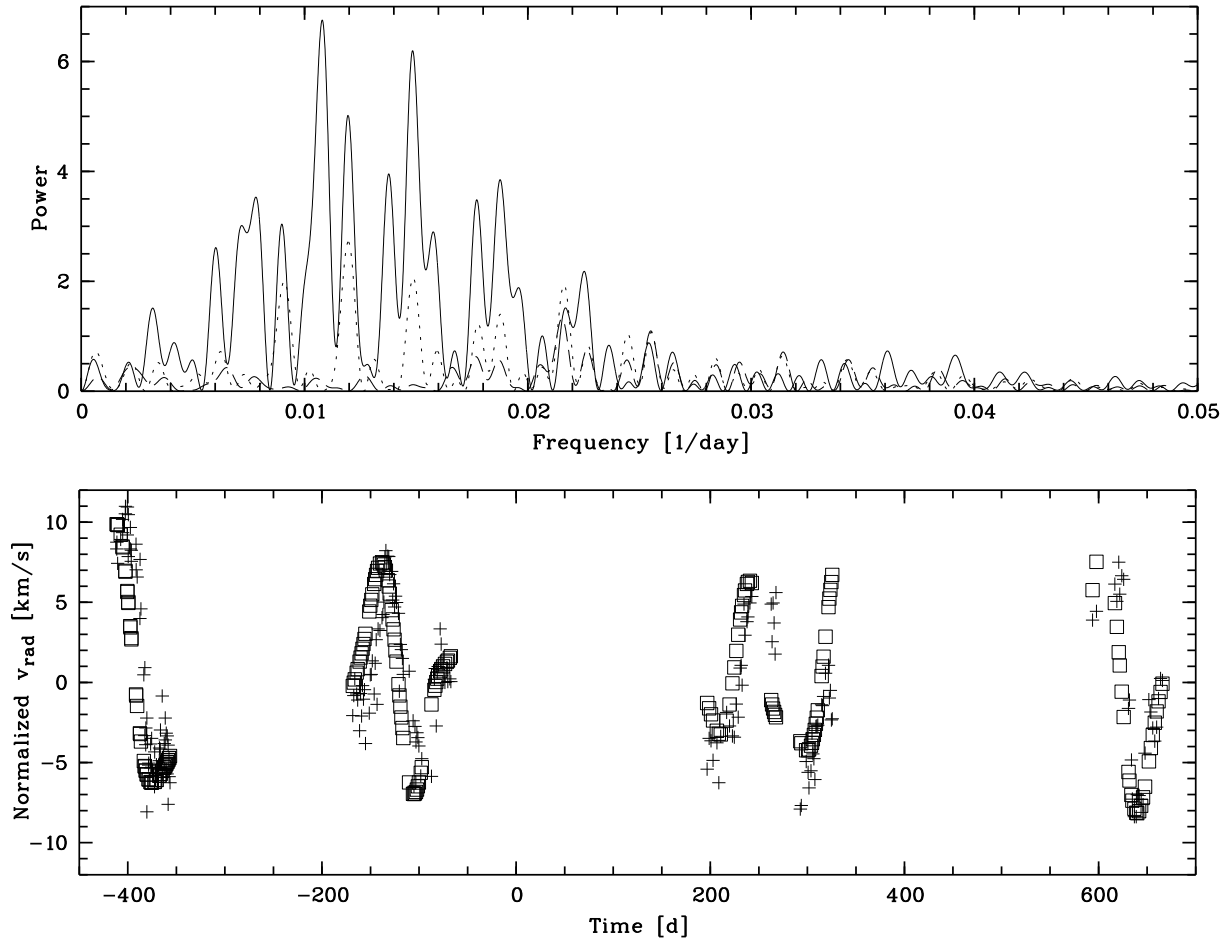
Figure 3.17: Results of the period analyses of the v_{rad} (He I λ5876) curve using the CLEAN method. Top: power spectra, solid: original data, dots: after first iteration, dashes: after second iteration. Bottom: crosses: normalized v_{rad} curve, squares: Fourier model using the three dominant periods.

In order to test the above results and check the importance of the time scales besides the main periods we recreated the respective data curves using the results from the Fourier analyses. We found that the dominating periods already restored the basic trends and overall shapes of the curves and that including the minor periods closely reassembled the complete data curves. Figure 3.17 (top) shows the power spectra corresponding to the three main periodograms found in the CLEAN analyses of the v_{rad} curve from the He I λ5876 line. The discovery and removal of the respective strongest frequency peaks and the successively decreasing power are clearly visible. In Fig. 3.17 (bottom) we show the normalized v_{rad} curve in crosses and overplot in squares the reconstructed sine/cosine function using the three periods of 92.7, 83.6 and 46.4 days. We can see that the reconstructed v_{rad} curve fits the observations very well.

3.6 Photospheric Models

As mentioned in chapter 2 the synthetic modeling of LBV spectra is a challenging task even for state-of-the-art numerical codes on current high-speed computers. No current program includes *all* possible effects in LBV atmospheres (e.g. NLTE, expanding atmosphere, electron scattering, pulsation, rotation, magnetic fields, ...). It is thus necessary to assess the influence of the specific parameters and select a particular code to optimally model the spectroscopic region of interest.
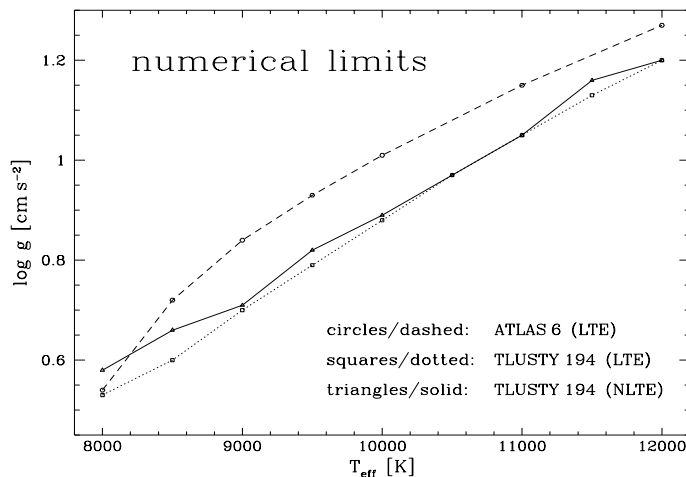
Figure 3.18: Numerical instability limits of ATLAS 6 (from Table 4 of Sterken et al., 1991) and TLUSTY 194.

Furthermore, due to the close vicinity of LBVs to their respective Eddington limits, a good convergence of the synthetic atmospheres can pose a considerable problem (see chapter 1 and 2 for arguments why LBVs are considered to be close to their respective Eddington limits).

As we have seen in the previous sections, HD 160529 exhibits certain spectral lines with minimal wind influence which originate in a narrow region at the stellar surface. Thus we can take advantage of the currently available, highly sophisticated, plane-parallel, hydrostatic codes to model these lines.

We chose the publicly available codes TLUSTY 194 and SYNSPEC 41 for the calculations of synthetic models (Hubeny et al. 1995)[6] because these programs allow departure from LTE which is relevant for hot stars ($T_{\text{eff}} \gtrsim 10\,000$ K) with low surface gravity (see section 2.1). Becker & Butler (1990) showed that NLTE calculations are crucial to get reliable stellar parameters from fitting LBV-spectra because non-LTE effects can change the profiles and equivalent widths of spectral lines in this regime of the Hertzsprung-Russell diagram (HRD).

TLUSTY 194 uses a hybrid CL/ALI scheme which combines the advantages of CL ("globalness" and fast convergence rate) and ALI (speed of computation) with the concept of superlevels (see section 2.1 for an explanation of the terms and concepts used). With these methods the program is able to calculate synthetic stellar atmospheres in non-LTE with full line-blanketing. A detailed description of the TLUSTY 194 code is given by Hubeny et al. (1995).

We have found that these codes are able to converge their atmosphere calculations at much smaller $\log g$ values than for example the ATLAS 6 code (Kurucz 1979), indicating that ATLAS 6 interrupts due to a numerical instability before the physical instability of the Eddington limit is reached. The difference of the Newtonian gravity ($\log g_{grav}$) and the acceleration due to radiation pressure ($\log g_{rad}$) is of the order of 0.06 dex for our TLUSTY 194 atmospheres at their numerical limits. In Figure 3.18 we have plotted the numerical limits of our calculations with TLUSTY 194 together with the ATLAS 6 limits of Sterken et al. (1991, their Table 4).

To determine the photospheric stellar parameters of HD 160529 we followed the method of Sterken et al. (1991) of calculating a grid of synthetic models as close as possible to the Eddington limit ($g_{grav} = g_{rad} + g_{turb} + g_{rot}$). For HD 160529 these limitations are especially important for constraining the possible parameter range because we cannot use ionization balances (all spectral lines are in one individual ionization state, see section 3.6.1).

---

[6]We are indebted to Ivan Hubeny and Thierry Lanz who provided the initial input files to calculate model atmospheres appropriate for cool LBVs and gratefully acknowledge their subsequent support during the numerical calculations.

All synthetic spectra were calculated using the following sequential scheme:
first, a simple LTE model is calculated with TLUSTY 194. The next step is a NLTE/C (continuum only) model, where the lines are assumed to be in detailed radiative balance. The final model is NLTE/L including all lines explicitly. The models calculate atmospheres with 91 NLTE levels or superlevels of H, He I, C I, C II, Mg I, Mg II, Si I, and Si II internally. Other elements in various excitation and ionization states were included using the line lists provided with the programs (stand of October 1995). SYNSPEC 41 is used to create synthetic spectra based on the TLUSTY 194 atmospheres. Its input parameters (in particular rotational convolution, turbulence velocities, doppler shift, abundances and spectral resolution) are altered until optimal fits of the observed lines are reached.

The starting grid of TLUSTY 194 models was calculated with $T_{\text{eff}} = 8\,000$ K to $12\,000$ K in steps of $\Delta T = 500$ K using solar abundances. To simulate the physical instability of the Eddington limit empirically we reduced the $\log g$ values in steps of 0.01 until the code reached its critical numerical limits. The first fully converging synthetic models are used as lower limits for T_{eff}, $\log g$ and the element abundance. The instrumental profile was taken into account by convolving the resulting synthetic spectra with a Gaussian function to a resolution of 0.22 Å.

The grid of models was extended by decreasing the temperature-grid steps to $\Delta T = 100$ K and varying the parameters in a range close to the numerical limits; the best fitting spectra were selected to represent the stellar photosphere. The results are presented in the following section.

3.6.1   Stellar Parameters of the Mean Photosphere

Temperature, Surface Gravity and Abundances

As previously mentioned the He I and the highest Balmer lines are formed very deep in the atmosphere of HD 160529 (their line profiles have the lowest radial velocities and relatively good symmetry and are in pure weak absorption (i.e. not much wind influenced)). T_{eff} and $\log g$ values of the photosphere were thus determined by fitting synthetic spectra to these lines in the averaged spectrum.

To excite the He I $\lambda 4471$ line, the codes need a minimum temperature of $T_{\text{eff}} = 10\,000$ K, while for temperatures greater than $12\,000$ K the synthetic He I lines become too strong. The $\log g$ values for the
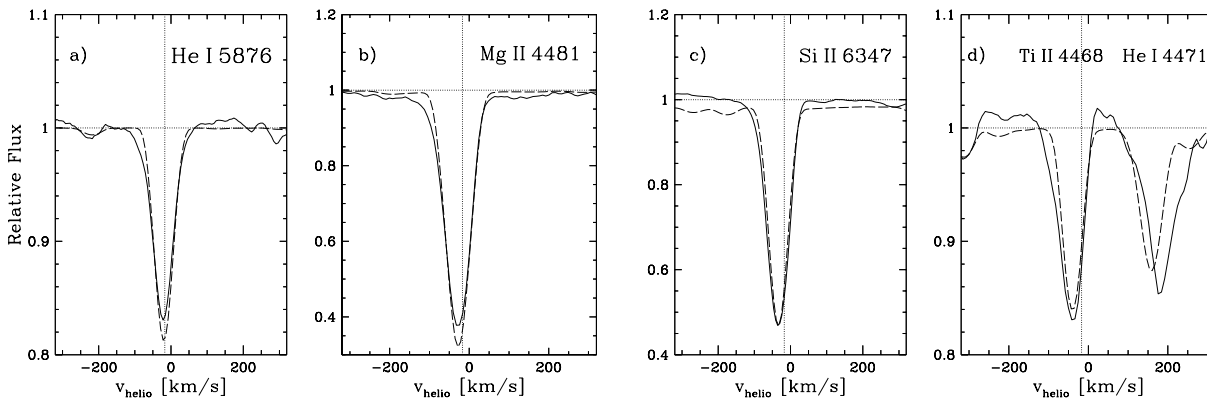
Figure 3.19: The observed mean photospheric spectral lines (thick solid lines) and the corresponding synthetic spectra from TLUSTY 194/SYNSPEC 41 (thin dashed lines). The vertical and horizontal dotted lines represent the adopted systemic velocity ($v_{\text{sys}} = -17\,\text{km s}^{-1}$) and the normalized continuum. Model parameter: a: $v_{\text{rad}} = -20\,\text{km s}^{-1}$, $T_{\text{eff}} = 11\,200$ K, b: $v_{\text{rad}} = -28\,\text{km s}^{-1}$, $T_{\text{eff}} = 9\,000$ K, c: $v_{\text{rad}} = -33\,\text{km s}^{-1}$, $T_{\text{eff}} = 8\,500$ K, d: $v_{\text{rad}} = -40\,\text{km s}^{-1}$, $T_{\text{eff}} = 10\,500$ K. All models use solar abundances, $\log g = 1.13$, a rotation velocity of $v_{\text{rot}} = 35\,\text{km s}^{-1}$ and a microturbulence velocity of $\xi_{\text{micro}} = 15\,\text{km s}^{-1}$.

He I line fits range from 0.97 for $T_{\text{eff}} = 10\,500$ K to 1.28 for $T_{\text{eff}} = 12\,000$ K with the best fit around $T_{\text{eff}} = 11\,200$ K, $\log g = 1.13$ and He abundances close to the solar values. Reasonably good fits of He I $\lambda 4471$ and He I $\lambda 5876$ could also be achieved by increasing the helium abundances (up to ~ 2 x solar) while simultaneously decreasing the microturbulence values (down to $\sim 10\,\text{km s}^{-1}$). At 11 200 K, the Mg II $\lambda 4481$ line can be fitted well only with unrealistically high abundances (~ 100 x solar), however at $T_{\text{eff}} = 9\,000$ K, $\log g = 1.13$ a good fit can be obtained with solar values too (Figure 3.19b). The Mg II $\lambda 4481$ line is also blue-shifted by ca. $-8\,\text{km s}^{-1}$ with respect to the He lines indicating that Mg lines are formed further out in the stellar atmosphere, where the stellar wind reaches higher velocities and the temperature may have dropped by ~ 2000 K. Spectral lines intensities of heavier elements (e.g. Fe II, Ti II) also get stronger at lower temperatures, so that good agreements with the observations can be achieved at these low $\log g$ values with solar abundances.

Figure 3.19 shows a sample of photospheric lines from the mean observed spectrum (solid) and their best fitting synthetic spectra (dashed). We can see the decreasing temperature trend with increasing distance from the stellar surface: He I $\lambda 5876$: $v_{\text{rad}} = -20\,\text{km s}^{-1}$, $T_{\text{eff}} = 11\,200$ K, Mg II $\lambda 4481$: $v_{\text{rad}} = -28\,\text{km s}^{-1}$, $T_{\text{eff}} = 9\,000$ K, Si II $\lambda 6347$: $v_{\text{rad}} = -33\,\text{km s}^{-1}$, $T_{\text{eff}} = 8\,500$ K. The Ti II $\lambda 4468$ line at $v_{\text{rad}} = -40\,\text{km s}^{-1}$ already exhibits relatively strong wind influence (much shallower blue line wing) and thus the *absolute* temperature determination from this line might not be very reliable.

The low $\log g$ values from the He-line fits can be verified by calculating a grid of synthetic NLTE models with different $\log g$ values around the Balmer jump region (i.e. from $3650 - 3700$ Å): the higher the Balmer line the deeper it is formed in the atmosphere and the closer it is to its neighbor in the Balmer series. At a certain point consecutive lines overlap each other and form the Balmer jump area. The
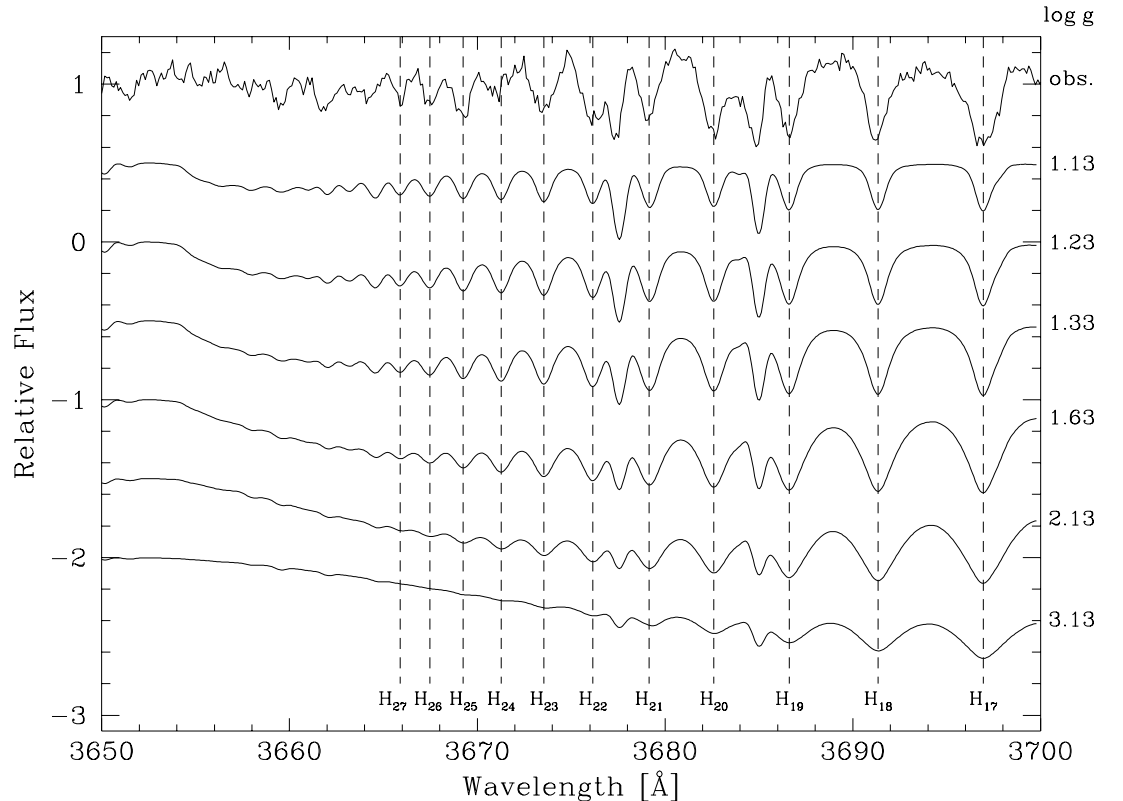
Figure 3.20: Observed mean spectrum (thick line) and synthetic model spectra (thin lines, y-offset: -0.5 dex) with the relevant parameters (i.e. T_{eff}, v_{sys}, $v \sin i$, ξ_{micro}) of Table 3.11, solar abundances and the noted $\log g$ values.
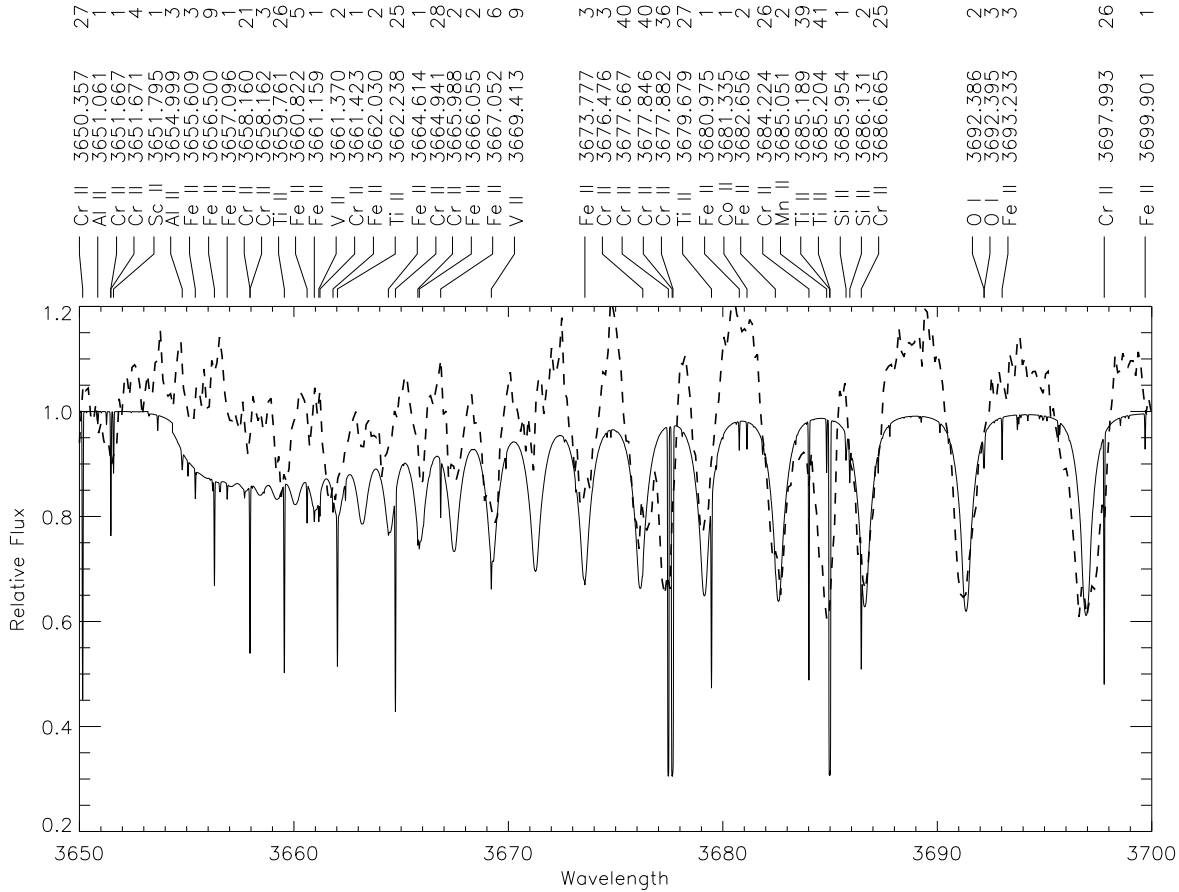
Figure 3.21: Solid line: NLTE model spectrum with $T_{\mathrm{eff}} = 11\,200\,\mathrm{K}$, $\log g = 1.13$ and solar abundances, zero rotation and turbulence velocities and no instrumental profile convolution. Dashed line: observed mean spectrum.

width of the Balmer lines is determined by the linear Stark effect which is related to the ion and electron pressure in the atmosphere which in turn is correlated with the surrounding gravity. Thus the highest observable Balmer line can be used as a measure of the surface gravity.

In Figure 3.20 we compare the synthetic spectra for $T_{\mathrm{eff}} = 11\,200\,\mathrm{K}$ and solar abundances with the observed mean spectrum: the line broadening effect of increasing $\log g$ on the Balmer series is clearly visible. Despite the low S/N ratio and the bad continuum determination in the blue range of our spectrum we can observe Balmer lines as high as $\sim\mathrm{H}_{27}/\mathrm{H}_{28}$. In the synthetic spectra with the lowest $\log g$ value we can distinguish the Balmer lines until $\sim\mathrm{H}_{28}/\mathrm{H}_{29}$. Changing the He abundance has no visible effect on the synthetic spectra in this wavelength range, but the inclusion of a more extended line list and more accurate atomic data might change the calculated line profiles.

We use $T_{\mathrm{eff}} = 11\,200\,\mathrm{K}$, $\log g = 1.13$ and solar abundances for our further analysis as these values achieve the best spectral fits for the He I lines and consistently for the high Balmer lines as well.

To illustrate the number and accuracy of the atomic lines that were included in our calculations we show in Figure 3.21 the NLTE spectrum without convolution (i.e. $v_{\mathrm{rot}} = 0$, no instrumental profile, no turbulence). The synthetic spectrum and the annotation of lines is shifted with the radial velocity of $-17\,\mathrm{km\,s^{-1}}$; the text in the line identification legend specifies the element and its ionization state and the numbers give the rest wavelengths from the atomic line lists. The last entries of the annotated lines are approximate weights of the equivalent widths of the contributing spectral lines.

Table 3.8: Extract of Table 12 (corresponding to Fig. 3.22) of Meynet et al. (1994).

age	mass	$\log L$	$\log T_{\text{eff}}$	X	Y	$\log \dot{M}$	marks
[10^6 yrs]	[$M_\odot$]	[$L_\odot$]	[K]	[mass fraction]		[$M_\odot \text{yr}^{-1}$]	
0.005	39.975	5.376	4.641	0.680	0.300	-6.426	A
4.391	32.065	5.626	4.240	0.679	0.300	-5.102	B
4.407	31.940	5.655	4.269	0.679	0.300	-5.087	C
4.413	31.730	5.626	3.779	0.679	0.300	-3.996	D
4.447	21.713	5.776	3.771	0.548	0.431	-3.539	E
4.468	18.774	5.759	4.157	0.206	0.773	-4.097	F
4.542	14.024	5.460	4.542	0.000	0.980	-4.352	G
4.563	12.831	5.399	4.506	0.000	0.767	-4.225	H
5.008	5.028	5.142	4.798	0.000	0.262	-5.246	I

Luminosity, Radius and Mass

We take the luminosity of $\log(L/L_\odot) = 5.6$ from Sterken et al. (1991) as a reasonable value, supported by our independent distance determination (later in this section).

The radius was derived using the Stefan-Boltzmann law: $L = 4\pi R^2 \sigma T_{\text{eff}}^4$. With $T_{\text{eff}} = 11\,200\,$K and $\log(L/L_\odot) = 5.6$ we get $R = 168\,R_\odot$.

Using the previously derived surface gravity of $\log g = 1.13$ we calculated the current stellar mass to be $M_\star = \frac{R^2 g}{G} = 14\,M_\odot$.

By comparing the location of HD 160529 in the Hertzsprung-Russell diagram with evolutionary tracks of Meynet et al. (1994) (calculated with double mass-loss rates on the main-sequence and WNL phases) we derive a mass on the Zero-Age-Main-Sequence (ZAMS) of $M_{ZAMS} \approx 40\,M_\odot$. We assume hereby that HD 160529 is evolving to cooler temperatures, i.e. the star is in a pre-RSG (RSG = Red SuperGiant) phase. This is supported from our spectral line-fits where we derived helium abundances close to solar values at the stellar surface, which is in good agreement with the abundances used in the evolutionary models for a star in pre-RSG phase with initial mass of $40\,M_\odot$. Table 3.8 is an extract of the evolutionary track tables used in the calculations of Meynet et al. (1994). The position of HD 160529 in the HRD is located between marks C and D. At this point the hydrogen and helium fractions are still close to solar abundances. The time a star needs to evolve from C to D is about 60 000 years which is of the same order as the estimated LBV-lifetime (Bohannan 1997).

We scrutinized the mean spectrum of HD 160529 for CNO lines in various ionization states, but a clear detection could not be found. Sometimes, spectral lines can be seen at the wavelength of a certain CNO line, but then no further lines of the same ionization state and/or multiplet could be found so that we attribute these features to line blends or weak lines from other elements. This is mainly due to the rather low oscillator strengths (i.e. $\log gf$ values) of most CNO lines in the visual range but it also rules out strong enhancements of CNO processed material in the stellar atmosphere, thus supporting the relatively young evolutionary status of HD 160529.

We note that this result is in contrast to the findings of Sterken et al. (1991) who obtained an initial mass of $25\,M_\odot$ by assuming a post-RSG evolutionary status for HD 160529 and then placing the star in the evolutionary tracks of Maeder & Meynet (1988). The evolutionary models of Meynet et al. (1994) com-
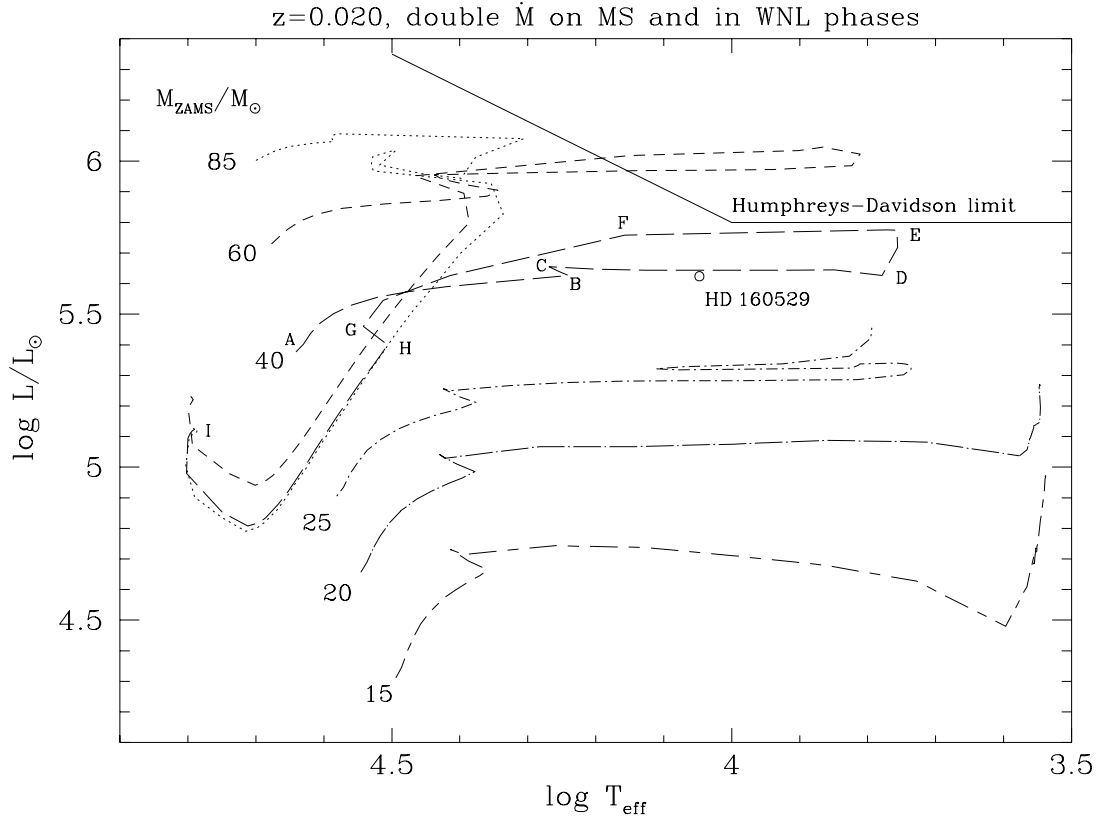
Figure 3.22: HRD with evolutionary tracks of Meynet et al. (1994) including Humphreys-Davidson limit (solid line) and the location of HD 160529 (small circle). Important stages are marked for the track with $M_{ZAMS} = 40\,M_\odot$ (see Table 3.8 for details).

pute the chemical compositions more accurately and apply improved opacities and nuclear cross-sections which significantly change the involved time scales with respect to earlier models (i.e. the models of Maeder & Meynet (1988) have larger time scales). Also using higher mass-loss rates in the calculations (as appropriate for LBVs) modifies the resulting evolutionary tracks. The evolutionary track with $M_{ZAMS} = 25\,M_\odot$ in the Meynet et al. (1994) models is definitely too far away from the position of HD 160529 in the HRD; we thus estimate $M_{ZAMS} \approx 35-40\,M_\odot$ for HD 160529 (see Figure 3.22).

Instead of reasoning that the large difference of $M_\star$ and M_{ZAMS} is due to a post-RSG evolutionary state, the discrepancy could be explained by mass loss through stellar wind and pulsation mechanisms as proposed by Kiriakidis et al. (1993) and Langer et al. (1994). In their evolutionary scenarios massive stars ($M \gtrsim 40\,M_\odot$) undergo a phase of pulsational instability immediately after they leave the main sequence where they are forced in an evolutionary loop. The mass loss induced by pulsation mechanisms might be up to an order of magnitude higher than the mass-loss rates due to radiation pressure. As we have seen evidence for pulsation occurring in HD 160529, it seems plausible that the star might have crossed such phases of increased mass loss (possibly multiple times), thus accounting for the current low mass value.

In Table 3.8 we have listed some values from the calculations of Meynet et al. (1994) for solar abundances and double mass-loss rates in the main sequence (MS) and WNL states. X and Y are the surface abundances in mass fractions of H and ^{4}He. Putting HD 160529 in the corresponding Hertzsprung-Russell diagram (Fig. 3.22) will place the star between states C and D. This would agree well with our derived solar He-abundance because at that point the surface abundances are still more or less unchanged. Also the derived mass-loss rate of $\dot{M} \approx 10^{-5}\,M_\odot\mathrm{yr}^{-1}$ is in accordance with the tabulated values.

Table 3.9: Maximum rotation velocities within Eddington limit.

T_{eff} [K]	g_{rad} [cm s^{-2}]	g_{grav} [cm s^{-2}]	g_{rot} [cm s^{-2}]	$\log g_{rad}$ [cgs]	$\log g_{grav}$ [cgs]	$\log g_{rot}$ [cgs]	max. v_{rot} [km s^{-1}]
8000	2.632	3.802	1.170	0.420	0.580	0.068	36.980
8500	3.355	4.571	1.216	0.526	0.660	0.085	37.710
9000	4.216	5.129	0.912	0.625	0.710	-0.040	32.658
9500	5.234	6.607	1.372	0.719	0.820	0.137	40.060
10000	6.427	7.762	1.336	0.808	0.890	0.126	39.523
10500	7.812	9.333	1.521	0.893	0.970	0.182	42.172
11000	9.409	11.220	1.811	0.974	1.050	0.258	46.018
11500	11.240	14.454	3.214	1.051	1.160	0.507	61.306
12000	13.326	15.849	2.523	1.125	1.200	0.402	54.313

He surface abundances are known only for a few LBVs where they show a very narrow range of values; e.g. Crowther (1997) gives: H / He = 2 − 2.5 x solar (by number). However if we would assume a He content of two times solar for HD 160529 we would need to decrease the surface gravity to compensate the line strengthening effect on the He lines in the spectrum (see Table 3.10), which would in turn decrease the stellar mass even further.

Velocities and Periods

For the analysis of the spectral time-series it is crucial to get good estimates of the relevant velocities and time scales. The following measurements and relations were used to obtain these quantities:

- Rotational Velocity (v_{rot}):

v_{rot} was derived from the rotational broadening of our SYNSPEC 41 models for the He I and Mg II lines. The best agreement with the observed spectrum was achieved with $v_{\text{rot}} = v \sin i = 35 \pm^{5}_{10}$ km s^{-1}. The upper limit for the rotational period is thus given by: $P_{\text{rot}}/\sin i = 2\pi R_{\star}/v \sin i = 243 \pm^{62}_{13}$ days.

According to Reid et al. (1993) the projected rotational velocities can be derived from the maximum half-width of double-peaked features in the temporal variance spectra if the variations are due to non-radial pulsations but are overestimated if the line formation takes place in material with radial velocity components above the photosphere. Measuring the TVS features of the He I, Mg II and Si II lines results in $v_{\text{rot}} \approx 45$ km s^{-1}, i.e. about 10 km s^{-1} more than the previous method of fitting synthetic spectra to the photospheric lines. However the TVS features do not show a consistently well-defined double-peaked profile with steep flanks so that we estimate correspondingly larger errors for this method. As we have seen previous indications of radial pulsations and wind influence even in the He I lines our spectroscopically derived v_{rot} value of $35 \pm^{5}_{10}$ km s^{-1} is consistent with the likely overestimated value from the TVS method. We thus use the value of $35 \pm^{5}_{10}$ km s^{-1} for v_{rot} in our further analysis.

The maximum possible rotation for a star can be calculated via: $g_{rot} < g_{grav} - g_{rad} - g_{turb}$. For a first-order estimate we take g_{grav} from the numerical limits of the TLUSTY 194/SYNSPEC 41 code, compute the radiation pressure via: $g_{rad} = k/c\, \sigma\, T_{\text{eff}}^4$ (using k = 0.34 as mean opacity, c as the speed of light and σ as Stefan-Boltzmann constant) and neglect the acceleration from turbulent forces. The resulting values for $v_{\text{rot,max}}$ are listed in Table 3.9. We see that our value of $35 \pm^{5}_{10}$ km s^{-1} is still well within the stability region at $T_{\text{eff}} \gtrsim 11\,000$ K. However adding a turbulence velocity of $10 - 15$ km s^{-1} would bring the star

very close to its Eddington limit in our crude approximation. The last stable atmospheres of the much more sophisticated TLUSTY 194 models (where rotation and turbulence are included in the calculations) leave a margin of $\log g \approx 0.06$ before the Eddington limit is reached.

- Break-up Velocity (v_{break}):

  The lower limit for the rotational period can be derived by calculating the break-up velocity $v_{\mathrm{break}} = \sqrt{G\,M_\star/R_\star} = 126\,\mathrm{km\,s^{-1}}$; the corresponding period is: $P_{\mathrm{rot,break}} = 2\pi R_\star/v_{\mathrm{break}} = 68\,\mathrm{days}$.

- Escape Velocity (v_{esc}):

  The escape velocity was calculated via: $v_{\mathrm{esc}} = \sqrt{(1-\Gamma)}\,\sqrt{2\,g\,R_\star}$, with the Eddington factor $\Gamma = \frac{\sigma_e L}{4\pi c G M_\star} = 0.73$. With an adopted value of $\sigma_e = 0.33$, which assumes solar abundances and continuous opacity due solely to electron scattering, we derive $v_{\mathrm{esc}} = 93\,\mathrm{km\,s^{-1}}$.

  The derived gamma factor is well within the typical range of Γ found for other LBVs: $\Gamma \approx 0.7 - 0.8$ (Stahl 1991 b).

- Microturbulence Velocity (ξ_{micro}):

  The microturbulence velocity of $\xi_{\mathrm{micro}} = 15\pm5\,\mathrm{km\,s^{-1}}$ was also derived from our model fits and agrees well with the usual values for thermal and turbulent velocities found in B supergiants and LBVs (de Koter et al. 1996).

- Systemic Velocity (v_{sys}):

  From the center of the He I lines in the mean spectrum we derived $v_{\mathrm{sys}} = -17\,\mathrm{km\,s^{-1}}$. This line originates deep in the atmosphere and is thus a probe for photospheric conditions in a star with an effective temperature around $\sim 11\,000\,\mathrm{K}$.

  The observed radial velocity variations of this line are almost sinusoidal (see Figure 3.17) and quite symmetric around the mean value (see the TVS spectra of He I λ5876 in Figure 3.13) indicating pulsations at the stellar surface. This interpretation is supported by the simultaneous observed variations of the equivalent widths which are expected as a consequence of temperature variations in a non-radial-pulsation (NRP) scenario.

  This value of v_{sys} agrees with measurements of the center of the P Cygni profiles for Hα and Hβ (see Figure 3.2 c). To determine the center of the P Cygni line profiles we created a mirror image of these lines and displayed them in such a way that the blue edge of the absorption component and the red edge of the emission component of the mirror image coincided (for a more detailed description of this technique see Wolf & Stahl 1982).

  Furthermore the radial velocities of the higher Balmer lines (positions measured in the absorption line cores from Hα to the highest discernible Balmer line H 27) approach this value asymptotically. Figures 3.2 and 3.20 show the observed Balmer series and the measured progression.

- Fundamental Radial Pulsation Period ($P_{\mathrm{rad,fund}}$):

  A further important intrinsic time scale of the star is the radial fundamental pulsation period. $P_{\mathrm{rad,fund}}$ was computed according to Lovy et al. (1984)[7] via: $P_{\mathrm{rad,fund}} = Q * \sqrt{(R_\star{}^3/M_\star)}$, with a pulsation constant $\log Q = -0.054\,M_{bol} - 0.864\,\log(T_{\mathrm{eff}}) + 1.635$. For a temperature of $8\,000 - 10\,000\,\mathrm{K}$ we get $\log Q \approx -1.4$. Their formula applies to stars with moderate mass loss near the main sequence. Increased

---

[7]Using the fitting formula from Lovy et al. (1984): $\log P_{fit,fund} = -0.275\,M_{bol} - 3.918\,\log(T_{\mathrm{eff}}) + 14.543$ results in even smaller pulsation periods (by about a factor 0.5).
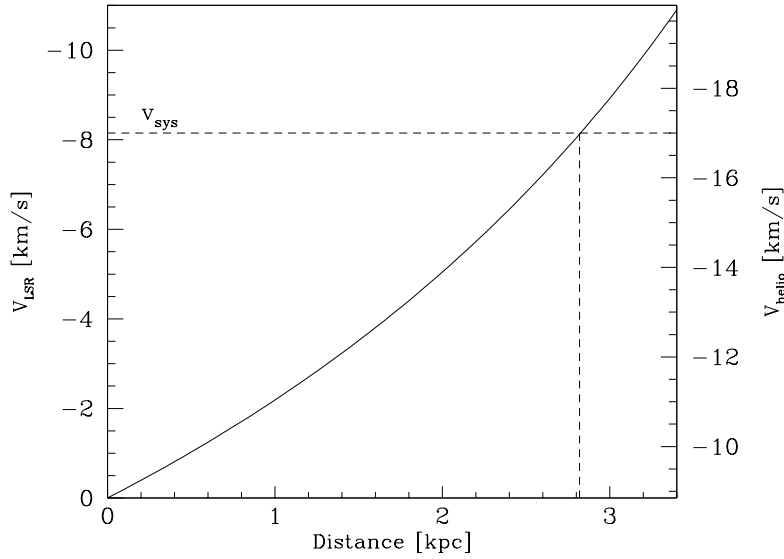
Figure 3.23: The galactic rotation curve for HD 160529. The adopted systemic velocity is marked.

mass loss leads to a decrease of the pulsational periods (on the order of $15-25\%$). On the other hand the periods of post-RSG stars tend to increase up to a factor of 2. The derived value of $P_{\mathrm{rad,fund}} = 24$ days lies well below the lower limit of the rotational periods even considering the possibility of a post RSG status for HD 160529. Therefore the possibility of a discrimination between rotation and pulsation as sources of stellar variability arises for HD 160529.

Distance Determination

Assuming that the velocity of a star is due to the differential rotation of its host galaxy one can determine its kinematic distance.

We converted our heliocentric corrected spectra to velocities of the local standard of rest (LSR) velocity frame, assuming a solar motion of $20\,\mathrm{km\,s^{-1}}$ toward the Apex ($\alpha = 18^h, \delta = +30^o$ or $l \approx 56^o, b \approx +23^o$ (Unsöld & Baschek 1988)). The galactic rotation curve for HD 160529 was calculated with the IAU standard rotation parameters, i.e. a flat rotation curve $\Theta = 220\,\mathrm{km\,s^{-1}}$ and $R_\odot = 8.5\,\mathrm{kpc}$ as recommended by Fich et al. (1989).

Adopting $-17\pm 2\,\mathrm{km\,s^{-1}}$ as the systemic velocity for HD 160529, its velocity with respect to the local standard of rest is $v_{\mathrm{LSR}} = -8.15 \pm 2\,\mathrm{km\,s^{-1}}$. Considering that the proper motion of HD 160529 is not known, we adopt an uncertainty of $\pm 5\,\mathrm{km\,s^{-1}}$ (rather than $\pm 2\,\mathrm{km\,s^{-1}}$) for this method which leads to a kinematic distance of $d = 2.8^{+0.9}_{-1.4}\,\mathrm{kpc}$ (see Figure 3.23).

This result is also supported by the velocity structure of the interstellar Na I and Ca II lines of our mean spectrum. By separating the strongly variable stellar components from the stable interstellar lines we get LSR velocities of about $-2\,\mathrm{km\,s^{-1}}$ for the Na D lines, thus giving a minimum distance of $\sim 0.6\,\mathrm{kpc}$. However the measured equivalent width of the Na D lines of $\sim 0.8\,\text{Å}$ and the high interstellar reddening of $E_{(B-V)} \approx 1.10$ suggest a considerably larger distance (see Crowther et al. 1995 for this method of distance determination).

Note that HD 160529 is located close to the dark cloud at $l = 358$, $b = 1$ (Feitzinger & Stüwe 1986) and within the H I cloud at $l = 15 - 345$, $b = -7 - +7$ (Riegel & Crutcher 1972). Both clouds are within a distance of 170 pc (so HD 160529 is located well beyond them) but they might influence the Na D and

Table 3.10: Tolerance ranges of stellar parameters.

T_{eff}	$\log g$	$R_\star$	$M_\star$	Γ	v_{esc}	v_{break}	$P_{\mathrm{rot,break}}$	$P_{\mathrm{rad,fund}}$	$P_{\mathrm{rot}}/\sin i$
[K]	[cgs]	[$R_\odot$]	[$M_\odot$]		[km s^{-1}]	[km s^{-1}]	[days]	[days]	[days]
8000	0.58 [$]	330.03	15.11	0.672	75.69	93.45	178.75	90.47	477.27
8500	0.66 [$]	292.35	14.26	0.712	73.15	96.44	153.43	74.54	422.77
9000	0.71 [$]	260.77	12.73	0.798	61.33	96.48	136.80	59.72	377.10
9500	0.82 [$]	234.04	13.21	0.769	70.52	103.74	114.19	48.68	338.45
10000	0.89 [$]	211.22	12.64	0.804	66.96	106.82	100.08	39.89	305.45
10000	1.25 [†]	211.22	28.95	0.351	184.24	161.69	66.12	39.89	305.45
10000	1.37 [‡]	211.22	38.17	0.266	224.91	185.64	57.59	39.89	305.45
10500	0.97 [$]	191.58	12.50	0.812	68.33	111.55	86.93	32.84	277.05
10500	1.07 [†]	191.58	15.74	0.645	105.42	125.17	77.47	32.84	277.05
10500	1.17 [‡]	191.58	19.81	0.513	138.66	140.44	69.05	32.84	277.05
11000	1.05 [$]	174.56	12.48	0.814	71.23	116.76	75.67	27.46	252.44
11000	1.09 [†]	174.56	13.68	0.742	87.77	122.26	72.27	27.46	252.44
11000	1.15 [‡]	174.56	15.71	0.647	110.15	131.00	67.44	27.46	252.44
11200	1.13 [$]	168.38	13.96	0.728	92.81	125.73	67.78	24.22	243.50
11200	1.17 [‡]	168.38	15.31	0.664	108.00	131.66	64.73	24.22	243.50
11500	1.16 [$]	159.71	12.56	0.809	75.74	122.45	66.01	23.05	230.97
11500	1.18 [†]	159.71	14.09	0.721	96.93	129.71	62.32	23.05	230.97
11500	1.23 [‡]	159.71	15.81	0.642	116.20	137.40	58.84	23.05	230.97
12000	1.20 [$]	146.68	12.45	0.816	77.14	127.20	58.37	19.64	212.12
12000	1.22 [†]	146.68	13.03	0.779	86.47	130.16	57.04	19.64	212.12
12000	1.28 [‡]	146.68	14.96	0.679	111.79	139.47	53.23	19.64	212.12

[$] min. $\log g$: numerical limits of TLUSTY 194 NLTE calculations
[†] max. $\log g$: 2× solar He abundance – good fit of He lines
[‡] max. $\log g$: 1× solar He abundance – good fit of He lines

Ca K / H line profiles which show a complex structure[8].

Sterken et al. (1991) determined the distance to HD 160529 by assuming equal absolute brightnesses for HD 160529 and its "twin" LBV R110 in the LMC. Their derived distance of $d = 2.5$ kpc is in good agreement with our independent distance determination. Leitherer et al. (1995) assumed an error of 40 % for this spectroscopic distance determination which matches our adopted uncertainties.

Accuracies of Derived Parameters

In Table 3.10 we give the numerical limits of our NLTE–TLUSTY 194 models together with the maximum $\log g$-values with which we could still produce a reasonably good fit for the He I lines and calculate other stellar parameters using $\log(L/L_\odot) = 5.6$. He lines could not be produced with TLUSTY 194 at temperatures lower than 10 000 K. However because HD 160529 has been assigned temperatures of $T_{\mathrm{eff}} = 8\,000 - 9\,500$ K in the past (see Table 3.1) we have included the values for the numerical limits of

---

[8]Recent STIS observations of Carinae have shown that ISM lines can be variable on a time scale of months to years (Leitherer, private communication). However, the Na D and Ca K / H lines at HD 160529 are variable on time scales of days and have line profiles similar to observed stellar excitation lines so that strong stellar contributions must exist.

Table 3.11: Stellar parameters from modeling the mean photosphere of HD 160529. The values of the parameter ranges marked with [†] are taken from the literature.

parameter	d	$E_{(B-V)}$	Sp.Type	$L_\star$	M_{bol}
unit	[kpc]	[mag]		[L$_\odot$]	[mag]
best value	2.5	1.10	B8Ia$^+$	$4\,10^5$	-8.9
range	$1.4 - 3.7$	$1.10 - 1.22^†$	A2Ia $-$ B8Ia†		$-8.5 - -9.7^†$
parameter	T_{eff}	$\log g$	$R_\star$	$M_\star$	M_{ZAMS}
unit	[K]	[cgs]	[R$_\odot$]	[M$_\odot$]	[M$_\odot$]
best value	11 200	1.13	168	14	40
range	$10\,000 - 12\,000$	$1.11 - 1.37$	$147 - 211$	$13 - 38$	$35 - 40$
parameter	Y	Γ	v_{sys}	v_{esc}	v_{break}
unit	[% by mass]		[km s^{-1}]	[km s^{-1}]	[km s^{-1}]
best value	32.8	0.73	-17	93	126
range	$27.9 - 43.6$	$0.3 - 0.8$	$-14 - -20$	$86 - 225$	$122 - 186$
parameter	$v \sin i$	ξ_{micro}	$P_{\mathrm{rot,break}}$	$P_{\mathrm{rot}}/\sin i$	$P_{\mathrm{rad,fund}}$
unit	[km s^{-1}]	[km s^{-1}]	[days]	[days]	[days]
best value	35	15	68	243	24
range	$25 - 40$	$10 - 20$	$57 - 69$	$230 - 305$	$20 - 40$

T_{eff} and $\log g$ in this range to estimate the full realm of changes a LBV can undergo during its moderate variability cycles.

The range of tolerances reaches a minimum around $T_{\mathrm{eff}} = 11\,200$ K which is also the temperature where we come closest to the respective Eddington limit in our line fits. For this temperature we can only increase the He content to $1.2\times$ solar and still get a reasonable good fit to the He lines.

We have thus chosen the values in row $T_{\mathrm{eff}} = 11\,200$ K as the best representation of the photospheric stellar parameters because these values produce the best fits of the He I lines while simultaneously reaching closest to the Eddington limit. Table 3.11 gives a summary of the adopted and derived stellar parameters together with the estimated accuracies. The ranges are taken from corresponding values of Table 3.10 or from the literature if no further restrictions were available, but are updated when possible (i.e. from other considerations like the Balmer limits for $\log g$, good fits of photospheric spectral lines, ...).

Note that the differences in the accuracy and use of laboratory wavelengths of spectral lines also affects some stellar parameters although not in a fundamental way (for a discussion on λ_{lab} see section 1.5).

Consistency Tests of Stellar Parameters

In order to check the accuracy of our derived values we have applied some tests and other methods to determine stellar parameters:

- All elements, with the possible exception of Mg, are in a unique ionization state in the observed spectrum. Thus we can only derive rough upper and lower limits, e.g. from the simultaneous observation of the Mg II and Si II spectral lines a temperature range of $7\,000\,\mathrm{K} \lesssim T_{\mathrm{eff}} \lesssim 13\,000\,\mathrm{K}$ can be estimated.

- Ionization balance of Mg I and Mg II:

  only the three Mg I lines (i.e. $\lambda 3832, \lambda 3838, \lambda 5183$) with the highest oscillator strengths and lowest excitation potentials might be observable in HD 160529. Unfortunately these lines have extremely low S/N even in the averaged spectrum (they are in the bluest part of our observing range) and are additionally blended by Fe II lines (certainly for Mg I $\lambda 5183$ but probably for the other two Mg I lines as well) so that their equivalent widths measurement are not reliable. The Mg I lines might also be influenced by the stellar wind so that the resulting ionization balances which are usually the most reliable tools to derive temperatures and $\log g$ values cannot be used in the case of HD 160529.

- Classical spectral type determination schemes (e.g. comparing equivalent widths of $H\gamma$ with Ca K) are not possible because there are no good standard stars for such extreme objects as LBVs. In particular the strong wind lines (i.e. P Cygni profiles) complicate the situation.

- Determine T_{eff}, $\log g$ from He I $\lambda 5876$ / Mg II $\lambda 4481$ balance:

  in the left plot of Figure 3.24 we draw the equivalent width ratios of He I $\lambda 5876$ / Mg II $\lambda 4481$ for different $\log g$ value ($1.2 - 2.2$) as a function of T_{eff} as calculated by ATLAS 8 models[9]. Using the lowest stable $\log g$ model ($\log g = 1.2$) to be as close as possible to the Eddington limit and using the observed He I $\lambda 5876$ / Mg II $\lambda 4481$ values of $\sim 0.3 \pm 0.05$ dex we get a temperature estimate of $T_{\mathrm{eff}} = 10\,100 - 11\,200$ K. As previously noted we see that the ATLAS models interrupt at relatively low $\log g$ / T_{eff} values. Nevertheless the resulting values are similar to our previous results using more sophisticated models.

- Determine T_{eff}, $\log g$ from $H\delta$ equivalent width curve:

  In the right plot of Figure 3.24 we applied the VCS theory (Vidal et al. 1973) for the broadening of Balmer lines to calculate the equivalent widths of the $H\delta$ line as a function of $\log g$ and T_{eff}. The measured $W_\lambda (H\delta)$ values in our observed spectra are about 920 ± 110 mÅ. Considering the neglect of a wind influence and the relatively high error bars in the W_λ measurements (because of bad Gaussian fits and low S/N ratio around $H\delta$) the resulting function agrees well with our previously derived $\log g$ and T_{eff} values for HD 160529. E.g. adapting a possible temperature range of $10\,000 - 11\,500$ K we get corresponding $\log g$ values of $1.0 - 1.2$.

- As a final sanity check we calculated the current stellar parameter values back to the ZAMS using the evolutionary models of Meynet et al. (1994) and assuming a constant rotation period of 243 days. We obtain the following results:

Parameter	Unit	Current	ZAMS
$M_\star$	$M_\odot$	14	40
$R_\star$	$R_\odot$	168	8.5
T_{eff}	K	40 000	43 750
L	$L_\odot$	400 000	237 700
v_{break}	km s^{-1}	126	7 115
v_{rot}	km s^{-1}	35	297

  As the resulting values are within realistic ranges we are confident that our results are reasonable.

---

[9]TLUSTY 194 does not automatically include a list of the equivalent widths of the computed spectral lines, so we have used a small grid of ATLAS 8 models where W_λ is listed in the output. The data for Figure 3.24 has been computed by Kaufer (1996) and was kindly placed at our disposal for these consistency tests.
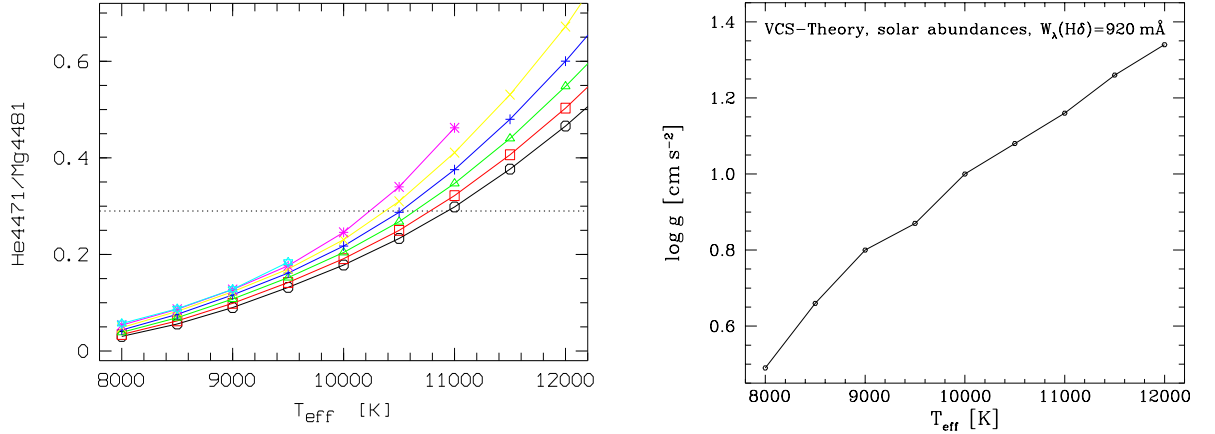
Figure 3.24: *Left*: He I $\lambda4471$ to Mg II $\lambda4481$ ratio from Synthetic ATLAS 8 models; $\log g = 1.2$ ($*$), 1.4 ($\times$), 1.6 (+), 1.8 ($\triangle$), 2.0 ($\square$), 2.2 ($\circ$). The dashed horizontal line represents the measured value (0.29) from our mean spectrum. *Right*: Results of Hδ-line fits (equivalent width $W_\lambda = 920$ mÅ) with VCS theory.

3.6.2 Photospheric Parameter Variations

As a first-order approximation we can use the previously calculated grid of TLUSTY 194 models and compare them with the observed line-profile variations to estimate the range of variability of the photospheric parameters.

The wavelength region from 4459 to 4486 Å is particularly suited to probing the photospheric temperature variations: here we can measure the temperature sensitive Ti II $\lambda4468$ line and can simultaneously use the He I $\lambda4471$ and Mg II $\lambda4481$ lines as controls of the results. In the left plot of Figure 3.25 the spectra of the observing run in 1993 are plotted in this wavelength range. The LPVs of Ti II $\lambda4468$ are clearly visible while the He I $\lambda4471$ and Mg II $\lambda4481$ do not show strong variation patterns.

The right plot of Figure 3.25 shows the TLUSTY 194 models with $\log g = 1.30$ and $T_{\rm eff} = 9000 - 12\,000$ K. We use the synthetic spectra with $\log g = 1.30$ because the Ti II $\lambda4468$ NLTE-models with $\log g = 1.13$ are numerically unstable for $T_{\rm eff} > 11\,200$ K. However the converging models with $\log g = 1.13$ and $T_{\rm eff} = 9000 - 11\,200$ K exhibit the same behavior as the $\log g = 1.30$ models. As previously mentioned He I lines are not formed below $T_{\rm eff} = 10\,000$ K.

Comparing the observed and the synthetic Ti II $\lambda4468$ line spectra we see that the atmospheric temperature increases from $\sim 10\,000$ K around JD-2449050, where the Ti II $\lambda4468$ lines are stronger than the He I $\lambda4471$ lines, to $\sim 11\,500$ K around JD-2449096, where the Ti II $\lambda4468$ lines are much weaker than the He I $\lambda4471$ lines.

As we have discussed before (see section 3.6.1) the lower atmosphere seems to have a strong temperature gradient. As Ti II $\lambda4468$ is formed mainly at a small distance away from the photosphere the temperature at the stellar surface might actually be higher than indicated above. Because Ti II $\lambda4468$ also exhibits some wind influence the *absolute* temperature determined might not be very accurate. However we are confident in the *differential* value of the above results, i.e. that temperature variations of up to $\Delta T_{\rm eff} \approx 1500$ K exist in the photospheric regions of HD 160529.

Let us carry out some simple calculations to see what consequences a variable photospheric temperature would have on other observable and physical parameters:

To simplify the relations let us assume a variable temperature of 10 % of $T_{\rm eff}$:
$\Delta T_{\rm eff} = 0.1\,T_{\rm eff}$, so that $T_{\rm max} = 1.1\,T_{\rm eff}$.
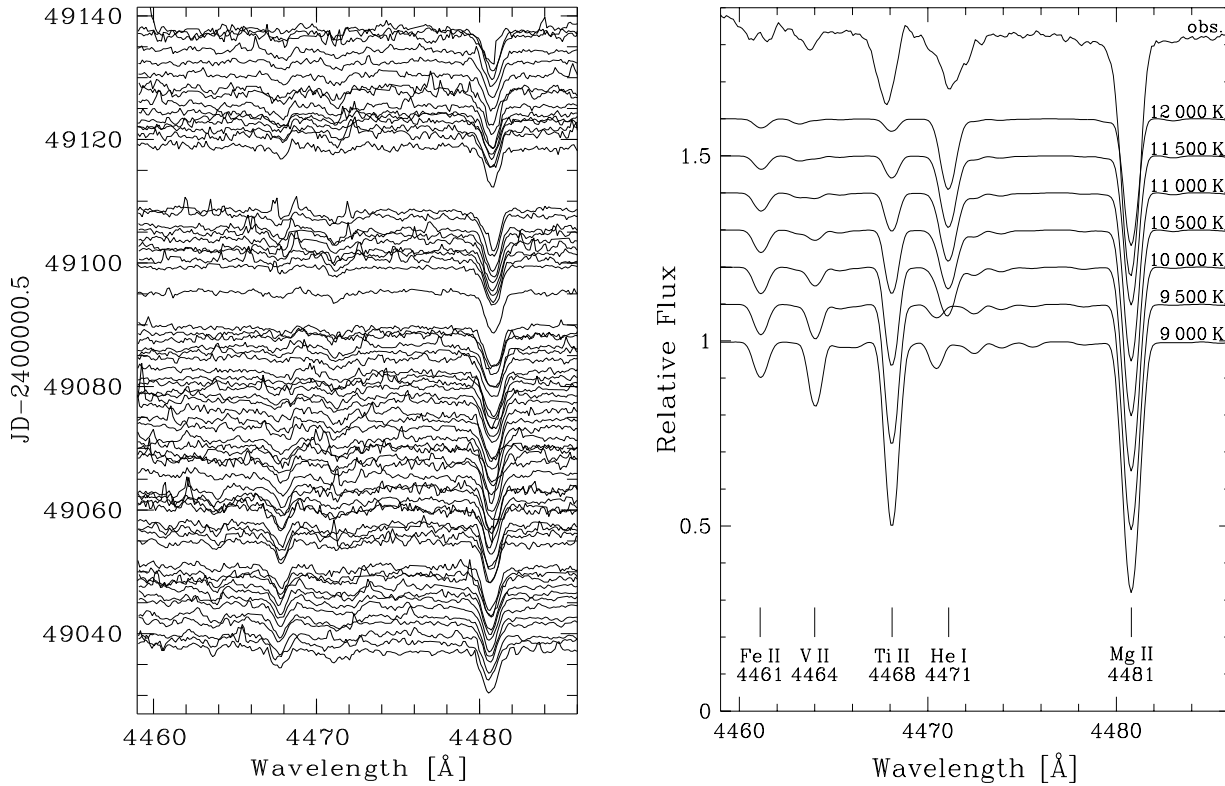
Figure 3.25: *Left*: spectral time-series of the observing run in 1993. *Right*: observed mean spectrum of 1993 (thick line) and TLUSTY 194 models with $\log g = 1.30$ and annotated T_{eff}. The models are blue-shifted by $-28 \, \text{km s}^{-1}$.

Assuming that the stellar radius does not change and using the Stefan-Boltzmann law ($L = 4 \pi R^2 \sigma T_{\text{eff}}^4$) we get: $L_{\text{max}} = (1.1 L)^4 = 1.1^4 L = 1.464 \, L$.

Using the definition of apparent magnitudes ($\Delta mag = 2.5 \log \Delta L$) we get a maximum Δmag of 0.414.

As BA supergiants have their peak flux output in the visual range we can in first order associate the observed visual photometric variation (δy) with this bolometric luminosity variation (Δmag). In 1992 y variations of $6.72 - 6.82 \, \text{mag}$ ($\delta y = 0.1 \, \text{mag}$) were measured which is about 0.3 mag less than expected from the above calculation. However we can use radius variations to counteract the temperature induced luminosity increase. Using the same formulae as above leads to required radius changes of about 7 % to balance the excess brightness of 0.3 mag.

Note that in the above arguments we deviate from the usual assumption of a constant bolometric luminosity during the moderate LBV-outbursts or microvariations. Leitherer (1997) suggested this possibility as an alternative to explain mass-loss variations like those observed e.g. in S Dor and R 71, as luminosity variation by a factor of a few might easily go undetected, which might be the case for HD 160529 as well. However if L is constant during our observations we only need to increase the radius variations by an additional few percent to balance the temperature variations.

As we see in the next section, radius variations on the order of 10 % can occur in LBVs (results from radial pulsation models assuming $L = $ constant) so that our "back-of-the-envelope" calculations actually provide reasonable estimates and supply another argument for pulsation being the driving mechanism of the observed LPVs.

3.6.3 Pulsation Models

In this section we use a non-radial pulsational code to model the photospheric LPVs and show results from a radial pulsation model with stellar parameters similar to HD 160529 (courtesy of the Los Alamos group of Cox, Guzik, Despain and colleagues).

We have seen indications for radial as well as non-radial pulsations in the photospheric LPVs and TVS as well as arguments pertaining to the observed photometric observations. Pure radial pulsations seem unlikely to cause the observed line profile variations because they cannot produce the observed retrograde and prograde variation patterns in the quotient spectra. Also their expected harmonic frequencies are about a factor $2-5$ smaller than the dominant time scales derived from our Fourier analyses; overtones have even smaller periods. However interfering radial pulsation modes with similar periods might produce modulations with *apparent* time scales longer than the fundamental pulsation period. Also radial non-adiabatic strange modes can have larger fundamental periods that could be close to the observed time scales (see e.g. strange modes of type I in Saio et al. 1984).

In section 3.5.1 and 3.5.2 we have seen that the LPVs are mostly concentrated in a small range of velocities around the center of the spectral line. These V/R type variations are usually interpreted as deviations from the spherical symmetry in stellar outflows if they are seen in wind lines (Kaufer et al. 1996) but often indicate non-radial pulsations when found in photospheric LPVs (Kaufer et al. 1997 b).

As observed in the quotient spectra of He I λ5876 and Si II λ6347 we see both retrograde and prograde
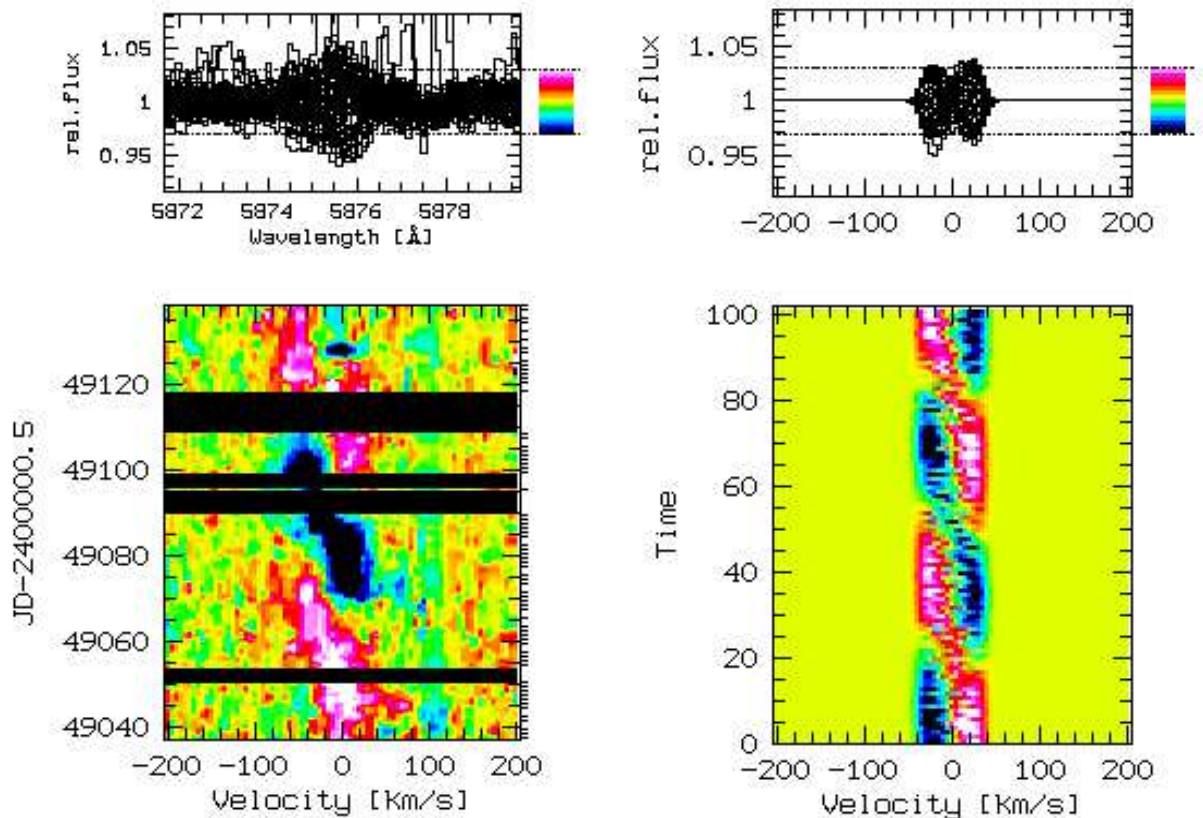
Figure 3.26: *Left*: dynamical quotient spectra of the He I λ5876 line in the observing run of 1993. Note that the velocity scale is not corrected for the systemic velocity here. *Right*: simulation of non-radial pulsation with stellar parameters of Table 3.11 and $\sin i = 1$, $l = +m = 1$, $\sigma_{\mathrm{nrp}} = \frac{2\pi}{81}\,\mathrm{d}^{-1}$.

traveling variations features. Particularly in the dynamical quotient spectra of the He I $\lambda5876$ line in the observing run of 1993 we see the photospheric variation features clearly moving across the line profile. Because the features are moving retrograde, i.e. *against* the direction of the rotation, they cannot be caused by strictly corotating features like magnetic fields which are "frozen" at the stellar surface (similar to sunspots) but have to be ascribed to real traveling disturbances along the stellar surface. This behavior is a typical signature of non-radial pulsations with retrograde moving velocity-fields. To model the observed line-profile variations we have calculated a NRP simulation using the numerical Monte-Carlo code of Kaufer (1996) with a NRP-amplitude of $\sim 8\,\mathrm{km\,s}^{-1}$ ($\approx 0.23\,v\sin i$, corresponding to the typically observed v_{rad}-variations of the He I $\lambda5876$ line).

The meridional sectors can be estimated from the number of simultaneous observed pseudo-emission or -absorption features. For He I $\lambda5876$ in 1993 this is $|m| \approx 1$ and for Si II $\lambda6347$ in 1995 we get $|m| \approx 2$ (note that we never see more than two V/R variation features at the same time). The NRP-frequency of the model $\sigma_{\mathrm{nrp}} = \frac{2\pi}{81}\,\mathrm{d}^{-1}$ is a factor 3 larger than the rotational frequency $\Omega_{\mathrm{rot}} = \frac{2\pi}{243}\,\mathrm{d}^{-1}$.
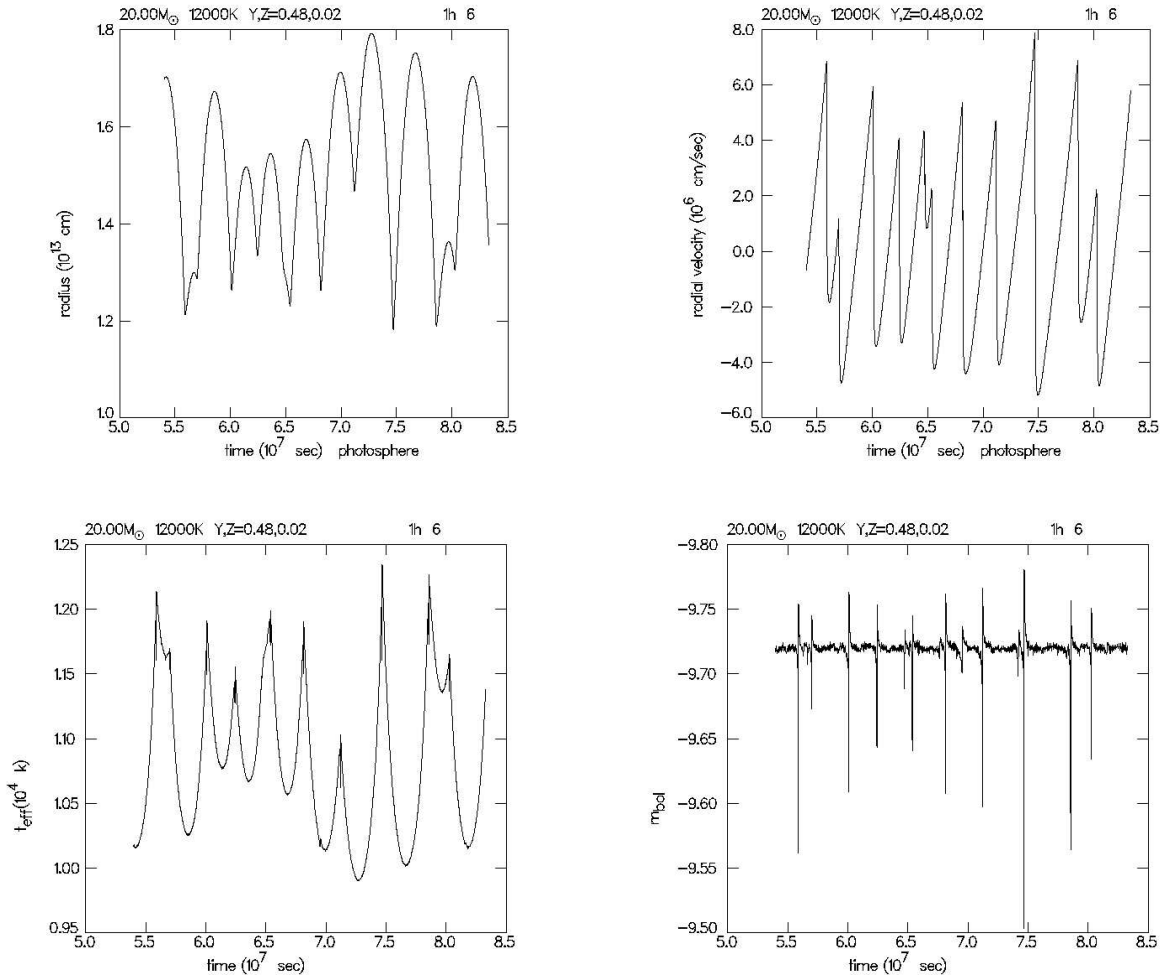
Figure 3.27: Results from non-linear hydrodynamical radial-pulsation models (Guzik, private communication): variations of radius, radial velocity, effective temperature and bolometric luminosity due to radial pulsations of a star with: $M_{ZAMS} = 50\,\mathrm{M}_\odot$, $M_\star = 20\,\mathrm{M}_\odot$, log $L_\star/\mathrm{L}_\odot = 5.76$, Y = 0.48. Note that the model assumes a constant bolometric luminosity that is derived from the effective temperature and radius at the photosphere. The sharp peaks in m_{bol} are thus only artifacts of the numerical calculations.

Due to the retrograde direction of the NRP quantum numbers ($l = +m = 1$) the resulting measured NRP-frequency is even higher: $\sigma_{\mathrm{nrp,meas}} = -m(\sigma_{\mathrm{nrp}} + \Omega_{\mathrm{rot}}) = \frac{2\pi}{61}\,\mathrm{d}^{-1}$. In Figure 3.26 we show the observed dynamical quotient spectra (left) and a non-radial simulation (right) with the stellar parameters of Table 3.11 and $\sin i = 1$. Note that the corresponding non-radial pulsation period of 61 days did appear in the Fourier analyses with only a small power at certain data sets. It needs to be emphasized that such a clear pulsation-like structure as in the above example was not observed in any other spectral line or at a different observing period. Rather the single pulsation modes are hidden in the complex LPV patterns due to the multi-periodicity of the velocity fields so that a relatively wide range of time scales could be constructed via interactions of various NRP modes and the stellar rotation.

Guzik et al. (1997) have calculated non-linear hydrodynamical RP models[10] with different masses and chemical abundances. They show that stars in the parameter range of LBVs are likely to pulsate in many modes simultaneously, with frequencies very similar to what we see in our data for HD 160529. Figure 3.27 shows their results for a star with $M_{ZAMS} = 50\,\mathrm{M}_\odot$, which has lost $30\,\mathrm{M}_\odot$ during its evolution and shows the predicted pulsations. It has not yet had a giant outburst which is probably also the case for HD 160529. In their models the He and Fe contents play an important role in driving the pulsations and leading to instabilities which may be observed as LBV-like outbursts. For the lower mass and luminosity LBVs like HD 160529, there is considerably less iron line opacity driving, and pulsations are almost all caused by the helium ionization κ effect.

The above model results in periods of $\sim 20-40\,\mathrm{days}$ ($\sim 2-5\,10^6\,\mathrm{sec}$) and variations in radial velocity and temperature that are similar to our observations of the He I 11 5876 and Ti II λ4468 line variability measurements. Also their predicted radius variation, on the order of $30\,\mathrm{R}_\odot$ (using $R_\star = 200\,\mathrm{R}_\odot$), is in accordance with our rough estimates for HD 160529. The combination of radial and non-radial pulsations provide a physical explanation that is fully consistent with the observed photometric LPVs.

3.7 Stellar Wind Models

The best indicators of stellar winds in the optical wavelength region are the Balmer lines with P Cygni profiles, with Hα as the dominant transition. To model the observed Balmer lines we first calculate stationary models using the averaged Balmer profiles as representations of the undisturbed wind. Then we explore different variability mechanisms and finally model the dynamical spectra as deviations from their mean state.

The recently developed SEIDYNAMIC-code of Rivinius et al. (1997) was used to model the Hα − Hδ lines of HD 160529. The code is based on the SEI method described by Lamers et al. (1987) and was modified by Rivinius et al. (1997) to study the stationary and dynamical winds of early B hypergiants. A detailed description of SEIDYNAMIC is given in their paper; hence we only summarize the most important features here:

- The radiative transfer equation is solved in the two-level approximation.

- Non-LTE departure coefficients are calculated separately with the Sobolev code (TSOB) described by Bastian (1982) and Stahl et al. (1983) and are modulated via a damping function of the form:

$$b_{n,new}(x) = 1 + (b_n(x) - 1)\exp\left(\frac{-x}{R_\star h_n}\right). \tag{3.1}$$

The damping function is introduced to suppress the unrealistic rise of the b-factors for levels $3-6$ after a local minimum at a distance of $\sim 5-10\,\mathrm{R}_\star$ (see Fig. 3.29 left). The scale height h_n can be

---

[10]Non-radial pulsation modes are not considered in their calculations.

regarded as a "confidence radius" within which the departure coefficients are trusted.

- The main wind parameters are implemented in the following ways:

  wind velocity: (beta law)

  $$v(x) = v_0 + (v_\infty - v_0)\left(1 - \frac{R_\star}{x}\right)^\beta,$$ (3.2)

  temperature: (power law)

  $$T(x) = T_{\text{outer}} + (T_{\text{inner}} - T_{\text{outer}})\left(\frac{x}{R_\star}\right)^{-\gamma},$$ (3.3)

  density: (from continuity equation)

  $$\rho(x) = \rho_{c,ave}\frac{v_o}{v(x)}\left(\frac{R_\star}{x}\right)^2,$$ (3.4)

  with the flux density of the wind:

  $$\rho_{c,ave} = \frac{\dot{M}}{4\pi v_0 R_\star^2}.$$ (3.5)

- Thomson scattering on free electrons is included using the method of Scuderi et al. (1994) and the redistribution function from Mihalas (1978).

- The time-dependent variations in the wind can be modeled with outward moving density variations either in the form of blobs and clumps in front of the stellar disk or as spherically symmetric shells. The underlying stellar continuum can be changed as well.

3.7.1 Stationary Wind Models

Starting with the values of the stellar parameters derived from the photospheric models we calculated a series of stationary wind models to explore the effects of changing parameters in the SEIDYNAMIC code on the Balmer lines. The final models were obtained by minimizing the residuals between the observed and synthetic spectra of *all* modeled Balmer lines[11]. Note that the spectra with the minimum residuals do not fit the broad emission wings very well. Figure 3.28 shows that the absorption component gets "filled in" if we fit the central emission simultaneously with the broad wings. We attribute this behavior to the way electron scattering is included in the code: rather than including non-coherent scattering in the radiative transfer function to calculate the Balmer lines, SEIDYNAMIC only redistributes the emission intensity into the line wings. For low-gravity A supergiants Santolaya-Rey et al. (1997) have shown that the correct treatment of incoherent *photospheric* electron scattering is crucial to obtain correct fit values and we expect that this is the case for HD 160529 as well.

Another explanation would be that the mass-loss rates as derived by fitting the emission component and the electron scattering wings actually do differ: this could happen if substantial clumping exists in the wind of HD 160529, as the optical depth of the Hα line is proportional to the density squared while the

---

[11]With our code it is possible to model a single Balmer line equally well with a rather wide range of stellar parameters. The constraint to minimize the residuals of *all* modeled Balmer lines (i.e. Hα – Hδ) significantly reduces the number of possible solutions.
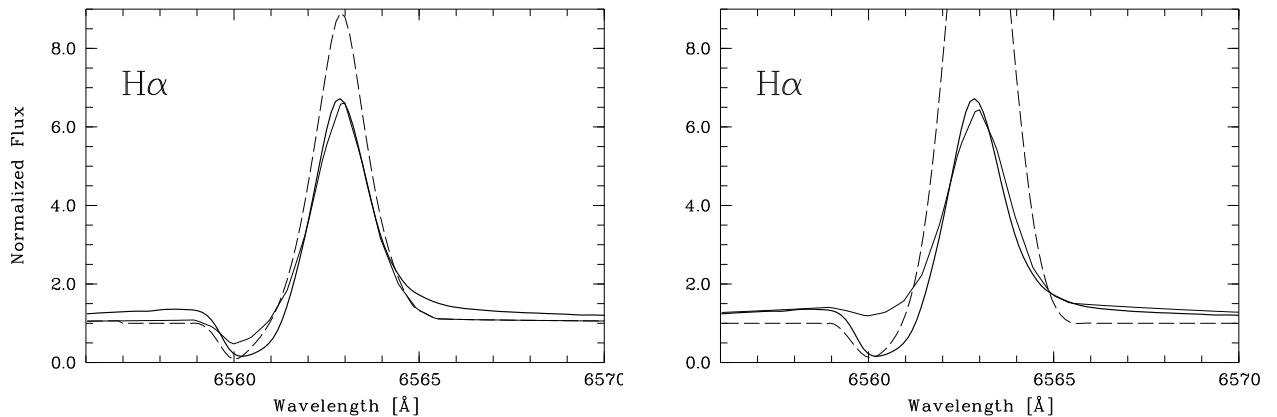
Figure 3.28: The averaged observed Hα line of 1993 (thick line) and the calculated synthetic model (thin line). The dashed line is the model before Thompson scattering is applied. *Left*: model with parameter values of Table 3.12 with minimum residuals for all Balmer lines. *Right*: model fitting simultaneously emission line *and* wings. For this model we have increased the mass-loss rate and wind-law exponents to: $\dot{M} = 22 \times 10^{-6} \, M_\odot \mathrm{yr}^{-1}$, $\beta = 5.5$. Note that the other Balmer lines (i.e. Hβ, Hγ, Hδ) are not fitted well with these values.

electron scattering depends linearly on the density (Hillier 1991). This might be possible although we have not seen any significant substructures in the wind lines that would indicate strong inhomogeneities (in particular see the ultra-high resolution spectra of HD 160529 in the next chapter). The model calculations used here have too many intrinsic simplifications to justify any further speculations.

Stellar Parameter of the Static Wind

- Departure Coefficients:

    It was found that the departure coefficients have a strong effect on the resulting line profiles. Due to their unrealistic rise at certain levels and the artificial damping function, their absolute values are not very reliable. However the form and relative values of the b-factors are consistent for different sets that can reproduce the relative line strengths of the Balmer series. Figure 3.29 shows their behavior, which agrees quite well with the more exact NLTE calculations of the "recombined" (i.e. low temperature) model of P Cygni from Najarro (1995, his Figure 3.1d).

- Helium Ionization and Abundance:

    For the temperatures under consideration here, i.e. under $\sim 12\,000$ K, all helium atoms are neutral. The helium abundance ϵ does not affect the Balmer line profiles strongly and we obtain good fits for values between $\epsilon = 0.11 - 0.20$ (i.e. around solar values or slightly higher).

- Velocities:

    Terminal velocities are often estimated from the blue edge of the absorption components of the Hα profiles. For HD 160529 the resulting values (not subtracting v_{sys} and including the strong Hα variation of 1994: v_{rad} (blue edge) ≈ -170 to $-210\,\mathrm{km\,s}^{-1}$ (see Figure 3.2 c)) indicate that v_∞ is not constant from year to year, although it appears rather stable during an individual observing run (see Figure 3.11).

    Usually v_∞ can be measured more accurately from the violet extent of the black absorption trough of saturated lines (see e.g. Lamers et al. 1995). Hence we retrieved the high-resolution spectrum of HD 160529 (observed in 1992) from the IUE archive. The uncertainties in the wavelength calibration of IUE were corrected by measuring the velocity shift between the interstellar Mg I $\lambda 2852$ UV line and the
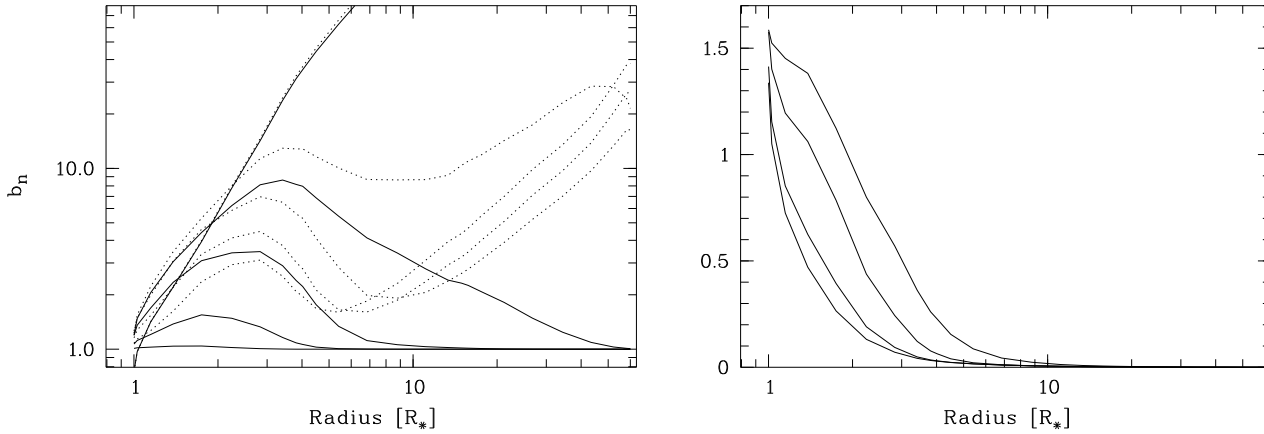
Figure 3.29: *Left*: NLTE departure coefficients of hydrogen levels 2 to 6 calculated for the 1993 Balmer line models. *Right*: b-factors of levels 3 to 6 divided by level 2. Solid lines: modified coefficients $(b_{n,new})$ after applied damping function, dotted lines: original values (b_n) calculated by TSOB.

Na I doublet in our well-calibrated optical spectra and correcting the IUE wavelength scale accordingly. Stahl et al. (1991 b) showed that v_∞ can be reliably derived from the strongest Fe II lines for LBVs, while the Mg II resonance lines are less suitable due to optical depth effects from the high mass loss (see Fig. 3.30).

We measure a value of about $-200\,\mathrm{km\,s^{-1}}$ from the blue edge of the saturated UV Fe II lines, which is about $40\,\mathrm{km\,s^{-1}}$ larger than the value measured from the optical spectra of 1992. We cannot exclude that the value of v_∞ has changed dramatically in a few weeks or months between our observations of 1992 and the IUE exposure. However it seems more likely that the blue edge of the Hα absorption component appears red-shifted by a "filling"-effect from the strong electron scattering wings and the general effects of the dense, turbulent outflowing matter. Note that in our SEIDYNAMIC calculations we need to use lower values for v_∞ because the models for $v_\infty \gtrsim 200\,\mathrm{km\,s^{-1}}$ always yield absorption components that are too blue-shifted. Thus the simplifications in our numerical wind models (in particular the core-halo approximation and electron scattering mechanism) might result in underestimating the terminal velocities.

The initial velocity at the lower boundary of the wind (v_0) and the turbulent velocity (v_{turb}) that is needed to broaden the line synthetic line components to fit the observed P Cygni profiles, were varied close to the sound speed. Good fit results were achieved for values in the range of $10-20\,\mathrm{km\,s^{-1}}$ for both parameters.

The exponent for the velocity law was varied from $1-6$ and the best fits were found for $\beta=4.0$. Note that Stahl et al. (1991 b) found values of $\beta=3-4$ appropriate to describe A supergiant winds.

● Temperatures:

We set the temperature at the sonic point $(T_{inner}$ in Equation 3.3) equal to the temperature derived from the Ti II line models, i.e. $T_{inner}=8500\,\mathrm{K}$ (see section 3.6.1 and Figure 3.19 d), which is close to the gray approximation of $T_{inner}=0.81\,T_{eff}$. As we have seen seen before, the Ti II lines already exhibit relatively strong wind influence and deviate from the photospheric LPV patterns so that the onset of the stellar wind can be identified with the Ti II line originating region.

For the outer temperature we used $T_{outer} \approx 5000\,\mathrm{K}$. This is the value used by Leitherer et al. (1995) for the electron temperature to model the radio flux of HD 160529. Note that for OB stars the relation of $T_{electron}=0.4\,T_{eff}$ is often used (Leitherer & Robert 1991) which would yield about 4500 K assuming
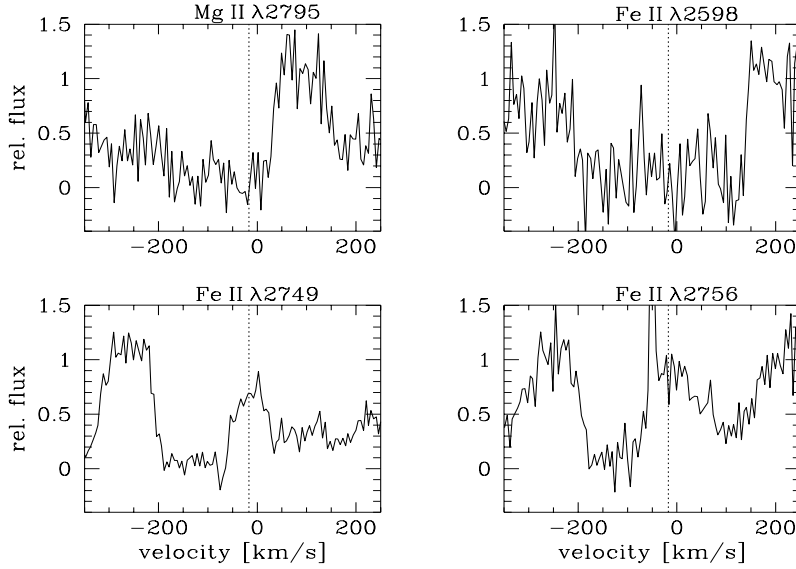
Figure 3.30: Selected strong Fe II lines and the Mg II λ2795 resonance line from the high-resolution IUE spectrum of 1992. The dotted line represents the adopted systemic velocity.

$T_{\text{eff}} = 11\,200$ K. However varying T_{outer} has only very small effects on the resulting line profile so that we refrain from a more detailed examination of this parameter.

The exponent of the temperature law was varied between 0.1 and 0.5 and it was found that a shallow temperature law (i.e. $\gamma = 0.1$) achieved the best fitting results. Note that this is in contrast to the value of $\gamma = 0.5$ that is usually suitable for B hypergiants (Rivinius et al. 1997). See section 2.6.5 of Najarro (1995) for a discussion on the temperature structure of stellar winds.

- Photospheric Profile:

For the photospheric absorption component we used the previously calculated models from TLUSTY 194. Note that the small emission-effect due to NLTE as mentioned in Hubeny & Leitherer (1989) is already included in the models and clearly visible in the photospheric Hα-line profile.

- Mass Loss Rates:

Leitherer et al. 1995 calculated the mass-loss rate of HD 160529 from measurements of its radio flux to $\dot{M}_{radio} = 13 \pm_{5}^{10} \times 10^{-6}\,M_{\odot}\text{yr}^{-1}$. This method does not depend strongly on assumptions of the geometry of the radiation-emitting region (Schmid-Burgk 1982) and is thus a highly accurate method of mass-loss determination. We have varied the mass-loss rates in our models around this value and achieved our best fitting model for $\dot{M} = 11 \times 10^{-6}\,M_{\odot}\text{yr}^{-1}$. Again we get a wide range of possible values for this parameter and expect a correspondingly large error bar due to the approximations in our models. However the close proximity of our $\dot{M}$ values and $\dot{M}_{radio}$ indicates that the outflow structure in HD 160529 probably does not deviate strongly from spherical symmetry.

It is important to note here that, while keeping other stellar parameters constant (at values listed in Table 3.12), increasing $\dot{M}$ to values higher than about $20 \times 10^{-6}\,M_{\odot}\text{yr}^{-1}$ does *not* increase the Hα emission line strength any more. Rather, intensity and equivalent width stop growing very suddenly and then even reverse their dependence on the mass-loss rate. This behavior can be explained by a *self-absorption* mechanism: as $\dot{M}$ is increased, the opacity in the wind increases and gets optically thick at a certain value of $\dot{M}$. At this point the wind material starts absorbing the radiation from deeper atmospheric levels so that the emission line core (originating from regions close to the stellar surface) gets gradually "blocked out" and the observed emission line strength decreases with growing mass-loss rates. Such wind conditions probably exist at other LBVs as well (e.g. many LBVs exhibits similar wind properties and spectral
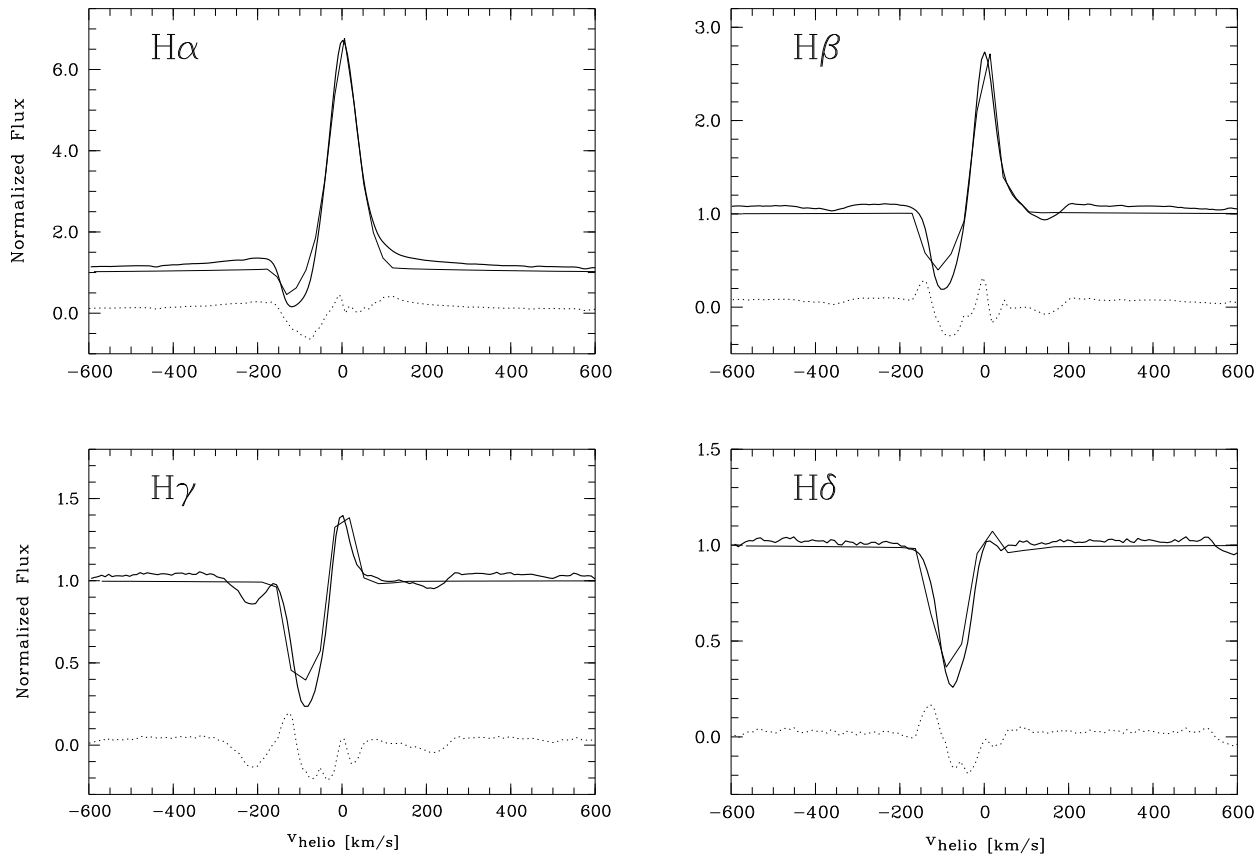
Figure 3.31: The calculated (thin lines) and observed (thick lines) averaged Balmer-line profiles of 1993, representing the stationary wind. The residuals are plotted under the profiles (dotted lines). The models use the parameter values of Table 3.12.

appearances during maximum (i.e. when the stars are coolest and brightest); see Leitherer et al. 1994 for AG Car and Leitherer 1997 and Crowther 1997 for a general overview of LBV wind quantities); these conditions complicate the exact determination of mass-loss rates for LBVs where wind densities achieve such extremely high values.

In Table 3.12 we list the stellar parameter values derived from our wind models for simultaneous fits of the Hα to Hδ lines. As in Table 3.11 we give the range of values that result in relatively good fits and the best fitting values. The effects of changing the parameter values on the synthetic spectra follow the same trends as described in Najarro (1995) and Kudritzki et al. (1999). We point out again that our *absolute* values are not extremely accurate because of the simplifications of the wind models applied (i.e. mainly the approximate NLTE treatment, the core-halo ("screen") electron scattering inclusion and the spherical symmetry). Our main goal, however, is to study the relationships between the photospheric and wind parameters during a given variability cycle, i.e. we search for *relative* dependences. We expect that the relative quantities are to first order less affected by the inaccuracies in our model calculations so that the results of the mean Balmer line fits can serve as a good starting point to explore the wind variability mechanisms.

Table 3.12: Stellar parameters from modeling the mean wind structure of HD 160529. The values for $\dot{M}_{radio}$ (marked with [†]) are from Leitherer et al. (1995).

parameter	v_∞	β	v_{turb}/v_∞	v_0
unit	[km s^{-1}]		[km s^{-1}]	[km s^{-1}]
best value	140	4.0	0.070	15
range	135 – 200	2.0 – 6.0	0.045 – 0.140	10 – 20
parameter	T_{eff}	T_{inner}	T_{outer}	γ
unit	[K]	[K]	[K]	
best value	11 500	8500	5000	0.1
range	11 000 – 12 000	8100 – 9500	4000 – 6000	0.1 – 0.5
parameter	$\dot{M}$	$\dot{M}_{radio}$[†]	$R_\star$	ϵ
unit	[$10^{-6}\,M_\odot\text{yr}^{-1}$]	[$10^{-6}\,M_\odot\text{yr}^{-1}$]	[$R_\odot$]	
best value	11.0	13.0	160	0.15
range	7.0 – 40.0	8.0 – 23.0	150 – 180	0.11 – 0.20

3.7.2 Yearly Variations of the Average Wind Structure

Figure 3.2 shows the mean yearly spectra where we can see variations of the absorption components in the Hα profiles that are not visible during the individual observing cycles. In particular in the mean spectrum of 1994, Hα exhibits a strongly blue-shifted and broader absorption and a smaller emission intensity (hereafter "1994-event"). In Figure 3.32 we have plotted the averaged spectrum of the observations from 1994 together with the synthetic models. The only difference from the models of Figure 3.31 is an increased terminal velocity, from 140 km s^{-1} (1993) to 170 km s^{-1} (1994). This results in a blue-shifted absorption component and a reduction of the emission strength due to a "thinner" wind (i.e. a reduced density). Modeling the Balmer profiles by changing $\dot{M}$ does not lead to satisfactory fitting results: adapting $\dot{M}$ to fit the Hα-emission/absorption does not reproduce the observed absorption/emission component. As noted in chapter 1.1 mass-loss rates in stellar winds are basically determined by the conditions below the sonic point while terminal velocities are controlled in the supersonic regions, indicating that variations in the conditions above the sonic point are responsible for the observed changes.

We have seen that this event influences predominantly the major wind line Hα but leaves the other lines unaffected. In particular the microvariability patterns and time scales remain unchanged. We conclude that the immediate causes of this event are probably due to different physical mechanisms than the microvariations. In particular the previously suggested pulsations cannot have changed strongly in 1994 because the photospheric LPVs are not influenced. This agrees with the above suggestion of supersonic origins of the year-to-year variabilities of the Balmer profiles.

We speculate that the "1994-event" and possibly all Hα-variations of the mean spectra in the yearly observing cycles arise from changes in the ionization structure in the extended wind regions. As shown by Najarro (1995) in a recombined wind (i.e. H and He are neutral) the second level of hydrogen is kept overpopulated due to the strong optical depth of Lα which significantly increases the opacity of the Balmer lines and causes the strong absorption dips of the Balmer P Cyg profiles. As shown in Figure 3.29a the NLTE departure coefficients decrease in strength for higher Balmer lines. The effects of a variable ionization structure thus affect mostly the Balmer lines formed in the outermost layers (Hα and Hβ) and decrease for higher hydrogen levels as these Balmer lines become optically thinner and form closer to the star.
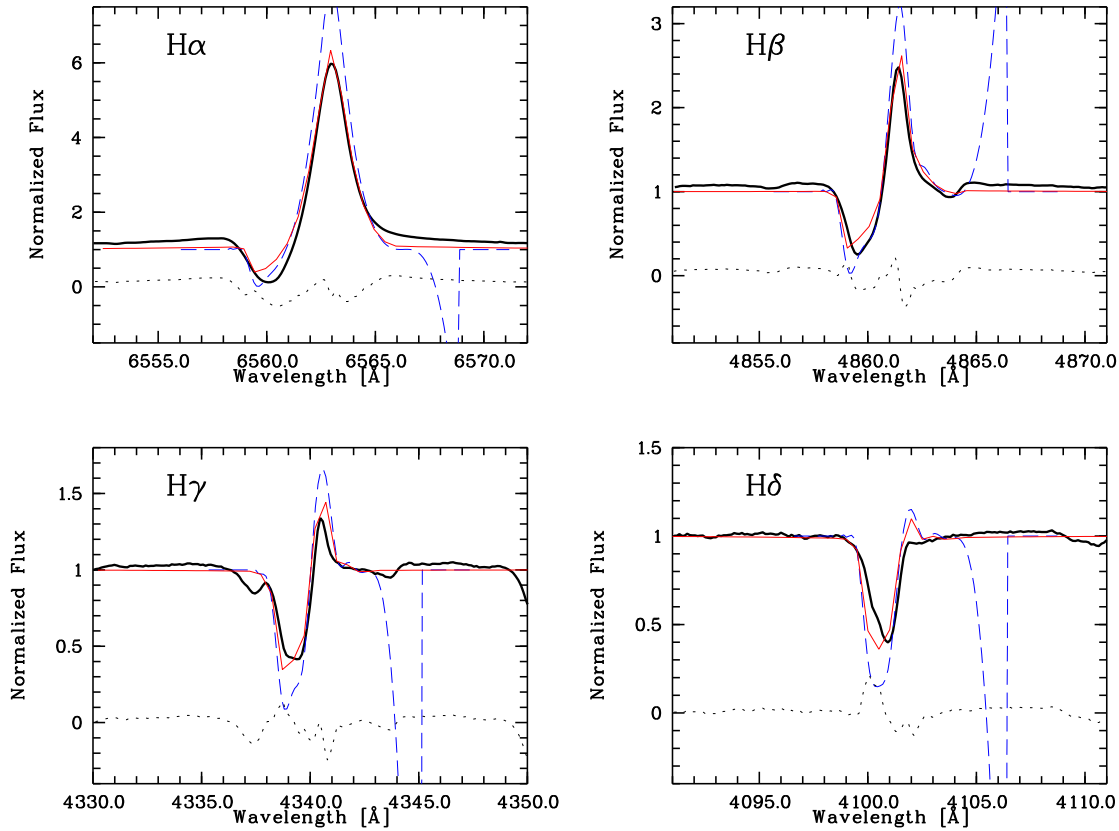
Figure 3.32: The calculated (thin lines) and observed (thick lines) averaged Balmer-line profiles of 1994, representing the stationary wind. The residuals are plotted under the profiles (dotted lines). The dashed lines are the models before applying the electron scattering (the peaks around +200 kms are numerical artifacts caused by the integration limits of the calculations). The models use the parameter values of Table 3.12 except that the terminal wind velocity is set to $v_\infty = -170\,\mathrm{km\,s^{-1}}$.

This argument is supported by the location of HD 160529 around a so-called "bi-stability" region: by studying the UV P Cygni lines of 117 stars with spectral types ranging from O to F, Lamers et al. (1995) found two discontinuities in the $v_\infty / v_{\mathrm{esc}}$ ratios: the dominant change occurs around $T_{\mathrm{eff}} \approx 21\,000\,\mathrm{K}$ where the ratio drops sharply from ~ 2.6 at the high-temperature side to ~ 1.3 at the low-temperature side. A smaller discontinuity at $\sim 10\,000\,\mathrm{K}$ where the ratio drops to about 0.7 is also visible. Note that Stahl et al. (1991 b) found values of $v_\infty / v_{\mathrm{esc}} \approx 1.5 - 2$ for A hypergiants and de Jager (1984) found values of $0.4 - 1.2$ for Ia$^+$ stars. Vink et al. (1999) investigated the bi-stability effect around 21 000 K and found that the jump is due to an increase in the line acceleration of Fe III below the sonic point. Around 10 000 K the Fe II lines are the main wind driving forces and we expect that a similar effect (i.e. changes in the Fe II ionization balance) can cause the velocity jump observed in the Hα lines of HD 160529. Our previous grid of TLUSTY 194 models for Fe II $\lambda 6248$ lines shows an abrupt decrease of the line strength for temperatures lower than 8500 K and larger than 11 500 K while in between these temperatures the Fe II $\lambda 6248$ line does not vary strongly. Considering the previously determined temperatures variations in the lower wind region of about 1500 K, one can conjecture that changes of the wind temperature influence the Fe II ionization balance sufficiently to account for the observed year-to-year Balmer line variations[12].

---

[12]The main mechanism that drives hot star winds is the transfer of photospheric photon momentum to the stellar atmosphere through absorption by spectral lines ("line-driven wind"). In stars with temperatures around 10 000 K the dominant absorbers are singly ionized iron atoms (i.e. Fe II or Fe$^+$) which then transfer their momentum via Coulomb-interaction to the bulk of the wind plasma (i.e. hydrogen and helium). If the temperature drops sufficiently for Fe$^+$ to recombine, the now neutral iron atoms cannot interact by Coulomb-collisions anymore and the wind structure changes.

Leitherer et al. (1989) performed calculations for LBV atmospheres around $T_{\mathrm{eff}} = 8000 - 16\,000$ K and found that ionization changes induced in subphotospheric regions can explain the observed spectral changes of LBVs between their minimum and maximum states (i.e. during the *moderate* variation cycle). As argued above, we have seen indications of variations in supersonic regions during the *microvariation* cycle of HD 160529 in a similar temperature range so that their calculations of the ionization structures might be applicable in this case as well. To our knowledge, a detailed theoretical study of the wind driving mechanisms and spectral line forces in the temperature range of $8000 - 12\,000$ K has not been carried out recently, i.e. using highly accurate unified models that do not apply the core-halo approximation of our models or the codes of Leitherer et al. (1989). Such computations are crucial to getting quantitative results for the effects that are responsible for the detailed long and short term wind variations seen in HD 160529.

In the following section we examine to first order possible relationships between photospheric and wind line variations *during an observing cycle*.

3.7.3 Dynamical Wind Models

In principle the observed wind line variabilities can be pinned down to three mechanisms[13]:

- Changing the ionization structure of the wind (i.e. the fraction and distribution of the ions which are predominantly driving the wind: Fe II (Fe III) for wind temperatures around $10\,000$ K ($20\,000$ K)).

- Changing the wind density.

- Changing the photospheric continuum flux.

These three mechanisms are not independent of each other; rather a major change in one parameter causes others to change as well. For example if the radiation from the stellar disk increases drastically it might ionize more metal lines which changes the ionization structure of the wind (say Fe II into Fe III). If these ions drive the outflowing material more effectively the velocity structure and in turn the density of the wind is affected too. This is the case for B supergiants where two bistability regions are found (Lamers et al. 1995; also see discussion in previous section).

In this section we study the effects from changing the density and continuum flux. A detailed study of the ionization structure is not possible with the used numerical code and thus is discussed only qualitatively.

Variations of the Wind Density

In order to model density variations we have to choose a wind geometry. The two basic possibilities are:

- Spherical symmetry in the wind and density variations ("shells").

- Spherically symmetric wind and randomly distributed inhomogeneities ("blob" or "clumps").

Shell ejections are observable as variations of the whole P Cygni profile: the increased density contributes equally to the emission as well as the absorption strength. Small local inhomogeneities on the other hand increase the optical depth of the wind line according to their specific radial velocities which form discrete absorption components (DACs) superimposed on the stationary line profiles. Such features are frequently found in B supergiants or Wolf-Rayet stars and were modeled with SEIDYNAMIC by Rivinius et al. (1997) for ζ^1 Sco.

---

[13]Note that the first two mechanisms are actual *physical* changes in the wind structure while the third point only changes the spectral lines because of the normalization of the spectra.
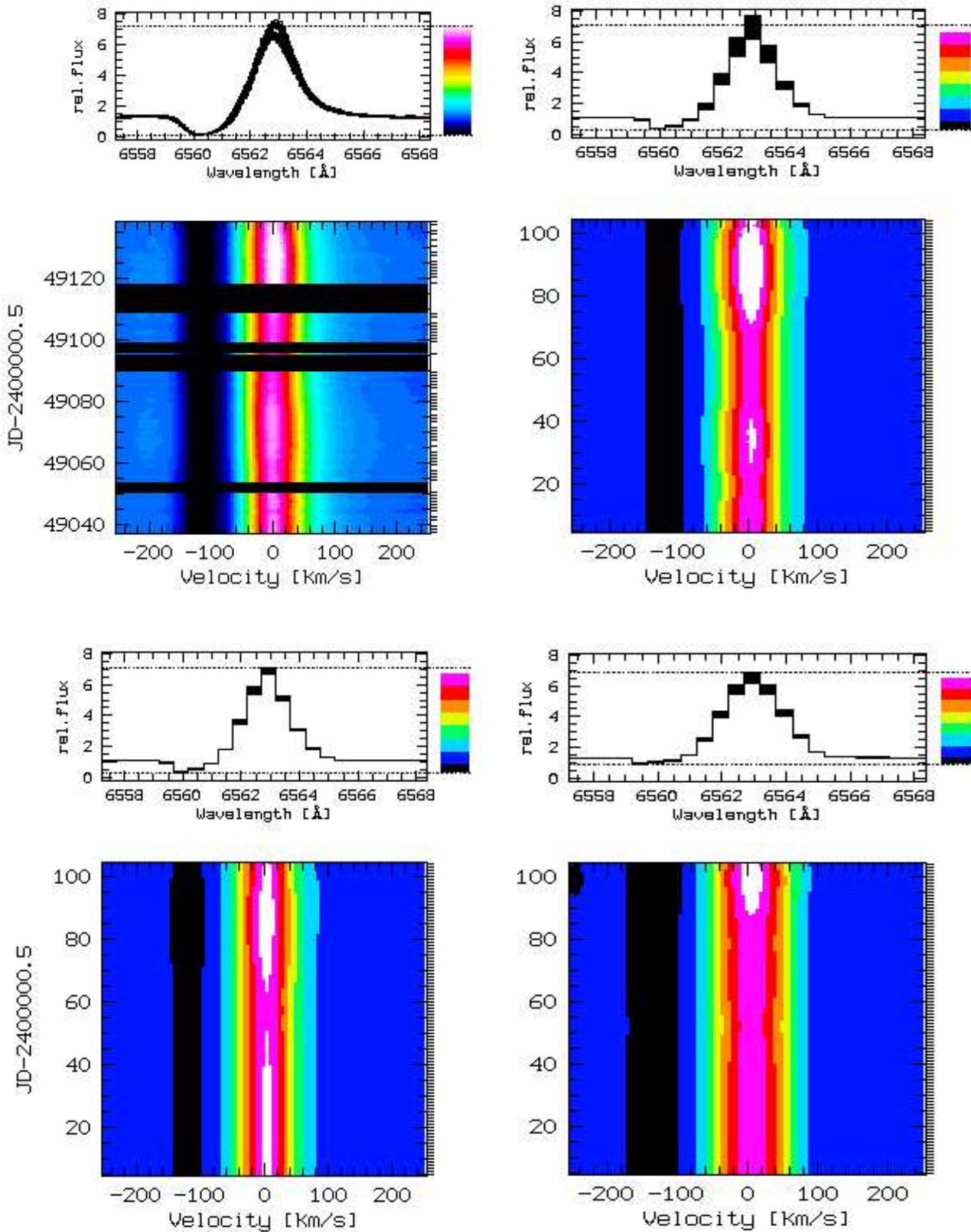
Figure 3.33: Top/left: observed dynamical spectrum of the Hα line in 1993. Top/right: modeled dynamical Hα spectrum with $\dot{M} = 11\ 10^{-6}\,\mathrm{M_\odot yr^{-1}}$, $\beta = 4.0$, continuum variations of 10 % and no time shift. Bottom/left: modeled dynamical Hα spectrum with $\dot{M} = 11\ 10^{-6}\,\mathrm{M_\odot yr^{-1}}$, $\beta = 4$, density variations of 50 % and a time shift of −80 days. Bottom/right: modeled dynamical Hα spectrum with $\dot{M} = 44\ 10^{-6}\,\mathrm{M_\odot yr^{-1}}$, $\beta = 4.0$, density variations of 50 % and a time shift of −80 days.
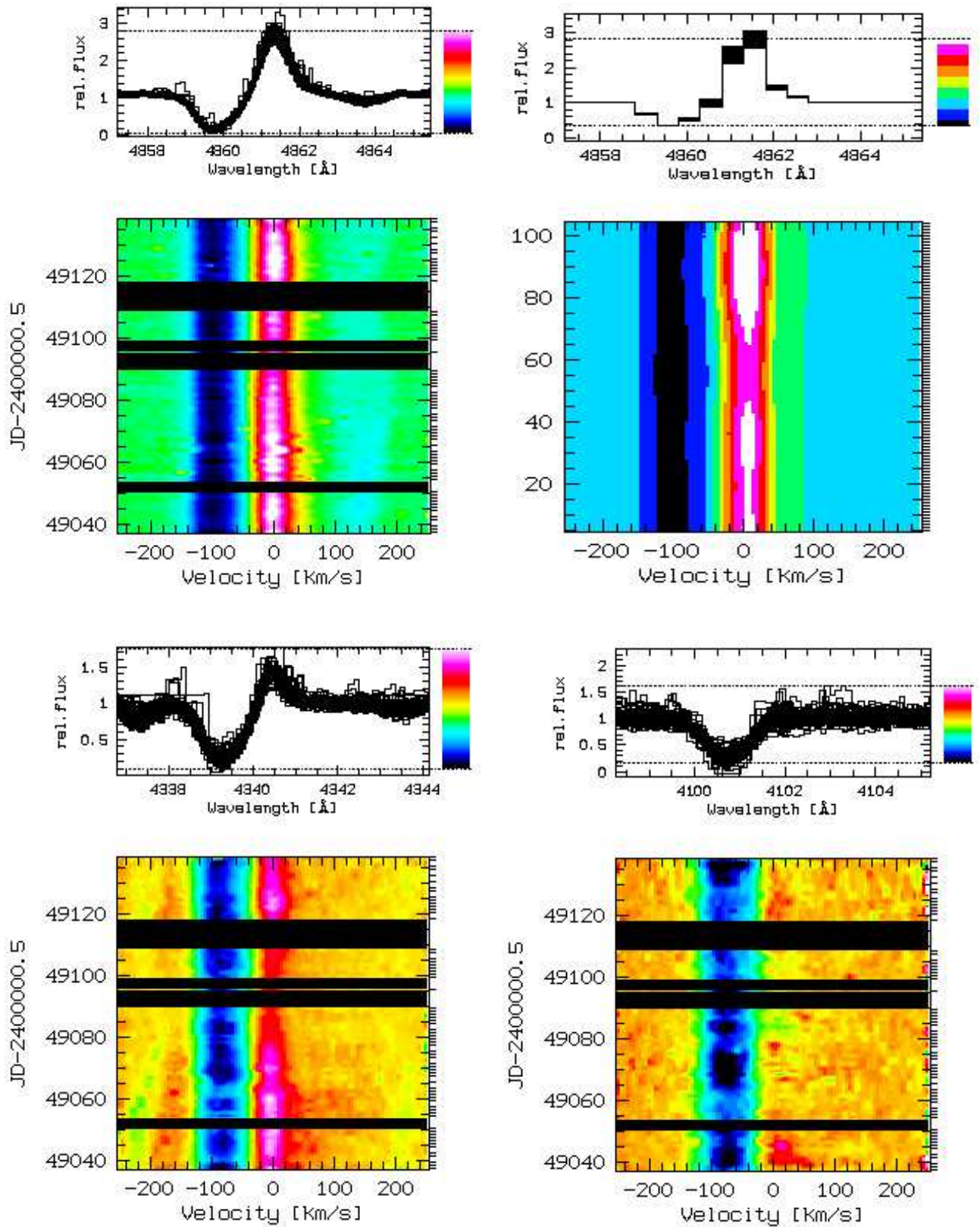
Figure 3.34: Top/left: observed dynamical spectrum of the Hβ line in 1993. Top/right: modeled dynamical Hβ spectrum with $\dot{M} = 11\ 10^{-6}\,\mathrm{M_\odot yr^{-1}}$, $\beta = 4.0$, continuum variations of Figure 3.33. Bottom/left: observed dynamical spectrum of the Hγ line in 1993. Bottom/right: observed dynamical spectrum of the Hδ line in 1993.

However the LPVs of HD 160529 do not show outward moving narrow line features. Instead the observed spectral variabilities are characterized by line variations at a more or less constant velocity or show a cyclic behavior in the case of photometric LPVs. The strongest wind lines (Hα, Hβ) exhibit black, saturated absorption components where no variability is observed. Weaker lines like Hγ and the Fe II lines do show variability over the whole P Cygni profile although their variation amplitude is quite small and might not be correlated.

The density variations were implemented by multiplying a "correction factor" times the average flux density in the wind (Equation 3.5). To see if the wind line variations are correlated with the photospheric LPVs we use the radial velocity curve of the He I λ5876 line for comparisons. The applied density perturbations were derived from a smoothed spline fit of the $v_{\rm rad}$ (He I λ5876) curve. The function was inverted so that the maximum negative velocities would represent the maximum increase in density and then normalized to a mean value of unity (see solid curve of Figure 3.16). The amplitude of the correction function was varied to model the flux values of the Hα line and represent the density variations required to fit the wind lines. As argued in section 3.5 we suggest that the $v_{\rm rad}$-curves of the photospheric lines are caused by pulsations of the stellar surface which might introduce density perturbations into the wind. Using again a beta-law for the propagation of the density variations, the time needed to reach the Balmer line forming region depends strongly on the value of β. This time delay was accounted for by shifting the density correction function backward in time until a good agreement with the Hα variability was reached.

We have also varied the velocity law for the density perturbations and the input mass-loss rate to study their effects on the dynamical wind. All other parameters were taken from the previously derived static model.

Even allowing the whole envelope to change its density by 50%, the variations of ρ are not sufficient to explain observed variations of the Hα emission strength if used with low $\dot{M}$ values (about $7-15 \times 10^{-6}\,{\rm M_\odot yr^{-1}}$). With higher mass-loss rates, i.e. $\dot{M}$ larger than $\sim 20 \times 10^{-6}\,{\rm M_\odot yr^{-1}}$, we can reproduce the intensity variations of the Hα emission, however then the line shape is not fitted well, i.e. the emission and absorption components of the P Cygni profiles are wider than observed and the emission component is too strong. Furthermore in order to achieve the correct time alignment of the observed and modeled LPVs we need to shift the density perturbation curve 80 days backwards to account for the time delay of the traveling features when using the same value for the velocity law exponent as obtained for the mean wind ($\beta = 4$). However this means that we use an inaccurate correction function: our observing runs are not long enough for the adopted $v_{\rm rad}$ (He I λ5876) curve to reach back in time as far as needed. Thus we cannot model the Hα emission variations with density perturbations if the travel time scale is greater than the observing run. Smaller β-values yield shorter time delays but then the density perturbations (even up to 50% of the whole wind density) are too small to achieve the observed emission variations. The lower plots of Figure 3.33 illustrate the described ρ–model behavior.

In conclusion we can say that realistic density variations on the order of $10-20\%$ (as e.g. observed in B supergiants by Rivinius et al. 1997) cannot cause the observed Balmer line variations. Note that because of this circumstance, HD 160529 could have significant density variations in its outflow without providing directly observable spectral symptoms. The reason for this situation might be that the wind conditions are close to the previously discussed self-absorption parameter space: increasing the wind density even in large amounts might not achieve a significant increase in the line emission if the opacity in the wind gets optically thick and acts as a counter measure.

Variations of the Continuum Flux

As described in section 3.5.3, variations of the continuum flux have immediate effects on the corresponding spectral lines when the spectra are normalized. We have used the same correction function as in the previous density variation models. Again we varied the amplitude of the correction curve to fit the observed emission line variations but this time did not include a time shift.

The top/right plot in Figure 3.33 is the result of a model run using an amplitude of about $\pm 5\%$ in the continuum flux variations. We can see that the model reproduces the observations very well: the line shape and variation patterns as well as the time dependencies are all fitted nicely. As consistency tests we have calculated dynamical models for $H\beta$, $H\gamma$ and $H\delta$ using the same correction function and obtain again very good fit results (see the top plots of Figure 3.34 for the observations and models of the $H\beta$ line in 1993). We conclude from the good fit results that variations of the underlying continuum are probably the main cause of the observed wind line variabilities.

In the lower plots of Figure 3.34 we show the observed dynamical spectra of $H\gamma$ and $H\delta$ in 1993. These lines exhibit the same behavior as $H\alpha$ and $H\beta$, although they are much less influenced by the stellar wind. Careful inspection of the dynamical $H\delta$ spectrum in the lower/right plot of Figure 3.34 detects a faint emission component for $H\delta$ as well, that follows the same behavior as the $H\alpha - H\gamma$ lines. Furthermore the non-saturated absorption components of $H\gamma$ and $H\delta$ show no significant signs of radial velocity variations as would be expected for outward moving density enhancements like blobs or shells so that these LPVs also support the argument for continuum flux variations. The small intensity variations in the $H\gamma$ and $H\delta$ absorption lines could be due to slight changes in the ionization balance of the metal lines that may affect the line intensities without radial velocity changes. However, to disentangle the contributions in detail, better numerical models are needed, so we postpone further studies to a later time.

3.8   Summary and Discussion

For the first time the galactic Luminous Blue Variable HD 160529 was observed *spectroscopically* over a time period of four years ($1992 - 1995$) on $55 - 129$ consecutive nights per year. These observations provide a unique data set with high spectral and temporal resolution to examine the observed variability and study the dynamical mechanisms in LBV atmospheres.

By studying the dynamical behavior of selected diagnostic spectral lines we have probed the conditions at various depths of the stellar atmosphere. We can distinguish four classes of diagnostic lines[14]:

1. *Photospheric lines*: these lines are always in absorption and show quite symmetric line profiles with v_{rad}-values of $0 - 20\,\mathrm{km\,s^{-1}}$. Their variability patterns are very regular and follow sharply defined time scales of 92.5 ± 1 days. Examples are: He I $\lambda 5876$, Mg II $\lambda 4481$ and Si II $\lambda 6347$.

2. *Transition lines*: these lines have profiles with shallow blue wings, absorption components with v_{rad}-values between ~ 15 and $\sim 60\,\mathrm{km\,s^{-1}}$ and sometimes weak emission components. Their variability patterns are very complex and irregular and they exhibit time scales with low power on the order of $20 - 115$ days. Examples are: Ti II $\lambda 4468$, Fe II $\lambda 6248$ and $H\delta$.

3. *Wind lines*: these lines have P Cygni profiles with strong emission components and absorption components with v_{rad}-values greater than $60\,\mathrm{km\,s^{-1}}$. Their variability patterns are less regular than the photospheric lines and have larger pseudo-periods of about $114 - 127$ days. Examples are: $H\alpha$, $H\beta$ and $H\gamma$.

---

[14]In this chapter we assume negative v_{rad}-values for all absorption lines and a systemic velocity of $v_{\mathrm{sys}} = -17\,\mathrm{km\,s^{-1}}$ to be subtracted from the discussed radial velocity values.

4. *Envelope lines*: these lines are excited at temperatures much lower than T_{eff} and have profiles with multiple absorption components ($v_{\mathrm{rad}} \gtrsim 60\,\mathrm{km\,s^{-1}}$) and weak emissions. Mainly the absorption line strengths are variable but slowly outward moving features might be possible as well. The complex line profiles, and in particular the ISM and hydrogen line blends, prevent reliable results from Fourier analyses or model fits. Examples are: Na I and Ca II lines.

We called the second group of spectral lines *transitional* because their line profiles and radial velocity values indicate that the respective line forming regions are influenced strongly by both the photospheric variability mechanisms and the wind conditions. Thus these lines are in a transition region between the two extreme atmospheric conditions (i.e. wind dominated or photospheric). Note that this transition region encompasses the sonic point with velocities around $15-20\,\mathrm{km\,s^{-1}}$; hence its conditions strongly influence the main wind parameters $\dot{M}$ and v_∞ (see section 3.7).

A detailed study of the above line classes is necessary to achieve good constraints in the model calculations of the respective spectral analyses and learn more about the conditions in the extended stellar atmospheres of LBVs.

In the following sections we summarize and discuss the results from our observations and analyses. We also present some thoughts about the possibilities of binary systems causing the observed variations and draft future prospects in this research area.

3.8.1 Summary and Discussion of the Results

Studying the mean spectra of the respective observing cycles we can see that the photospheric lines are basically constant on a yearly basis (see Figure 3.1 a – e) indicating that the average photospheric conditions remain constant over the whole observing campaign. However, the transition, wind and envelope lines exhibit significant year-to-year variations (see Figures 3.1 f, 3.2 b – f and 3.6). A closer study of the time dependence of the LPVs, in particular using dynamical spectra, reveals that all spectral lines are variable on a time scale of days. The respective dynamical quotient spectra show that the variations occur as pseudo-absorption and emission features that are symmetric about the systemic velocity. Usually the LPVs patterns are stationary and mainly vary in their strengths but occasionally prograde and retrograde moving variation features can be observed as well (see Figures 3.5 left, 3.8 – 3.10 and 3.26).

The temporal variance spectra (Figure 3.13) confirm the above results but also allow a quantification of the observed LPVs: the photospheric lines always show a double-peaked TVS profile that is quite symmetric about the systemic velocity (around $v_{\mathrm{sys}}\pm20-40\,\mathrm{km\,s^{-1}}$). The separation of the peaks from v_{sys} is increasing with increasing radial velocity of the lines (e.g. in 1992 the peaks of the He I $\lambda5876$ line are at $v_{\mathrm{sys}}\pm25\,\mathrm{km\,s^{-1}}$, while they are at $v_{\mathrm{sys}}\pm40\,\mathrm{km\,s^{-1}}$ for the Si II $\lambda6347$ line). The transition, wind and envelope lines exhibit additional blue-shifted peaks and generally more complex TVS profiles indicating that, although the photospheric variability mechanisms are present in these lines, additional effects contribute to their LPVs. The double-peaked structure of the photospheric TVS lines is indicative of simultaneous radial and non-radial pulsations: the RP contribute mainly to the line wings while NRP modes provide the main contribution at the line cores due to traveling bumps crossing the complete profile. Kaufer et al. (1997 b) found a very similar situation in the photospheres of other BA supergiants. The far blue-shifted TVS peaks of the non-photospheric lines can be explained by slowly outward moving density enhancements in the wind which might have been produced by previous shell ejections or by wind interactions with the ambient medium moving at different velocities and building up density enhancements in the interaction zones. Axially symmetric outflow structures (e.g. rotational modulation of wind lines and corotating magnetic fields) as found in BA supergiants winds by Kaufer et al. (1996)

cannot cause the observed TVS and LPV patterns, as such mechanisms fail to explain the retrograde moving variation patterns and the non-existing counterpart of the far blue-shifted TVS peaks.

Note that we also did not see evidence for outward moving density enhancements in the LPVs or TVS. This is in contrast to studies of Of supergiants (Eversberg et al. 1998) and W-R stars (Moffat & Robert 1992), which show TVS profiles that cover the whole line forming region and are interpreted as outward moving density perturbations.

The equivalent widths (W_λ), radial velocities ($v_{\rm rad}$) and intensities (I) of the spectral lines were measured with automatic routines using direct line integrations (for W_λ) and Gaussian fits (for $v_{\rm rad}$ and I) to get objective results. We see that $v_{\rm rad}$ variations dominate in the photosphere while W_λ variations are the major source of the wind-LPVs. Comparing the various spectral line values and the photometric variations obtained during Sterkens's LTPV program, we detect a correlation between these parameters: as the equivalent width of Ti II $\lambda4468$ decreases, the star gets brighter (y decreases), W_λ of Hα decreases and the radial velocity of He I $\lambda5876$ increases (see Figures 3.15 right and 3.16). Using the W_λ (Ti II $\lambda4468$) curve as temperature indicator, we can interpret this behavior as an increase in temperature (W_λ(Ti II $\lambda4468$) decreases) thus simultaneously raising the continuum flux which decreases W_λ(Hα) in the normalization step of the data reduction. The time lag of the wind variations compared to the W_λ (Ti II $\lambda4468$) variations indicates the existence of an additional mechanism that requires travel time to affect the wind line regions. The sinusoidal $v_{\rm rad}$ curve of He I $\lambda5876$ is consistent with radial and/or non-radial pulsations at the stellar surface which could cause the observed atmospheric temperature variations and might also trigger density variations in the wind that could account for the mentioned different time dependencies of the considered data curves.

The above spectroscopic and photometric data sets have been used in Fourier analyses to determine the periodicity and dominant time scales of the variations. We find that the predominant time scales of the photometric and spectroscopic variabilities are within a similar range, around $92-127$ days. The photospheric periods are very closely defined at 92.5 ± 1 days while the wind lines show a larger spread of time scales (about $114-127$ days). The analyses sometimes yield up to four additional shorter periods with smaller power indicating a multi-periodicity of the LPVs. These minor periods are required for a detailed reconstruction of the variability curves, while the dominant periods determine their general behavior (see Figure 3.17). This result is consistent with the previous argument of pulsations causing temperature variations that are immediately visible in all spectral lines (through the changing continuum flux) and that wind lines are additionally influenced by density perturbations in the outer atmosphere which do not affect the photospheric spectral lines but lead to different time scales of the wind variations.

To test the previous theories and get quantitative results for the atmospheric conditions in HD 160529 we modeled the mean line profiles and the observed LPVs with static and dynamic atmospheric codes. We have chosen highly sophisticated plane-parallel codes (TLUSTY 194 and SYNSPEC 41) to model the photospheric lines and relatively simple spherical hydrodynamic codes (SEIDYNAMIC) to model the wind lines. We realize the shortcomings of these methods as LBVs are in a parameter range where basically all imaginable effects (expanding, possibly nonspherical, atmospheres, NLTE-effects, ...) can be important. However, to get initial results of the *dominating* mechanisms at work in the respective atmospheric regions, the above approaches appear justified and return reasonable results. The resulting main stellar parameters of the mean photosphere are: $T_{\rm eff} = 11\,200$ K, $\log g = 1.13$, $R_\star = 168$ R$_\odot$, $M_\star = 14$ M$_\odot$, $M_{ZAMS} = 40$ M$_\odot$, $v_{\rm sys} = -17$ km s^{-1}, $v_{\rm esc} = 93$ km s^{-1}, $v_{\rm break} = 126$ km s^{-1}, $v\sin i = 35$ km s^{-1}, $\xi_{\rm micro} = 15$ km s^{-1}, $P_{\rm rot,break} = 68$ days, $P_{\rm rot}/\sin i = 243$ days, $P_{\rm rad,fund} = 24$ days and the mean wind models yield: $v_\infty = 140$ km s^{-1}, $\beta = 4$, $v_0 = 15$ km s^{-1}, $\dot{M} = 11\,10^{-6}$ M$_\odot$yr^{-1}. Here we have listed the results from the photospheric analyses for parameters that provided different values from the wind-model fits as

we expect that the approximations in the SEIDYNAMIC models yield larger errors than the TLUSTY 194 models whose results have been validated by various consistency tests (see section 3.6.1). Tables 3.11 and 3.12 list all results of the different analyses together with the error ranges.

We note the rather large mass discrepancy between the current mass of $M_\star = 14\,M_\odot$, as determined from the spectral line fits (via T_{eff} and $\log g$), and $M_{ZAMS} = 40\,M_\odot$, as indicated in Figure 3.22 by comparing the location of HD 160529 in the Hertzsprung-Russell diagram with evolutionary tracks of Meynet et al. (1994). We arrive at this result because we assume that HD 160529 is evolving to cooler temperatures as we get the best line fits with models using solar abundances, thus indicating a relatively young evolutionary status of this star. This argument is supported by the lack of forbidden nebular lines (forbidden lines are excited by collisions into metastable levels which require high densities) and the absence of a nebula around HD 160529[15]: as most LBVs exhibit a surrounding nebula (either formed by strong dense winds, shell ejections and/or super-outbursts, see Nota et al. 1995), its absence suggests that HD 160529 entered the LBV phase only recently and is not old enough to have formed an observable nebula. To explain the mass discrepancy, we suggest that HD 160529 might have undergone various evolutionary "loops" with high mass-loss phases. Such scenarios were proposed by Kiriakidis et al. (1993) and Langer et al. (1994) for pulsating stars with $M \gtrsim 40\,M_\odot$, which could explain the large mass loss of HD 160529 from the ZAMS to the current LBV state. These phases could also produce density-enhanced shells in the envelope of HD 160529 which would account for the far blue-shifted absorption lines that we have seen in the Na D and Ca K / H lines.

Also notice that the rotational period ($P_{\mathrm{rot}}/\sin i = 243\pm^{62}_{13}$ days) is much larger than the time scales derived from the Fourier analysis (92 – 127 days). Even considering that $P_{\mathrm{rot}}/\sin i$ gives only an upper limit for the period, purely rotational modulated mechanisms like magnetic fields on the stellar surface seem unlikely.

The previously used temperature dependence of the Ti II λ4468 line is verified by TLUSTY 194 -models in section 3.6.2, where we derive a variable temperature structure of the lower atmosphere in the range of $T_{\mathrm{eff}} \approx 10\,000 - 11\,500$ K. Our previous arguments for PR- *and* NRP-modulated photospheric LPVs are supported by radial pulsation models (courtesy of Dr. J. Guzik) using stellar parameters similar to HD 160529, which yield global variations of radius, radial velocities and effective temperature similar to our observed and deduced values (see Figure 3.27) and the reconstruction of the dynamical quotient spectra of He I λ5876 in 1993 by simple, low-order non-radial pulsation models (see Figure 2.26). In general the observed LPVs have a more complex structure than the above example which we ascribe to the previously indicated multi-periodicity of the pulsation modes. However, we can estimate the meridional sectors from the simultaneous observed pseudo-emission or -absorption features and get a maximum value of $|m| \lesssim 2$.

From our SEIDYNAMIC-model fits of the wind lines we gain the following important results:

- The correct treatment of NLTE departure coefficients and electron scattering are essential to derive reliable quantitative results from the Balmer line fits. The SEIDYNAMIC-models are not sophisticated enough to yield good *absolute* parameter values but are nevertheless sufficient to reliably estimate *relative* variations in the wind of HD 160529.

- We obtained different results for the mass-loss rate by fitting the wings and the emission component of the Hα line (i.e. the $\dot{M}$-values of the line-wing fits are a factor of 2-5 larger than the line-emission fits, see Figure 3.28). Taking these results at face value could indicate significant

---

[15] Nota et al. (private communication) imaged HD 160529 in various filters with the STScI-coronograph mounted at the NTT and failed to detect an obvious nebula.

clumping as the strength of electron scattering wings is proportional to the density, whereas the total line emission is proportional to the density squared (Hillier 1991). However the simplifications in our models (in particular the incorrect treatment of electron scattering and NLTE and the core-halo approximation) prevent conclusive results.

- The determination of $\dot{M}$ using Balmer line fits is additionally complicated by the closeness of the wind conditions in HD 160529 to a *self-absorption* regime of the outflowing matter: as $\dot{M}$ is increased to more than about $20 \times 10^{-6}\,M_{\odot}yr^{-1}$ the model Hα emission line strengths cease to increase and reverse their dependencies on the mass-loss rates. We speculate that this behavior is an opacity effect where, at a certain value of $\dot{M}$, the wind material gets so dense that it becomes optically thick and starts absorbing the radiation from deeper atmospheric levels, thus "blocking out" the emission line core radiation from deeper atmospheric levels and decreasing the observable emission line strength.

- We observe variations of the Hα profiles in the mean yearly spectra that are not visible during the individual observing cycles, i.e. blue-shifted, broader absorption and smaller emission intensities. We could reproduce this behavior by changing the v_{∞} values in the models while keeping all other parameters constant (see Figure 3.32). Note that varying $\dot{M}$ did not produce satisfactory Balmer line fits, indicating that changing conditions in the supersonic part of the wind cause these particular LPVs (in first order approximation mass-loss rates are determined by the conditions below the sonic point while terminal velocities are controlled in the supersonic regions). We conjecture that ionization changes in the extended wind regions might be responsible for these variations: we have seen evidence for a variable temperature structure of the transition region (variable Ti II λ4468 lines) and found indications for changing densities in the wind regions (time lag from photospheric- to wind-LPVs and possible radius variations). Both parameters have strong effects on the ionization structure of the outflow material in BA supergiants (Kaufer et al. 1997 a) and could cause the observed LPVs. Supporting this argument is the bi-stability mechanism around $T_{\text{eff}} \approx 10\,000$ K found by Lamers et al. (1995), that is presumably caused by changes in the ionization balance of singly ionized metal lines.

- To explore connections between the photospheric LPVs and the wind variabilities during an observing run, we used the v_{rad}-curve of He I λ5876 as best indicator of the photospheric conditions to create a "correction" function that was multiplied with the examined parameter values. We find that changing the wind density does not produce good fits for the dynamical spectra while varying the continuum flux reproduces the temporal dependence of the Balmer lines very well (see Figures 3.33 amd 3.34). Note, however, that in our models density variations in the range of $10-20\,\%$ (as found in early-B hypergiants by Rivinius et al. 1997) do not produce large observable effects on the Balmer lines (probably due to the above mentioned self-absorption mechanism) so that significant density variations might occur in the wind of HD 160529 that would be undetectable in the optical spectra.

The line profile shapes (P Cygni-type with multiple absorption components) and fast LPVs (time scales of days) of the Na I and Ca II lines signify strong stellar contributions in these profiles. Usually these lines are very weak in BA supergiant spectra (apart from the ISM lines) because the atmospheric temperatures are too high. However, assuming the temperature drops monotonically with a shallow power law, as indicated in section 3.7.1, then the Na D and Ca K / H resonance lines would be formed far out in the stellar envelope where the temperature is low enough to allow for recombination of these lines. It is conceivable that at this distance the wind runs into previously ejected, slowly moving material (which might have occurred in the evolutionary loops with extreme mass-loss rates as suggested above to explain

the discrepancy between the current mass and M_{ZAMS}) or the ISM. In either case the density of the outflow increases drastically in the interaction zone and shocks occur that might excite the sodium and calcium lines. Ultimatively, nebulae form out of these interaction regions. The fact that no nebula was detected around HD 160529 supports our previous argument that this star only recently left its main-sequence state to become an LBV. Note that, if the envelope-line forming regions are at a distance of about 50 $R_\star$ or more, wind material traveling at an average speed of about 200 km s^{-1} would need at least one year to arrive at that location (light travel times would be on the order of hours). Thus the variations of the Na D and Ca K / Ca H lines are difficult to correlate with the observed photospheric- and wind-LPVs. We refer to chapter 12 of Lamers & Cassinelli (1999) and the suggested reading references there for further information about possible outer envelope developments of stellar winds.

Comparing our results with the findings of Kaufer (1996) we can see that the photospheric variations of HD 160529 are rather similar to those found for other *normal* BA supergiants: although our LPVs exhibit higher amplitudes, the principal mechanism of the line variabilities can be attributed to radial and non-radial pulsations in both cases. The wind variations, however, are different in our study: we find a close connection between the wind and photospheric LPVs through the continuum flux variations while normal BA supergiants wind variations seem to be disconnected from the photospheric LPVs. Rather they are dominated by rotational modulations for which we found no evidence in our study. Outward moving density perturbations in the inner wind regions, as reported by Rivinius et al. (1997) in early-B hypergiants, have not been found in our spectra. As already mentioned by Kaufer (1996) we stress again the importance of the ionization structure in the stellar outflows for stars with temperatures around $T_{\mathrm{eff}} \approx 10\,000$ K, which needs to be calculated in detail to get correct quantitative results for the wind parameters.

Concluding we find that low-order radial and non-radial pulsations can consistently account for all the microvariations of HD 160529: RPs and NRPs directly affect the stellar surface and can explain the photospheric LPVs. They can also induce the wind variations via temperature fluctuations, which in turn influence the continuum flux and the ionization structure of the wind, and might trigger density variations in the stellar outflow, which would explain the slightly longer and more irregular time-dependent behavior of the wind-LPVs (note that the dynamical time scale for the Hα line forming region around $1-5$ $R_\star$ is on the order of a few days to weeks).

Analyzing the causes for the pulsations themselves is beyond the scope of this thesis. However recent research of strange mode instabilities (SMIs) provides promising mechanisms as these SMIs seem to occur naturally in stars with high luminosity-to-mass values, which correspond with the evolutionary phases of LBVs (see Glatzel 1997, 1998). More detailed calculations with hydrodynamic codes that consider the important effects found in this thesis, will deliver quantitative results to gain further insight into the LBV mechanisms.

3.8.2   Notes about a Binary Scenario

It is well known that about $30-50$ % of OB and W-R stars are binary systems (Vanbeveren 1994, Kenyon & Gallagher 1985). If we assume that LBVs are a standard evolutionary state for essentially every massive star, then the LBV populations should reflect the above binary fraction. However of the $25-40$ well-known LBVs and LBV-candidates (Bohannan 1997 lists 31 recognized LBVs) only three are established binaries (i.e. HD 5980, R 81, η Car). It follows that the companion star, if present, is difficult to detect. A possible scenario is that the companion star(s) is (are) buried in a common envelope. For HD 160529 the flux distribution is known over a wide wavelength range (see Blomme et al. 1997) and thus a distant companion (no common envelope) would have probably been detected in the spectral

energy distribution (although it might be hard to see for very hot or very cool stars or if the companion has the same spectral type). Also the variations induced in a binary system are usually much better defined (i.e. have very distinct periods) and have longer time scales (e.g. 5.5 yrs for η Car; see Damineli 1997) than what we observe in HD 160529. However the periods of a very close binary system with HD 160529 as the giant component could be similar to the time scales that we observe in the LPVs (order of weeks to months).

A common envelope scenario is most likely the case for η Car: e.g. Lamers et al. (1998) suggested a close binary scenario with a separation of 15 AU and two massive stars ($60 - 80\,M_\odot$ and $50 - 70\,M_\odot$). The strong wind interaction of those massive stars could produce the observed bipolar structure of the Homunculus nebula (see page ix of thesis) and account for the discrepancies in the element abundances of nebula and nucleus as well as exhibit the previously found 5.5 yr periods in near infra-red spectral lines and photometric data (Damineli 1997). Kenyon & Gallagher (1985) proposed an even more complex binary model with an accretion disk mimicking a photosphere of a rather cool temperature ($\sim 10\,000\,K$) dominating the luminosity of the whole system with radiation pressure instabilities that may cause additional variations.

It is conceivable to imagine a scenario where the common envelope of a binary system emits the radiation that we considered as photospheric and a small companion star rotating around HD 160529 at a short distance would introduce disturbances of the common envelope in a way that would cause the observed spectral and photometric variations. In fact, Tubessing et al. (1999) analyzed photometric and spectroscopic data of R 81 and derived a period of about 74.5 days from the photospheric data and observed variations of the Hα line that are similar to the time scales and LPVs of HD 160529.

However, even in the above three case of LBVs that are expected to be binary systems, their variability is not necessarily *dominated* by binary interactions. Following the principle that the simplest explanation which accounts for all the observations has the highest chance of being correct, we favor the model of pulsations being responsible for the observed LPVs in HD 160529.

Using the above binary fraction of OB and W-R stars we can also draft a counterargument: as all LBVs are known to be variable but not all LBVs are binary systems, the binary system interaction cannot be the sole mechanism of the LBV variability. In contrast hydrodynamical models of hot stars show that pulsations occurs naturally when the luminosity-to-mass ratio gets as high as observed for LBVs (Glatzel 1997) so that this mechanism is a more likely candidate to explain LBV variabilities in general.

3.8.3 Future Prospects

The simple models that we used in our analyses were appropriate for our goal of getting first results and indications of the physical mechanisms at work in the atmosphere of HD 160529. The huge amount of data that were collected and analyzed here made this step necessary as calculating physically correct models for each spectrum would be beyond the numerical capabilities of present day computer facilities.

With this first step completed, it is now important to see what effects the neglected physical mechanisms have on our results. Very sophisticated models exist now to treat various effects like shocks (Feldmeier 1995), clumping of outflows (Feldmeier 1999), corotating interactive regions (Owocki 1999), pulsations (Guzik et al. 1999, Glatzel 1997) and "unified codes" that calculate photosphere and wind simultaneously without simplifications like the Sobolev or the core-halo approximation of our models and apply a correct treatment of electron scattering mechanisms (Santolaya-Rey et al. 1997).

All the listed mechanisms might be important in the atmospheres of LBVs and contribute to their spectral variability. The unique data set presented here is available to the scientific community (published on

CDROM by Stahl 1995) and can be used to test the various effects.

In particular calculations of the exact line forming regions (e.g. photosphere including the influence of the stellar wind), have to be carried out for a detailed analysis. First attempts have been made by the author and collaborators using the ISA/WINDSPEC-codes of Alex de Koter & Ivan Hubeny and EMISSEI of Henny Lamers & Jeroen van Gent, and the initial results have been presented by Gäng et al. (1997). Further studies are needed to improve the results obtained in this research project and collaborations in this field are currently in progress.

Chapter 4:   Wind Structure and Mass Loss in LBVs

4.1   Introduction

It has been known for some time that the broad emission line profiles of W-R stars exhibit narrow-line features in emission as well as absorption (e.g. Brown & Richardson 1995). The narrow emission features are likely to be due to regions of locally enhanced densities, indicating clumping and/or asymmetries in the wind structure. These effects have dramatic consequences on the derived wind parameters: including inhomogeneities is an important contribution in the calculation of precise mass-loss rates which might significantly affect the stellar evolution of these massive stars and provide clues whether the winds of LBV stars are driven by radiation pressure alone, or whether other driving mechanisms, such as stellar pulsations and shocks, may be significant.

Several factors indicate that LBV stars too may have irregular or clumpy winds:

- LBVs are known to have variable mass-loss rates and/or to shift in and out of the W-R phase (e.g. AG Car, see Leitherer et al. 1994).

- Infrared observations with the ISO satellite indicate the existence of inhomogeneities in the circumstellar envelope of the LBV-prototype P Cygni (Lamers et al. 1996).

- Finally, coronographic images of LBV nebulae exhibit clumpy substructures (Nota et al. 1995).

Systematic studies of inhomogeneities in spectral lines have been carried out by Moffat & Robert (1992) for W-R stars and by Eversberg et al. (1998) for the Of supergiant ζ Pup where outward moving stochastic substructures were found in the wind lines. In these objects the wind speeds are an order of magnitude higher than in LBVs so inhomogeneities can be found in relatively low-resolution spectra. In LBVs however, we need spectra with a resolution of better than $\sim 10\,\mathrm{km\,s^{-1}}$ (approximately the thermal velocity).

A systematic survey of such observations has so far not been attempted. Consequently we applied for observing time and acquired high-resolution spectra of LBVs to tackle the question of substructures in LBV winds. The quality (i.e. high S/N ratios) of the spectra is equally important to their resolution in order to distinguish real line features from the background noise. These conditions served as constraints for our target selection: we aimed to observe as many LBVs as possible at a given site to get results that might be generalized for all LBVs and required that the objects are bright enough to achieve a S/N ratio of about 100 per spectra with resolutions greater than 50 000.

Note that the plots and discussions in this chapter are "work in progress". We do not attempt to analyze the spectra here or make conclusions about the physical mechanisms and outflow geometries. Rather we present the spectra and discuss the observed line profiles with emphasis on the detected inhomogeneities (in section 4.3). The merit of presenting these high-quality (high-resolution *and* high S/N) spectra in this thesis is to publish the data and make it available as a general reference to the astronomical community.

Initial simple models of the P Cygni spectra have been carried out by the author and collaborators (see Gäng et al. 1997). More sophisticated models, using the "unified" code of Dr. J. Puls, are planned and collaborations with the Munich group around Dr. R. Kudritzki are in progress, but will be presented in a future paper.

4.2   Observations and Instrumentation

The observations for this ultra-high resolution project have been carried out with different instruments on three observing sites. This allowed us to observe most confirmed LBVs brighter than $V \lesssim 11.0$ in the Galaxy and the Large and Small Magellanic Clouds. We aimed to cover the whole optical wavelength range with our spectra and achieve a typical S/N ratio of 100 for a single, well exposed spectrum with a resolving power of at least 50 000. A detailed description of the obtained spectra is presented in following sections for each observing run.

As a constraint we set the maximum exposure time to 1 hour to avoid the excess accumulation of cosmic ray hits and took multiple exposures of the same object. This allowed us to remove cosmics effectively and check for short-term variations in the line profiles (as previously detected for hot stars of various spectral and luminosity classes; e.g. see: Kaufer et al. (1996) for β Ori (B8Iab), Eversberg et al. (1998) for ζ Pup (O4I(n)f) and Moffat & Robert (1992) for W-R stars).

Due to the echelle configuration the cross-dispersed spectra from our observations at UCLES/AAT and CFT/KPNO covered the optical wavelength range almost continuously. For our observations with CES we had to select specific "observing windows" since the long-slit configuration allowed a maximum wavelength range of only ~ 80 Å and a concatenation of about 50 windows to cover the whole optical range is not feasible. We concentrated in this case on the highest Balmer lines and some diagnostic He I, Fe II, Si II and Mg II lines.

4.2.1   CFT/KPNO

The observations were carried out on May 20−22, 1996 with the spectrograph at the Coudé Feed Telescope (CFT) at the Kitt Peak National Observatory (KPNO). We used various gratings and setups to ensure an optimal throughput and the large F3KB–CCD (3072 x 1024, 15 μm pixel) to cover a wide wavelength region. The spectrographic setup resulted in a pixel dispersion of approximately 0.017 Å/pix at 4000 Å and 0.025 Å/pix at 7000 Å. The spectral resolution was measured from the $FWHM$ of the Na D and Ca K / H ISM lines to be R≈ 100 000.

The instrument was not changed during the night to ensure the necessary stability to enable consistent high-quality calibration exposures.

With counts ranging from 3 000 to 40 000 ADU we stayed in the linear range of the CCD response ($\sim$0.1 %). The only exception were the red exposures of α Leo where we reached a maximum countrate of $\sim$60 000 ADU (CCD linearity ca. 1 %).

To obtain an optimal data calibration we collected a series of bias and internal flatfield exposures three times per night (i.e. at the beginning, middle and end) and took Thorium-Argon (ThAr) images about once per hour. We also observed a couple of standard stars to check for the reality of weak features (e.g. by observing fast rotating stars with similar spectral type we got the positions and strengths of telluric lines affecting our spectra). The complete observing log is given in Table 4.1.

4.2.2   UCLES/AAT

The observations at the Anglo-Australian Telescope (AAT) were carried out by Dr. Jessica Chapman on October 3 and 4, 1995, with the University College London Echelle Spectrograph (UCLES) mounted at the 3.9 m telescope[1]. The Tektronix CCD (1024 x 1024 pixel, pixel size: 24 x 24 μm) was used with two

---

[1]The data from additional observations with this instrument in January 1996 could not be utilized: due to a software error the cross disperser was moved at a random time after the initial setup. This resulted in an arbitrary shift in the dispersion

Table 4.1: Observing campaign at CFT/KPNO. The S/N values are taken around: $a : \lambda = 4500\,\text{Å}, b : \lambda = 5400\,\text{Å}, c : \lambda = 6100\,\text{Å}$.

Object	V	Exposures	Date	Spectral range	typ. S/N
α Leo	1.35	4 x 200 sec	May 20, 1996	$3925 - 4665\,\text{Å}$	150^a
		4 x 200 sec	May 21, 1996	$4460 - 5700\,\text{Å}$	190^b
		4 x 200 sec	May 22, 1996	$5413 - 7055\,\text{Å}$	250^c
ρ Leo	3.85	3 x 1000 sec	May 20, 1996	$3925 - 4665\,\text{Å}$	110^a
		3 x 1000 sec	May 21, 1996	$4460 - 5700\,\text{Å}$	135^b
		4 x 1000 sec	May 22, 1996	$5413 - 7055\,\text{Å}$	175^c
τ Her	3.90	2 x 1000 sec	May 20, 1996	$3925 - 4665\,\text{Å}$	90^a
		2 x 1000 sec	May 21, 1996	$4460 - 5700\,\text{Å}$	115^b
		3 x 1000 sec	May 22, 1996	$5413 - 7055\,\text{Å}$	140^c
P Cyg	4.81	7 x 1500 sec	May 20, 1996	$3925 - 4665\,\text{Å}$	60^a
		5 x 1200 sec	May 20, 1996	$3925 - 4665\,\text{Å}$	85^b
		6 x 1500 sec	May 21, 1996	$4460 - 5700\,\text{Å}$	85^b
		4 x 1200 sec	May 21, 1996	$4460 - 5700\,\text{Å}$	85^b
		3 x 1100 sec	May 21, 1996	$4460 - 5700\,\text{Å}$	85^b
		6 x 1500 sec	May 22, 1996	$5413 - 7055\,\text{Å}$	130^c
		3 x 1300 sec	May 22, 1996	$5413 - 7055\,\text{Å}$	130^c
		3 x 1100 sec	May 22, 1996	$5413 - 7055\,\text{Å}$	130^c

gratings (31.6 lines/mm and 79 lines/mm) at three positions (central wavelengths (λ_c): 3949 Å, 5417 Å with grating 31.6 and 5592 Å with grating 79). This setup covered a wavelength range of 3600 Å to 7240 Å with a gap from 4450 Å to 4580 Å. In the red end of the spectrum ($\lambda > 5770$ Å) adjacent echelle orders of the same grating setup did not overlap; however the different free spectral range of the two gratings minimized the resulting gaps in the spectra. For $\lambda \gtrsim 6900$ Å we had only the highest two orders of the 79 lines/mm-grating with large gaps available which showed almost only telluric lines. We therefore confine the discussed wavelength region to $3600 - 6800$ Å.

Both gratings give the same dispersion and differ mainly in the free spectral range. Thus averaging and combining spectra during the data reduction did not affect the spectral resolution.

The intrinsic stability of this instrument is <0.01 pixels (≈ 15 m/s peak to peak) as measured with repeated 1 min exposures over one hour (AAO Observers' Guide, 4th edition (1991), page 74). Returning from a changed grating setting is possible with a typical RMS accuracy of 0.2 pixels.

The linearity of the CCD is better than 1% up to 7300 Å with fringing in the red as the main contributor; the readout is ADC limited to 65535 and never reaches saturation, which occurs at about 450000 electrons/pixel.

The instrumental setup resulted in a pixel dispersion of 0.077 Å/pix at 7200 Å and 0.036 Å/pix at 3600 Å which yields a resolving power of R$\approx 50\,000$ as measured from the $FWHM$ of typical strong ThAr comparison lines.

---

direction and moved the desired observing window out of the efficient region of the CCD (as the echelle response is a strong function of wavelength offset from the center of the free spectral range, the S/N of the data dropped steeply). We are thus not including those spectra in this observing sample.

Table 4.2: Observing campaign at UCLES/AAT. The S/N values are taken
around the center of the corresponding wavelength region (i.e. λ_c).

Object	V	Exposures	Date	λ_c	Spectral range	typ. S/N
R 71	9.8	3 x 480 sec	Oct 3, 1995	3949 Å	3600 – 4450 Å	20
		3 x 480 sec	Oct 3, 1995	5417 Å	4580 – 6950 Å	25
		2 x 480 sec	Oct 3, 1995	5592 Å	4740 – 7240 Å	30
HD 160529	6.7	3 x 120 sec	Oct 4, 1995	3949 Å	3600 – 4450 Å	40
		2 x 120 sec	Oct 4, 1995	5417 Å	4580 – 6950 Å	130
		2 x 60 sec	Oct 4, 1995	5417 Å	4580 – 6950 Å	90
		4 x 60 sec	Oct 4, 1995	5592 Å	4740 – 7240 Å	100
HD 168607	8.3	3 x 200 sec	Oct 4, 1995	3949 Å	3600 – 4450 Å	25
		6 x 100 sec	Oct 4, 1995	5417 Å	4580 – 6950 Å	65
		2 x 200 sec	Oct 4, 1995	5592 Å	4740 – 7240 Å	100
		3 x 100 sec	Oct 4, 1995	5592 Å	4740 – 7240 Å	75
HD 168625	8.4	5 x 180 sec	Oct 4, 1995	3949 Å	3600 – 4450 Å	25
		3 x 200 sec	Oct 4, 1995	3949 Å	3600 – 4450 Å	20
		3 x 200 sec	Oct 4, 1995	5417 Å	4580 – 6950 Å	75
		4 x 120 sec	Oct 4, 1995	5592 Å	4740 – 7240 Å	65
R 40	10.7	3 x 600 sec	Oct 4, 1995	3949 Å	3600 – 4450 Å	40
		3 x 600 sec	Oct 4, 1995	5417 Å	4580 – 6950 Å	60
		4 x 600 sec	Oct 4, 1995	5592 Å	4740 – 7240 Å	70
HD 5980	9.3	3 x 600 sec	Oct 4, 1995	3949 Å	3600 – 4450 Å	50
		3 x 600 sec	Oct 4, 1995	5417 Å	4580 – 6950 Å	40
		3 x 600 sec	Oct 4, 1995	5592 Å	4740 – 7240 Å	30
R 81	10.4	4 x 600 sec	Oct 4, 1995	3949 Å	3600 – 4450 Å	45
		4 x 600 sec	Oct 4, 1995	5417 Å	4580 – 6950 Å	60
		3 x 600 sec	Oct 4, 1995	5592 Å	4740 – 7240 Å	60
S Dor	10.0	2 x 720 sec	Oct 4, 1995	3949 Å	3600 – 4450 Å	55
		1 x 720 sec	Oct 4, 1995	5417 Å	4580 – 6950 Å	95
		1 x 285 sec	Oct 4, 1995	5417 Å	4580 – 6950 Å	55
		2 x 600 sec	Oct 4, 1995	5592 Å	4740 – 7240 Å	90

Bias frames, flatfield exposures of quartz lamps and Thorium-Argon calibration images were taken at least once per hour and every time the grating setting was changed.

The complete observing log is given in Table 4.2.

4.2.3   CES/CAT

The observations were carried out on April 5 – 12, 1996 via remote control from the ESO headquarters in Garching/Germany. The spectra were obtained with the Coudé Echelle Spectrometer (CES) which is permanently fed by the Coudé Auxiliary Telescope (CAT) at the ESO/La Silla observing site.

We used the long camera and the ESO-CCD #38 (Loral/Lesser) with 2688 x 512 pixel, pixel size: 15 x 15 μm (corresponding to 0.56 x 0.45 arcsec) which is the best available instrumental setup for optimizing throughput at spectral resolutions under 75 000. To maintain a high efficiency over the whole

Table 4.3: Observing campaign at CES/CAT. The S/N values are taken from the respective 4.th-band spectra (see multiband description on page 95) at the continuum around the center of the corresponding wavelength region.

Object	V	Exposures	Date	Spectral range	typ. S/N
HD 94491	6.2	2 x 300 sec	Apr 05, 1996	6523 – 6602 Å	250
		2 x 300 sec	Apr 06, 1996	6324 – 6392 Å	240
		2 x 300 sec	Apr 07, 1996	4835 – 4886 Å	70
		3 x 300 sec	Apr 08, 1996	4456 – 4504 Å	70
		2 x 300 sec	Apr 09, 1996	4320 – 4369 Å	80
		2 x 300 sec	Apr 10, 1996	4320 – 4369 Å	70
		2 x 300 sec	Apr 11, 1996	4455 – 4503 Å	55
		2 x 300 sec	Apr 12, 1996	6324 – 6392 Å	250
HD 80077	7.6	3 x 1800 sec	Apr 05, 1996	6523 – 6602 Å	150
		3 x 1800 sec	Apr 06, 1996	6324 – 6392 Å	140
		3 x 1800 sec	Apr 07, 1996	4835 – 4886 Å	75
		4 x 1800 sec	Apr 08, 1996	4456 – 4504 Å	55
		4 x 2400 sec	Apr 09, 1996	4320 – 4369 Å	70
HR Car	8.6	4 x 1800 sec	Apr 05, 1996	6523 – 6602 Å	120
		4 x 2400 sec	Apr 06, 1996	6324 – 6392 Å	115
		4 x 2400 sec	Apr 07, 1996	4835 – 4886 Å	70
		4 x 2400 sec	Apr 08, 1996	4456 – 4504 Å	60
		4 x 2400 sec	Apr 09, 1996	4320 – 4369 Å	70
		4 x 2400 sec	Apr 10, 1996	4320 – 4369 Å	65
AG Car	6.9	4 x 600 sec	Apr 05, 1996	6523 – 6602 Å	120
		3 x 1200 sec	Apr 06, 1996	6324 – 6392 Å	135
		3 x 1200 sec	Apr 07, 1996	4835 – 4886 Å	90
		4 x 2300 sec	Apr 08, 1996	4456 – 4504 Å	100
		4 x 1800 sec	Apr 09, 1996	4320 – 4369 Å	125
η Car	6.2	4 x 1300 sec	Apr 10, 1996	4320 – 4369 Å	120
		3 x 1300 sec	Apr 11, 1996	4456 – 4504 Å	80
		4 x 1300 sec	Apr 11, 1996	4835 – 4886 Å	100
		5 x 600 sec	Apr 12, 1996	6324 – 6392 Å	110
		10 x 300 sec	Apr 12, 1996	6523 – 6602 Å	200
HD 326823	9.0	3 x 1800 sec	Apr 05, 1996	6523 – 6602 Å	65
		2 x 2400 sec	Apr 06, 1996	6324 – 6392 Å	70
		2 x 3300 sec	Apr 06, 1996	6324 – 6392 Å	65
		4 x 2400 sec	Apr 07, 1996	4835 – 4886 Å	45
		5 x 2400 sec	Apr 10, 1996	4320 – 4369 Å	40
		2 x 2400 sec	Apr 11, 1996	4455 – 4503 Å	40
HD 316285	9.1	4 x 3300 sec	Apr 10, 1996	4320 – 4369 Å	30
		3 x 3300 sec	Apr 11, 1996	4455 – 4503 Å	25
		3 x 1800 sec	Apr 11, 1996	4835 – 4886 Å	30
		4 x 2400 sec	Apr 12, 1996	6324 – 6392 Å	75
		4 x 3300 sec	Apr 12, 1996	6523 – 6602 Å	110
HD 169454	6.6	3 x 1300 sec	Apr 05, 1996	6523 – 6602 Å	130
		3 x 1300 sec	Apr 06, 1996	6324 – 6392 Å	120
		3 x 1200 sec	Apr 07, 1996	4835 – 4886 Å	90
		4 x 2300 sec	Apr 08, 1996	4456 – 4504 Å	90
		4 x 1200 sec	Apr 09, 1996	4320 – 4369 Å	80

observed wavelength region we selected the blue or red observing "path" at the crosspoint of 5200 Å (as recommended). The paths were never changed during the night to minimize the technical overhead time. Except for the last two nights the observed wavelength ranges were also kept constant during the night to maintain a high stability of the instrument and facilitate the wavelength calibration.

With relatively short exposure times of less than 40 min we generally avoided the A/D saturation of the CCD. The linearity of this chip is better than 1 % up to a limit of approximately 100 000 electrons/pixel. This limit was never reached in the continuum of our observed spectra (except the saturated exposures of η Car which were taken out of the sample) but could be exceeded sometimes in the strong emission lines (i.e. in Hα). We will consider this when we discuss the observed spectra individually later.

The instrumental setup yields a pixel dispersion of 0.029 Å/pix at 6530 Å and 0.019 Å/pix at 4330 Å which resulted in a resolving power of R$\approx$ 60 000 as measured from the *FWHM* of a sample of strong ThAr lines.

To obtain an optimal data calibration we collected a series of bias and internal flatfield exposures in the beginning and end of the night and took a few Thorium-Argon (ThAr) images about once per hour. We also observed a standard star to check for the reality of weak features (e.g. by observing fast rotating stars with similar spectral type we get the positions and strengths of telluric lines affecting our spectra). The complete observing log is given in Table 4.3.

4.3   Data Reduction

To reach the goal of this project and deliver excellent spectra with very high resolution *and* simultaneously covering a wide wavelength range we sometimes operated at the technical limit of the observing instruments. Some reduction steps of the resulting data were thus quite challenging and a considerable effort was spent to achieve the best possible wavelength calibration and continuum determination. To facilitate similar projects in the future we give here a detailed description of the applied data reduction procedures.

All spectra have been reduced with standard IRAF-routines for coudé and echelle spectra. The first steps to remove the "detector signature" are always the same: trim the two-dimensional CCD image to remove the overscan region and include only "good data", remove DC-offset (i.e. subtract the bias level) and correct pixel-to-pixel gain variations using flatfield (FF) images (i.e. divide the object frames by the normalized flatfield exposures).

It is important to check that the flatfield images match the illumination function of the objects along the spatial direction – a mismatch can produce artificial effects in the data rather than improving it! For our data at the AAT a significant misalignment of the illuminated FF and object orders was detected and consequently the flatfielding step was not carried out. Fortunately due to the excellent characteristics of the CCD (linearity better than 1 % and very good cosmetics) this has no significant influence on the resulting flux measurements.

4.3.1   Cross-dispersed (Echelle) Spectra

We describe here the extraction, calibration and normalization steps that were applied to the cross-dispersed images of our observations at CFT/KPNO. The deviations from this routine which were required for the UCLES-data are described at the end of this section.

CFT/KPNO-Spectra

The combination of the CCD response and echelle blaze function produced a complicated instrumental profile in these observations which can ordinarily only be corrected with a high order polynominal or spline fit. This would in turn also remove the shallow broad wings of the emission lines in our P Cygni spectra. We decided therefore to correct the instrumental profile in two steps:

1. The blaze function was corrected with a second-order spline fit in the two-dimensional wavelength-order frame. Merging the orders at this state would lead to ripples with a width of ca. 5 times the width of a single echelle order and amplitudes of roughly 15 % of the continuum level as well as artificial peaks at the positions of the order-overlaps due to the steep blaze-gradient at the order edges.

2. These effects can be corrected efficiently in the single order frame with a low-order polynominal fit (3. order chebyshev function), leaving well rectified spectral pieces which can then be merged into a continuous spectrum.

For α Leo we used a high-order spline function for the continuum fit in step 2 thus removing essentially all broad stellar absorption lines (v_{rot}=329 km s^{-1}). This left only non-stellar narrow features (e.g. ISM and telluric lines) in its spectrum which we used to verify the detected narrow line features of the P Cygni spectrum.

The individual reduction steps are given in the following outline:

- The background subtraction and wavelength calibration was done with *doecslit*. We performed two-dimensional spline fits between the orders to determine the background (e.g. the scattered light) and used the optimal extraction algorithm to weight the spectral orders and remove cosmic rays. The dispersion was determined by interpolating the wavelengths of the closest ThAr exposures.

- The blazefunction was corrected by a two-dimensional second-order fit of a cubic spline function in the wavelength-order frame using *imsurfit*. The relatively large residuals at the order edges were removed by cutting off ~ 2 Å on either side of the image frames, still leaving ample overlapping regions.

- The orders were then normalized separately (with *continuum*) using low-order $(3-4)$ chebyshev-function fits at preset continuum windows. In a few cases where line contributions were visible all across the spectral order (e.g. Hα, Hβ) or when broad lines existed at the edge of the order the adjacent orders were merged together before setting the continuum windows. In these cases the blaze-correction produced well conformed overlapping regions so that the merger did not affect the line profiles.

- The now well-rectified spectral orders (especially at the edges) were then combined into a single continuous spectrum (with *scombine*). We individually trimmed the orders before the merging and applied two ramp functions to weight the spectra in the overlapping regions to make sure the line profiles were not affected by this reduction step.

- Finally the spectra were scaled to a heliocentric wavelength range using the middle of the exposure time with *dopcor*.

Some spectral lines (e.g. helium and hydrogen) have extremely broad emission wings (up to $\sim$100 Å for Hα) extending far beyond the typical width of one echelle order (60 – 90 Å depending on wavelength). Our treatment of this problem (see above) makes the continuum-determination somewhat more uncertain at these locations.

By comparing the overlapping regions of consecutive orders we estimate an average flux uncertainty in our P Cygni spectra of about 1 % with occasional peaks of about 5 % around the broad lines of Hα, Hβ and the strongest He II lines.

UCLES/AAT-Spectra

In our UCLES/AAT-spectra we normalized each order separately via division of a three-dimensional spline fit. The parameter (sample range, order of fit function, ...) for corresponding orders at multiple observations of the same objects were kept constant.

This simple approach leads to the same results as the more sophisticated method above if no extremely strong or broad lines are found in the spectrum and adjacent orders overlap with each other which is the case in the red range of our UCLES-spectra. In the blue range where the first statement is not fulfilled our orders also do not overlap anymore. We did not have a standard star spectrum available which could have helped with the continuum determination (see next section). Fortunately the broadest emission lines (Hα, Hβ) always fell in the center of the corresponding order so the line profiles were not affected by the gaps between the orders[2].

In the final step we merged all normalized orders back to a single spectrum and averaged them to improve the S/N ratio in a mean spectrum for each object.

The flux accuracy as measured from the difference of adjacent orders is generally better than 1 % except around the broadest Balmer lines (usually only Hα and Hβ) and the strongest He II lines where we estimate a continuum level uncertainty of $\sim$10 % due to the applied simple normalization method.

4.3.2   Long-slit (Coudé) Spectra

The next reduction steps follow the same principles as in the case of echelle spectra but exclude the specific routines dealing with the cross-dispersed data format. The following extraction and calibration steps were applied to the CES/CAT data:

- *Find spectrum on CCD.* This was done automatically by looking for the strongest peak in the spatial direction of the CCD frame. In a few cases where a strong ghost was present on the chip we interactively assigned the correct aperture.

- *Define extraction and background window.* The data extraction windows were set to a flexible width with the lower and upper aperture limits given at 5 % of the peak intensity. The background region was defined in a fixed region to the left and right of the center of the spatial profile where no ghosts were detectable.

- *Trace the center of the spatial profile as a function of the dispersion axis.* We used a low-order three-dimensional spline fit for the tracing; the typically achieved fit quality had a standard deviation of $\sim$0.2 pixel (i.e. the light loss is negligible for a typical aperture width of 20 – 30 pixel).

---

[2]The only exception are the spectra of HD 5980. Its emission lines during our observations were so broad and strong that they extended over multiple orders. The final merging to form a continuous spectrum produced artificial steps in the line profiles. We did not smooth these profiles any further since this would introduce subjective errors which would not improve the spectra.

- *Sum the spectrum within the extraction window.* We used the optimal extraction scheme with the cleaning option to extract the spectra. This method creates a noise model of the data, performs a variance weighted extraction and removes strongly deviating points (i.e. cosmic rays) from the data. However the noise model is not reliable when the counts reach the CCD-saturation limit. In the few cases when that happened we used the simple sum of pixels to extract the spectra[3].

- *Wavelength calibration.* The dispersion was determined by interpolating the wavelengths of the closest ThAr exposures. The dispersion function was determined by a three-dimensional spline fit (typ. order: $7-10$) with a RMS (root-mean-square) of $0.0010-0.0017$ (max. $\delta\lambda < 0.008$ Å, max. $\delta v < 0.3\,\mathrm{km\,s^{-1}}$). Figure 4.1 shows the high accuracy of our data reduction which allows us to take full advantage of our high resolution spectral observations.

In the normalization step we deviated from the previously developed routine for cross-dispersed data to rectify the spectra: since the instrumental constraints of CES do not allow observation of a broad wavelength region we had to concentrate on a sample of selected lines which were observed in high resolution. The maximum width of a λ-window in our setup was approximately 80 Å (around Hα).

Due to this small range it is hard to determine the correct continuum curve from the LBV-spectrum itself, especially around the strong Balmer lines where broad electron scattering wings complicate the situation even further. Also none of our individual observing ranges overlapped with another so we could not create a broad range by merging them.

We thus decided to use the continuum fit of our observed standard star HD 94491 as reference for all objects observed in the same night with identical instrumental setup.

Since HD 94491 has no emission lines (and thus also no electron scattering wings) and if there are no other irregularities in the instrument or from the star (which we can only assume here) its spectral continuum should be determined by its temperature and the instrumental response function alone. Its spectral curve after the wavelength calibration could be fitted very well at all observed wavelength regions.

To check these statements we compared the spectrum of a flatfield lamp (which is a very good approximation of a blackbody radiation) with the reference continuum fit. The good agreement of their spectral curves supports the assumption that a single temperature Planck function can be used to model the continuum of the standard star. In the case where HD 94491 had broad Balmer lines in its spectrum ($v\sin i \approx 183\,\mathrm{km\,s^{-1}}$) we used the continuum fit of HD 80077 to double-check the reference continuum curve.

HD 80077 is the most "well-behaved" (i.e. its mass-loss rate and variability are very low with respect to its luminosity) star of our sample and has rather weak emission lines (compared to the other LBVs) and thus also only weak electron scattering wings (if at all). This can be corrected by sampling the continuum only in the regions outside the maximum width of the electron scattering wings. The electron scattering wings were estimated via: $v_e = \sqrt{\frac{2kT}{m_e}}$ with the Boltzmann constant $k = 1.380\ 10^{-16}\frac{\mathrm{g\,cm^2}}{\mathrm{s^2\,K}}$ and the electron mass $m_e = 9.109\ 10^{-28}$ g.

Using a rather high temperature of 30 000 K we get $v_e \approx 950\,\mathrm{km\,s^{-1}}$; we thus sampled regions more than $1000\,\mathrm{km\,s^{-1}}$ away from the strong emission lines to account for the possible effects of electron scattering

---

[3]IRAF gives the option to produce a multidimensional spectrum where the variance-weighted, cleaned spectrum is put in the first data-band, the unweighted, uncleaned spectrum (simple sum) in the second band, the sky/background spectrum in the third band and the sigma spectrum (noise) in the fourth band. We activated this feature and checked its S/N values by calculating the square root of the pre-normalized pixel-counts. Since the noise in our data is dominated by Poisson statistics the two methods agreed usually quite well.
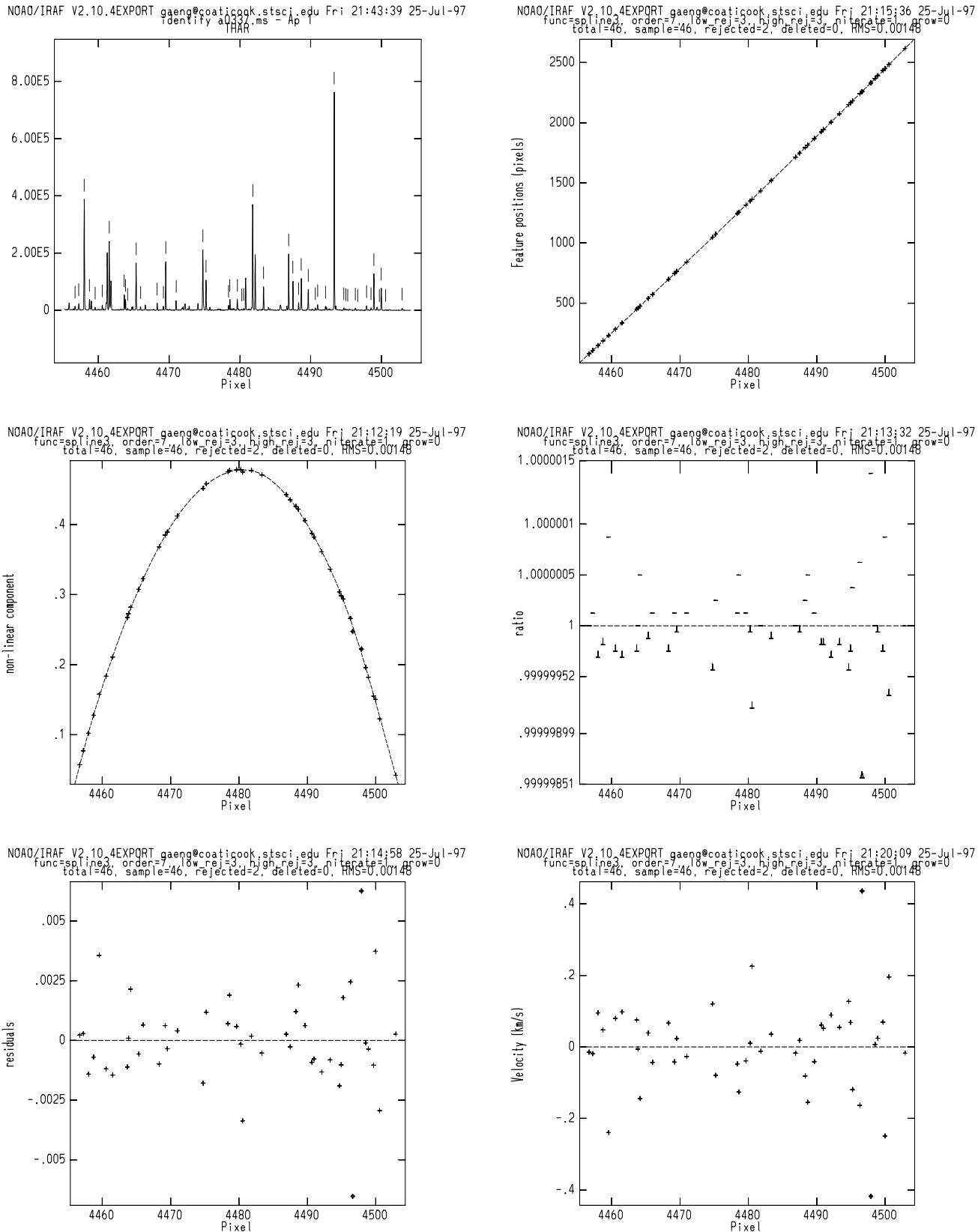
Figure 4.1: The plot in the upper left shows an observed ThAr spectrum around 4480 Å. The marked spectral lines were found in the identification database and used for the dispersion solution. The non-linear part of the dispersion solution is well behaved (middle left) and the residuals are very low (bottom plots).
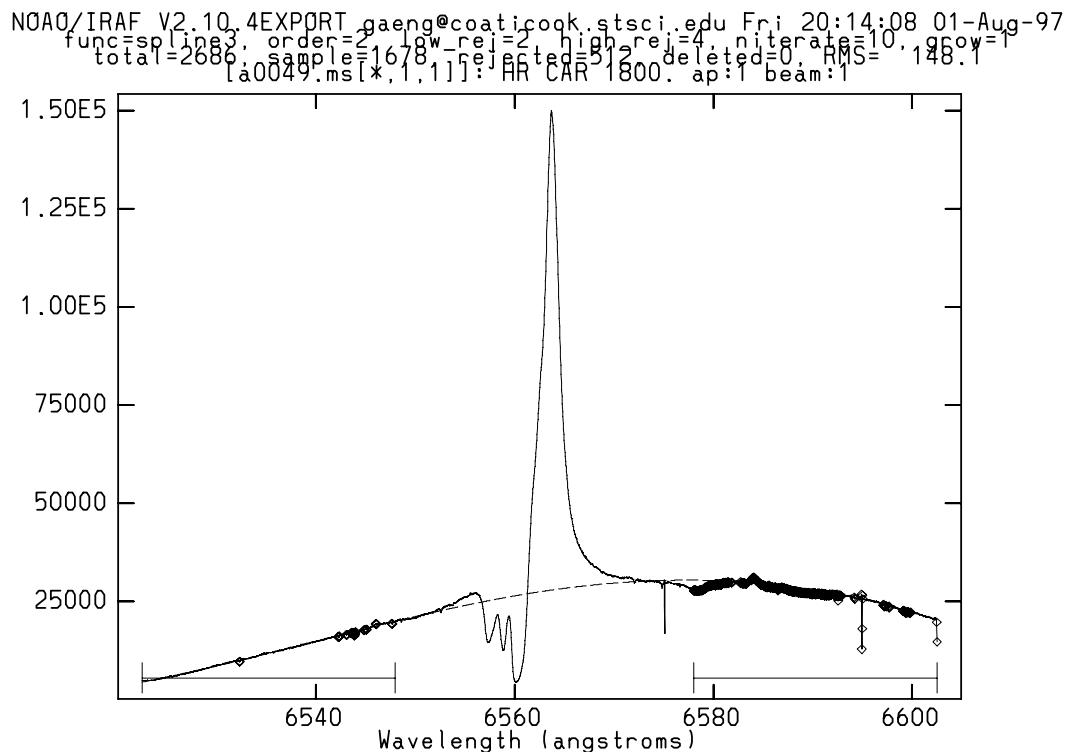
Figure 4.2: "Direct Continuum Fit" – spectrum of HR Car with continuum fit (2. order spline, dashed line) from preselected continuum windows (±15 Å away from Hα). Diamonds mark points rejected from the fit.

wings on the continuum.

Next we created a synthetic blackbody spectrum (with the task *mk1dspec* in IRAF) with a temperature of 15 400 K corresponding to a spectral type of B 5 V for HD 94491 (18 500 K → B 2 I for HD 80077)[4] in the respective wavelength regions. Dividing the blackbody spectrum by the reference continuum extracts the instrumental response function. Then we just had to multiply all object spectra with the response function to correct for the instrumental profile. Since our reference continuum fit was not flux calibrated we still had to normalize the spectra to unity which we did by dividing each spectrum with a second-order chebychev function. This correction was basically a constant shift and thus did not affect the individual line profiles.

This procedure is justified since the CCD is linear in the corresponding region (linearity better than 1 %, see above) and the temperature of the standard star could be accurately accounted for[5].

The superiority of our chosen procedure lies in the reduced user interaction which always introduces subjective decisions. This is well illustrated in Figures 4.2 and 4.3:

Figure 4.2 shows the spectrum of HR Car after the wavelength calibration step with a continuum fit (dashed line) that can be obtained by fitting the spectral curve in windows larger than ±15 Å away from Hα. In Figure 4.3 we have overplotted the normalized spectra of HR Car from this "direct" continuum

---

[4]The spectral type was taken from the Bright Star Catalogues Supplement for HD 94491 and from Carpay et al. (1989) for HD 80077; the corresponding temperatures are from Landolt-Börnstein, Volume 2b, Group VI, page 453.

[5]The used temperature of 15 400 K was taken as a typical value of a B 5 main sequence star. Even inaccuracies of a few thousand Kelvin would not change the Planck function very much in our wavelength regions since its peak is in the UV range around 2 000 Å and we observe in the optical wavelength region in the Rayleigh-Jeans part of the spectrum where the blackbody function has only a small gradient (see section on flux accuracies on page 99 for details).
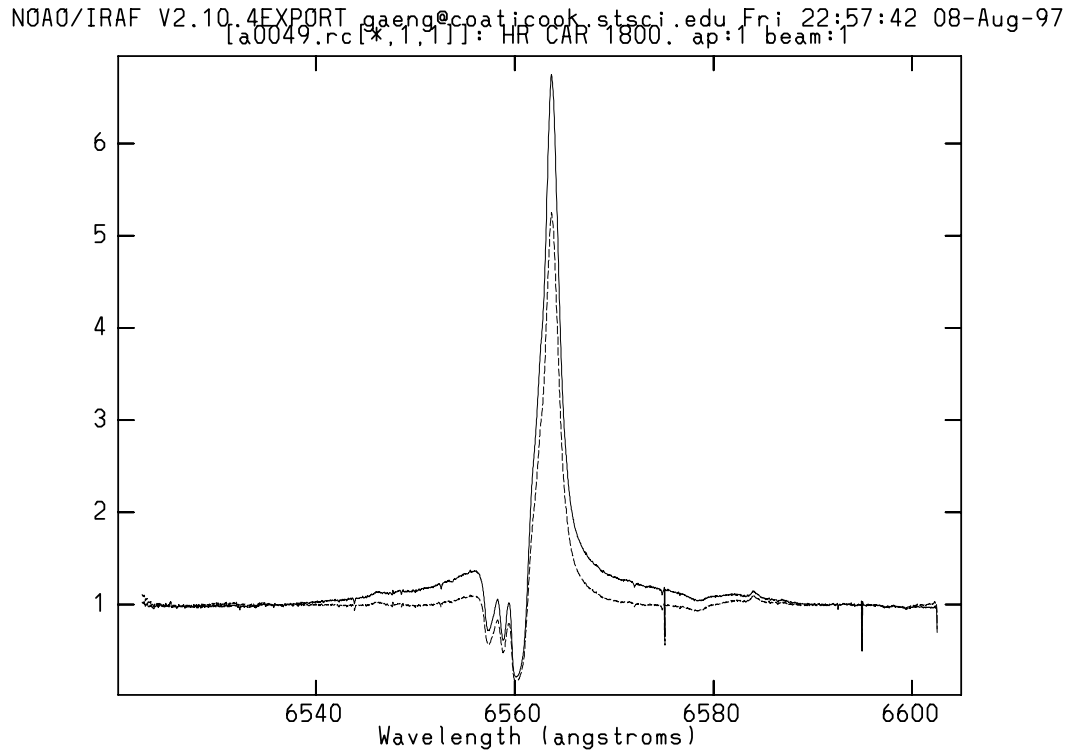
Figure 4.3: Normalized Spectra of HR Car, solid line: "response function" normalization, dashed line: "direct continuum fit" normalization.

fit (dashed) and after the normalization with the above described response function method.

The normalization from the "direct" fit (which seems quite reasonable at the first look) leads to a significant reduction of the $H\alpha$-emission strength and affects the whole line profile. Also the strength of the surrounding electron scattering wings is greatly suppressed. Modeling this line profile would result in inaccurate stellar parameters. In the case where no broad emission wings exist in the observed spectrum window and the continuum is easily detectable, the two methods lead to very similar results.

In the last steps we adjusted the wavelength scale to the heliocentric system and combined the corresponding object spectra (i.e. averaging the spectra using the mode as weight) to improve the S/N ratio. Stronger "cosmetic" defects arising from bad pixel columns in the CCD were also corrected during this time – almost no cosmic peaks could be detected, i.e. they were efficiently removed with the cleaning process described on page 95.

Flux Accuracy

The flux accuracy is determined by the detector linearity, the uncertainty of the temperature of the star used as reference for the continuum fits and the errors made by the fitting of the continuum itself. We estimated the following contributions to the total flux uncertainty:

- CCD linearity: $\leq 1\%$

- temperature: $\leq 0.5\%$

- continuum fit: $\sim 0.5-9.0\%$

The CCD linearity was taken from the CES/CAT operating manuals or the respective WWW pages (`http://www.eso.org/odt/cat_cesllr_38/linearity.html`).

The temperature uncertainty was estimated via the spectral type of HD 94491: it is noted as B 5 V ($\rightarrow T = 15\,400$ K) in the Bright Star Catalog Supplement and as B 3 IV/ V ($\rightarrow T \lesssim 18\,700$ K) in the SIMBAD archives. We assigned the two corresponding temperatures (table from Landolt-Börnstein, Volume 2b, Group VI, page 453) as the uncertainty levels and got the percentage value by comparing the corresponding Planck functions in the respective wavelength regions. As expected (see footnote on page 97) the difference is quite small since we operate in the rather flat Rayleigh-Jeans region longward of the maximum of the Planck function and in a narrow wavelength window.

The errors made by the fitting are the most substantial ones and, due to the involved interactive steps of choosing the "right" fitting function order and the spectral ranges, also very subjective. We estimated the errors here by comparing the temperature corrected fits of HD 94491 and HD 80077. Usually these two curves agree to within less than ∼0.5 % but reach a maximum difference of ∼9 % at the broad Balmer lines where the HD 94491-fit gets unreliable. The highly diverging continuum fits at the edges of the CCD were eliminated by cutting off 1 – 3 Å on either side of the observed spectral range.

In summary we estimate the average flux uncertainty of the CES spectra to be less than 2 % with occasional peaks of about 10 % around the broad lines of Hα and Hβ.

4.4 Spectral Characteristics of LBVs

In this section we describe the spectral characteristics of the mean optical spectra for each object with emphasis on detected substructures in the stellar lines.

None of the LBVs showed significant variations (i.e. larger than the uncertainties in the flux determination) in their spectra during our short snap-shot series (our longest series was four times 55 min exposures of HD 316285, see Table 4.3). Thus averaging the spectra only improved the signal-to-noise (S/N) ratios of the resulting mean spectrum without smearing out spectral features. This of course does not mean that the stars are not variable on longer time scales; we can only conclude that *during our observations the LBVs did not show any spectral variability greater than about 2 % on time scales of minutes to hours.*

The most prominent spectral features deviating from the shape of the general line profiles are marked by dashed vertical lines in the plots and are emphasized in the discussions. We restricted the marks to a maximum of six lines per figure so that the plots remained clear. Note that even the averaged spectra are sometimes not of sufficient quality to reliably detect and resolve all possible subfeatures and distinguish them from line blends or noise.

Except when noted differently, the zoomed line plots were created from the heliocentric spectra and were transformed into velocity space centered at the rest wavelength of the chosen lines (annotated are the element name, ionization state and rounded laboratory rest wavelength for each specific spectral line). Line blends (most notably Hε and Ca H) can thus be distinguished in the v-space plots. We always include all observed Balmer lines and the dominant helium lines in the plots as these lines are usually used for modeling to derive stellar parameters. We also plot the sodium and calcium lines when available, and sort all diagnostic lines in the plots by decreasing velocity to provide a rough measure of the line-forming regions in the LBV-winds.

Since the spectrum of P Cygni has the highest quality (i.e. highest resolution and S/N ratio) and covers the widest wavelength region and because this star often serves as prototype for analogies with other LBVs we concentrate on the detailed discussion of its spectrum (in particular in section 4.5) and then describe the remaining 15 object spectra.

4.4.1   P Cygni

Probably the most detailed analysis of P Cygni spectra has been carried out by Najarro (1995) but the star has been studied extensively by many scientists over the years. However, there are still open questions in interpreting observations, e.g.:

- Scuderi et al. (1994) found that the wind of P Cygni is fairly homogeneous: by fitting models to the Hα line the authors find the same results for the mass-loss rates by modeling the optical depth of the Hα line (proportional to the square of the density) as well for the electron scattering wings (linearly dependent on the density). The asymmetric distributions of clumps as detected in coronographic images of the P Cygni nebula (see e.g. Nota et al. 1995) are in contrast to this result. Furthermore the existence of inhomogeneities in the circumstellar envelope of P Cygni is also supported by recently obtained infrared observations with ISO (Lamers et al. 1996). This leads to contrary pictures of the physical conditions in P Cygni's extended atmosphere.

- The many observed forbidden lines in the spectrum of P Cygni probe the physical conditions of the stellar outflows at large distances from the star ($R \gtrsim 100\,\mathrm{R}_*$). In a recent paper, Israelian (1995) calculated a grid of theoretical synthetic spectra for P Cygni showing that line blending can mimic the complex [Fe II] line structure. He challenged previous interpretations of these line profiles as indications for inhomogeneities in the stellar wind.

- Markova (1994) reported line splitting and DACs in their P Cygni spectra but these features were not seen in the spectra of Stahl et al. (1993). This contradictory result could be due to the lower resolution of the spectra of Stahl et al. (1993) or a time dependence on the occurrence of the narrow features, but it is also possible that some of the structures reported by Markova (1994) are due to photographic noise (Markova's spectra had a higher resolution but a much lower S/N ratio than the typical spectra of Stahl et al.).

Our high-resolution, high S/N spectra of P Cygni should contribute to the understanding and solution of some of the above mentioned problem areas.

We have used the averaged spectrum of P Cygni as published by Stahl et al. (1993) to compare with our observations. Both spectra have very high S/N ratios (Stahl et al: $\sim$2000, our data: $\sim$450) but our data has a resolution that is about a factor 8 higher than the one of Stahl et al. (1993). In our plots we have included the data of Stahl et al. as small circles for some selected lines and a smoothed spectrum of our data that has a similar resolution of $\sim$ 12 000. It is clear that the lower resolution smears out the detailed substructures of the observed lines (see left plots of Figure 4.4). However, it is also possible that Stahl's spectrum "lost" some fine line features due to the averaging of the spectra which are variable on time scales as short as a few days but not on time scales of minutes to hours so that our observations are not influenced by this effect.

We have found previously undetected wiggles in some line profiles: most notably the Hα, He I λ5015, Na D and Ca H/K lines, which are visible in each individual spectrum. The detected features were checked for telluric lines (by comparing the spectra with that of the fast rotator α Leo) and pixel-to-pixel variations on the CCD as well as effects from the merging the orders. The wiggles seen in the Hα and some helium lines can be associated with telluric features. The helium features that are not identified with telluric lines do not have corresponding counterparts in the other helium lines so we assume that they are due to line blends from other stellar lines (see top plots of Figure 4.4). The Na I and Ca II lines, however, exhibit features that appear at the same velocity in all lines and are not associated with telluric lines (note that the high velocity features around $150-230\,\mathrm{km\,s^{-1}}$ show corresponding absorption in the modified α Leo-spectrum).
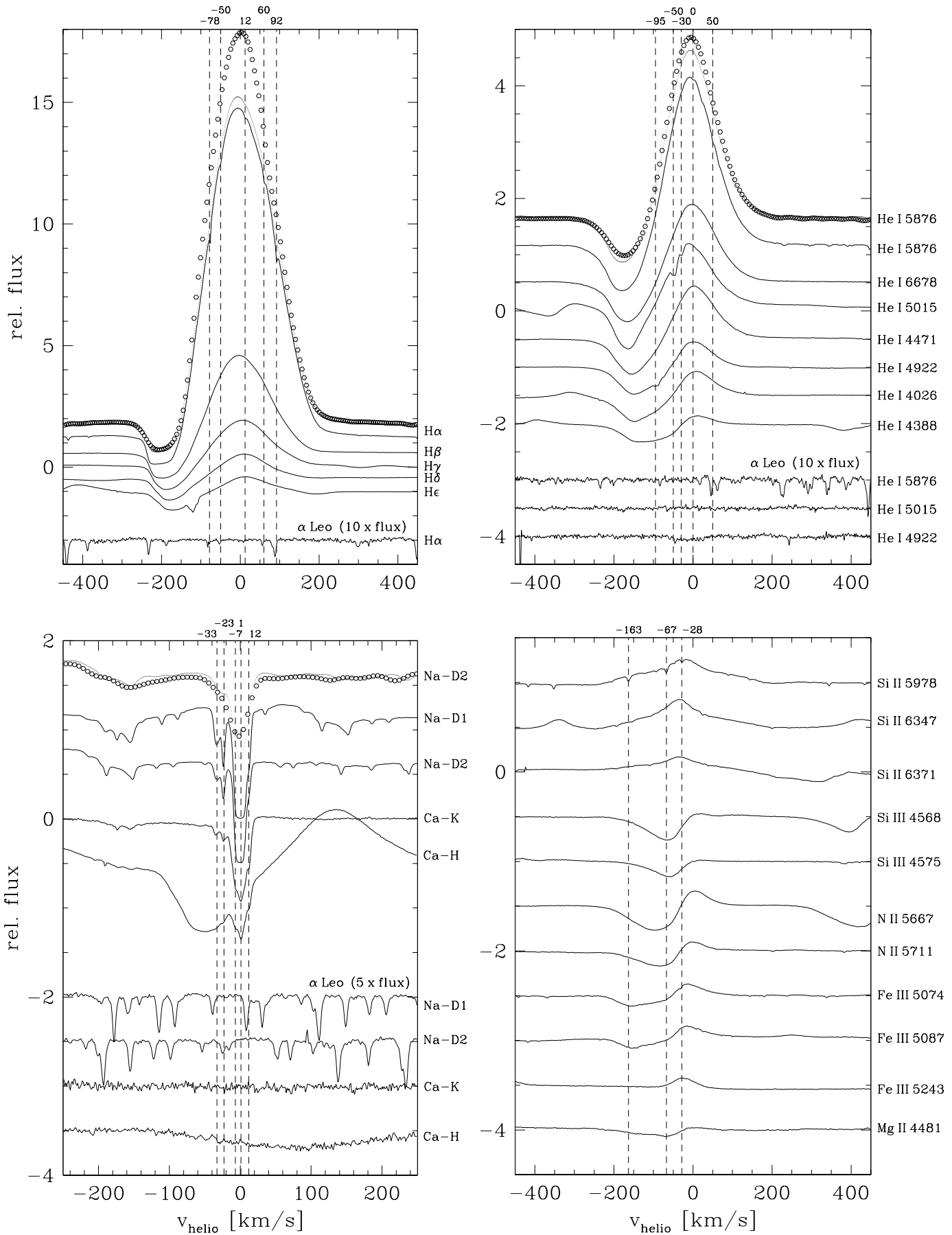
Figure 4.4: Selected line profiles of P Cygni in heliocentric velocity space. Successive spectral lines shifted by −0.5 dex in y are identified on the right side of the plots. The top numbers annotate spectral line inhomogeneities.
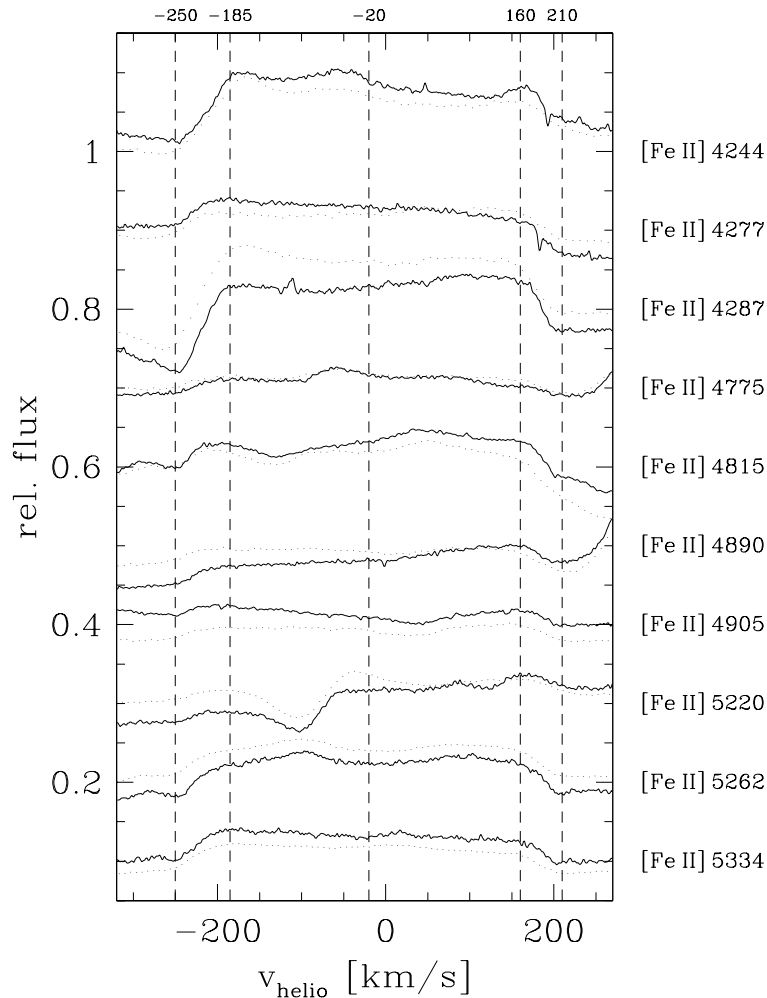
Figure 4.5: Selected forbidden emission lines (compare with Israelian 1995 and Stahl et al. 1991 a, 1993). The dotted spectra are from Stahl et al. (1993). Annotated are the approximate edges of the forbidden lines (i.e. the limits: –250, 210 km s^{-1} and the flat plateaus: –185, 160 km s^{-1}). The line center of –20 km s^{-1} is calculated from the mean of the line limits (i.e.: (210–250)/2).

In particular the absorption features around –33, –23, –7, 1 and 12 km s^{-1} seem significant. We note again that the lower resolution spectra are not sufficient to detect these features.

The problem now consists of separating the stellar contributions of the lines from the ISM absorptions. A detailed study of the line profiles might resolve some problems (see e.g. Welty et al. 1994) but probably the best way to distinguish the contributions is to study their temporal behavior. Initial examinations of spectral time series of P Cygni using data from Stahl et al. (1995) indicate considerable variations of the Na D lines on time scales of weeks to months. However for clear conclusions we might need to search for even faster variations as recent STIS observations indicate that ISM clouds might be variable on time scales of months (Leitherer, private communication).

Other atmospheric lines do not show significant substructures – the few features of the Si II lines are most likely due to line blends as well. Note that most atmospheric lines exhibit the typical P Cygni profile but that the Si II lines appear only in emission with a broad, triangular-shaped line profile. The general line profiles of our spectra and the observations of Stahl et al. (1993) are thus very similar – the main difference lies in the fine structure of the line profiles. The fact that the spectra remain fairly constant is evidence that P Cygni's atmospheric condition does not change much, confirming that the star is currently in a long quiescent phase.

In Figure 4.5 we compare our averaged spectrum with that of Stahl et al. (1993) for a sample of detected [Fe II] lines. Even with our superior resolution it is not possible to further resolve the line profiles. The wiggles on top of the line-plateaus could thus be formed by either blobs or clumps but are more likely effects of line blending as suggested by Israelian (1995).

4.4.2 Observations at UCLES/AAT

HD 160529

The Balmer lines show the usual progression towards lower velocities for the higher Balmer lines. Hα and Hβ have strong emission and wide shallow wings. Around $v_{\text{helio}} = 15\,\text{km}\,\text{s}^{-1}$ the Hδ and Hε lines exhibit a weak narrow absorption feature that is faintly visible in Hγ and H 8 as well. In higher and lower Balmer lines the feature is not visible but that might be due to a suppression by the strong emission parts in Hα and Hβ and the gradual weaking of the higher Balmer lines. An alternative explanation would be that this line-structure is actually only an apparent feature caused by the narrow emission part overlying the broad absorption line. This scenario explains better that the line feature is at a positive velocity and also explains naturally why it is only seen in a small range of Balmer lies (i.e. the decreasing wind influence from the low to the high Balmer lines weakens the emission). In spectral lines other than the Balmer lines this feature is not seen.

The photospheric lines show shallow blue wings extending to about $-100\,\text{km}\,\text{s}^{-1}$. The Fe II $\lambda6248$ lines exhibit complex line profiles with three rather narrow absorption components and one emission component. Similar profiles have been seen in our time series studies in the previous chapter which indicated
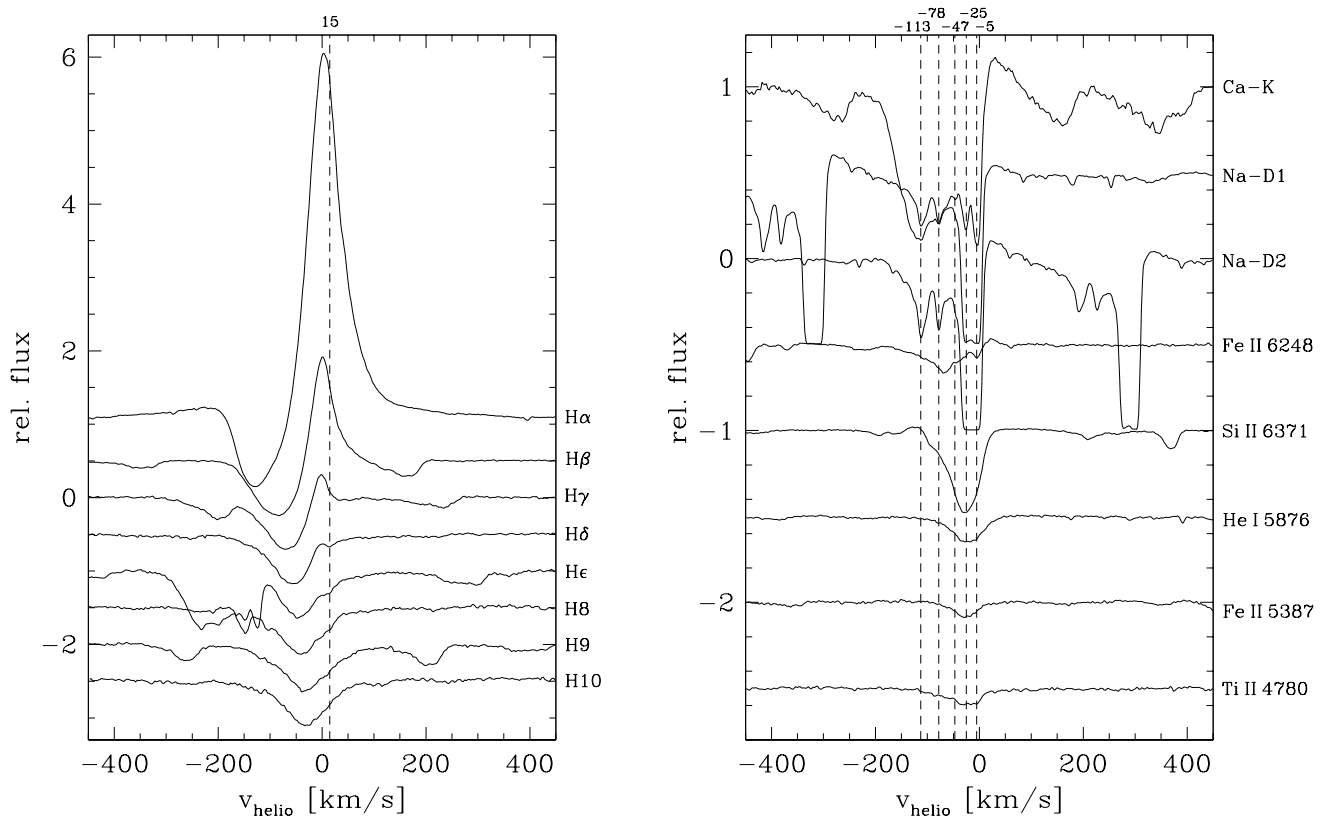
Figure 4.6: Selected line profiles of HD 160529 in heliocentric velocity space.

that this line originates in a transition zone between the photosphere and the wind and is highly variable.

The Na D and Ca K lines exhibit a structure similar to the Fe II $\lambda6248$ line in terms of complexity (i.e. multiple absorption features and an emission part) but the line components are much more pronounced with strong absorption features at -113, -78, -45, -25 and $-5\,\mathrm{km\,s^{-1}}$. These features exist for all three lines at the same velocity-location in the line profiles. As we have seen in chapter 3 the far blue-shifted features are variable on a time scale of days to weeks, indicating that they originate from the star rather than the ISM, thus providing a way to probe the conditions of the outer stellar envelope. Although the Fe II $\lambda6248$ line exhibits substructures at similar velocities, the line features might not be caused by the same physical mechanism as Fe II $\lambda6248$ is formed much closer to the stellar surface than the Na D and Ca K lines.

HD 168607

The Balmer lines of this star are slightly stronger than the ones from HD 160529 with similar broad shallow emission wings mainly in Hα. In Hα we see an additional strong absorption component at $-132\,\mathrm{km\,s^{-1}}$ which is also faintly visible in Hβ and possibly in some photospheric lines (e.g. Si II $\lambda6347$).

Only the dominant singly-ionized iron line Fe II $\lambda6248$ is discernible and shows a faint P Cygni profile – the weaker Fe II and Ti II lines are not visible. Together with the line strength of He I $\lambda5876$ this indicates a temperature of around $12\,000 - 14\,000\,\mathrm{K}$ which corresponds well with the B9 Ia spectral type classification by Walborn & Fitzpatrick (2000).
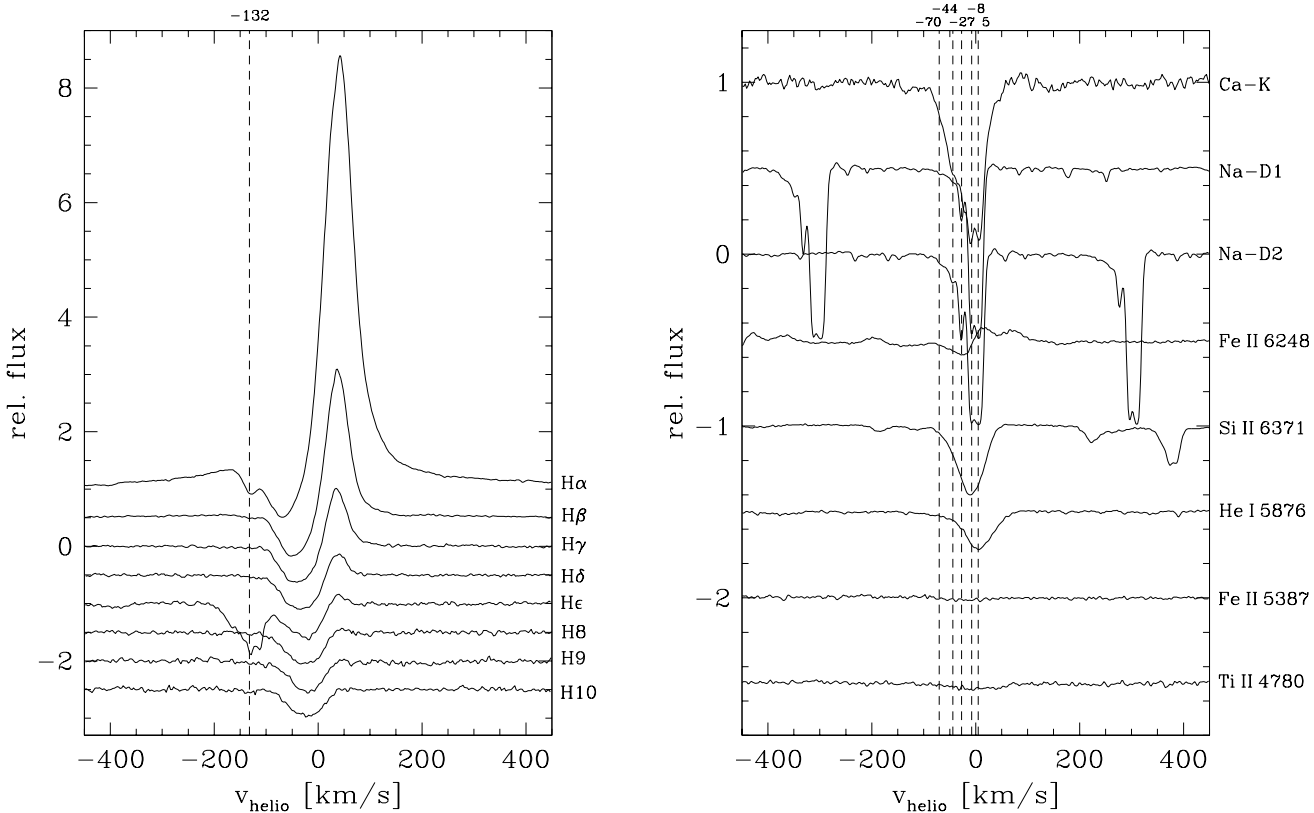
Figure 4.7: Selected line profiles of HD 168607 in heliocentric velocity space.

Sharp substructures are seen only in the Na D and Ca K lines with the most prominent ones at: −70, −44, −27, −8 and 5 km s^{-1}. Again the features are visible in all Na D and Ca K lines at the same velocity.

HD 168625

The spectral lines of this star are quite broad, possibly indicating a fairly high rotation velocity.

The Balmer lines are relatively weak for this star: only Hα and Hβ show a PCygni profile with rather faint emission parts. A weak wind is also indicated by the rather symmetric absorption profiles of the higher Balmer lines. Although the S/N ratio is not very high we can see a bump around −45 km s^{-1} in Hα and Hβ or alternatively an additional absorption part around −120 km s^{-1}. Judging from comparison of the absorption parts of the higher Balmer lines we favor the former scenario. The Hα-emission additionally exhibits a dent in its peak around 70 km s^{-1}.

The absence of Fe II and Ti II lines and the strong He I λ5876 line indicate a stellar temperature higher than ∼16 000 K. Note that Nota et al. (1996) observed the star around the same time and derived $T_{\mathrm{eff}} = 15\,000 \pm 2000$ K and found an expanding shell with ∼40 km s^{-1}. They observed also the nebula around this star with an inner elliptical shell and two outer loops suggesting a bipolar structure typical of LBV nebulae.

The Na D and Ca K lines have almost identical profiles as in HD 168607 and in particular the exact same substructure-velocities of −70, −44, −27, −8 and 5 km s^{-1}. The line profiles and the closeness of the HD 168625 and HD 168607 in the sky (separation ∼62") indicates that ISM clouds might be the
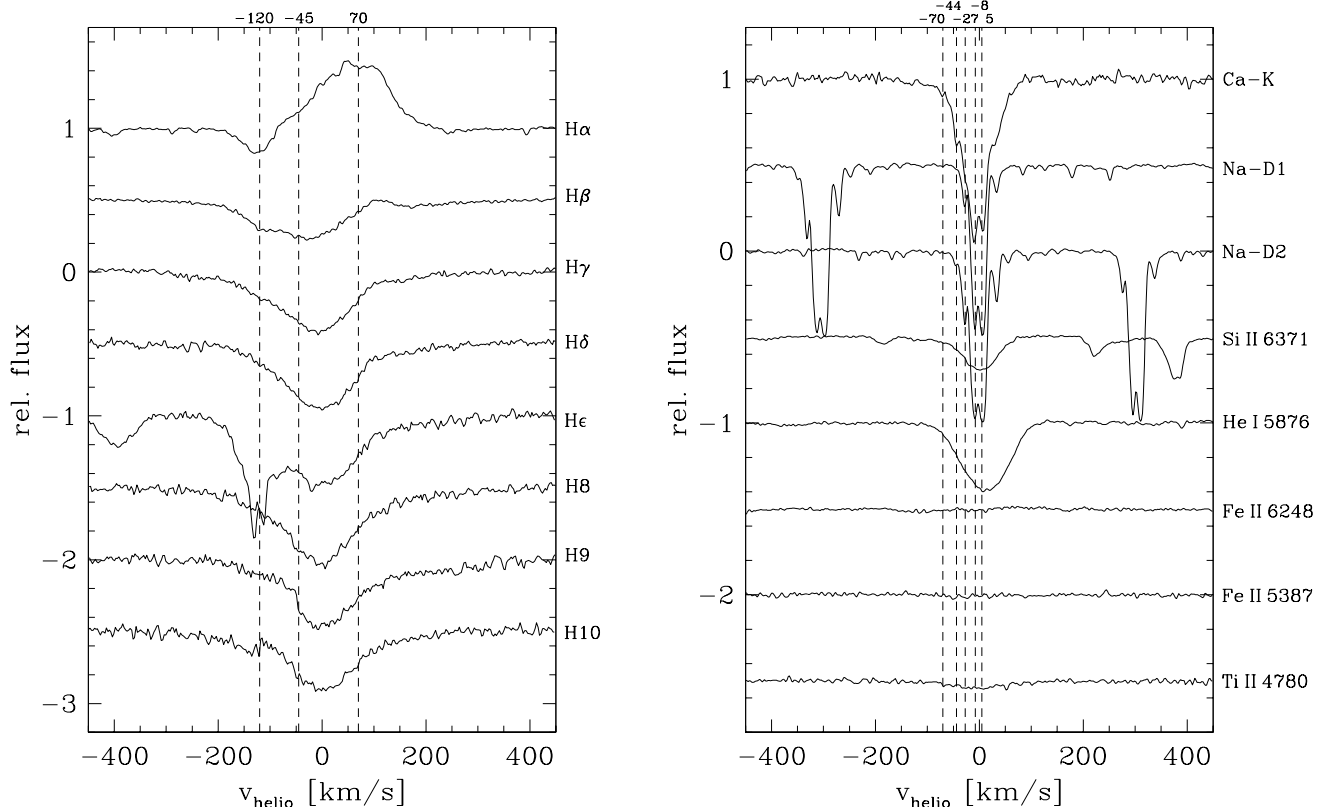
Figure 4.8: Selected line profiles of HD 168625 in heliocentric velocity space.

responsible absorbers in creating the NaD and CaK substructures. More features exist in these lines at higher positive (i.e. red-shifted) velocities which are probably of interstellar origin as well.

HD 5980

HD 5980 is a binary system that experienced a major outburst in Oct/Nov of 1994 (Barbá et al. (1995). During our observations of Oct 1995 the system was evolving back to its previous state where it exhibited a W-R type spectrum. However our spectra look actually rather similar to Nova outburst spectra (see e.g. Gäng 1993), indicating that we still see massive expanding shells in the Balmer and He line peaks. In particular the peaks at -160, 0, 160 and $520 \, \mathrm{km \, s^{-1}}$, that have the same shape and location in all Balmer and He I lines, are evidence for massive shells or clumps, moving in outward directions away for the star.

Note that the extreme width of the spectral lines for this object sometimes exceeded the range of an echelle order which produced the artifacts (i.e. flux shift in y-direction) in the spectral lines of Hγ, He II λ4686 and He II λ5411.

S Dor

The Balmer lines of S Dor exhibit strong P Cygni profiles, the usual progression of the higher Balmer lines and line wings for Hα on the order of $\pm 1500 \, \mathrm{km \, s^{-1}}$. Although the emission intensity of the Balmer lines are in the same range as in P Cygni their $FWHM$ is much smaller: $\sim 100 \, \mathrm{km \, s^{-1}}$ as compared to $\sim 200 \, \mathrm{km \, s^{-1}}$ for P Cygni. The absorption part of the Hα line shows two components at 175 and $225 \, \mathrm{km \, s^{-1}}$.
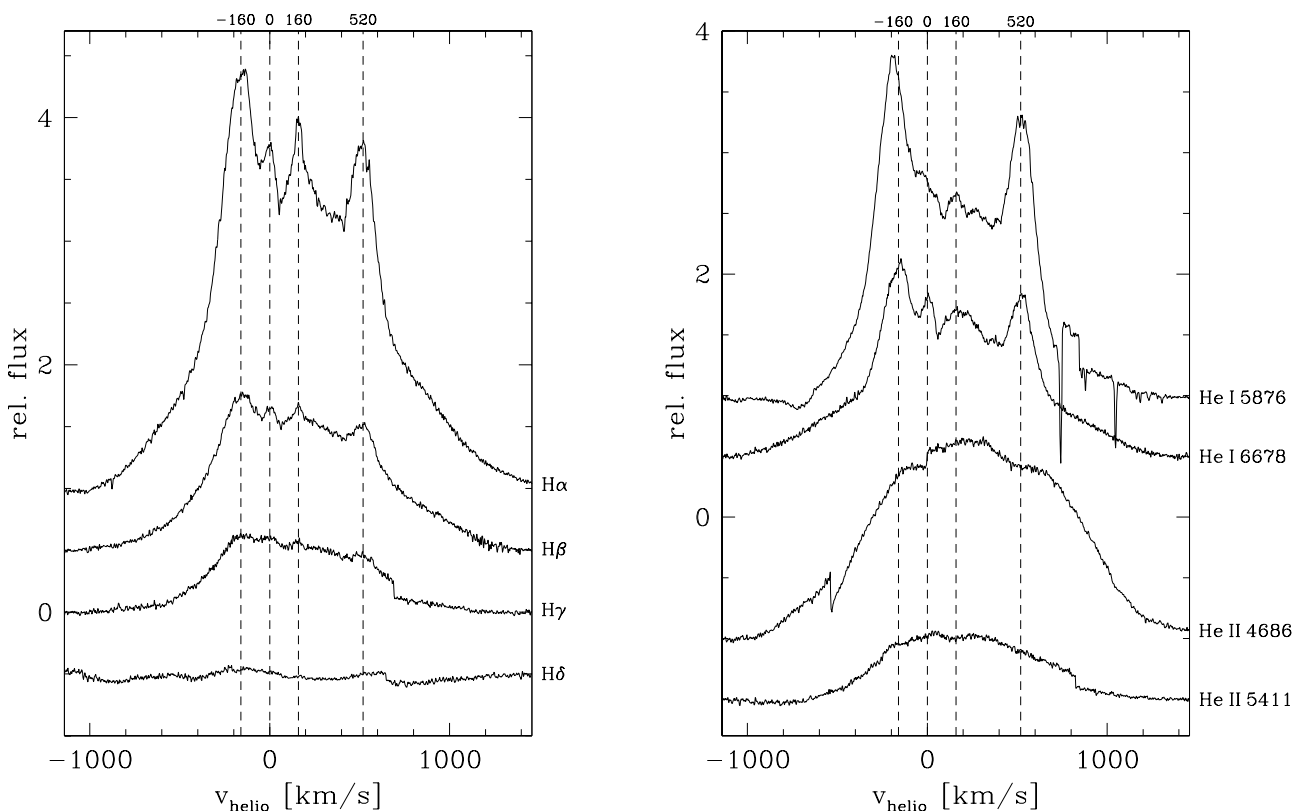
Figure 4.9: Selected line profiles of HD 5980 in heliocentric velocity space.

The non-hydrogen lines show a variety of profiles: the Fe II λ6248 and Ti II λ4780 lines exhibit PCygni profiles with strong emission components (W_λ(emission) $\approx$ 5 x W_λ(absorption)). Si II λ6347 exhibits a reverse PCygni profile with about equal strengths of the emission and absorption components. Note that line profiles with absorption components on the red side of the emission have been observed in S Dor and R 127 before, usually shortly after a historical maximum phase (Wolf & Kaufer 1997). The weak Fe II lines and He I λ5876 are so faint that they are almost not discernible. The line strengths (in particular H, He and Ti) indicate that S Dor was rather cool at the time of our observations – probably less than 9000 K. Note that in Oct 1999 S Dor was even cooler and exhibited F-type spectra with temperatures around 7500 K (Massey 2000).

Again the fine substructure is visible only in the Na D and Ca K lines at velocities of: 180, 206, 218 and 231 km s^{-1}. Note that the *galactic* ISM components do not affect these line profiles as they are shifted by the speed of the LMC (about 275 km s^{-1}); however the ISM clouds of the Large Magellanic Cloud now contribute to the Na D and Ca K lines. The dominating stellar components in those lines are broad PCygni profiles (in particular for Ca K).

R 40

The Balmer lines are relatively weak compared to other LBV spectra – only Hα and Hβ exhibit emission components. There is a possible line feature around 100 km s^{-1} which is clearly visible in the Hβ line and faintly detectable in Hγ. Hε might be influenced by it as well but the line blend with Ca H does not allow a clear identification. H 9 also shows a line inhomogeneity close to that velocity – although
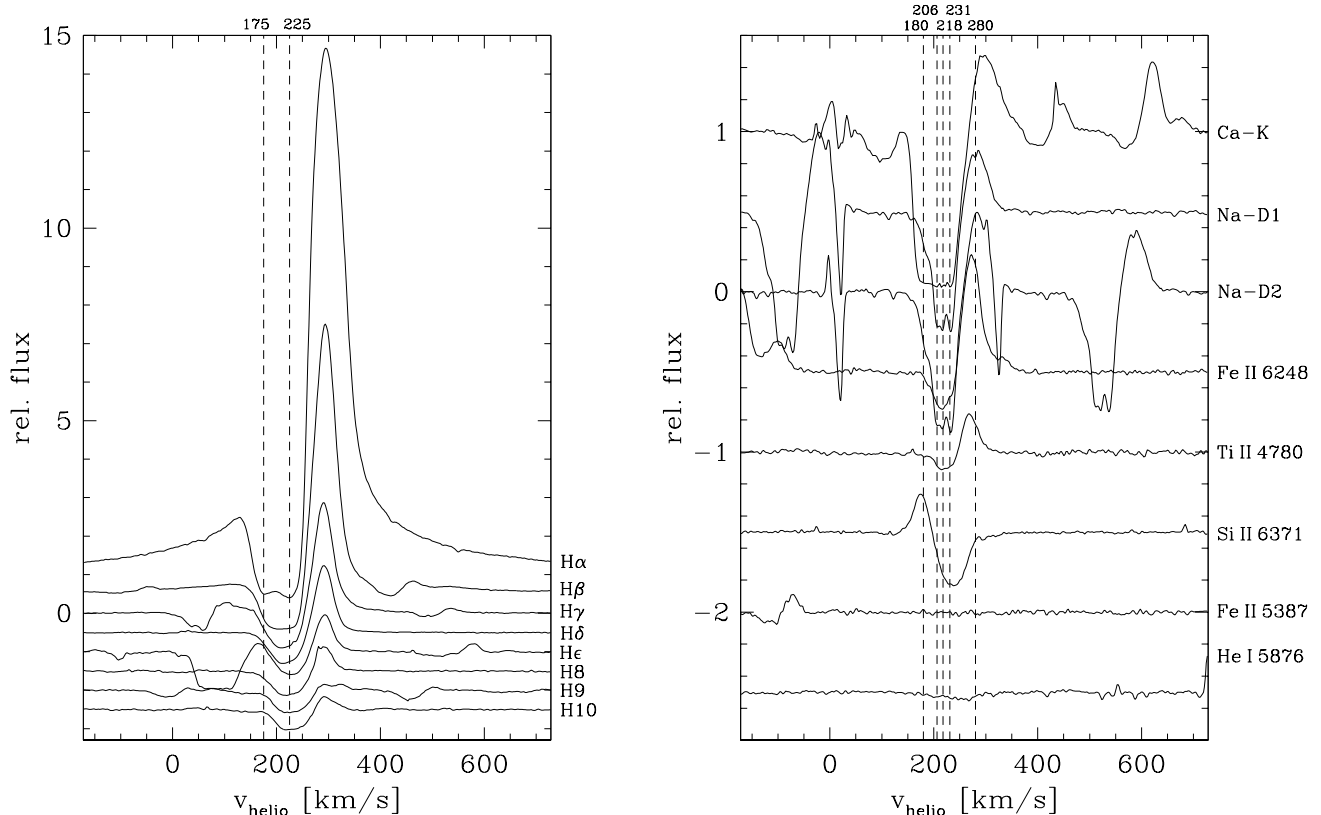
Figure 4.10: Selected line profiles of S Dor in heliocentric velocity space.

somewhat blue-shifted. The sharp peak at H 10 is an uncorrected cosmic ray event.

The metal absorption lines exhibit a small blue-shifted feature at $v_{helio} = 155\,km\,s^{-1}$, which was already discovered by Venn (1997) in high-resolution, high S/N CASPEC spectra and was attributed by her to a separate outflowing wind component. This component is also visible in the Na D lines in addition to finer components around 110, 142, 165, 174 and $205\,km\,s^{-1}$.

Note that the host galaxy of R 40 is the Small Magellanic Cloud so that the galactic ISM lines are shifted by about $160\,km\,s^{-1}$ (i.e. they are the blue-shifted, sharp absorption line doublets around $v_{helio} = 0$)..

Venn (1997) found that R 40 could be reliably analyzed with methods developed for normal A supergiants due to the small wind influence which might be due to the low metallicity of the SMC. The absence of emission components in any spectral lines apart from Hα and Hβ confirms this result. Their low temperature of $\sim$8000 K as derived by comparisons with other A supergiants is supported by the very weak He I λ5876 and Fe II lines in our spectra.

R 71

The Balmer lines of R 71 appear notably different when compared to the other hydrogen line profiles: the Hα and Hβ lines look more like pure emission lines with a superimposed small absorption dip, rather than the usual P Cygni profile. Thus the Balmer lines are highly reminiscent of B[e] stars where equatorial disks create such profiles. In fact, R 71 is known to have a surrounding nebula (Nota et al. 1997) and Waters et al. (1999) reported a detached dust shell as well. Also the higher Balmer lines do
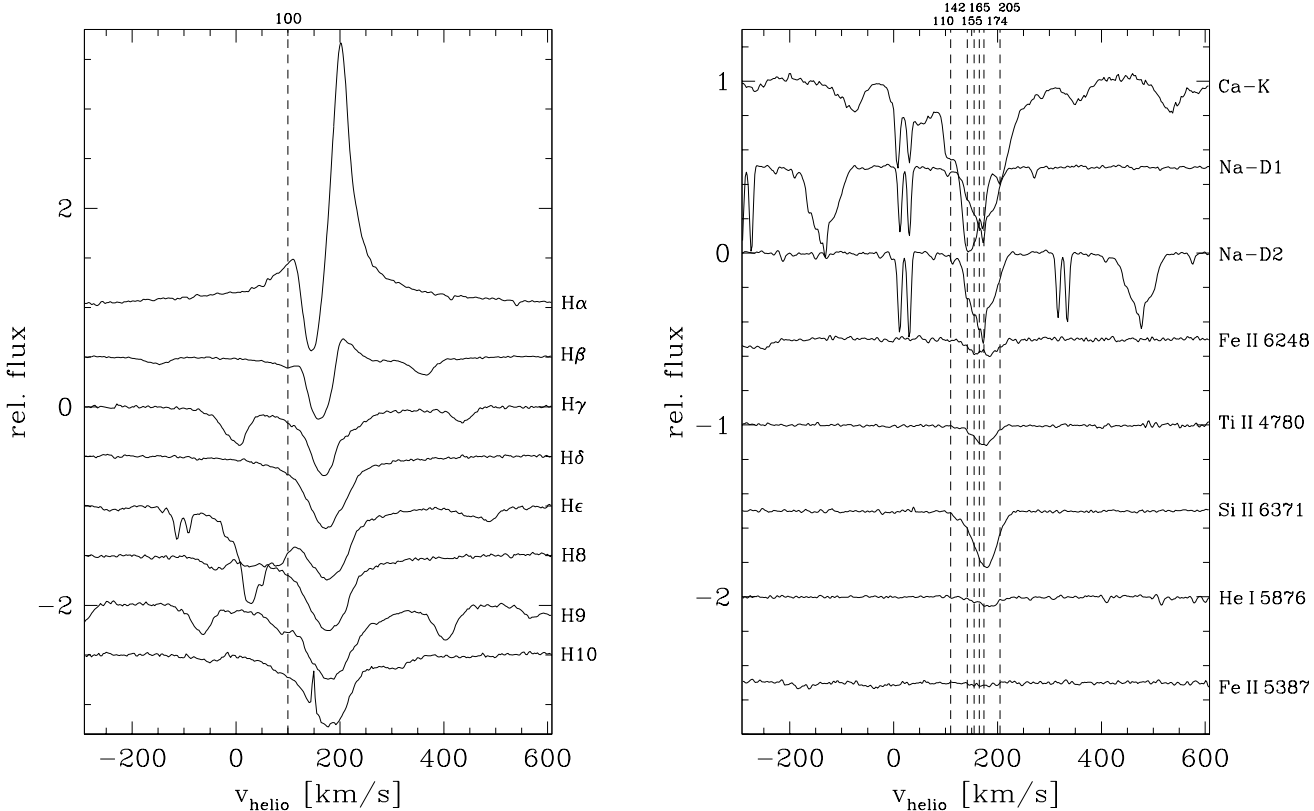
Figure 4.11: Selected line profiles of R 40 in heliocentric velocity space.

not progress towards lower velocities but rather remain fairly constant around $200\,\text{km}\,\text{s}^{-1}$. The dominant substructures are a strong absorption component at $155\,\text{km}\,\text{s}^{-1}$ and a minor one at $205\,\text{km}\,\text{s}^{-1}$.

The non-hydrogen lines follow the "special" line form of the Balmer lines: while the singly-ionized metal lines and Si II $\lambda6347$ are very faint, the He I $\lambda5876$ line actually exhibits two weak emission parts on the blue and red side of the absorption component. The absorption itself might have substructures at 192 and $218\,\text{km}\,\text{s}^{-1}$, although this could be an apparent effect of the low S/N ratio. The Na D lines also are very faint and do not exhibit their usual broad stellar "background" profile. Instead only subfeatures seem to exist which are not as well correlated within the Na D and Ca K lines are seen previously in other LBVs. The strongest substructures are seen in the Ca K line at 139, 160, 192, 218 and $243\,\text{km}\,\text{s}^{-1}$.

R 81

R 81 is an eclipsing binary system. Its spectroscopic and photometric variations were recently analyzed by Tubessing et al. (1999). The authors found strongly cyclical variation patterns with a period of about 74 days and suggested a morphology with circumstellar shells encompassing the whole system, to explain the observed line profile variations.

In our spectrum we recognize the typical Balmer line P Cygni-type profiles with broad emission wings in Hα and the progressive behavior of the higher Balmer lines. We can detect four distinct absorption-substructures at 130, 155, 200 and $280\,\text{km}\,\text{s}^{-1}$. The blue features remain fairly stable but the feature around $280\,\text{km}\,\text{s}^{-1}$ seems to be progressing towards lower velocities. Note that the feature is very broad in the higher Balmer lines and rather narrow in the Hα line where it is located on top of the emission
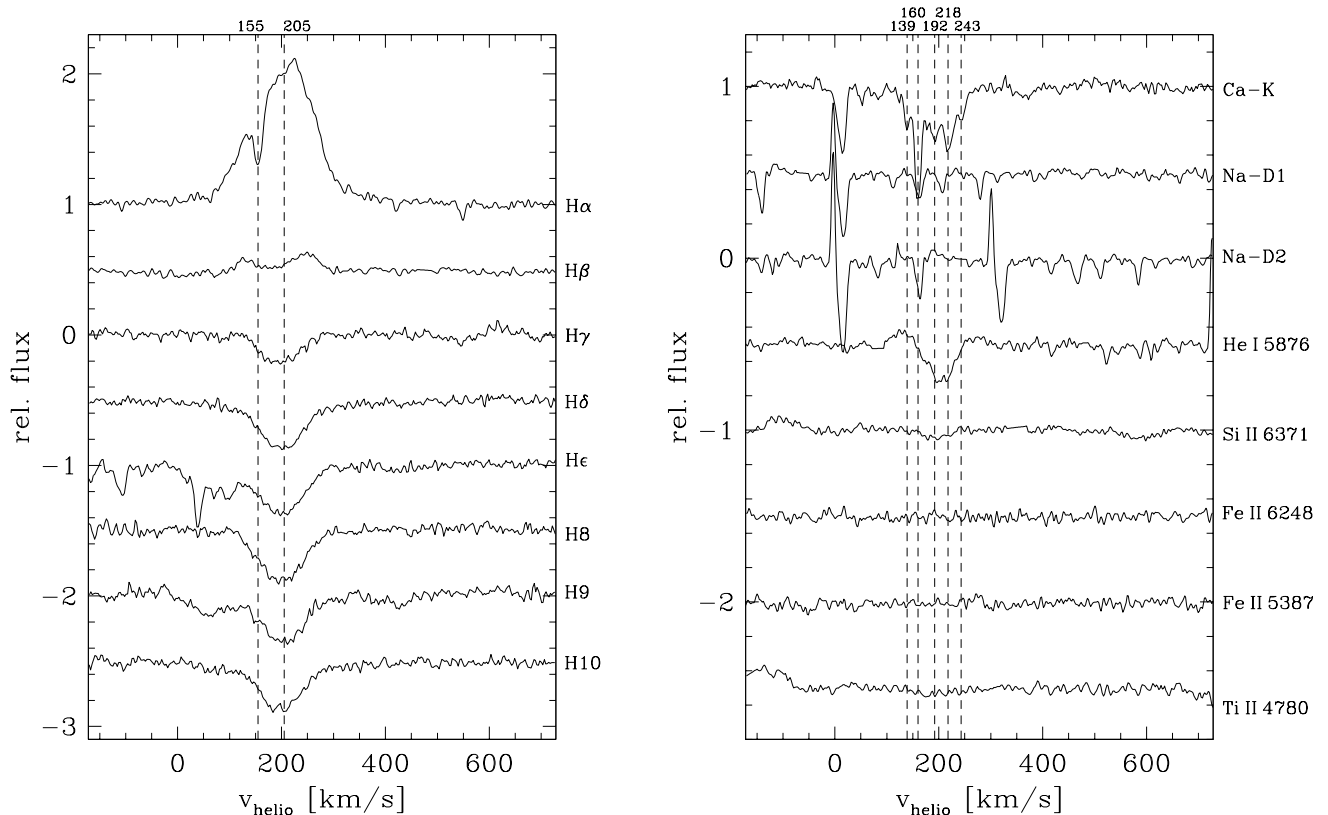
Figure 4.12: Selected line profiles of R 71 in heliocentric velocity space.

component.

As with R 71 we can hardly detect the metal lines in the spectrum but find a strong He I λ5876 line with shallow blue and red emissions around the absorption line. Also the Na D and Ca K lines have similar line profiles, where mainly the substructures can be seen. The dominant features are at velocities of 200, 221, 251, 267 and 280 km s^{-1}.

We conclude that both stars might have similar photospheric parameters although their wind and outer atmospheres are dominated by completely different processes. It might be possible to gain insights into the respective dominating processes of each system by comparing its spectra with the spectra of the other system, and so disentangle each system from its respective disturbing processes.

4.4.3   Observations at CES/CAT

In our CES/CATobservations we cover a much smaller wavelength region than in the other observations and are thus restricted to discussing fewer spectral lines. However, we took care to observe important diagnostic lines, like the strongest Balmer lines for wind diagnostics and the Mg II λ4481and Si II λ6347 lines to get information about the photosphere.

In a few observations (e.g. η Car and AG Car) the Hα line was over-exposed in the spectra; the upper part of the emission lines are not reliable in those cases and we cut off the unusable part when plotting the Balmer lines.
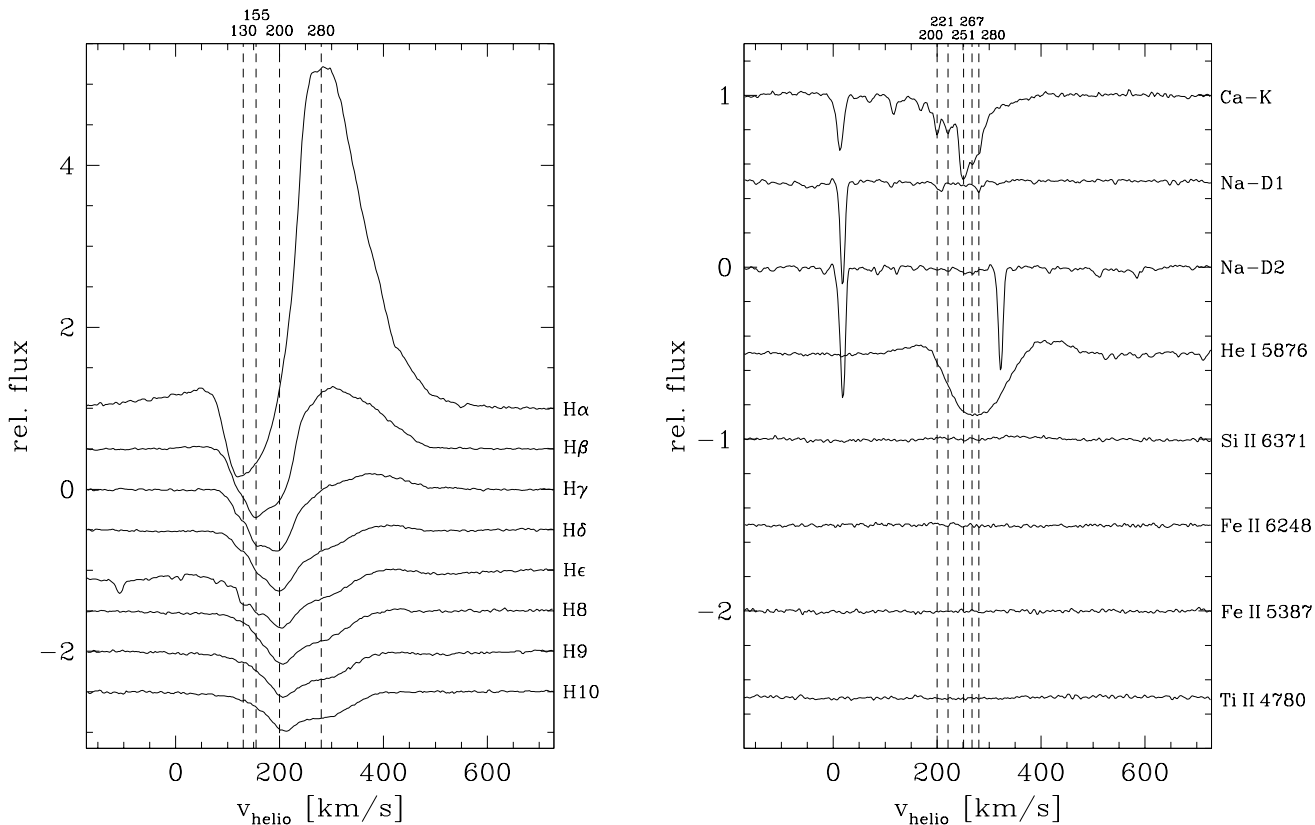
Figure 4.13: Selected line profiles of R 81 in heliocentric velocity space.

η Car

η Car is one of the most peculiar stars known. Although it has been studied extensively the system is still far from well understood. One reason is the complex composition of η Car: it was recently found to contain one or more close companion stars and it has a huge bipolar nebula with clumpy substructures (see image on page ix) – for more information on this object we refer to the special study session in the LBV-workshop "Luminous Blue Variables: Massive Stars in Transition", ASP Conference Series, Vol. 120, eds. A. Nota & H.J.G.L.M. Lamers, 1997.

The spectra of η Car deviate from all other studied LBV spectra here: they are characterized by extremely strong emission lines, many of which might originate in the nebula rather than the star itself. Most lines have general triangular shapes sometimes with finer substructures superimposed. It is hard to distinguish the many nebular emission peaks from substructures of η Car's spectrum itself. We note that the Balmer lines exhibit at least three common smaller line inhomogeneities at velocities of -330, -160 and $-75\,\mathrm{km\,s}^{-1}$. The He I and Si II lines exhibit a distinct structure around $-42\,\mathrm{km\,s}^{-1}$ that probably does not exist in the Mg II $\lambda4481$ line.

AG Car

The perhaps most comprehensive analysis of AG Car was carried out by Leitherer et al. (1994). The authors studied AG Car photometrically, spectroscopically and with polarization measurements over many years to cover the typical LBV moderate variability cycle. When comparing their optical spectra with our observations we find an excellent agreement with their spectra of May 20, 1992 when the star's stellar
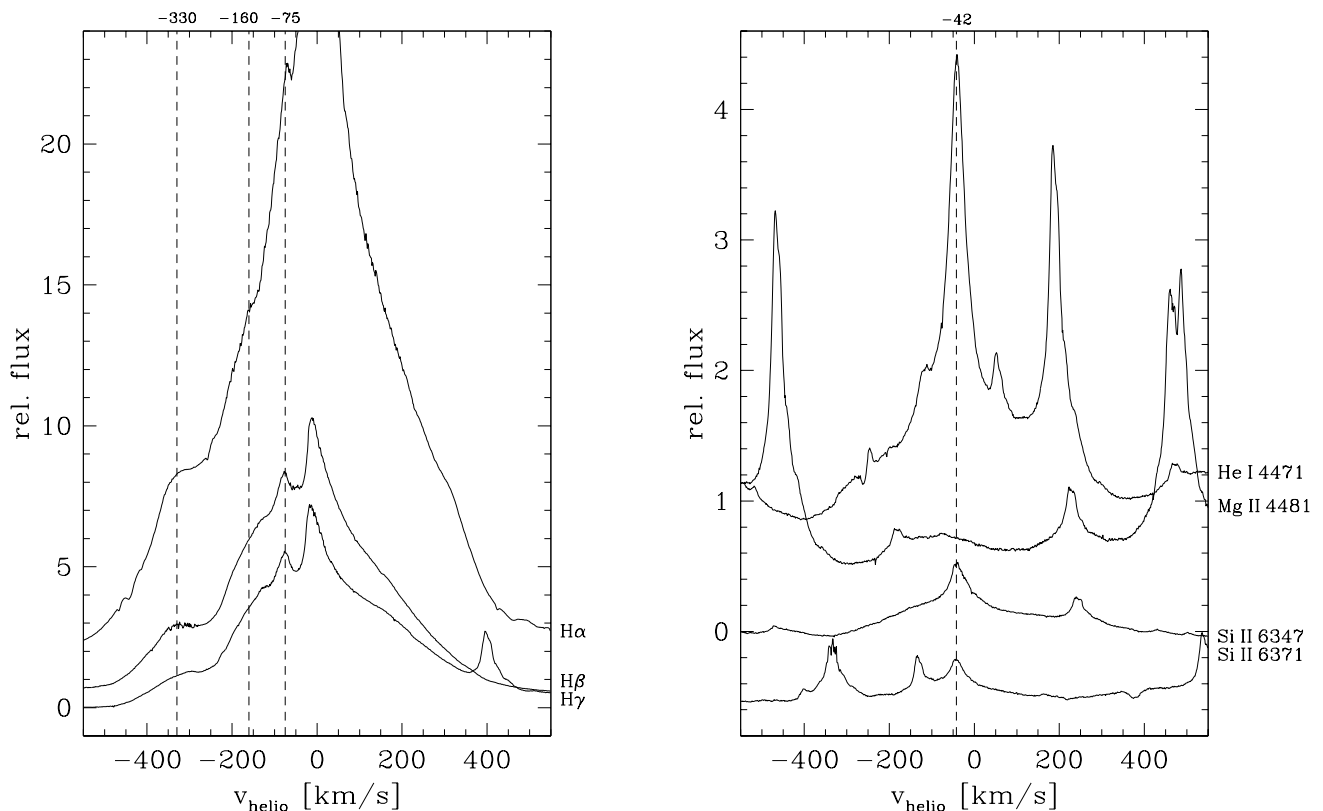
Figure 4.14: Selected line profiles of η Car in heliocentric velocity space.

brightness was increasing while its temperature was decreasing. Close to its visual maximum variable absorption components were detected in the Hα lines and explained by discrete expanding shells moving at constant velocity (they do not show radial velocity variations) with decreasing density (thus decreasing the line strengths of the respective absorption components).

These results were interpreted as variable outflows with density enhancements in the equatorial plane. The significant broad, shallow wings of the Hα line were attributed to electron scattering mechanisms in the outflow. Leitherer et al. (1994) concluded that the wind conditions in AG Car are actually similar to the ones of B[e] stars with slow, dense and faster, less dense winds occurring, that shape the spectral behavior of AG Car. Finally the authors suggested that the mechanism responsible for the observed variations has its origin in subphotospheric regions.

We conclude from the similarity of the spectra that during our observations in April 1996 the conditions of the stellar atmosphere were similar to the ones in March 1992 and the same effects produce our observed line substructures at $-98 \, \mathrm{km \, s^{-1}}$ in the Balmer lines and -70, -25 and $70 \, \mathrm{km \, s^{-1}}$ in the He I, Mg II and Si II lines. The He I λ4471 line is in strength and shape actually very similar to the Si,II λ6371 line but is shifted by about $+95 \, \mathrm{km \, s^{-1}}$ with respect to it. Note that the above velocity measurements mark the peaks of *emission* inhomogeneities in the respective spectral lines. Assuming shell ejections would produce additional absorption components in the line profiles and we have to measure those to estimate the velocities of the corresponding shell. However, here we just want to mark the most significant line inhomogeneities so either method will suffice.
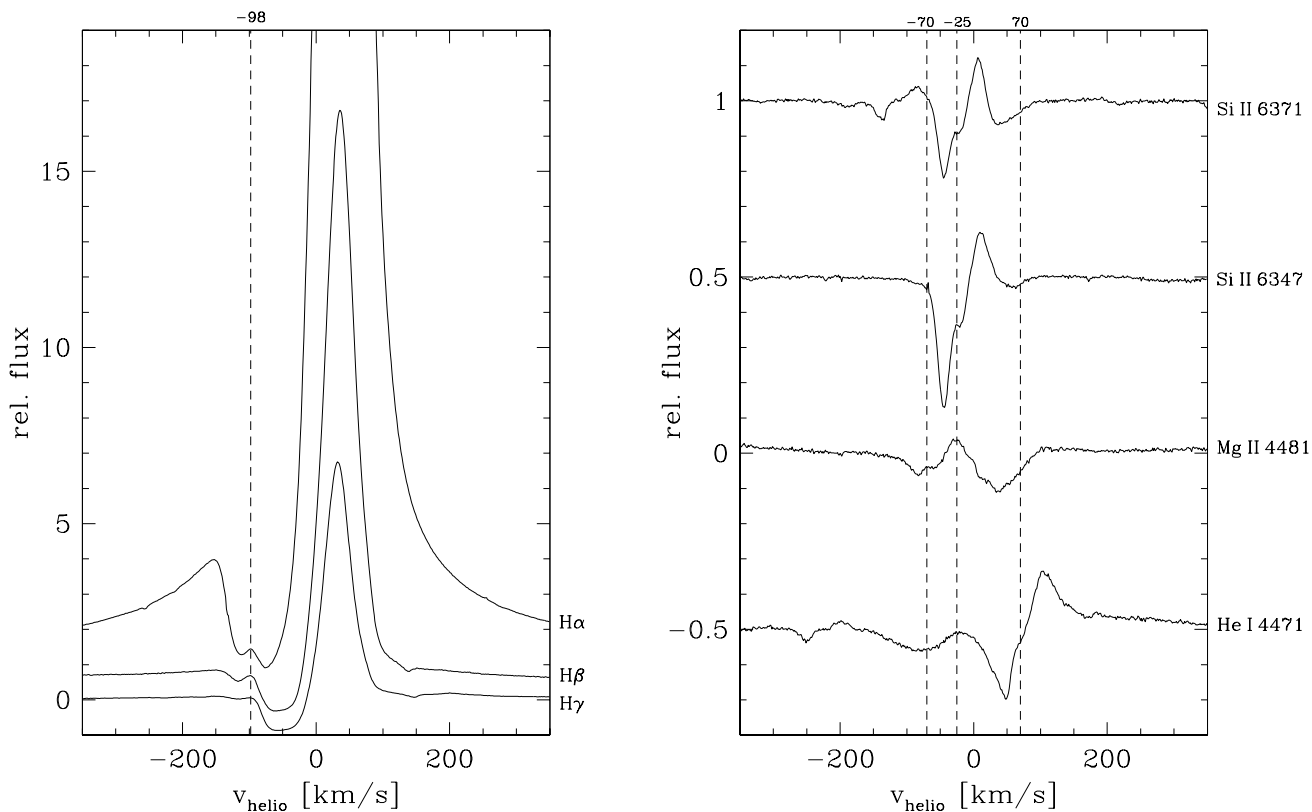
Figure 4.15: Selected line profiles of AG Car in heliocentric velocity space.

HR Car

As part of their study of the strongly bipolar HR Car nebula, Nota et al. (1997) obtained optical spectra of this star in May 1995 and January 1996. In the later observation the continuum flux had increased by about a factor of 12 and the Hα P Cygni-type line profile had changed significantly, i.e. a second absorption component developed in 1996 and the emission component evolved from a flat top profile in 1995 to a regular emission line in 1996. The authors suggest changes of the opacity in the inner wind regions as being responsible for the variations of the emission lines and shell ejections as possible causes of the second absorption component. They also mention (as did Leitherer et al. 1994) the possibility of radiative transfer effects creating the absorption components, as described by Hillier (1992).

In our spectra of April 1996 we see four significant subcomponents with the same velocities (i.e. -250, -180, -110, -30) in the Balmer lines. The much stronger emission line and electron scattering wings at Hα probably fill in the component at $-30\,\mathrm{km\,s}^{-1}$; nevertheless it can still be recognized as an asymmetry in the emission line profile. This fact (i.e. multiple absorption components at identical velocities in different lines) rules out radiative transfer effects as the responsible mechanism as these effects vary for different lines and are not present in all model calculations (Hillier 1992).

The blue-shifted components are not visible in other lines but the feature at $-30\,\mathrm{km\,s}^{-1}$ is visible as a line inhomogeneity in the magnesium and silicon lines as well. The He I $\lambda 4471$ line does not show the feature indicating that He I is formed closer to the stellar surface than the originating regions of the shells.

Although it is possible that the spectra of Nota et al. (1997) did not detect all existing absorption compo-
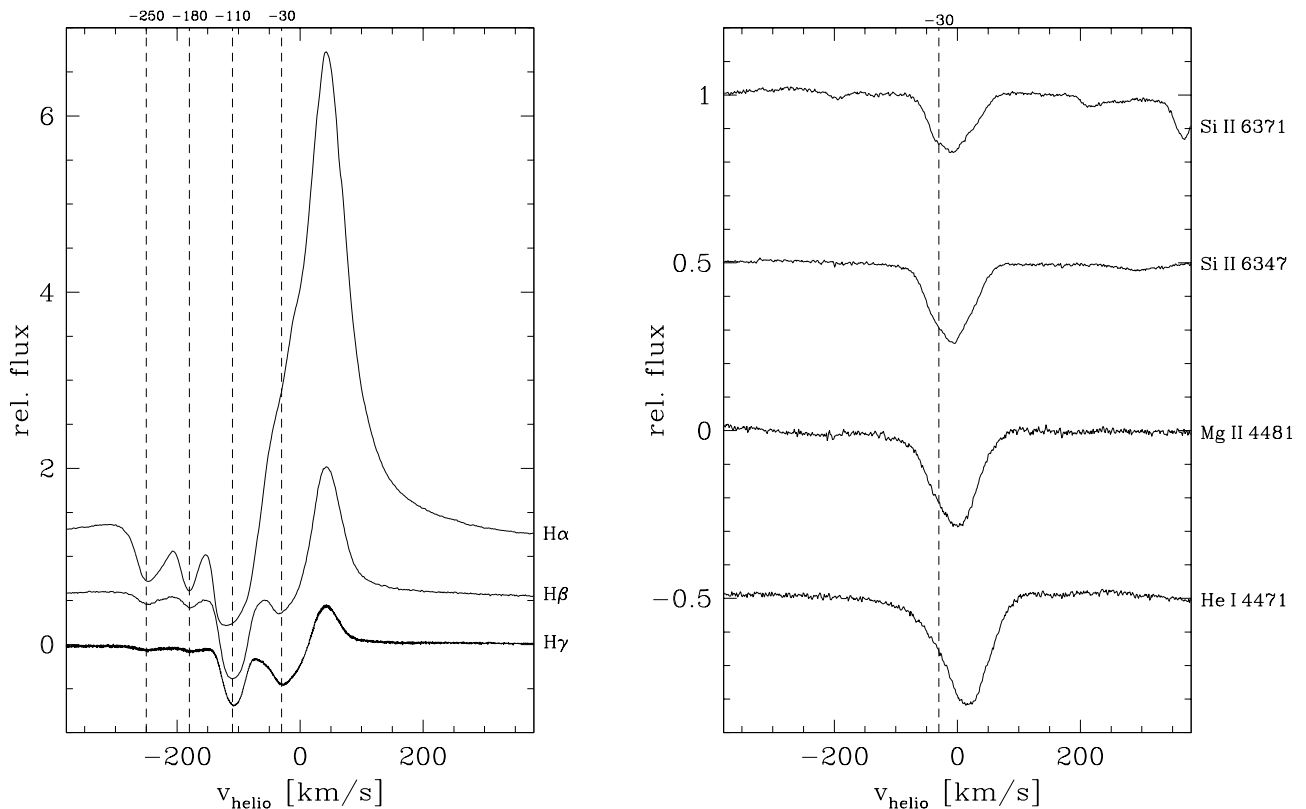
Figure 4.16: Selected line profiles of HR Car in heliocentric velocity space.

nents at the time due to their relatively low resolution of about $1-2\,\text{Å}$, the formation of one shell suggests that additional density perturbations might have developed in the time after their 1996, observations resulting in the multi-component absorption lines in our observation about three months later. Studying their zoom-plot of the Hα line profile in 1996 we detect a weak asymmetry in the emission part that could correspond to the $-30\,\text{km s}^{-1}$ feature which might indicate the originating region in the outflows where the shells get formed and ejected. However more detailed analyses and collaborations are needed to prove this suggestion.

HD 169454

HD 169454 was observed from 1992 to 1994 as part of the same spectroscopic monitoring program that also provided the data for the time series study of HD 160529 in chapter 3. Rivinius et al. (1997) analyzed the data and found outward moving line features in the absorption components of wind lines. The behavior of these features is reminiscent of the discrete absorption components (DACs) seen in O stars and is in both cases attributed to propagating non-spherical density perturbations (i.e. "blobs").

In our spectra of 1996 we cannot clearly detect these features although a weak, broad absorption feature is visible in the Hβ, He I λ4471 and Mg II λ4481 lines at $v_{\text{helio}} = -235\,\text{km s}^{-1}$. Note that the stronger absorption component of Hγ at this velocity is probably mainly caused by Stark broadening (as predicted by SEIDYNAMIC models). If the feature is real in the He I λ4471 and Mg II λ4481 lines it would confirm the findings of Rivinius et al. (1997) that the density disturbances originate at the base of the wind and then move outwards, as these lines are mainly formed in the photosphere (although they do show some
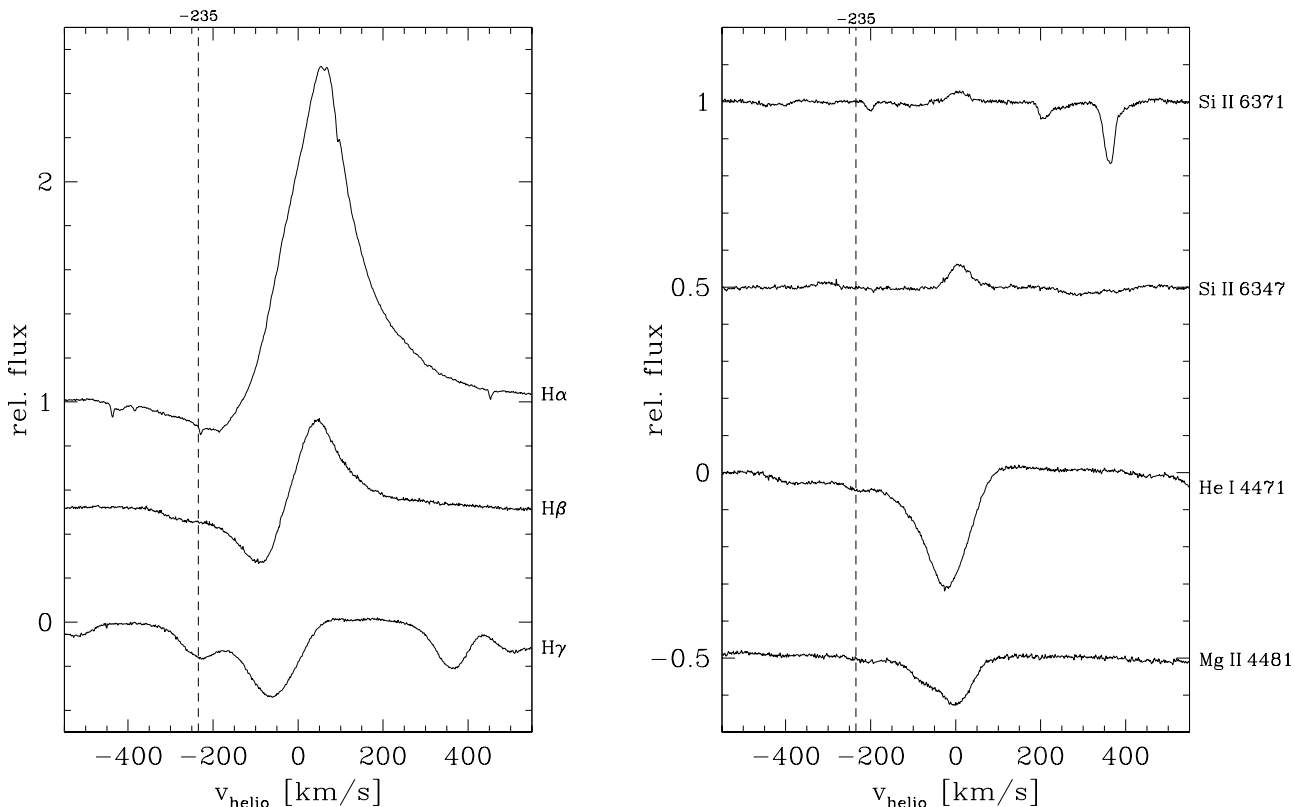
Figure 4.17: Selected line profiles of HD 169454 in heliocentric velocity space.

wind influence as indicated by the shallow blue line wings).

HD 316285

The Balmer lines of HD 316285 have a shape very similar to the ones seen in P Cygni but are even stronger (i.e. the intensity is higher by about 70 % and the *FW HM* is larger by a factor of 2), indicating a very strong wind. The most recent detailed analysis of this star was carried out by Hillier et al. (1998) who found that HD 316285 indeed has an extremely high mass-loss rate ($\gtrsim 2 \times 10^{-4}\,M_\odot\mathrm{yr}^{-1}$) and a performance number (= ratio of wind momentum to radiative momentum) that is 30 times greater than that of P Cygni. Although there is no photometric history of this object the authors suggest that HD 316285 is a LBV because of its spectral variability and its stellar properties and chemical content. Presumably HD 316285 is, like P Cygni, in a relatively quiescent phase of its LBV life where significant spectral variations but no major photometric changes occur.

Because of the low apparent brightness of the star we had to choose large exposure times for this object in order to get the desired high S/N ratios and so the telluric line blends are rather strong in the spectra. All marked narrow features in the Balmer line plot can be identified as telluric.

The line profiles of He I λ5015, Mg II λ4481 and the two Si II lines appear rather similar and are not shifted with respect to each other. The Si II lines exhibit a faint inhomogeneity/asymmetry in their profiles around $-210\,\mathrm{km\,s^{-1}}$. In the other two lines this feature is not visible but the reason could be that
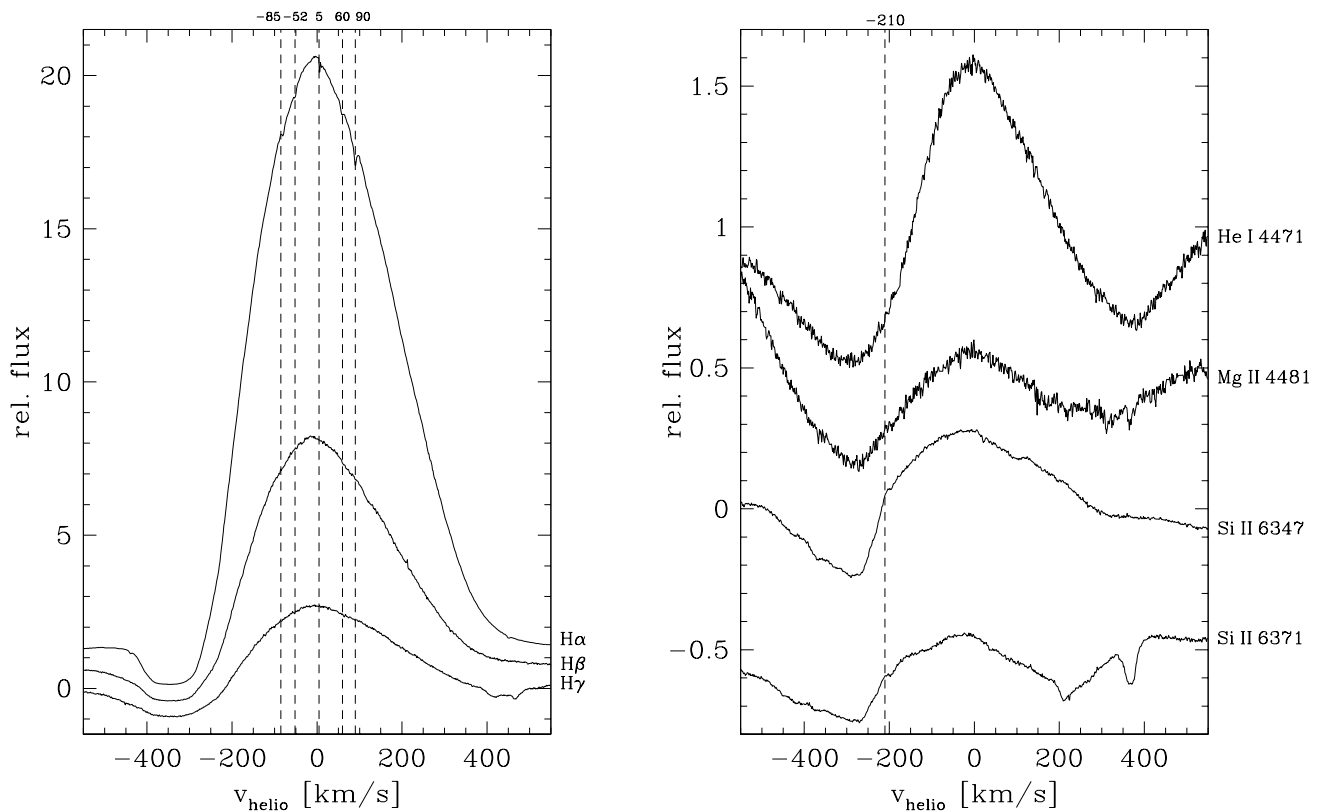
Figure 4.18: Selected line profiles of HD 316285 in heliocentric velocity space.

the S/N ratio of the blue lines is much lower.

HD 326823

In our spectra we confirm the double-peaked emission line structure of Hα as found by Sterken et al. (1995) and observe the same two peaks in the Hβ and Hγ lines. Also the forbidden [N II] lines at 6548 Å and 6583 Å are visible (see spectra in appendix). Note that our He I λ6678 line profile looks almost exactly like that of Sterken et al. (1995) from April 28, 1994 – even the smaller inhomogeneities on top of the red emission component exist. However, as HD 326823 exhibits strong night-to-night variations, we attribute this line profile as a chance event rather than some large-order atmospheric effect (note that Sterken et al. 1995 mentioned that the fast variations are of the same order of magnitude as the variations spanning decades).

In the Si II lines we can detect five distinct features at –230, –170, –70, 70 and 170 km s^{-1}. The symmetry of the two pairs of features at (–70, 70) km s^{-1} and (–170, 170) km s^{-1} could indicate two spherically expanding shells with a systemic velocity of 0 km s^{-1}. The features are less pronounced in the He I λ4471 line and almost indistinguishable in Mg II λ4481.
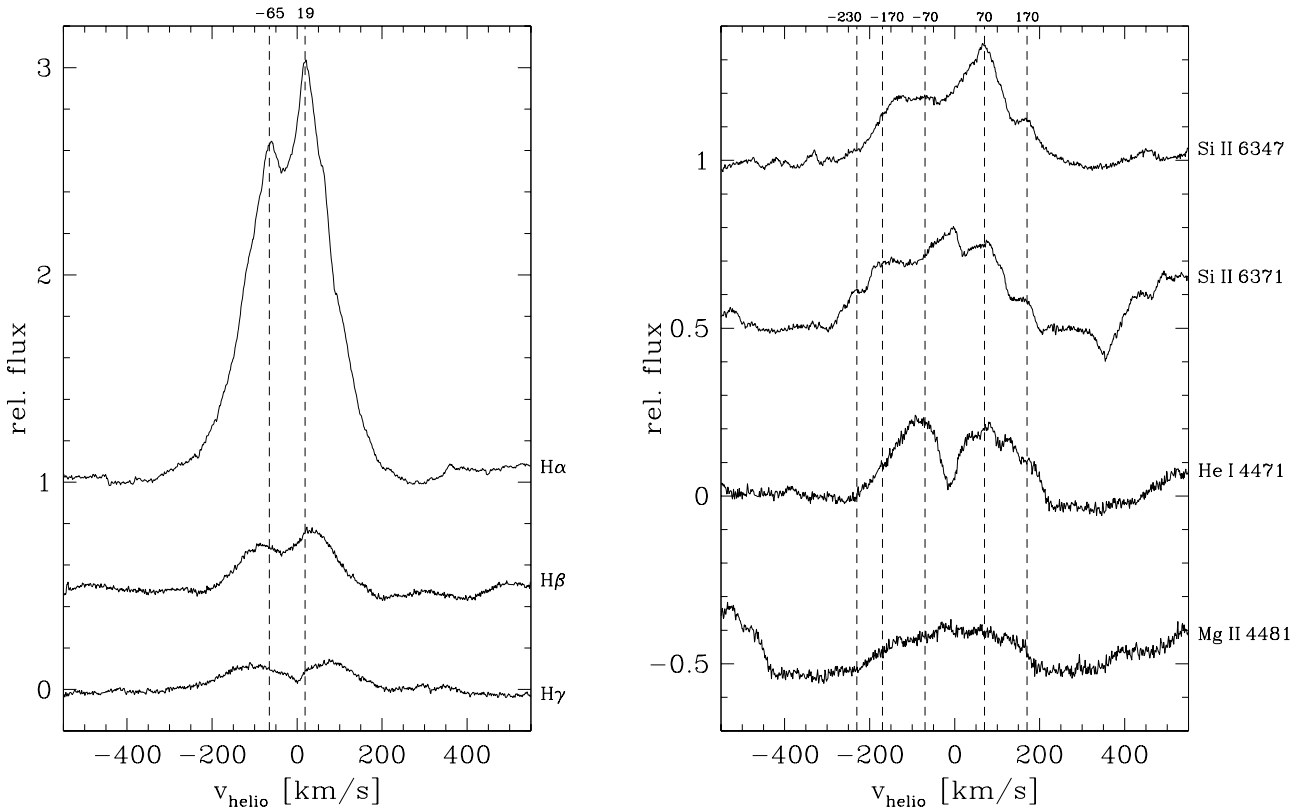
Figure 4.19: Selected line profiles of HD 326823 in heliocentric velocity space.

HD 80077

All Balmer lines exhibit a distinct line feature at $v_{\text{helio}} = -25\,\text{km}\,\text{s}^{-1}$.

A quick web-based literature search on the Astrophysics Data System (ADS)[6] for HD 80077 spectra yielded only one, fairly old spectrum (June 1984), published by Carpay et al. (1989) that was taken around Hα with a spectral resolution of 14 000. Their Figure 2 shows an Hα line profile that is similar to ours although no inhomogeneity is visible which is probably due to their lower spectral resolution. It is possible that no such feature existed in the spectra of HD 80077 in 1984 but the generally low variability and the similar line profile favors the former argument.

We can see the feature in the Si II 2 6347 line as well but it does not show up in the other line profiles. Assuming that some sort of density perturbation is responsible for the line feature (say a shell) we can estimate the originating location of the shell, i.e. in this case it is the area of the Si II 2 6347 line-forming region around $v_{\text{helio}} = 0\,\text{km}\,\text{s}^{-1}$.

---

[6]The URL for ADS is: `http://adsabs.harvard.edu/cgi-bin/nph-abs_connect`
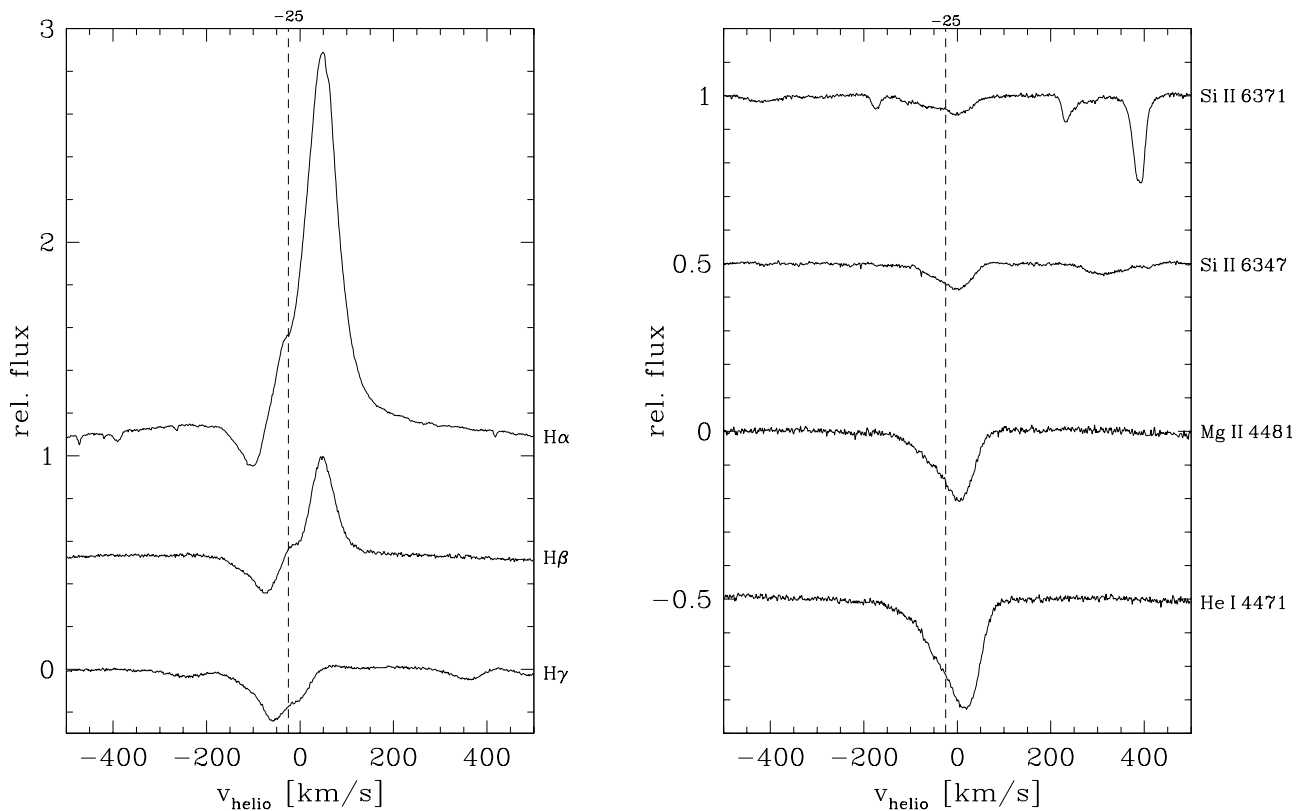
Figure 4.20: Selected line profiles of HD 80077 in heliocentric velocity space.

4.5   Summary and Discussion

4.5.1   Summary and Discussion of the Observations

In this section we summarize and discuss the observed spectra for this "ultra-high resolution" project. We discuss the P Cygni spectra in detail and then proceed with notes that apply for all observed objects.

P Cygni

So far all published spectral atlases of P Cygni achieved their high S/N ratio by averaging spectra obtained over several years to a mean spectrum (see Markova 1994 and Markova & Zamanov 1995, Stahl et al. 1991 a, 1993). Since the typical variability time scale of P Cygni is on the order of months (for photometric as well as spectroscopic variations; see Stahl et al. 1994) the averaging "smeared out" the line profiles so that possible weak sharp components cannot be detected in the mean spectrum. In our spectra we did not detect any significant variability so by averaging our data we only improved the S/N ratio without affecting the line profiles. Furthermore our spectra provide a superior resolution ($R \approx 100\,000$ compared to $R \approx 12\,000$ of Stahl et al. (1993) and $R \approx 18\,000$ (at 6500 Å) and $R \approx 21\,000$ (at 3800 Å) of Markova (1994) and Markova & Zamanov (1995) respectively).

While the group of Markova reported possible line splitting and DACs in their spectra these features could not be seen in the spectra of Stahl et al. (1993). Because of the lower resolution of the spectra of Stahl et al. (1993) and the low S/N ratio of the spectra of Markova (1994), this question could not be answered conclusively. Both observational constraints are resolved in our spectra and we can confirm the findings of Stahl et al. (1993) in that we cannot detect any definitive line splitting. However, from our one-time snapshot, it cannot be excluded that DACs are present at other times – it is possible that we just did not catch the optimal phase of the variability cycle and/or that these features are present predominantly in spectral lines outside our observing window (e.g. mainly the higher Balmer lines are expected to show these features).

Stahl et al. (1991 a) unexpectedly discovered forbidden Fe II lines in their averaged optical spectrum of P Cygni (S/N $\gtrsim$ 500, spectral resolution: 12 000). These lines show a flat-topped profile with sharp edges and have intensities of only a few percent of the continuum. With further averaging of a total of 119 spectra, the authors even reach a S/N ratio of about 2000 as measured at 5400 Å (Stahl et al. 1993). Our averaged spectrum achieves a S/N ratio of about 450 with a maximum value of 1100 in the emission part of Hα. Our spectrum is thus comparable with the above spectrum of Stahl et al. (1993) in terms of S/N ratio but has a superior resolution of $R \approx 100\,000$. However even in our spectra the [Fe II] cannot be further resolved. The observed substructures in the forbidden emission lines have a typical $FWHM$ of $\sim 60 - 100\,\mathrm{km\,s^{-1}}$ which is more typical for lines originating in the stellar wind closer to the star. Thus it seems that the structured profiles of the forbidden lines are indeed caused by line blending as suggested by Israelian (1995), rather than by single blobs or clumps in the extended atmosphere. However if the circumstellar envelope consists of many clumps with a broad velocity dispersion in the line of sight, their contribution to the emission lines could also produce the observed profiles.

Studying our spectra we see that the broad emission wings of the strongest hydrogen and helium lines (Hα, Hβ, Hγ, He 5876, He 6678) seem to scale with the corresponding emission strength. The mechanism forming these wings is thus most likely electron scattering although some NLTE contribution as found by Hubeny & Leitherer (1989) cannot be ruled out. The shallow, broad wings around the Hα, Hβ and Hγ lines have widths of about $1500 - 1000\,\mathrm{km\,s^{-1}}$ for the respective lines. Hα also shows an extension of the wing on the blue side of up to $\sim 5000\,\mathrm{km\,s^{-1}}$. led spectra also resolve for the first time the asymmetric, saturated but non-zero absorption profiles of the Hα and Hβ lines which exhibit similar

forms as "black" absorption troughs found in many UV lines. The absorption components of the higher Balmer lines and all helium lines (which are formed deeper in the stellar atmosphere) are not saturated anymore; rather they show the typical known P Cygni profile and exhibit a line progression (i.e. weaker lines are formed at lower velocities).

The Balmer lines appear smooth; all weak features in the Hα line could be associated with telluric features (see top/left plot of Figure 4.4). This supports the results of Scuderi et al. (1994), validating the "smooth-wind" assumption in synthetic models of the optical spectrum of P Cyg. It is also clear that high-quality data such as ours are *essential* if one wants to detect faint narrow-line features of blobs and clumps and distinguish them from telluric features. This result agrees with our previous argument of a homogeneous expanding shell at large distances from the star ($R \gtrsim 100\,R_\star$) as concluded from the forbidden [Fe II] line profiles. In contrast are the asymmetric distributions of clumps as detected in coronographic images of the P Cygni nebula (Nota et al. 1995) and the indication of inhomogeneities in the circumstellar envelope as derived from infrared observations with ISO (Lamers et al. 1996).

The seemingly contrary pictures of the physical condition in P Cygni's extended outflow region can be resolved by abandoning the assumption that the matter is either clumpy or homogeneously distributed *throughout* the outflow. Feldmeier (1999, in particular the discussion section) described a scenario that can explain all observational facts based on model simulations that extended to $100\,R_\star$ and applied the line-driven instability mechanism: dense shells occur only above $\sim 1.5\,R_\star$ so the Hα line-forming region of typically $1 - 1.5\,R_\star$ should not be significantly affected. An intermediate region of about $1.5 - 50\,R_\star$ is clumpy due to the line-driven instabilities (this can explain the inconsistencies between determining $\dot{M}$ from IR or optical data). Finally the outermost outflow part is rather smooth again, related to inefficient radiative cooling (i.e. internal thermal pressure leads to a re-expansion of the shells), which agrees with the smooth [Fe II] line profiles.

All LBVs

In the section 4.3 we discussed the observed spectra individually without cross-correlating the observations of other LBVs (i.e. for each LBV we described its mean spectrum, emphasizing substructures in the spectral lines and listed related references). Here we look at *all* spectra and discuss the common features with the goal of finding a global picture of the conditions in expanding LBV atmospheres.

The fact that none of the LBV spectra showed significant variations on time scales of minutes to hours indicates that the physical mechanisms responsible for the LBV variations in general do not have such high frequency components; rather the minimal time scales are on the order of days to weeks (e.g. as detected by Stahl et al. 1994 for P Cygni or see previous chapter for HD 160529). This might serve as a constraint for theories and models to explain the LBV variability mechanisms.

By ordering the line profiles with increasing velocities in our plots (i.e. line with largest v_{helio}-value on top of plots and line with lower v_{helio}-values successively decreasing) we created in first order approximation a probing scale through the stellar atmosphere (we assumed here the usual wind law where the velocity increases with radius). In those plots it is easy to see if line inhomogeneities follow a certain trend (like changing their velocities or strengths in different wind regions). We can estimate the line-forming region of possible blobs, clumps and/or shells by examining in which line the associated inhomogeneity-feature is first visible. An example is HD 80077 where we see a line feature at $-25\,\mathrm{km\,s^{-1}}$ in the all Balmer lines and faintly in the Si II 2 6347 line while the other lines that form deeper in the atmosphere do not exhibit this feature. Also weak, narrow features that e.g. only show up in the Hα line and not in the higher Balmer lines can be attributed to telluric line blends even if no comparison spectrum is available.

We see a general trend of inhomogeneities getting more pronounced and more frequent in spectral lines that are formed further out in the atmosphere: e.g.: many H, Fe, Na, and Ca lines show significant substructures while photospheric lines show mostly wind influence (shallow blue line wings) but not necessarily distinct line features. In particular the Ca II and Na I lines of all our observed stars show complex structures, usually with multiple sharp absorption components and often a broad emission component as well. The results of the variability studies in HD 160529 (chapter 3) and P Cygni (first tests using data from Stahl et al. 1995) indicate significant stellar contributions in these profiles and thus they might be used to study the conditions in the envelopes of LBVs.

This result has important consequences of the studies of ISM lines when LBVs are used as background stars (e.g. Welty et al. 1994 found 16! distinct ISM components in the Na D$_1$ line of P Cygni) but might not have considered stellar contributions. Separating the stellar and ISM contributions in these lines will thus be important in both studies.

The line-driven instability mechanism (Feldmeier 1999) that we discussed in the previous section, might explain the observed trend of inhomogeneities forming preferably in lines that originate further away from the stellar surface: the lower wind and photospheric regions are not influenced by the instability while the sodium and calcium lines (and possibly/partly Hα) might get formed in the intermediate wind region where the line-driven instability dominates and creates clumps and shells.

In certain stars corotating interactive regions (CIRs) can produce significant clumping of the wind close to the star (see recent 2D-CIR models of Owocki 1999). Clumpy LBV nebulae structures can be reproduced in detail by "ram-ram" pressure mechanisms and fast/slow wind models (García-Segura et al. 1996).

Other mechanisms might explain substructures that are seen in lines forming deeper in the atmosphere (e.g. pulsation triggered shell-ejections, sudden changes in the ionization structure of the atmosphere, ...)

A final explanation for the observed tendency of the line-substructures is that clumping exists close to the photosphere but is not visible because the density structure is not high enough to affect the photospheric line profiles and/or opacity conditions close to the photosphere do not allow the observation of clumps.

4.5.2   Future Prospects

We will perform a literature search for photometric observations that were carried out close to our spectroscopic observing runs to determine the state (maximum or minimum) of the respective object at that time. We will use this information to study whether inhomogeneities are a general feature in the winds of massive stars or if they only appear in certain evolutionary phases (note that by obtaining spectra for a large number of sources we should have observed LBVs in a wide range of atmospheric conditions). This clearly has important consequences for stellar evolutionary models and models for the wind-driving mechanisms.

The accurate modeling of the LBV spectra including possible clumping effects will provide highly accurate mass-loss rates and help to understand the physical effects at work in LBV atmospheres. This will determine the potential to use these extremely bright objects as "standard candles" in distant galaxies. In particular it might be possible to use their wind momentum - luminosity relation (WLR), similar to the galactic BA supergiants Kudritzki et al. (1999), as extragalactic distance indicator which would provide important constraints on cosmological evolution models.

As mentioned before we will collaborate with the Munich group of scientists including Dr. R. Kudritzki, to apply their highly sophisticated unified models for fitting the spectral lines of our data.

Chapter 5: Conclusion

In conclusion, we believe that we have met the goal of our thesis, namely, to provide the data and perform the analysis necessary to tackle some of the important open questions in the field of LBV research (see section 1.4).

In particular, we have presented the first detailed study of LBV line profile variations, using HD 160529 as an example, and have made initial analyses of spectral time series on which future, more sophisticated numerical models can be based.

The most important result from our analyses is that *all* observed spectral line variations can be explained by radial and non-radial pulsations. The additional effects in the stellar atmosphere (changes of the ionization structure and variable wind densities), that are needed to explain the detailed behavior of the wind lines, can be attributed to be triggered by pulsations as well. Thus, RPs and NRPs seem to be the underlying *physical* mechanisms that cause all observed line-profile variations in HD 160529.

The ultra-high-resolution snapshot spectra that we have acquired with colleagues are state-of-the-art: to our knowledge they are the most complete sample of such high-resolution, high S/N LBV spectra. The data is available to the scientific community (the publication of the spectra is in progress but immediate access can be provided by request).

Although the ultra-high-resolution LBV spectra have not yet been analyzed in detail, initial basic models have been calculated and preliminary results have been presented by Gäng et al. (1997).

Further studies building on these results are in progress; in particular, we are collaborating with the Munich group of Kudritzki to apply their sophisticated unified model code to analysis of the spectra presented in chapter 4.

In section 3.8 we have also discussed the possibility that HD 160529 might be a binary system with the observed line profile variations being the result of interactions with a companion star. However, we do not need to invoke this more complex model as we can explain all the observed line variations as consistent with the pulsations of a single star. Furthermore, if at least some LBVs are single stars, not all of the characteristic LBV behavior can be attributed to having multiple stars in the system.

Nevertheless the question of how many LBVs actually are multiple star systems is intriguing and the effects such systems might have on their spectral lines are not well known. Even the well studied LBVs η Car and R 81 have only recently been shown to be binary systems. Apart from simple stellar statistics, another argument for some more LBVs being binary systems might be the bipolar nebulae structures that are seen around many LBVs which could easily be explained by a companion star causing the deviation of the spherical outflow. However, the information available from our present data set is not well suited to addressing the issue of multiple stars, and this question must be deferred to another research project.

References

Anderson L.S., 1989, ApJ 339, 588

Auer L.H., Mihalas D., 1969, ApJ 158, 641

Barbá R., Niemela V., Baume G., Vazquez R., 1995, ApJ 446, L23

Barlow M.J, Cohen M., 1977, ApJ 213, 737

Bastian U., 1982, A&A 109, 245

Bates B., Gilheany S., 1990, MNRAS 243, 320

Beals C.S., 1951, Pub. Dominion Astrophys. Obs. 9, 1

Bernat A.P., Lambert D.L., 1978 PASP 90, 520

Becker S.R., Butler K., 1990, A&A 235, 326

Blomme R., Runacres M.C., 1995, A&A 309, 544

Blomme B., Runacres M.C., Vyverman K,. Cohen M., Leitherer C., Owocki S.P., 1997. In: Luminous Blue Variables: Massive Stars in Transition, ASP Conference Series, Vol. 120, eds. A. Nota & H.J.G.L.M. Lamers, p. 41

Blomme R., Runacres M.C., Vyverman K., Cohen M., Leitherer C., Owocki S.P., Haas M., 1998, Ap&SS 255, 145

Bohannan B., 1997. In: Luminous Blue Variables: Massive Stars in Transition, ASP Conference Series, Vol. 120, eds. A. Nota & H.J.G.L.M. Lamers, p. 3

Brown J.C., Richardson L.L., 1995. In: Wolf-Rayet Stars: Binaries Colliding Winds, Evolution, IAU Symp. 163, eds. K.A. van der Hucht & P.M. Williams, p. 186

Carpay J., De Jager C., Nieuwenhuijzen H., Moffat 1989, A&A 216, 143

Castor J.I., 1970, MNRAS 149, 111

Castor J.I., Abbott D.C., Klein J.K., 1975, ApJ 195, 157

Chiosi C., Maeder A., 1986, ARA&A 24, 329

Collozi R., 1993, A revised version of the ILLSS Catalogue, Bull. Inf. Centre Donnees Stellaires 43, 7

Conti P.S., 1984. In: Observational Tests of the Stellar Evolution Theory, eds. A. Maeder and A. Renzini, p. 233

Cox A.N., Guzik J.A., Soukup M.S., 1997. In: Luminous Blue Variables: Massive Stars in Transition, ASP Conference Series, Vol. 120, eds. A. Nota & H.J.G.L.M. Lamers, p. 133

Cox J.P., 1980. In: Theory of Stellar Pulsation, Princeton University Press

Cranmer S.R., 1996, Dissertation, University of Delaware

Cranmer S.R., Owocki S.P., 1996, ApJ 462, 469

Crowther P.A., Hillier D.J., Smith L.J., 1995, A&A 293, 172

Crowther P.A., 1997. In: Luminous Blue Variables: Massive Stars in Transition, ASP Conference Series, Vol. 120, eds. A. Nota & H.J.G.L.M. Lamers, p. 51

Damineli A., 1997. In: Luminous Blue Variables: Massive Stars in Transition, ASP Conference Series, Vol. 120, eds. A. Nota & H.J.G.L.M. Lamers, p. 272

Davidson K., 1989. In: Proceedings of the IAU Colloquium No. 113, Physics of Luminous Blue Variables, eds. K. Davidson, A.F.J. Moffat & H.J.G.L.M. Lamers, p. 101

Eversberg T., Lépine S., Moffat A.F.J., 1998, ApJ 494, 799

Feldmeier A., 1995, A&A 299 523

Feldmeier A., 1999. In: Proceedings of the IAU Colloquium No. 169, Variable and Non-spherical Stellar Winds in Luminous Hot Stars, Lecture Notes in Physics, Vol. 523, eds. B. Wolf, O. Stahl & A.W. Fullerton, p. 285

Feitzinger J.V. & Stüwe J.A., 1986, ApJ 305, 534

Fich M., Blitz L., Stark A.A., 1989, ApJ 342, 272

Fullerton A.W., 1990, Dissertation, University of Toronto

Fullerton A.W., Gies D.R., Bolton C.T., 1996, ApJS 103, 475

Gäng Th., 1993, Analyse hochaufgelöster Echelle–Spektren, Diplomarbeit, Landessternwarte Königstuhl, Universität Heidelberg

Gäng Th., Leitherer C., Wolf B., Stahl O., Chapman J., van Gent J., Lamers H.J.G.L.M., Scuderi S., 1997. In: Luminous Blue Variables: Massive Stars in Transition, ASP Conference Series, Vol. 120, eds. A. Nota & H.J.G.L.M. Lamers, p. 110

García-Segura G., Mac Low M-M, Langer N., 1996, A&A 305, 229

Glatzel W., 1997. In: Luminous Blue Variables: Massive Stars in Transition, ASP Conference Series, Vol. 120, eds. A. Nota & H.J.G.L.M. Lamers, p. 128

Glatzel W., 1998. In: A Half Century of Stellar Pulsation Interpretations: A Tribute to Arthur N. Cox, ASP Conference Series, Vol. 135, eds. P.A. Bradley & J. Guzik, p. 89

Guzik J.A., Cox A.N., Despain K.M., Soukup M.S., 1997. In: Luminous Blue Variables: Massive Stars in Transition, ASP Conference Series, Vol. 120, eds. A. Nota & H.J.G.L.M. Lamers, p. 138

Guzik J.A., Cox A.N., Despain K.M., Soukup M.S., 1999. In: Proceedings of the IAU Colloquium No. 169, Variable and Non-spherical Stellar Winds in Luminous Hot Stars, Lecture Notes in Physics, Vol. 523, eds. B. Wolf, O. Stahl & A.W. Fullerton, p. 337

Hillier D.J., 1991, A&A 247, 455

Hillier D.J., 1992. In: The Atmospheres of Early-Type Stars, eds. U. Heber & C.S. Jeffery, p. 105

Hillier D.J., Miller D.L., 1998, ApJ 496, 407

Hillier D.J., Crowther P.A., Najarro F., Fullerton A.W., 1998, A&A 340, 483

Hubeny I., Leitherer C., 1989, PASP 101, 114

Hubeny I., 1992. In: Lecture Notes in Physics, Vol. 401, eds. U. Heber & C.S. Jeffery, p. 377

Hubeny I., Lanz T., 1995, ApJ 439, 875

Hubeny I., 1996, atomic line lists distributed with TLUSTY 194/SYNSPEC 41 code

Humphreys R.M., Davidson K., 1994, PASP 106, 1025

Israelian G., 1995, A&A 300, 834 De Jager C., 1984, A&A 138, 246

Kaufer A., 1996, Dissertation, Landessternwarte Königstuhl, Universität Heidelberg

Kaufer A., Stahl O., Wolf B., Gäng Th., Gummersbach C.A., Kovács J., Mandel H., Szeifert Th., 1996, A&A 305, 887

Kaufer A., Stahl O., Wolf B., Gäng Th., Gummersbach C.A., Kovács J., Mandel H., Szeifert Th., 1997a, A&A 314, 599

Kaufer A., Stahl O., Wolf B., Fullerton A.W., Gäng Th., Gummersbach C.A., Jankovics I., Kovács J., Mandel H., Peitz J., Szeifert Th., 1997b, A&A 320, 273

Kenyon S.J, Gallagher J.S., 1985, ApJ 290, 542

Kiriakidis M., Fricke K.J., Glatzel W., 1993, MNRAS 264, 50

de Koter A., Ph.D. Thesis, University of Utrecht

de Koter A., Lamers H.J.G.L.M., Schmutz W., 1996, A&A 306, 501

de Koter A., 1997. In: Luminous Blue Variables: Massive Stars in Transition, ASP Conference Series, Vol. 120, eds. A. Nota & H.J.G.L.M. Lamers, p. 66

Kudritzki R.P., 1988. In: Radiation in moving gaseous media, Saas-Fee course No. 18, eds. Y. Chmielewski & T. Lanz.

Kudritzki R.P., Hummer D.G., 1990, ARA&A 28, 303

Kudritzki R.P., 1995, Quantitative Spectroscopy of Luminous Blue Stars in Distant Galaxies. In: ESO-Workshop: Science with the VLT, eds. J.R. Walsh & I.J. Danzinger, p. 246

Kudritzki R.P., Lennon D.J., Haser S.M., Puls J., Pauldrach A.W.A., Venn K., Voels S.A., 1996. In: Science with the Hubble Space Telescope – II, eds. P. Benvenuti, F.D. Machetto, E.J. Schreier, p. 285

Kudritzki R.P., Puls J., Lennon D.J., Venn K., Reetz J., Najarro F., McCarthy J.K., Herrero A., 1999, A&A 350, 970

Kurucz R.L., 1979, ApJS 40, 1

Kurucz R.L., 1992, The Stellar Populations of Galaxies. In: IAU Symposium No. 149, eds. A. Renzini & B. Barbuy, p. 225

Kurucz R., Bell B., 1995, CD-ROM No. 23: Atomic Line List, Smithsonian Astrophysical Observatory, Cambridge

Lamers H.J.G.L.M., 1987. In: Instabilities in Early-Type Stars, eds. H.J.G.L.M. Lamers & C.W.H. de Loore, p. 99

Lamers H.J.G.L.M., Cerruti-Sola M., Perinotto M., 1987, ApJ 314, 726

Lamers H.J.G.L.M., 1989. In: Physics of Luminous Blue Variables, eds. K. Davidson, A.F.J. Moffat, H.J.G.L.M. Lamers, IAU Colloquium 113, p. 271

Lamers H.J.G.L.M., Snow T.P., Lindholm D.M., 1995, ApJ 455, 269

Lamers H.J.G.L.M., 1995. In: Astrophysical Applications od Stellar Pulsation, ASP Conference Series, Vol. 83, eds. R.S. Stobie & P.A. Whitelock, p. 176

Lamers H.J.G.L.M., Najarro F., Kudritzki R.P., Morris P.W., Voors R.H.M., van Gent J.I., Waters L.B.F.M., de Graauw Th., Beintema D., Valentijn E.A., Hillier D.J., 1996, A&A 315, 229

Lamers H.J.G.L.M., 1997. In: Luminous Blue Variables: Massive Stars in Transition, ASP Conference Series, Vol. 120, eds. A. Nota & H.J.G.L.M. Lamers, p. 76

Lamers H.J.G.L.M., Livio M., Panagia N, Walborn N.R., 1998, ApJ 505, L131

Lamers H.J.G.L.M., Cassinelli J.P., 1999. In: Introduction to Stellar Winds, Cambridge University Press

Lamers H.J.G.L.M., Haser S, de Koter A, Leitherer C., ApJ 516, 872

Langer N., Hamann W.-R., Lennon M., Najarro F., Pauldrach A.W.A., Puls J., 1994, A&A 290, 819

Langer N., 1997. In: Luminous Blue Variables: Massive Stars in Transition, ASP Conference Series, Vol. 120, eds. A. Nota & H.J.G.L.M. Lamers, p. 83

Langer N., García-Segura G, Mac Low M-M., 1999, ApJ 520, L49

Ledoux P., 1951, ApJ 114, 373

Leitherer C., Schmutz W., Abbot D.C., Hamann W.-R., Wesselowski U., 1989, ApJ 346, 919

Leitherer C., Allen, R., Altner B., Damineli A., Drissen L., Idiart T., Lupie O., Nota A., Robert C., Schmutz W., Shore S.N., 1994, ApJ 428, 292

Leitherer C., Chapman J.M., Koribalski B., 1995, ApJ 450, 289

Leitherer C., 1997. In: Luminous Blue Variables: Massive Stars in Transition, ASP Conference Series, Vol. 120, eds. A. Nota & H.J.G.L.M. Lamers, p. 58

Lepine S., Moffat A.F.J., Henriksen R.N., 1996, ApJ 466, 392

Lomb N.R., 1976, Ap&SS 39, 447

Lovy D., Maeder A., Noëls A., Gabriel M., 1984, A&A 133, 307

Lucy L.B., 1976, ApJ 206, 499

Maeder A., Meynet G., 1988, A&AS 76, 411

Maeder A., 1992. In: Instabilities in evolved super- and hypergiants, eds. C. de Jager & H. Nieuwenhuijzen, p. 138

Mandel H., 1988, Dissertation, Landessternwarte Königstuhl, Universität Heidelberg

Mandel H., 1988, High Resolution Spectroscopy with a fiber-linked Echelle Spectrograph. In: IAU Symposium No. 132, eds. G. Cayrel de Strobel & M. Spite, p. 9

Markova M., 1994 A&AS 108, 561

Markova M., Zamanov R., 1995, A&AS 114, 499

Massey P., 2000, PASP in press

Meynet G., Maeder A., Schaller G., Schaerer D., Charbonnel C., 1994, A&A 103, 97

Mihalas D., 1978. In: Stellar Atmospheres, 2.nd edition, eds. G. Burbidge & M. Burbidge

Moffat A.F.J., Robert C., 1992, ASPC 22, 203

Moore Ch.E., 1972, A Multiplet Table of Astrophysical Interest, Part 1, Princeton Observatory, revised edition

Najarro F., 1995, Ph.D. Thesis, University of Munich

Najarro F., Hillier D.J., Stahl O., 1997, A&A 326, 1117

Nota A., Livio L., Clampin M., Schulte-Ladbeck R., 1995, ApJ 448, 788

Nota A., Pasquali A., Clampin M., Pollacco D., Scuseri S., Livio M., 1996, ApJ 473, 946

Nota A., Smith L., Pasquali A., Clampin M., Stroud M., 1997, ApJ 486, 338

Nota A., Clampin M., 1997. In: Luminous Blue Variables: Massive Stars in Transition, ASP Conference Series, Vol. 120, eds. A. Nota & H.J.G.L.M. Lamers, p. 303

Owocki S.P., Cranmer S.R., Gayley K.G., 1996, ApJ 472, 472L

Owocki S.P., 1999. In: Proceedings of the IAU Colloquium No. 169, Variable and Non-spherical Stellar Winds in Luminous Hot Stars, Lecture Notes in Physics, Vol. 523, eds. B. Wolf, O. Stahl & A.W. Fullerton, p. 294

Pauldrach A.W.A., Kudritzki R.P., Puls J., Butler K., Hunsinger J., 1994, A&A 283, 525

Pasquali A., Langer N., Schmutz W., Leitherer C., Nota A., Hubeny I., Moffat A.F.J., 1997, ApJ 478, 340

Prinja R.K., 1992. In: Nonisotropic and Variable Outflows from Stars, eds. L. Drissen, C. Leitherer, A. Nota, PASP Conf. Ser. 22, p. 167

Reid A.H.N., Bolton C.T., Crowe R.A., Fieldus M.S., Fullerton A.W., Gies D.R., Howarth I.D., McDavid D., Prinja R.K., Smith K.C., 1993, ApJ 417, 320

Riegel K.W., Crutcher R.M., 1972, A&A 18, 55

Rivinius Th., Stahl O., Wolf B., Kaufer A., Gäng Th., Gummersbach C.A., Jankovics I., Kovács J., Mandel H., Peitz J., Szeifert Th., Lamers H.J.G.L.M., 1997, A&A 318, 819

Saio H., Wheeler J.C., Cox J.P., 1984, ApJ 281, 318

Santolaya-Rey A.E., Puls J., Herrero A., 1997, A&A 488, 512

Scargle J.H., 1982, ApJ 263, 835

Schaller G., Schaerer D., Meynet G., Maeder A., 1992, A&AS 96, 269

Schmid-Burgk J.: 1982, A&A 108, 169

Schwarzenberg-Czerny A., 1993. In: Analysis of Astronomical Time Series, eds. P.J. Grosbøl, R.C.E. de Ruijsscher, ESO Conference and Workshop Proceedings, p. 47

Schrijvers C., Telting J.H., Aerts C., Ruymaekers E., Henrichs H.F., 1997, A&AS 121, 343

Scuderi S., Bonanno G., Spadaro D., Panagia N., Lamers H.J.G.L.M., de Koter A., 1994, ApJ 437, 465

Sobolev V.V., 1957, Soviet Astron.-A.J., 1, 678

Stahl O., Wolf B., Zickgraf F.-J., Bastian U., de Groot M.J.H., Leitherer C., 1983, A&A 120, 287

Stahl O., Mandel H., Szeifert Th., Wolf B., Zhao F., 1991 a, A&A 244, 467

Stahl O., Aab O., Smolinski J., Wolf B., 1991 b, A&A 252, 693

Stahl O., Mandel H., Wolf B., Gäng Th., Kaufer A., Kneer R., Szeifert Th., Zhao F., 1993, A&AS 99, 167

Stahl O., Wolf B., Gäng Th., Kaufer A., Mandel H., Szeifert Th., Zhao F., 1994, A&AS 107, 1

Stahl O., Kaufer A., Wolf B., Gäng Th., Gummersbach C., Kovács J., Mandel H., Rivinius Th., Szeifert Th., Zhao F., 1995, The Journal of Astronomical Data 1, 3

Stahl O., 1997. In: Luminous Blue Variables: Massive Stars in Transition, ASP Conference Series, Vol. 120, eds. A. Nota & H.J.G.L.M. Lamers, p. 100

Sterken C., 1981. In: The Most Massive Stars, eds. S. D'Odorico, D. Baade & K. Kjär, ESO workshop, p. 147

Sterken C., 1983, ESO Messenger 33, 10

Sterken C., Gosset E., Jüttner A., Stahl O., Wolf B., Axer M., 1991, A&A 247, 383

Sterken C., Stahl O., Wolf B., Szeifert Th., Jones A., 1995, A&A 303, 766

Stothers R.B., Chin C.A., 1993, ApJ 408, L85

Stothers R.B., Chin C.A., 1996, ApJ 468, 842

Telting J.H., Schrijvers C., 1997, A&A 317, 723

Townsend R.H.D., 1997, Dissertation, University College London

Tubessing S., Kaufer A., Schmid H.M., Stahl O., Wolf B., Maintz M., 1999. In: Thermal and Ionization Aspects of Flows from Hot Stars: Observations and Theory, ASP Conference Series, Tartu, Estonia, in press

Unno W., Osaki Y., Ando H., Shibahashi H., 1979. In: Nonradial Oscillations of Stars, University of Tokio Press

Unno W., Osaki Y., Ando H., Saio H., Shibahashi H., 1989. In: Nonradial Oscillations of Stars, 2.nd edition, University of Tokio Press

Unsöld A., Baschek B., 1988. In: Der neue Kosmos, 4th edn, Springer-Verlag, Berlin , p. 244

Vanbeveren D., 1994. In: Evolution of Massive Stars, eds. D. Vanbeveren, W. van Rensbergen & C. de Loore Space Science Reviews, Vol. 66, p. 327

Venn K.A., 1997. In: Luminous Blue Variables: Massive Stars in Transition, ASP Conference Series, Vol. 120, eds. A. Nota & H.J.G.L.M. Lamers, p. 95

Vidal C.R., Cooper J., Smith E.W., 1973, ApJS 25, 37

Vink J.S., de Koter A., Lamers H.J.G.L.M., A&A 350. 181

Walborn N.R., Fitzpatrick E.L., 2000, PASP in press

Waters L.B.F.M., Voors R.H.M., Morris P.W., Trams N.R., de Koter A., Lamers H.J.G.L.M.. In: Proceedings of the IAU Colloquium No. 169, Variable and Non-spherical Stellar Winds in Luminous Hot Stars, Lecture Notes in Physics, Vol. 523, eds. B. Wolf, O. Stahl & A.W. Fullerton, p. 381

Welty D.E., Hobbs L.M., Kulkarni V.P., 1994, ApJ 436, 152

Willis A.J., Howarth I.D., Stickland D.J., Heap S.R., 1989, ApJ 347, 413

Wolf B., Campusano L., Sterken C., 1974, A&A 36, 87

Wolf B., Stahl O., de Groot M.J.H., Sterken C., 1981, A&A 99, 351

Wolf B., Stahl O., 1982, A&A 112, 111

Wolf B., 1992, Luminous Blue Variables; Quiescent and eruptive states. In: Nonisotropic and Variable Outflows from Stars, ASP Conference Series Vol. 22, eds. L. Drissen, C. Leitherer & A. Nota, p. 327

Wolf B., Kaufer, A., 1997. In: Luminous Blue Variables: Massive Stars in Transition, ASP Conference Series, Vol. 120, eds. A. Nota & H.J.G.L.M. Lamers, p. 26

Appendix A: Spectral Catalogue (High Resolution, High S/N Mean Spectra)

In the following appendix we plot the mean heliocentric spectra of our high-resolution observations. For each object we summarize again the most important observing information. Note that no significant variations were observed during these observations so that averaging the spectra only improved the signal-to-noise (S/N) ratios without smearing of spectral features.

To our knowledge the given plots thus represent the highest quality (i.e. highest resolution *and* S/N) optical spectra of LBVs currently available and provide an ideal sample for sophisticated codes to model these objects.

The listed signal-to-noise ratios were derived using the typical S/N values of the individual spectra in the red wavelength region, as listed in Tables 4.1 – 4.3, and calculating the square root of the sum of the squared values, i.e.:

$$S_{mean} = \sqrt{\sum_{i=1}^{n} S_i^2}$$

with S_{mean} and S_i the mean and individual S/N ratios and n the number of individual spectra obtained in the respective wavelength region.

This approach is justified as we are in the photon dominated regime of noise with our high S/N spectra. The achieved values were rounded to the next zero-digit integer number and checked by measuring a few spectra interactively (with IRAF's splot routine) at the continuum level around 6400 Å. Note that the S/N ratio depends strongly on the observed wavelength region as the efficiency of the spectrographs decreases rapidly in the blue wavelength range. Also the S/N ratio in the strong emission lines can be substantially higher than the surrounding continuum values (e.g. the maximum S/N of the mean P Cygni spectrum in the Hα emission line is about 1100 compared to ∼450 for the continuum).

To take advantage of the high resolution we have stretched the spectra onto small y-axis plots and did not annotate the spectral lines to maximize the available space.

Table 1.1 lists the visual brightness and coordinates of the observed objects and gives a summary of the essential observing information (i.e. observing time, location, instrument and resolution). The details of each observation are listed in Tables 4.1 – 4.3.

A.1 Mean Spectrum of P Cygni

- Observing instrument: CFT/KPNO

- Observing date: May 20 – 22, 1996

- Observed wavelength range: 3920 – 7030 Å

- Spectral resolution: 100 000

- S/N ratio at 6400 Å: 450
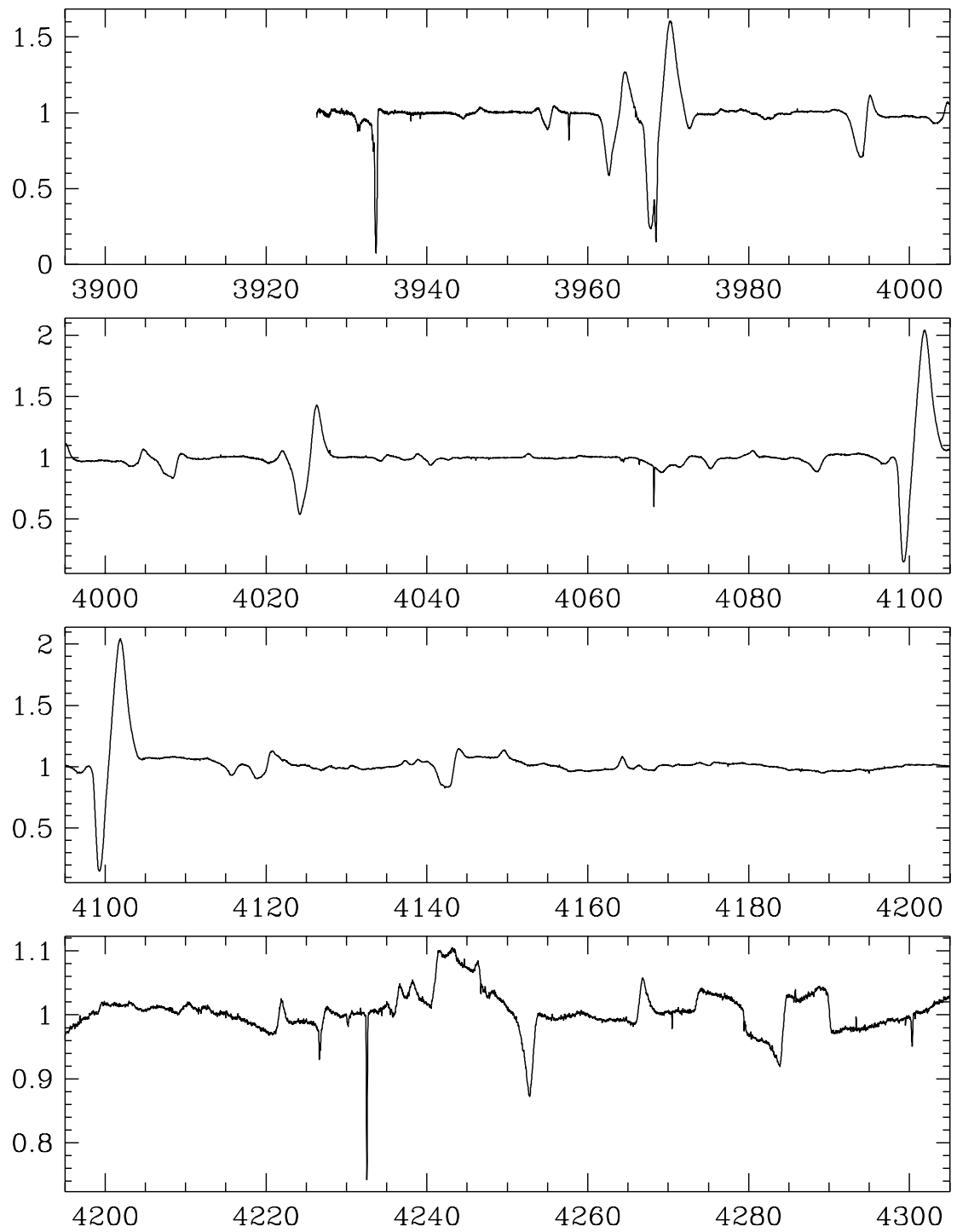
Figure A.1: Mean spectrum of P Cygni from 3900−4300 Å; observed on May 20, 1995.
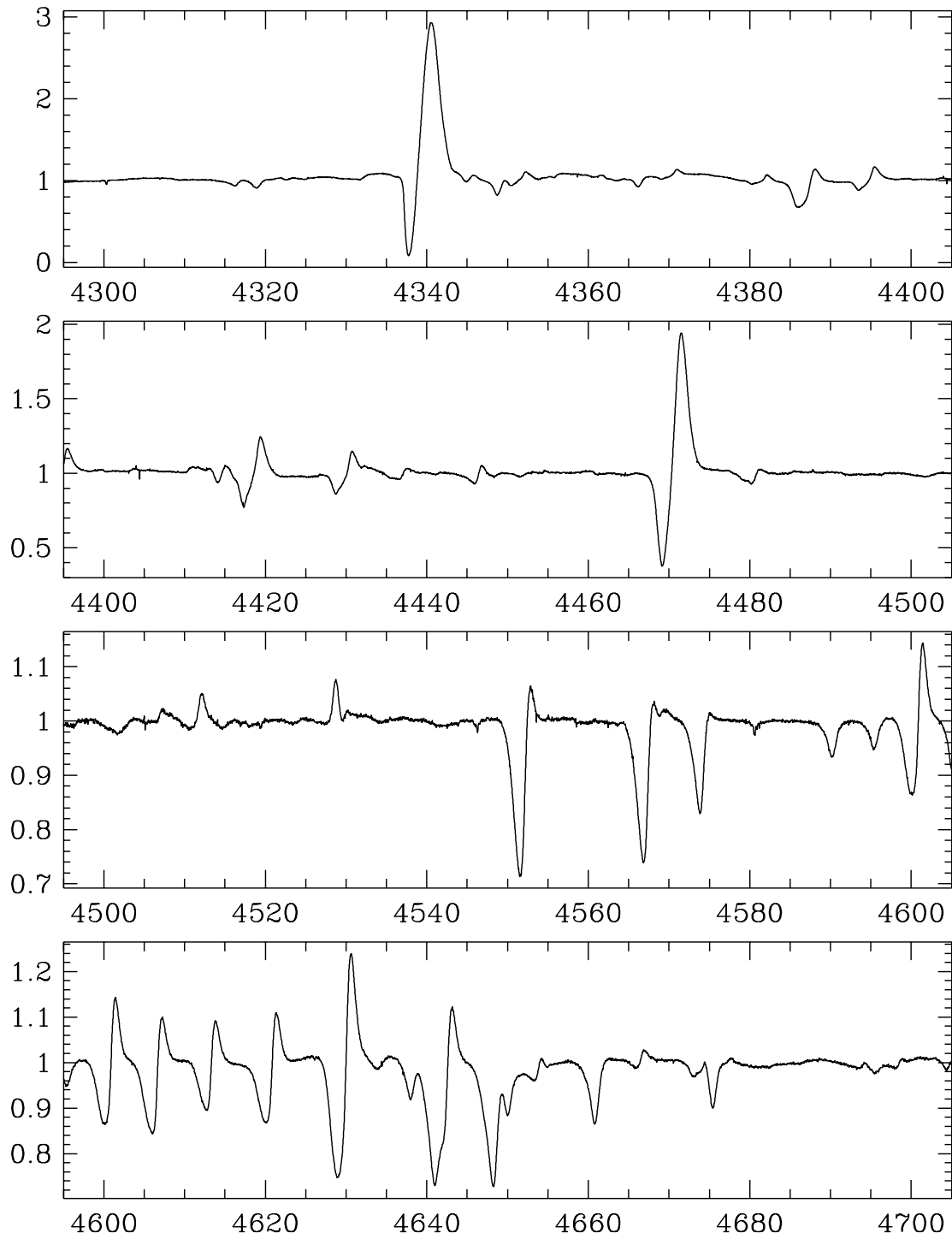
Figure A.2: Mean spectrum of P Cygni from 4300−4700 Å; observed on May 20 and May 21, 1995.
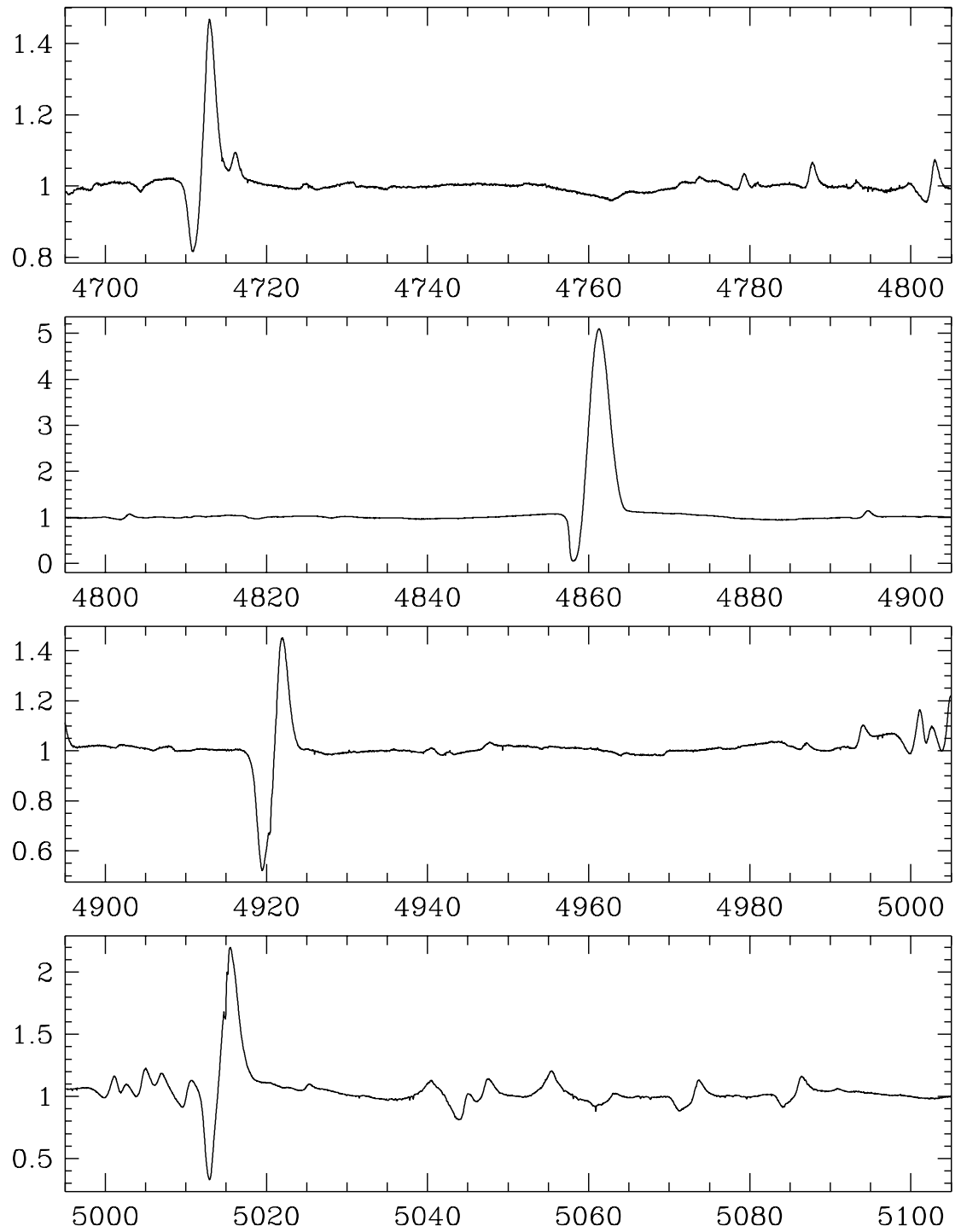
Figure A.3: Mean spectrum of P Cygni from 4700–5100 Å; observed on May 21, 1995.
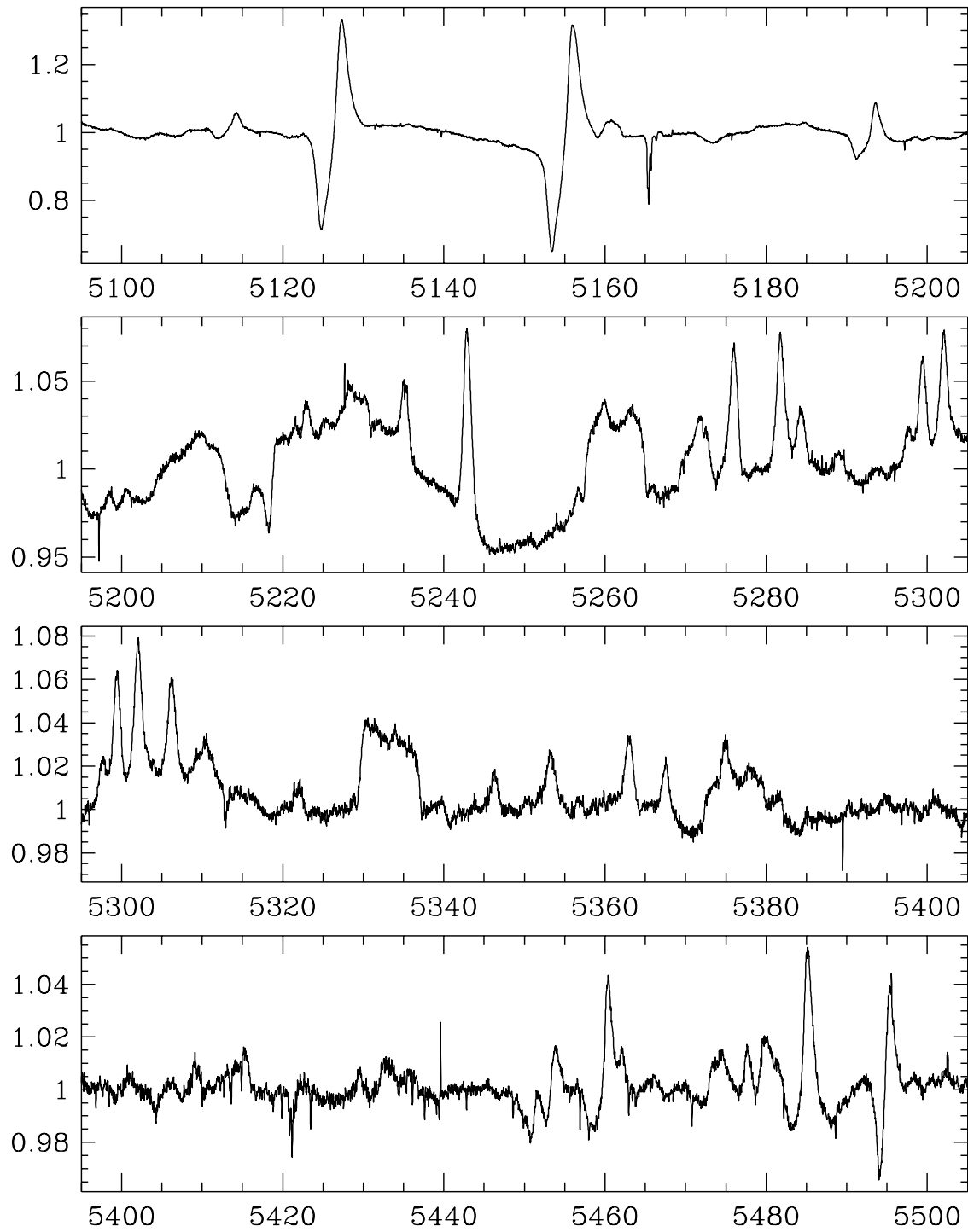
Figure A.4: Mean spectrum of P Cygni from 5100 – 5500 Å; observed on May 21, 1995.
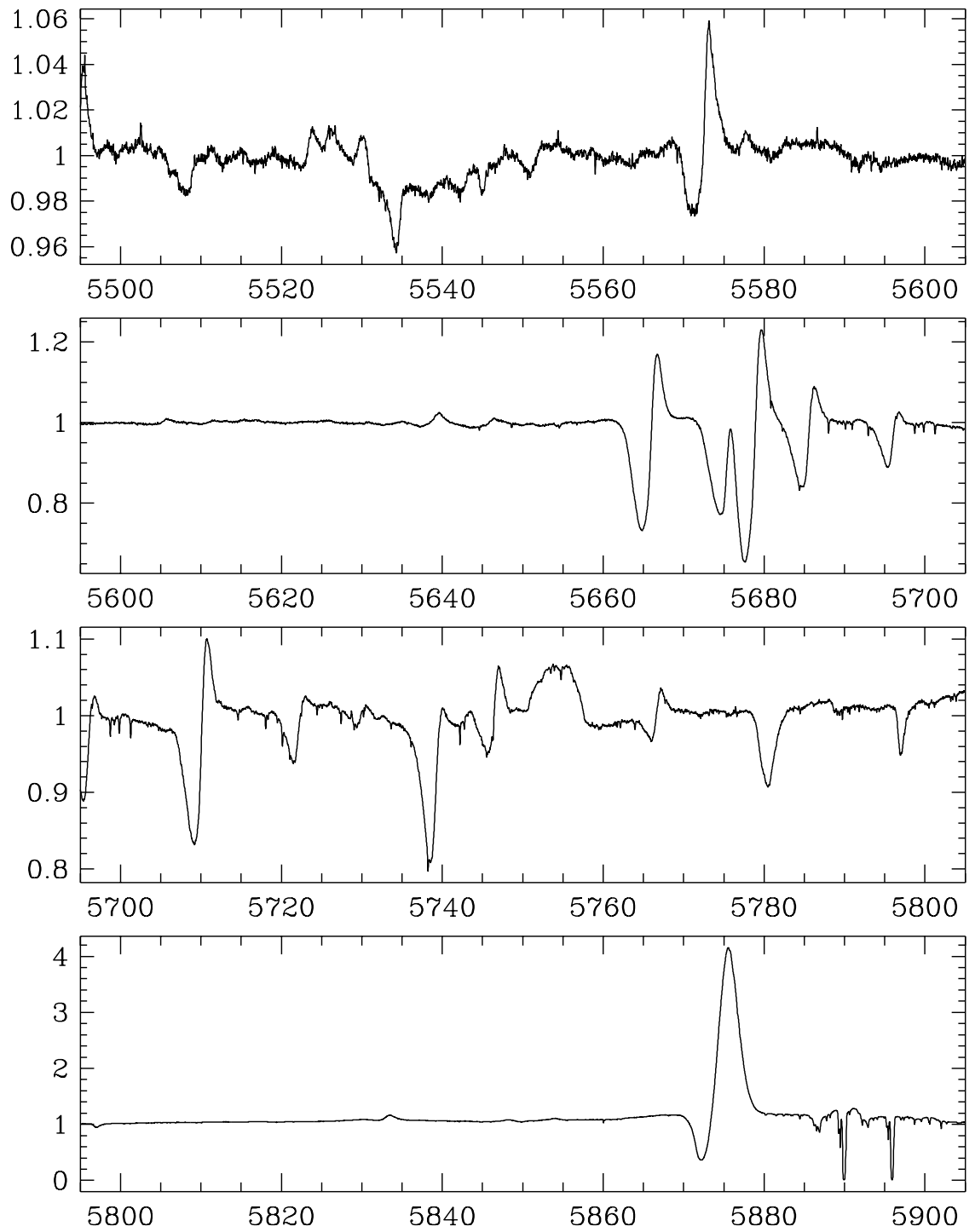
Figure A.5: Mean spectrum of P Cygni from 5500–5900 Å; observed on May 22, 1995.
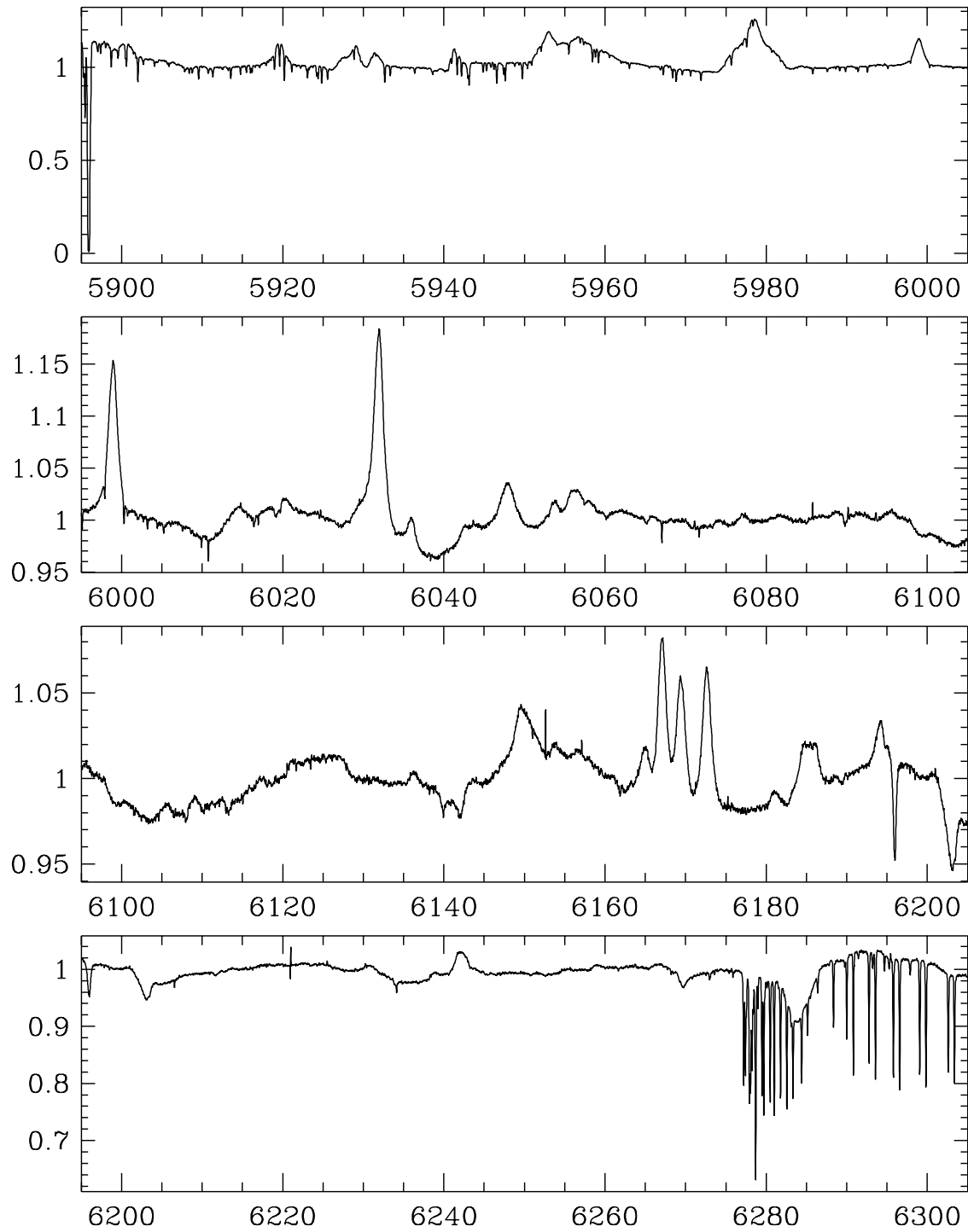
Figure A.6: Mean spectrum of P Cygni from 5900 – 6300 Å; observed on May 22, 1995.
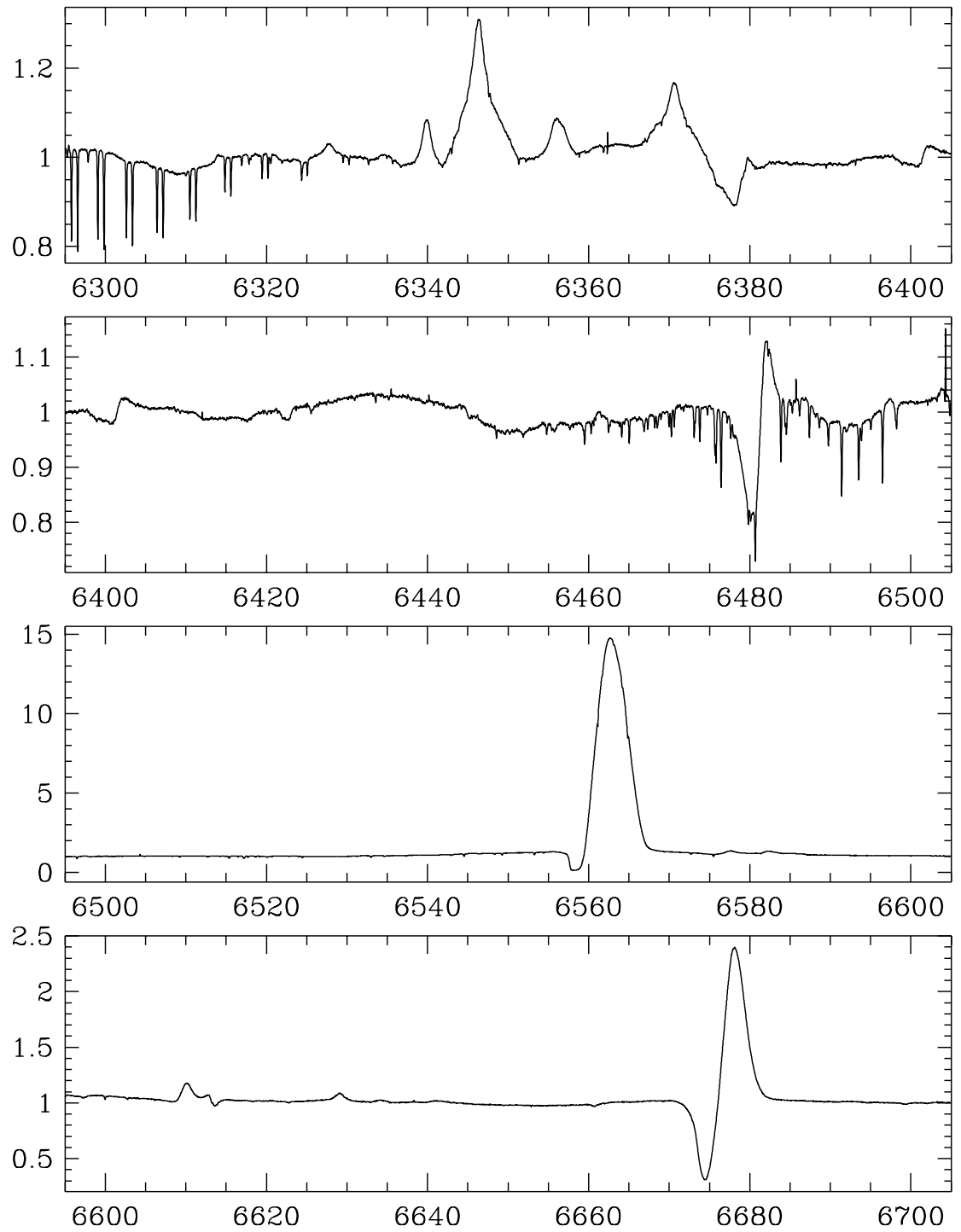
Figure A.7: Mean spectrum of P Cygni from 6300–6700 Å; observed on May 22, 1995.
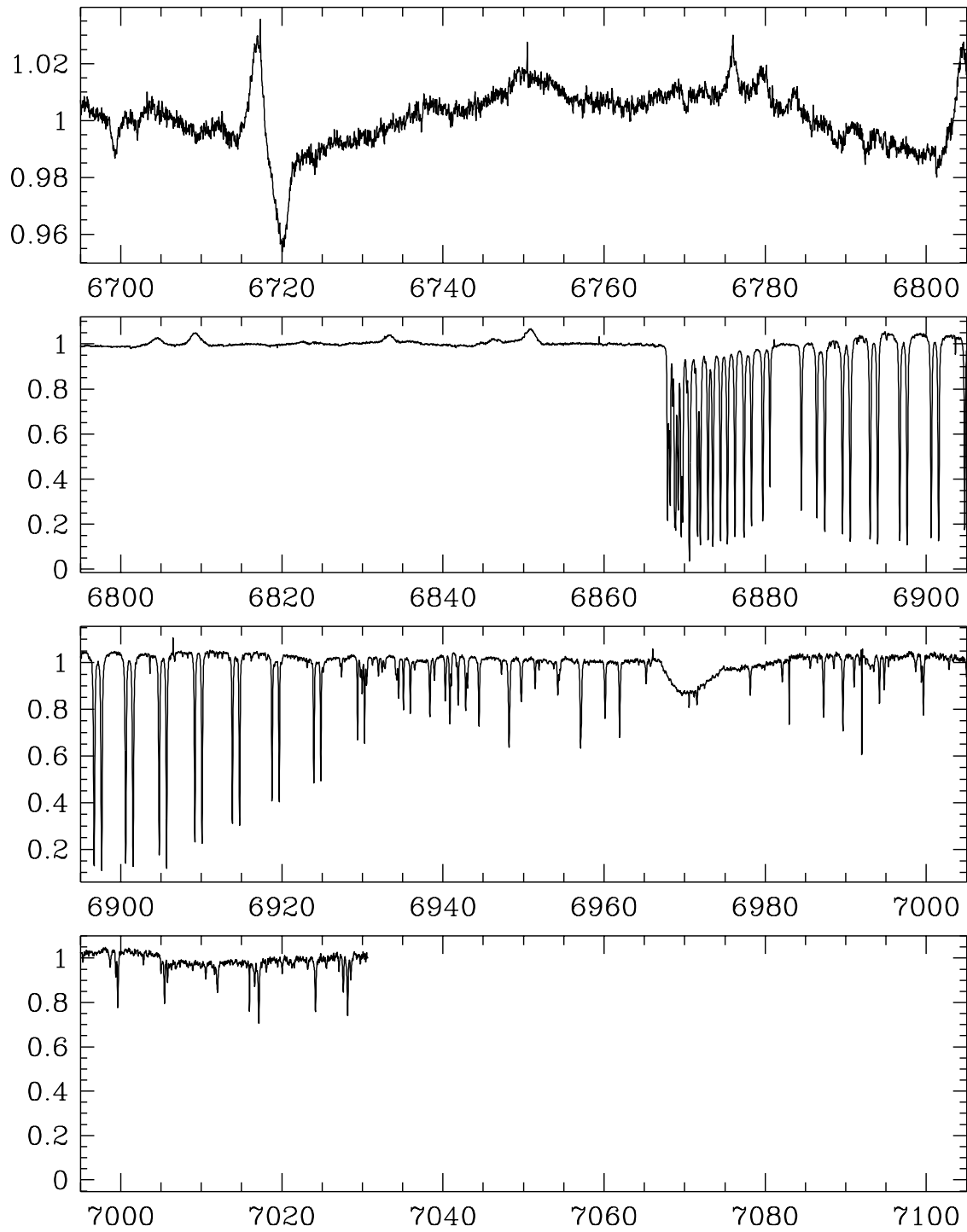
Figure A.8: Mean spectrum of P Cygni from 6700 − 7100 Å; observed on May 22, 1995.

A.2 Mean Spectrum of HD 160529

- Observing instrument: UCLES/AAT

- Observing date: October 4, 1995

- Observed wavelength range: $3600 - 6800$ Å

- Spectral resolution: 50 000

- S/N ratio at 6400 Å: 200
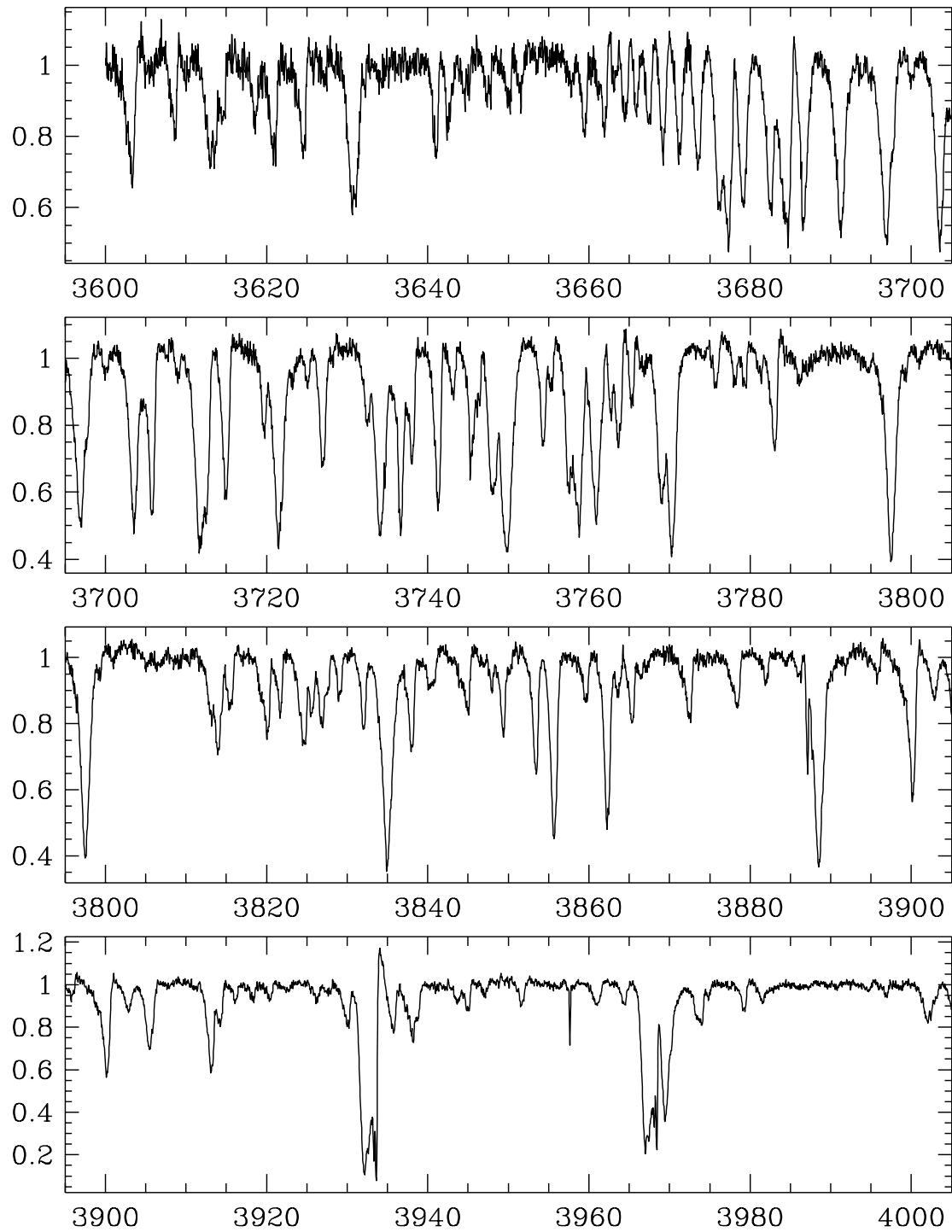
Figure A.9: Mean spectrum of HD 160529 from 3600–4000 Å; observed on Oct 4, 1995.
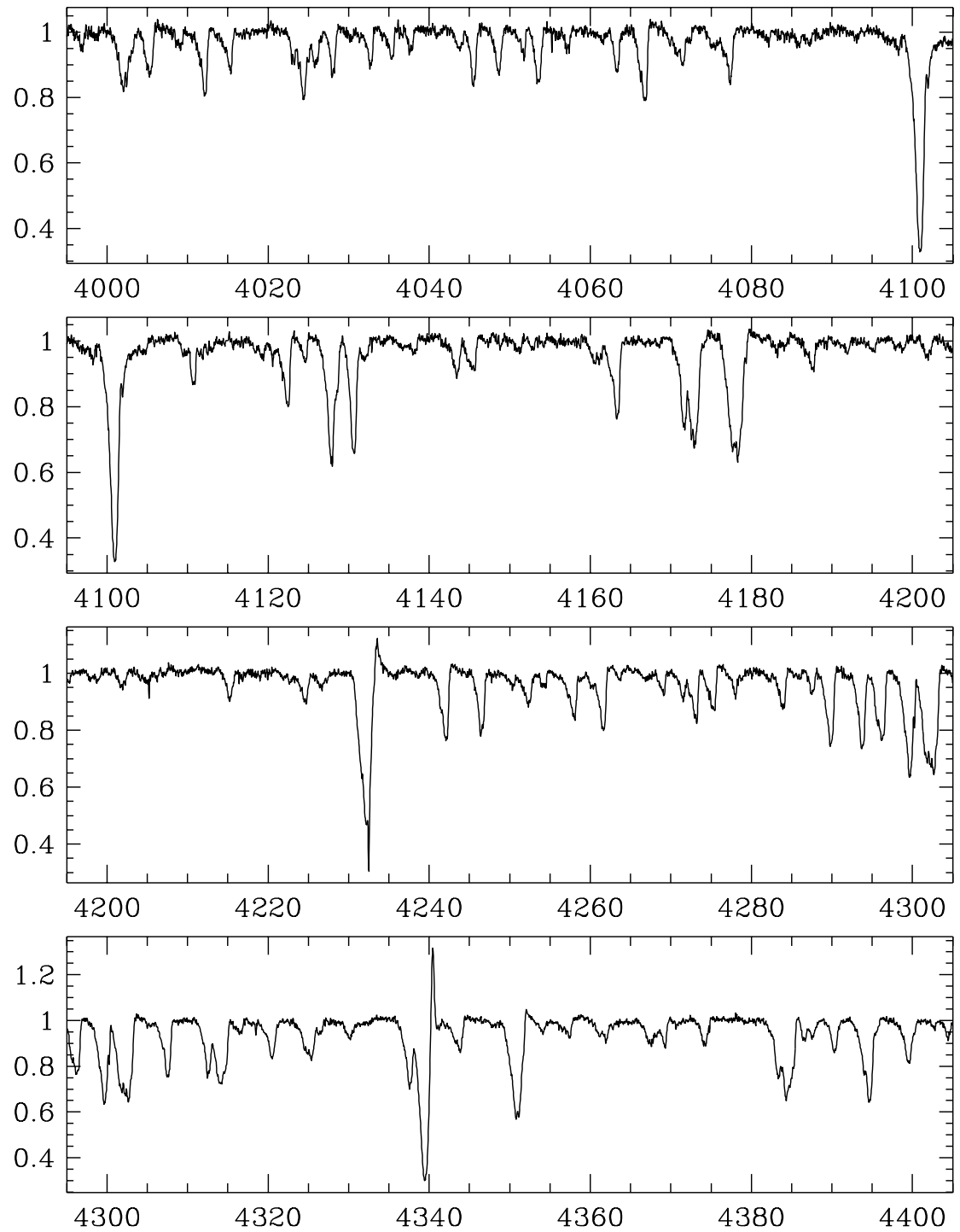
Figure A.10: Mean spectrum of HD 160529 from 4000–4400 Å; observed on Oct 4, 1995.
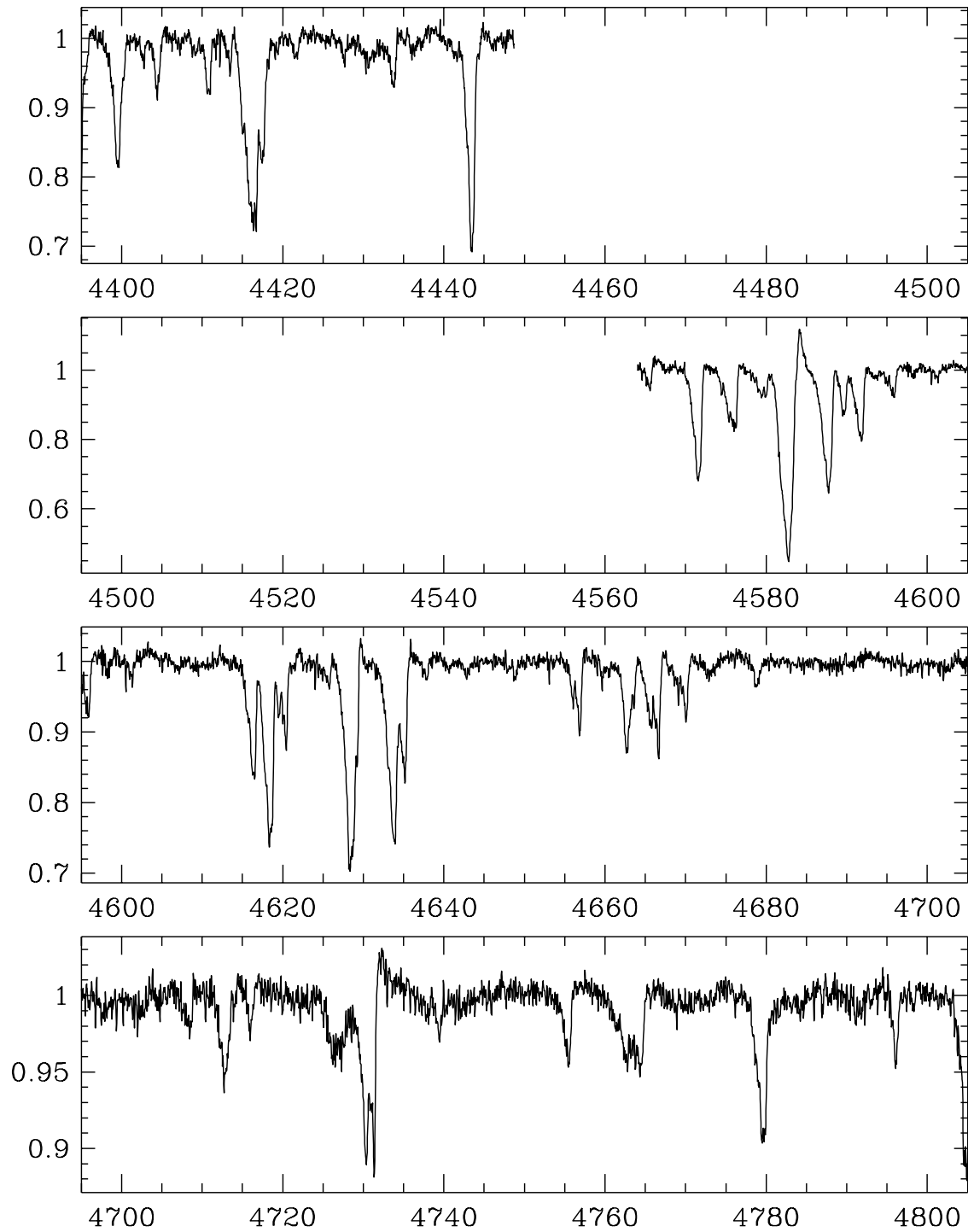
Figure A.11: Mean spectrum of HD 160529 from 4400−4800 Å; observed on Oct 4, 1995.
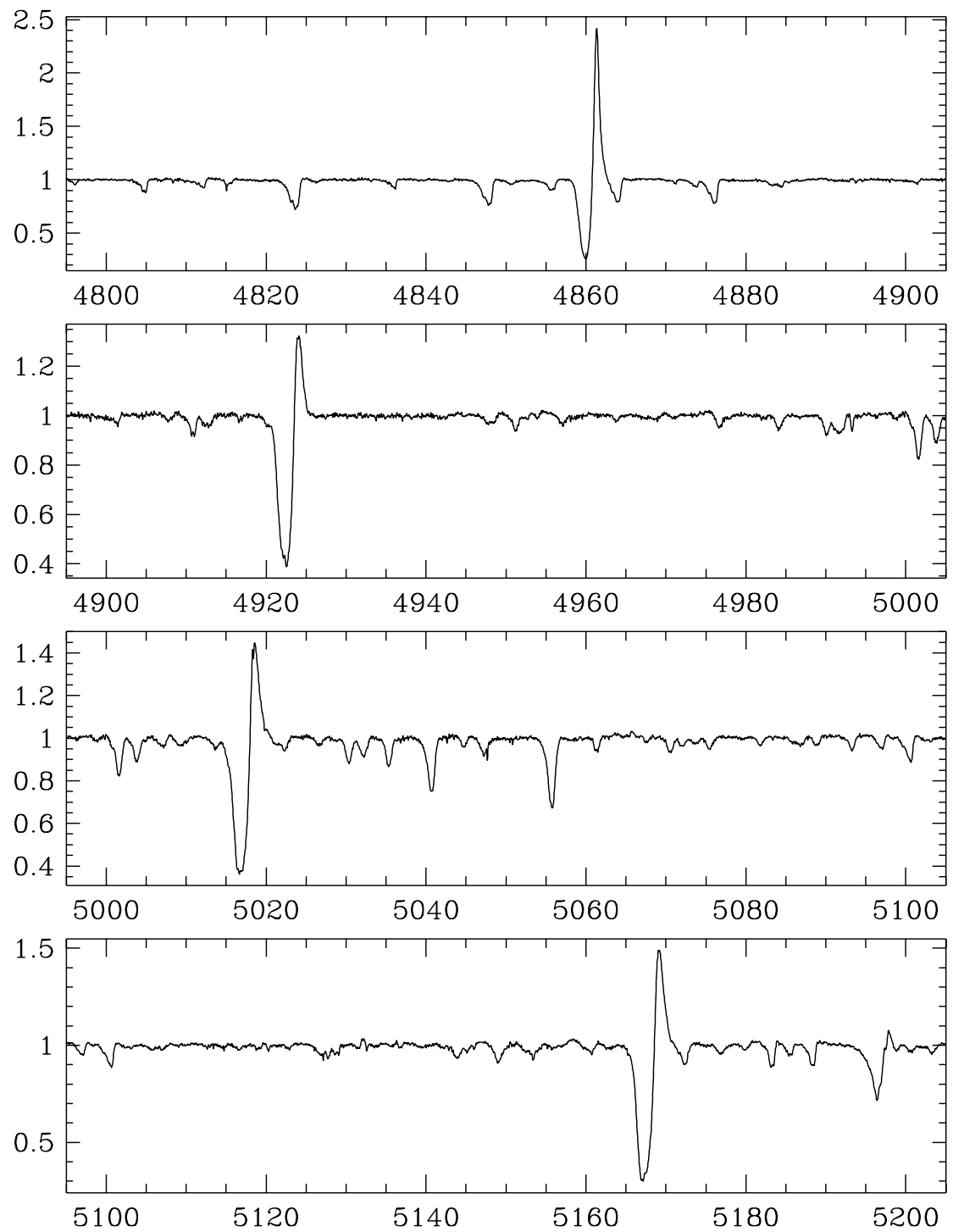
Figure A.12: Mean spectrum of HD 160529 from 4800 – 5200 Å; observed on Oct 4, 1995.
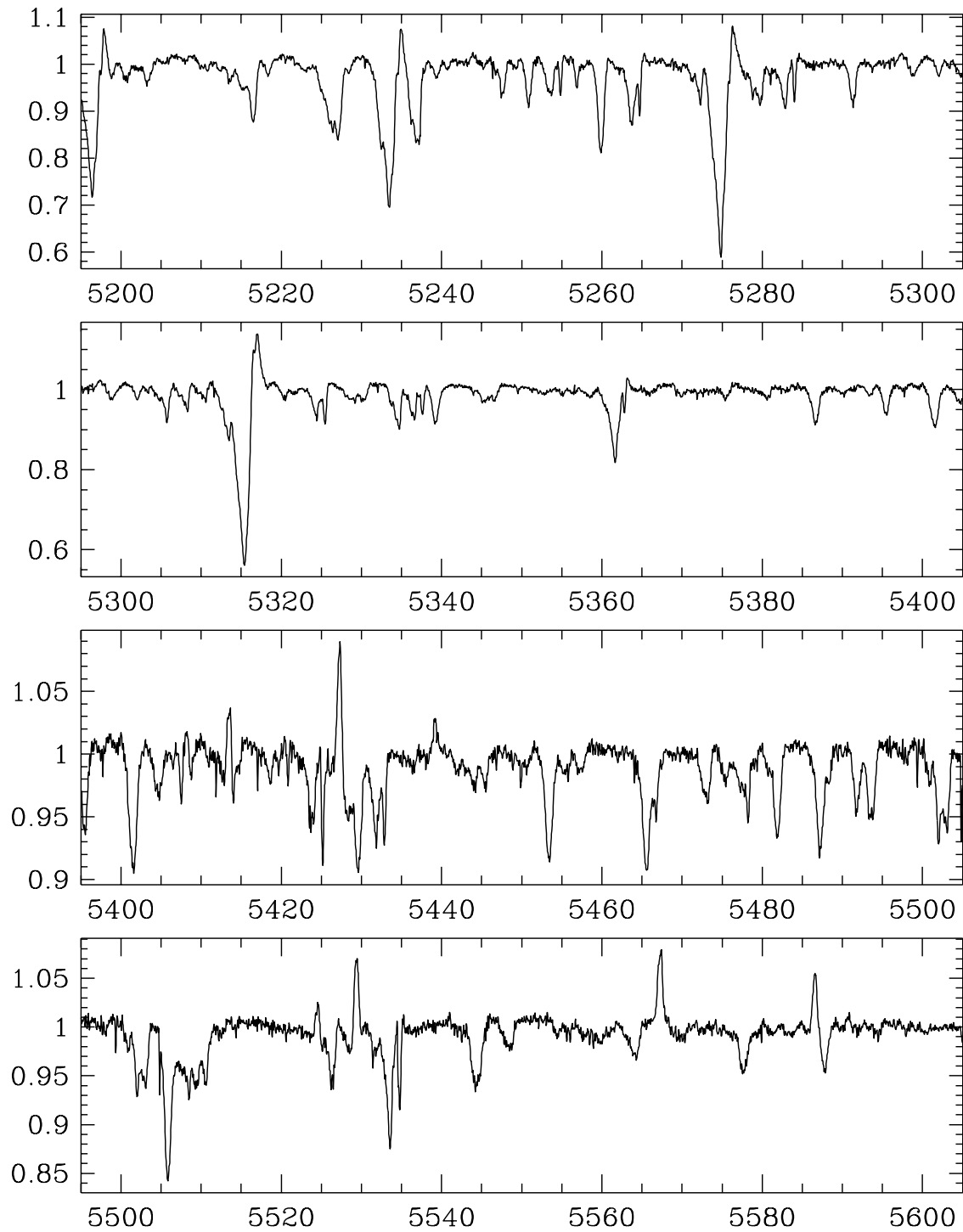
Figure A.13: Mean spectrum of HD 160529 from 5200−5600 Å; observed on Oct 4, 1995.
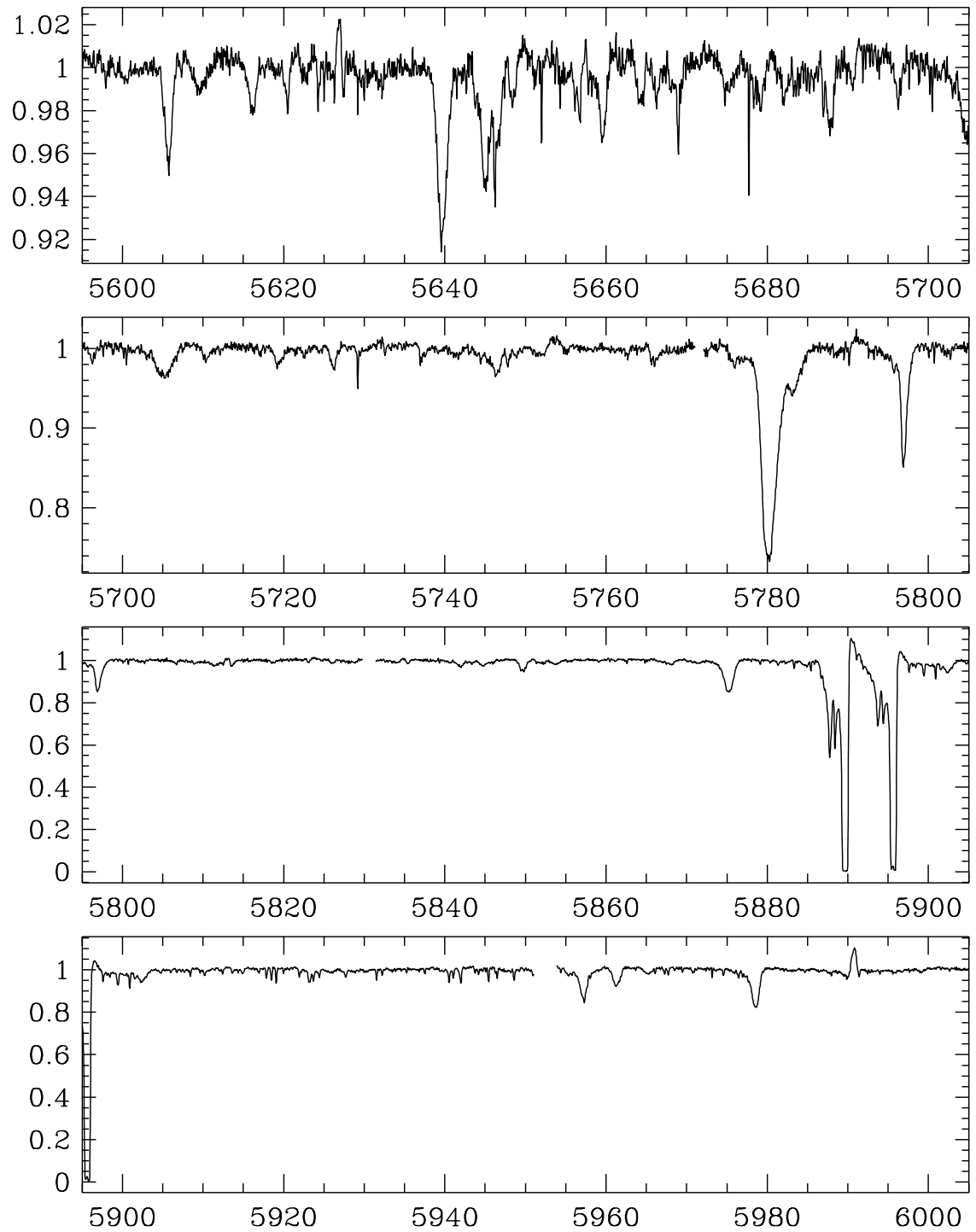
Figure A.14: Mean spectrum of HD 160529 from 5600 – 6000 Å; observed on Oct 4, 1995.
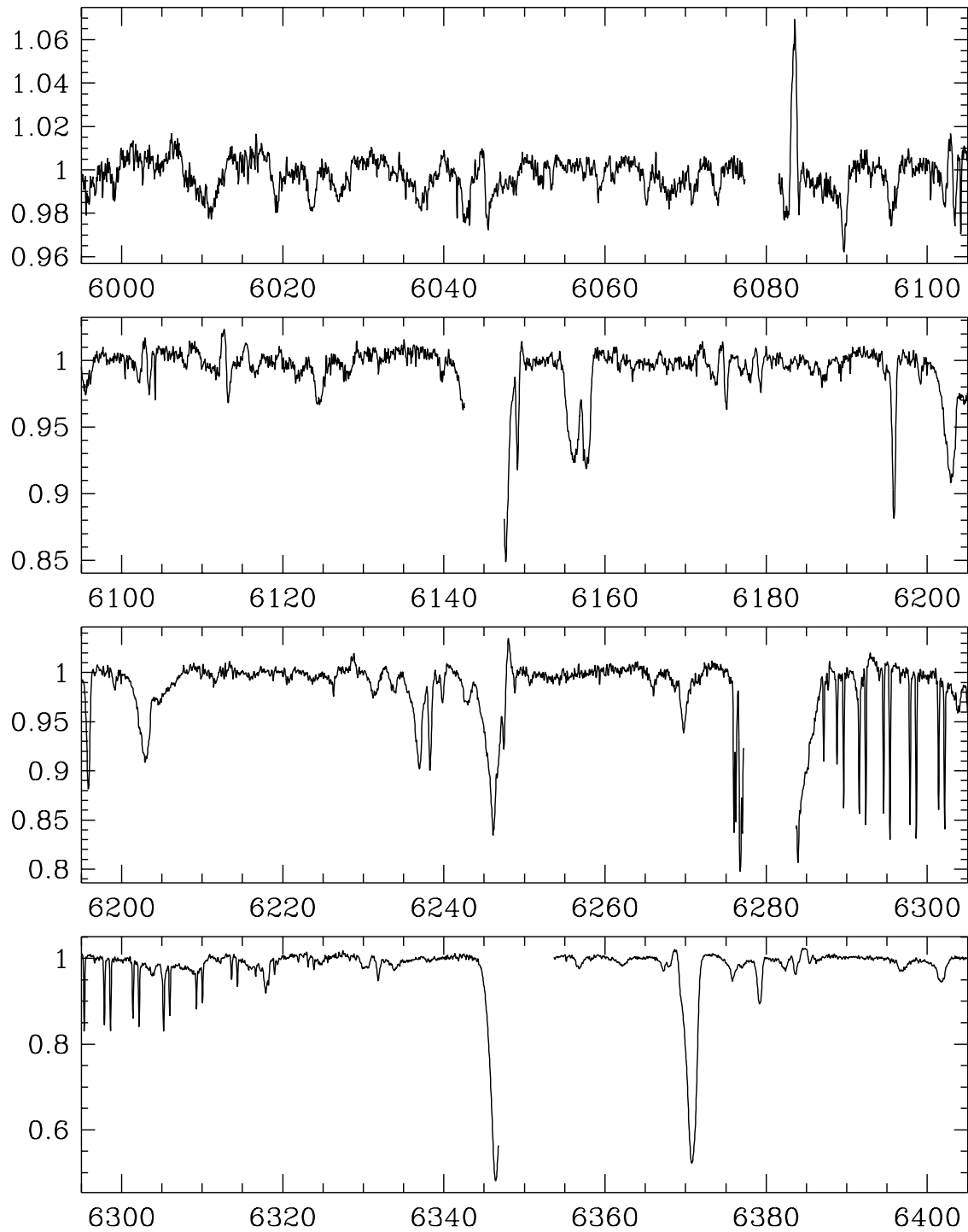
Figure A.15: Mean spectrum of HD 160529 from 6000 − 6400 Å; observed on Oct 4, 1995.
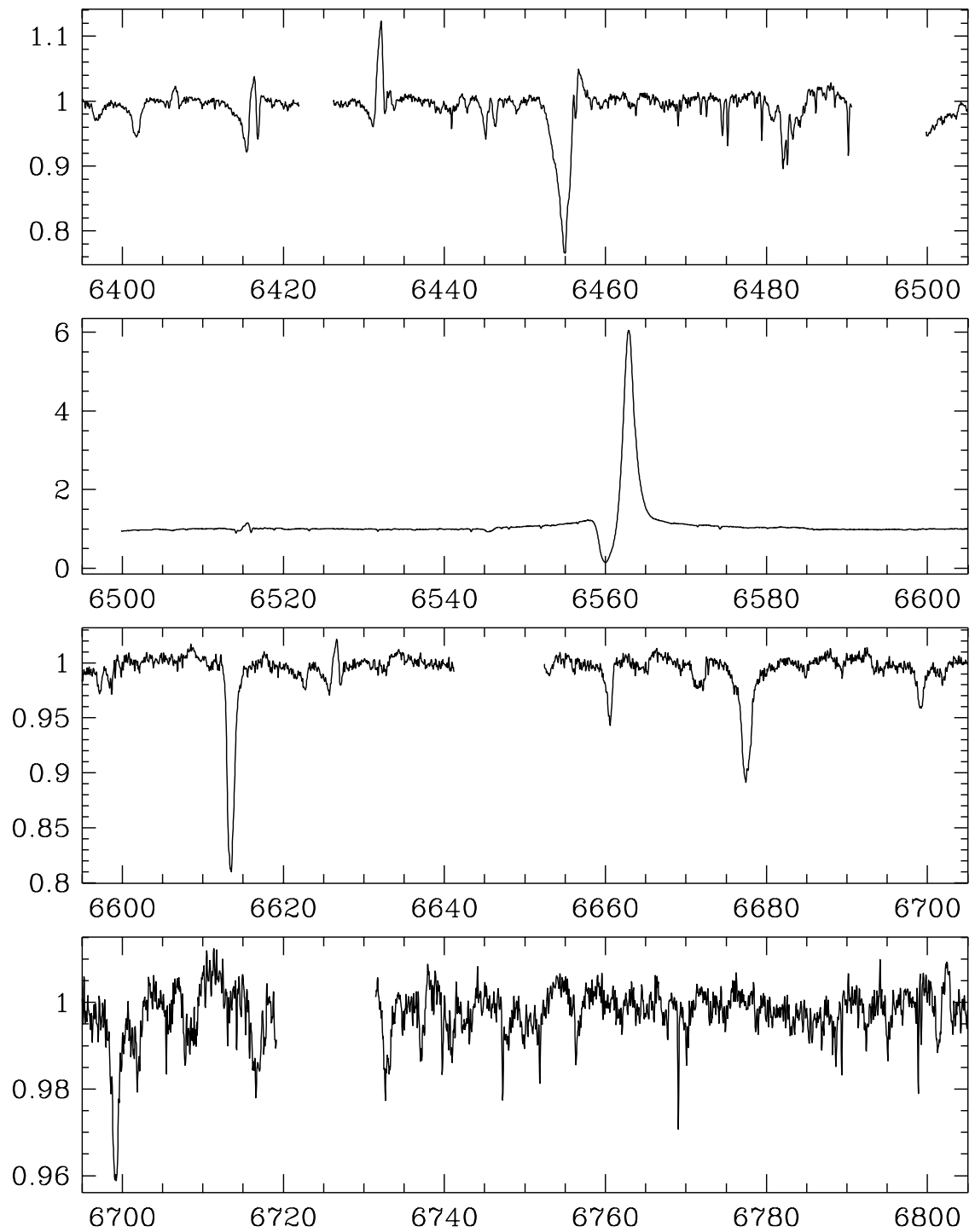
Figure A.16: Mean spectrum of HD 160529 from 6400 – 6800 Å; observed on Oct 4, 1995.

A.3 Mean Spectrum of HD 168607

- Observing instrument: UCLES/AAT

- Observing date: October 4, 1995

- Observed wavelength range: $3600 - 6800\,\text{Å}$

- Spectral resolution: $50\,000$

- S/N ratio at $6400\,\text{Å}$: 200
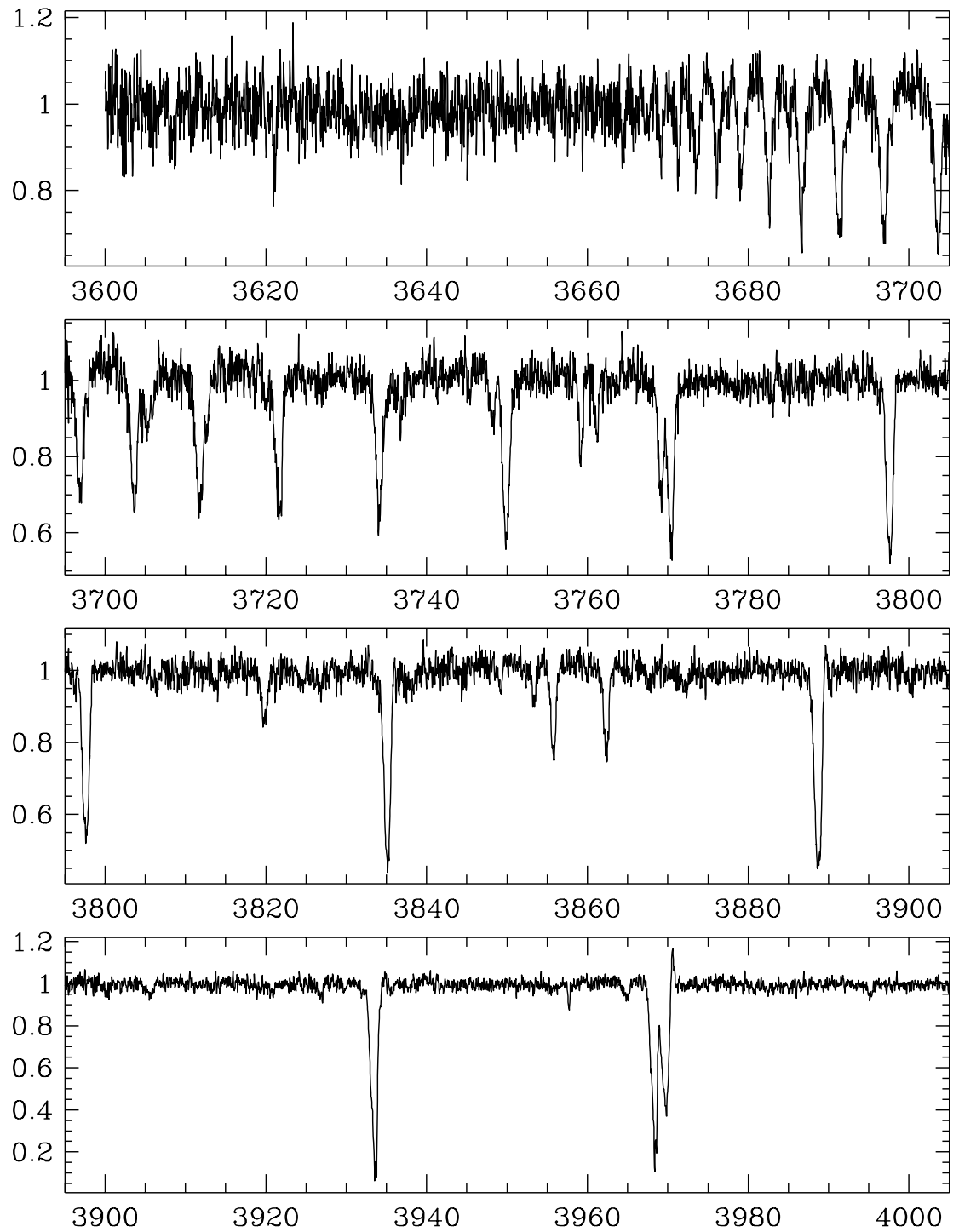
Figure A.17: Mean spectrum of HD 168607 from 3600–4000 Å; observed on Oct 4, 1995.
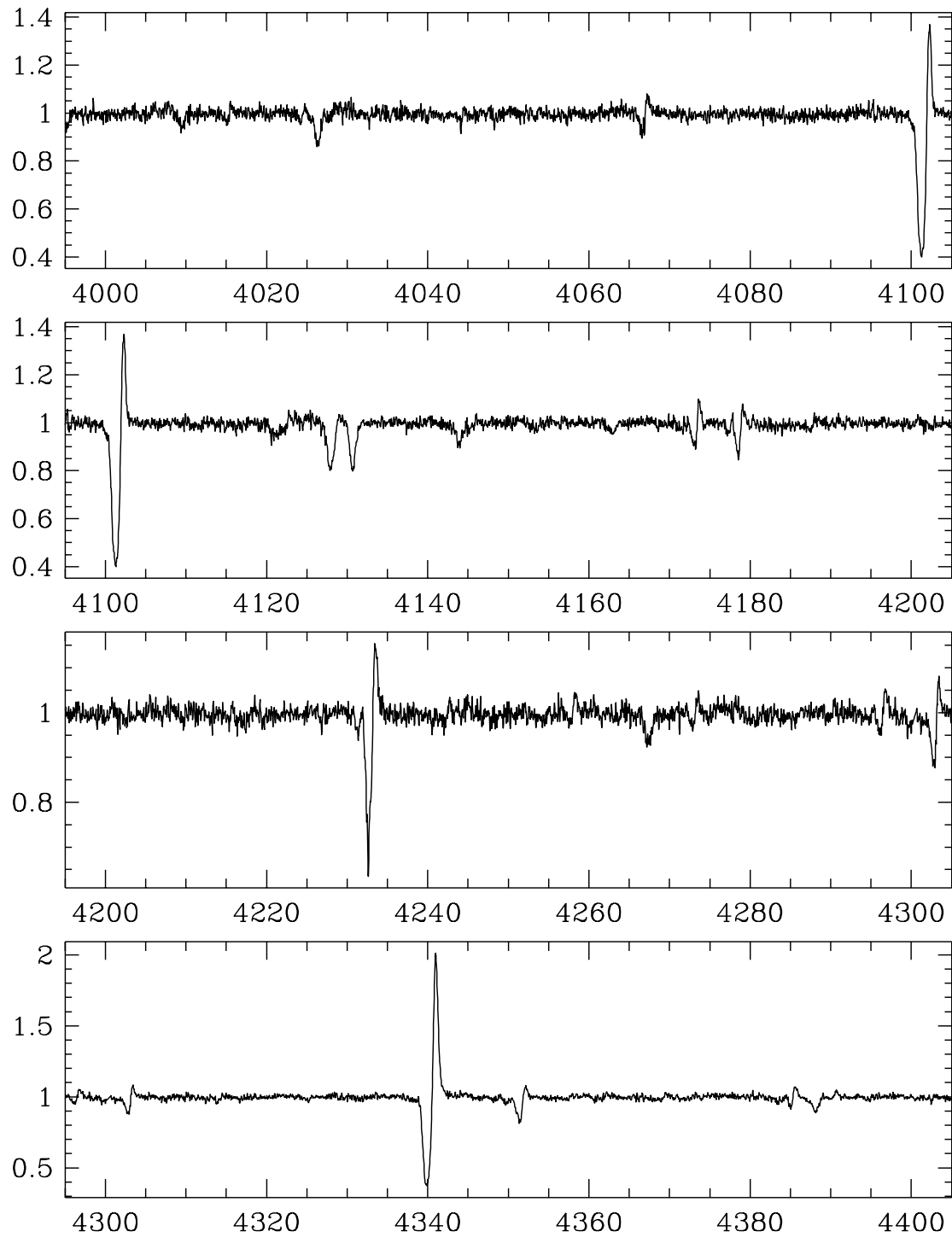
Figure A.18: Mean spectrum of HD 168607 from 4000−4400 Å; observed on Oct 4, 1995.
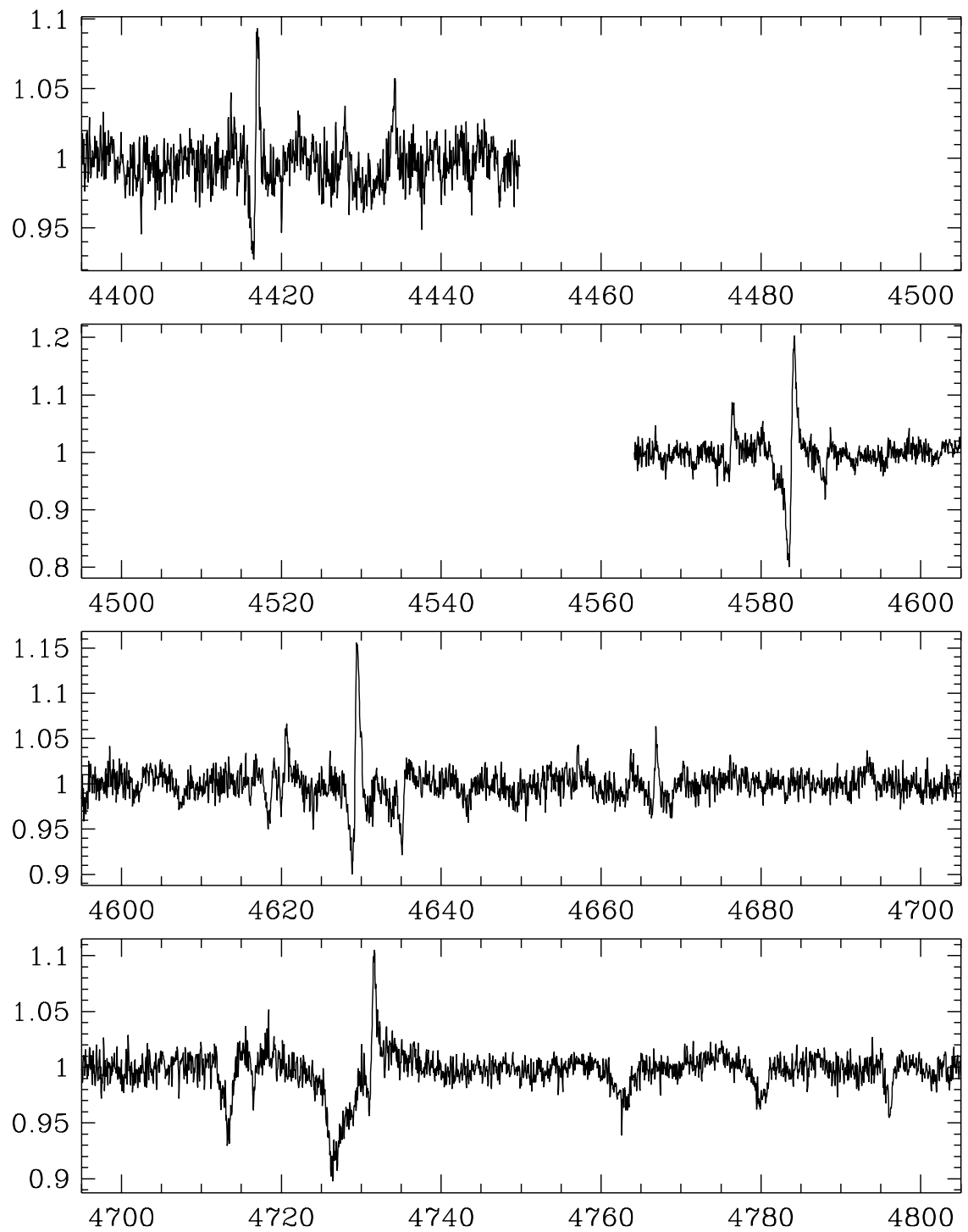
Figure A.19: Mean spectrum of HD 168607 from 4400 – 4800 Å; observed on Oct 4, 1995.
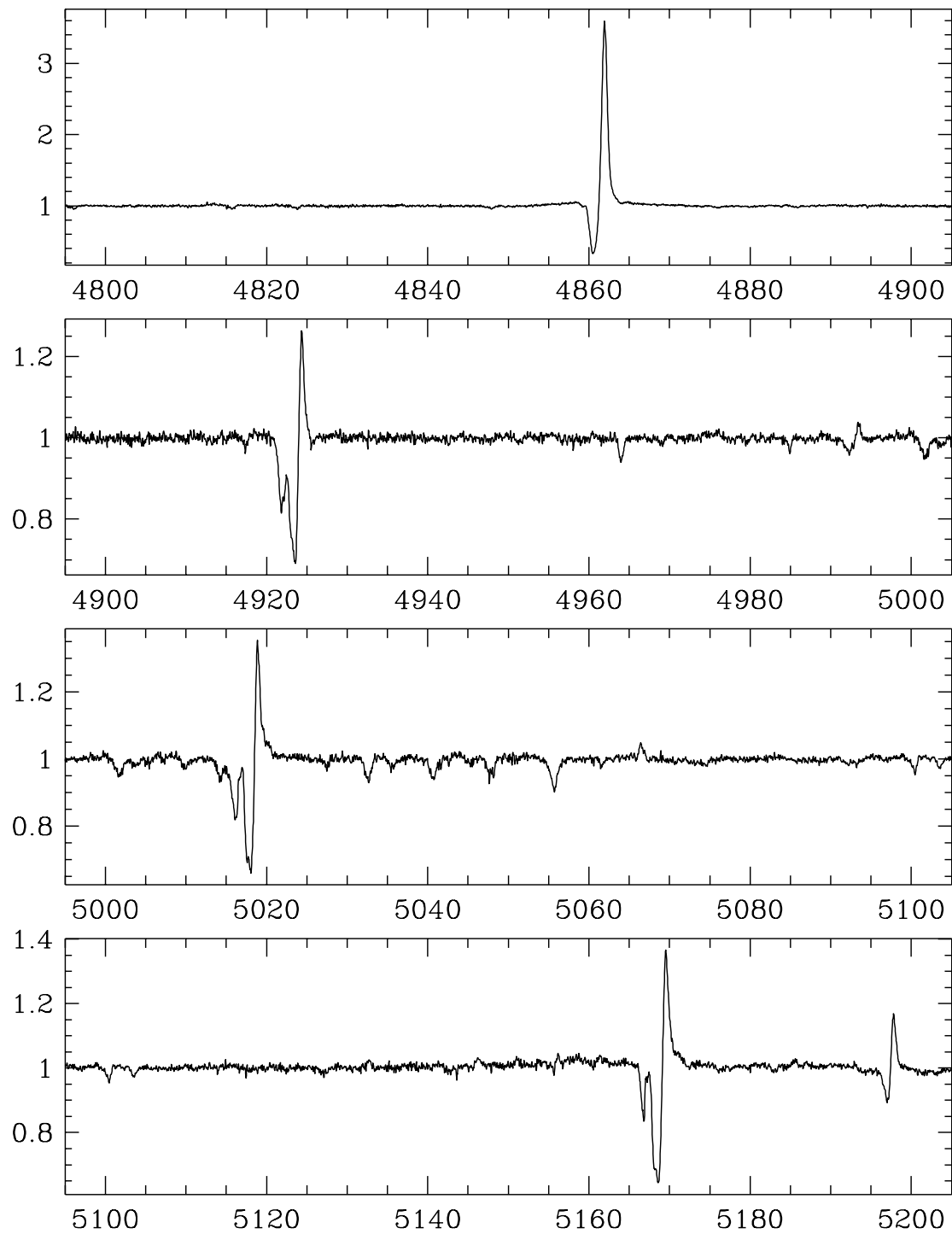
Figure A.20: Mean spectrum of HD 168607 from 4800−5200 Å; observed on Oct 4, 1995.
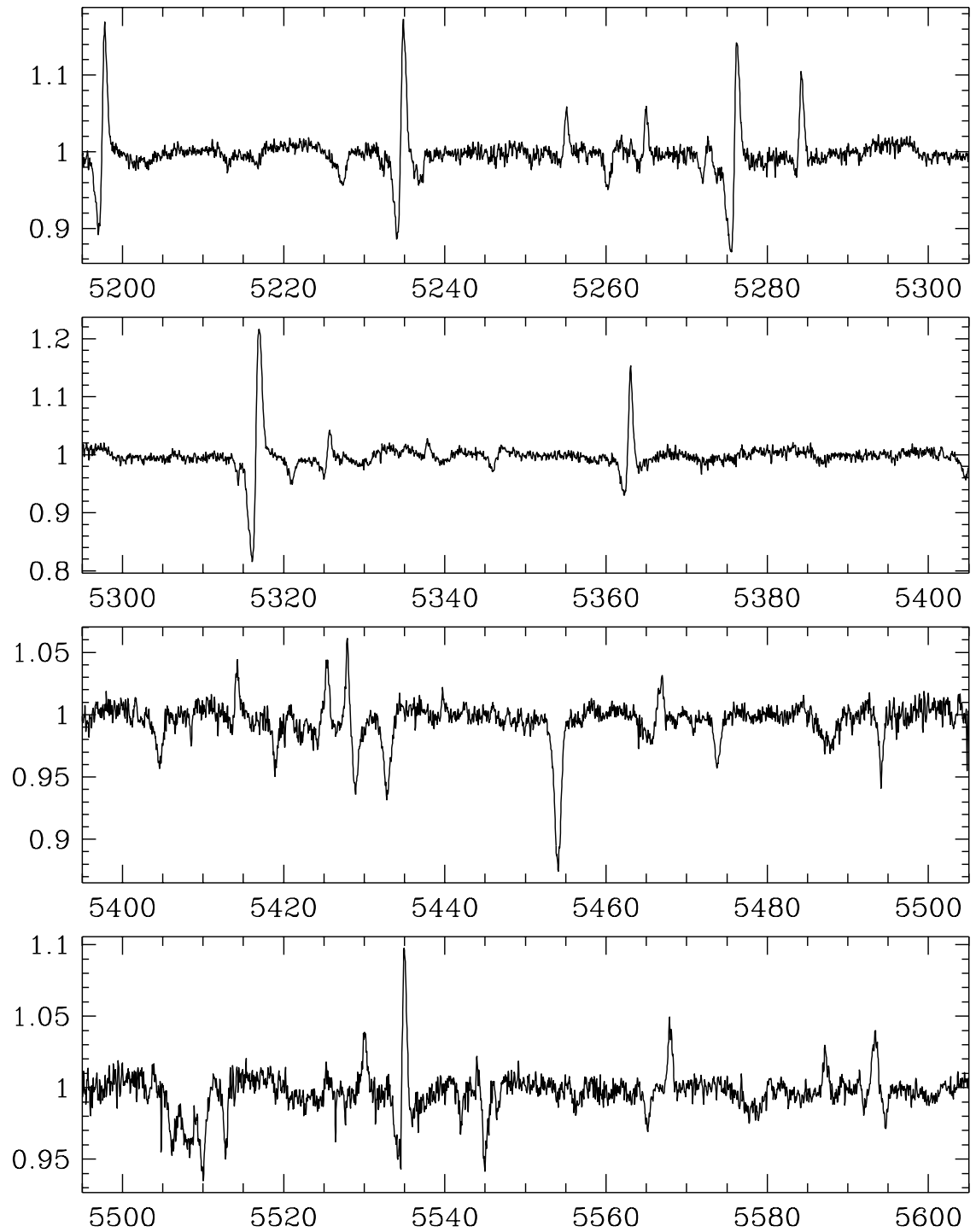
Figure A.21: Mean spectrum of HD 168607 from 5200 – 5600 Å; observed on Oct 4, 1995.
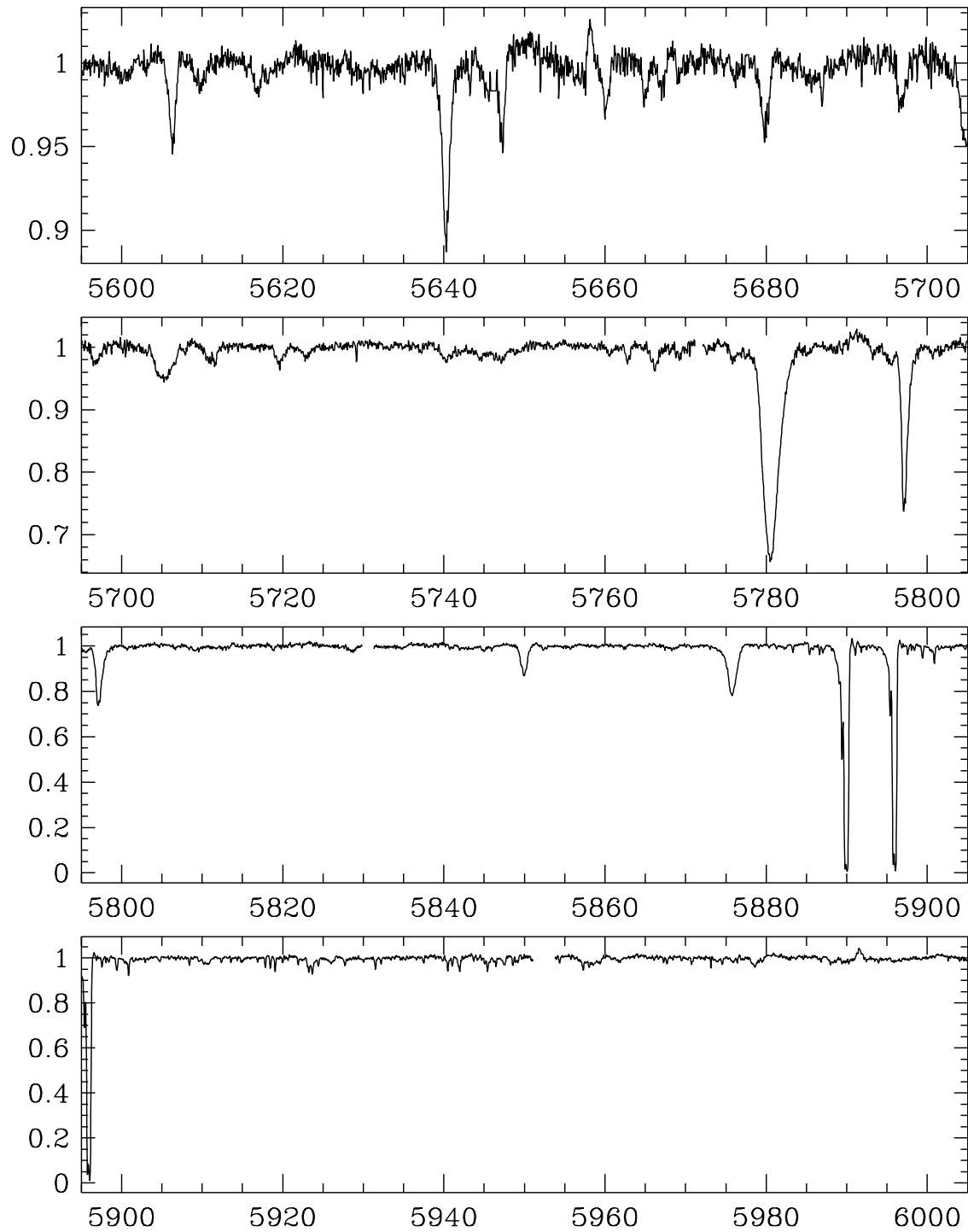
Figure A.22: Mean spectrum of HD 168607 from 5600 − 6000 Å; observed on Oct 4, 1995.
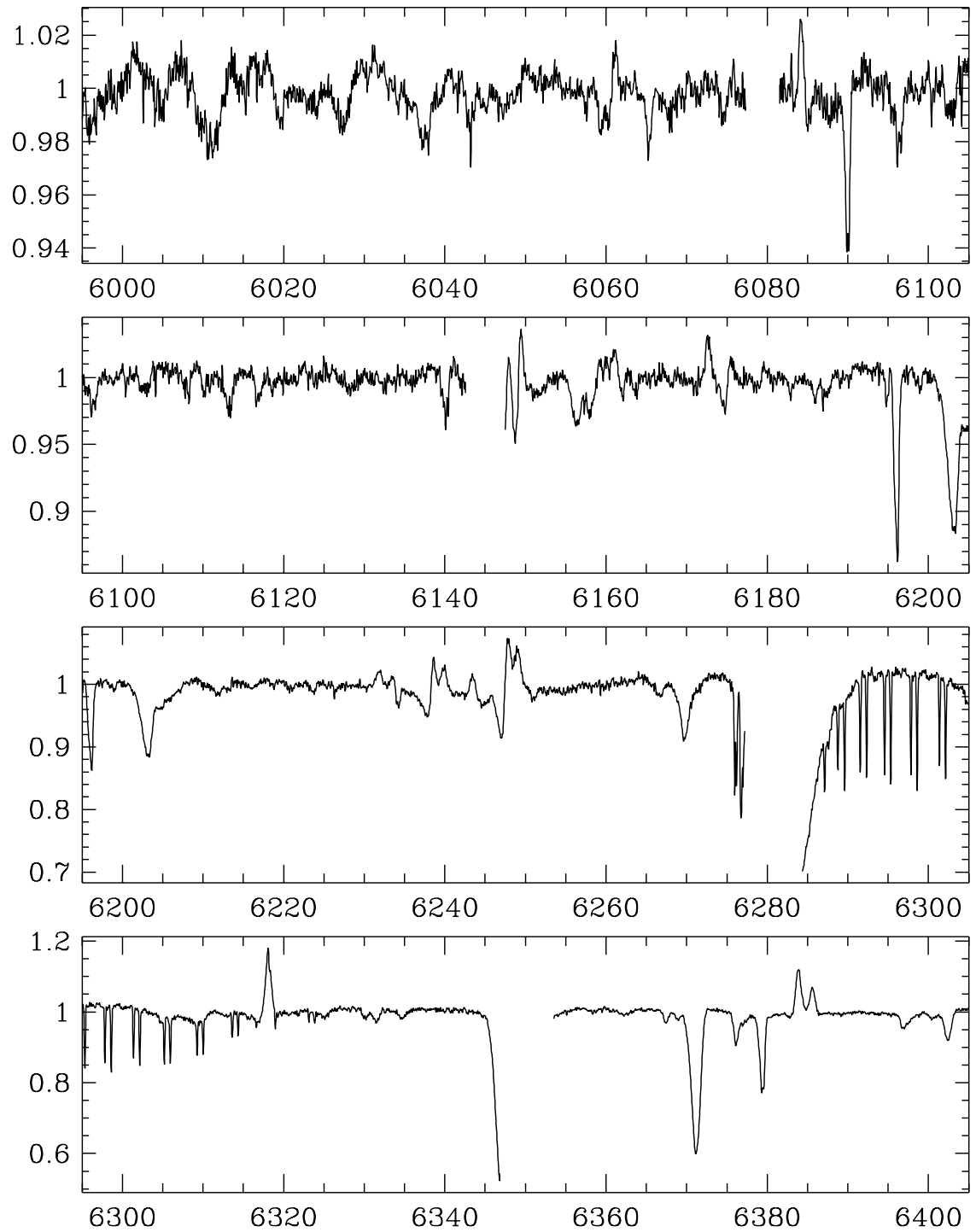
Figure A.23: Mean spectrum of HD 168607 from 6000 – 6400 Å; observed on Oct 4, 1995.
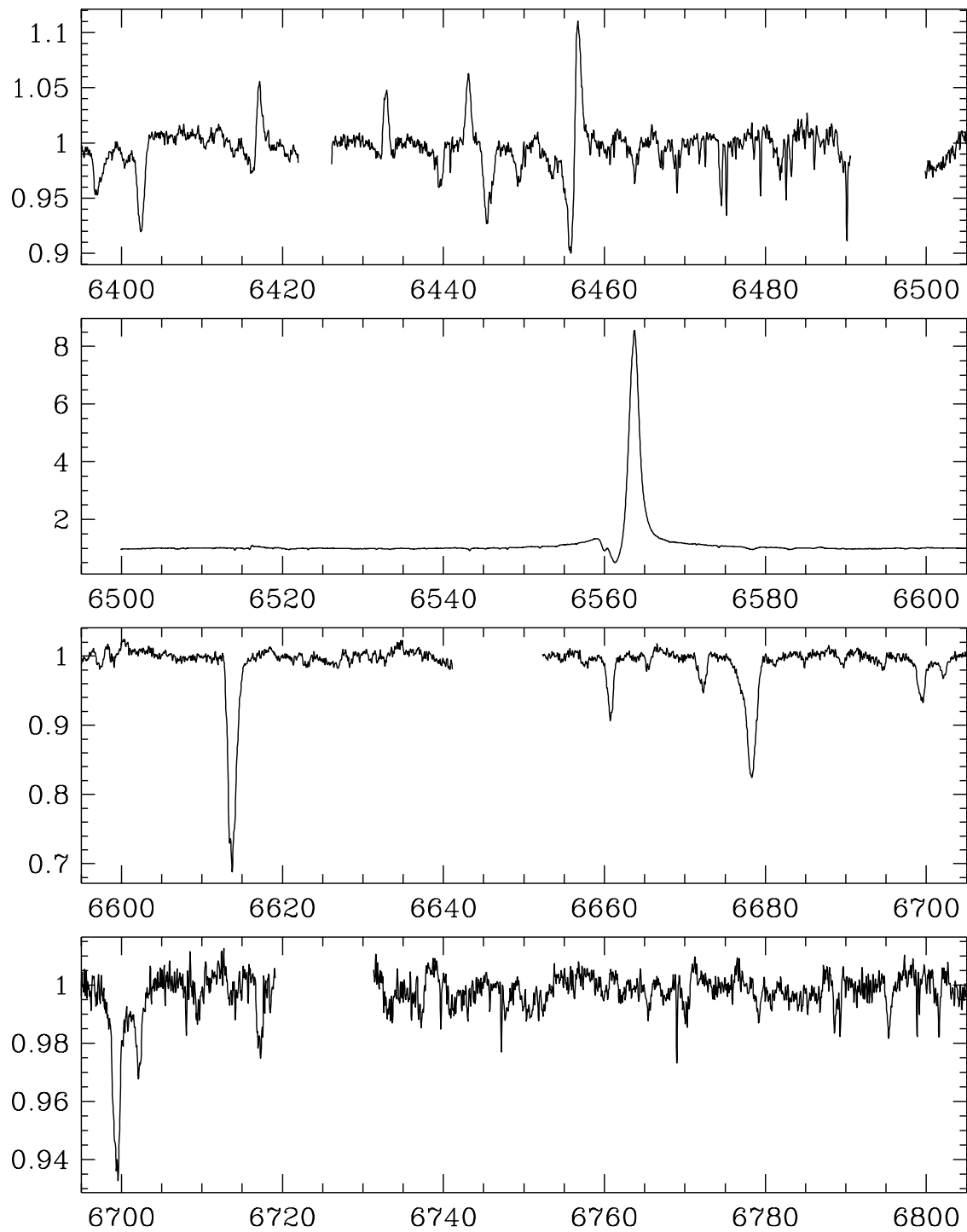
Figure A.24: Mean spectrum of HD 168607 from 6400 − 6800 Å; observed on Oct 4, 1995.

A.4   Mean Spectrum of HD 168625

- Observing instrument: UCLES/AAT

- Observing date: October 4, 1995

- Observed wavelength range: $3600 - 6800$ Å

- Spectral resolution: 50 000

- S/N ratio at 6400 Å: 130
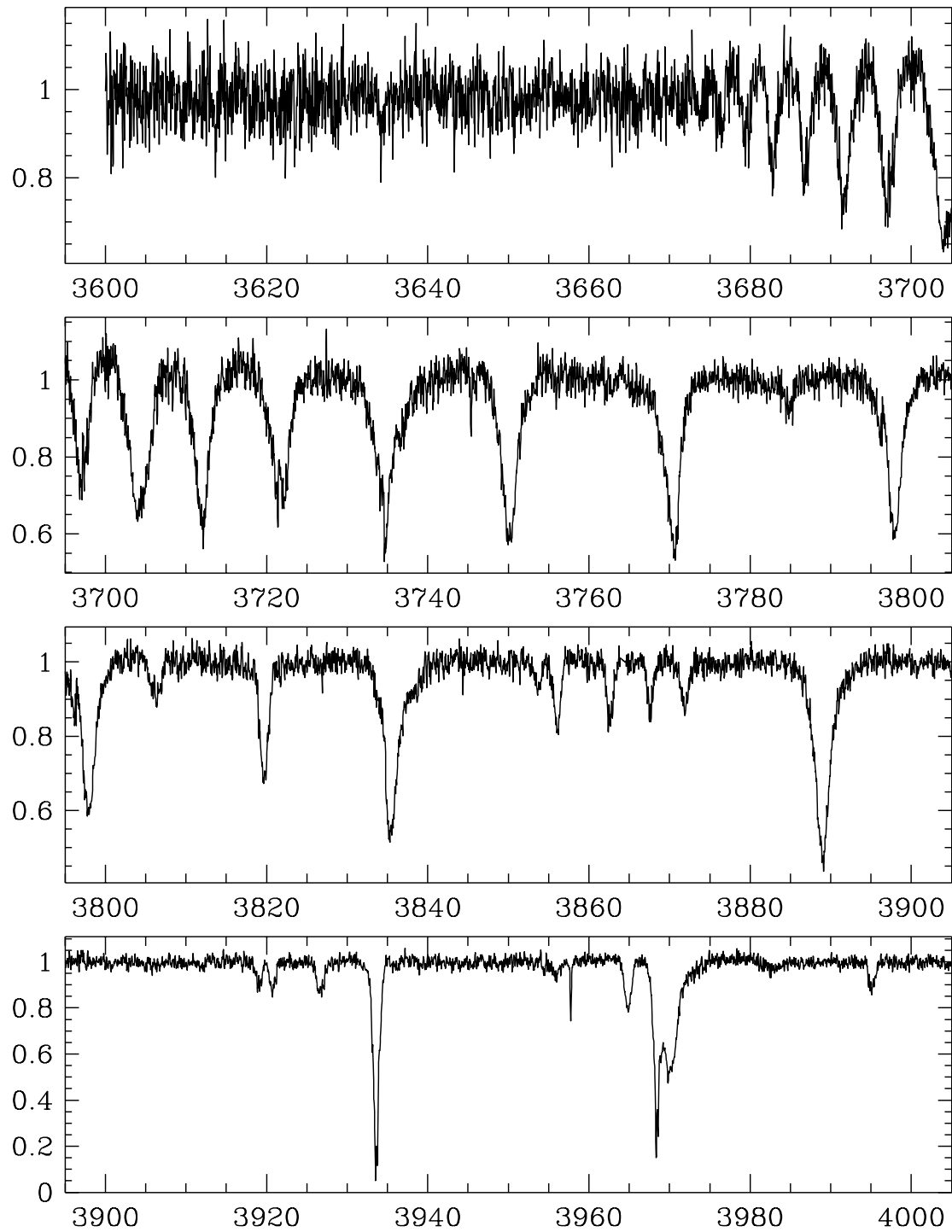
Figure A.25: Mean spectrum of HD 168625 from 3600−4000 Å; observed on Oct 4, 1995.
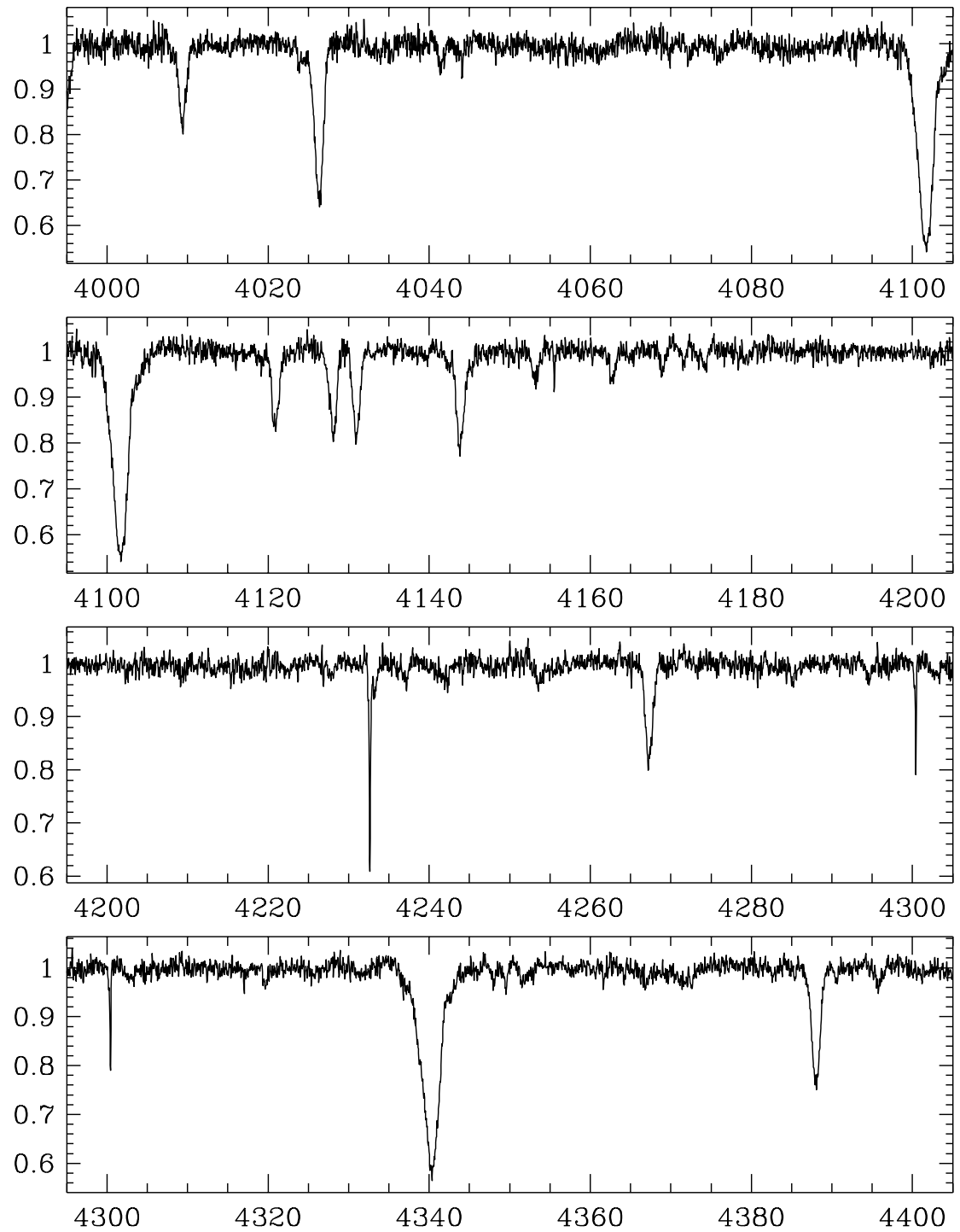
Figure A.26: Mean spectrum of HD 168625 from 4000 – 4400 Å; observed on Oct 4, 1995.
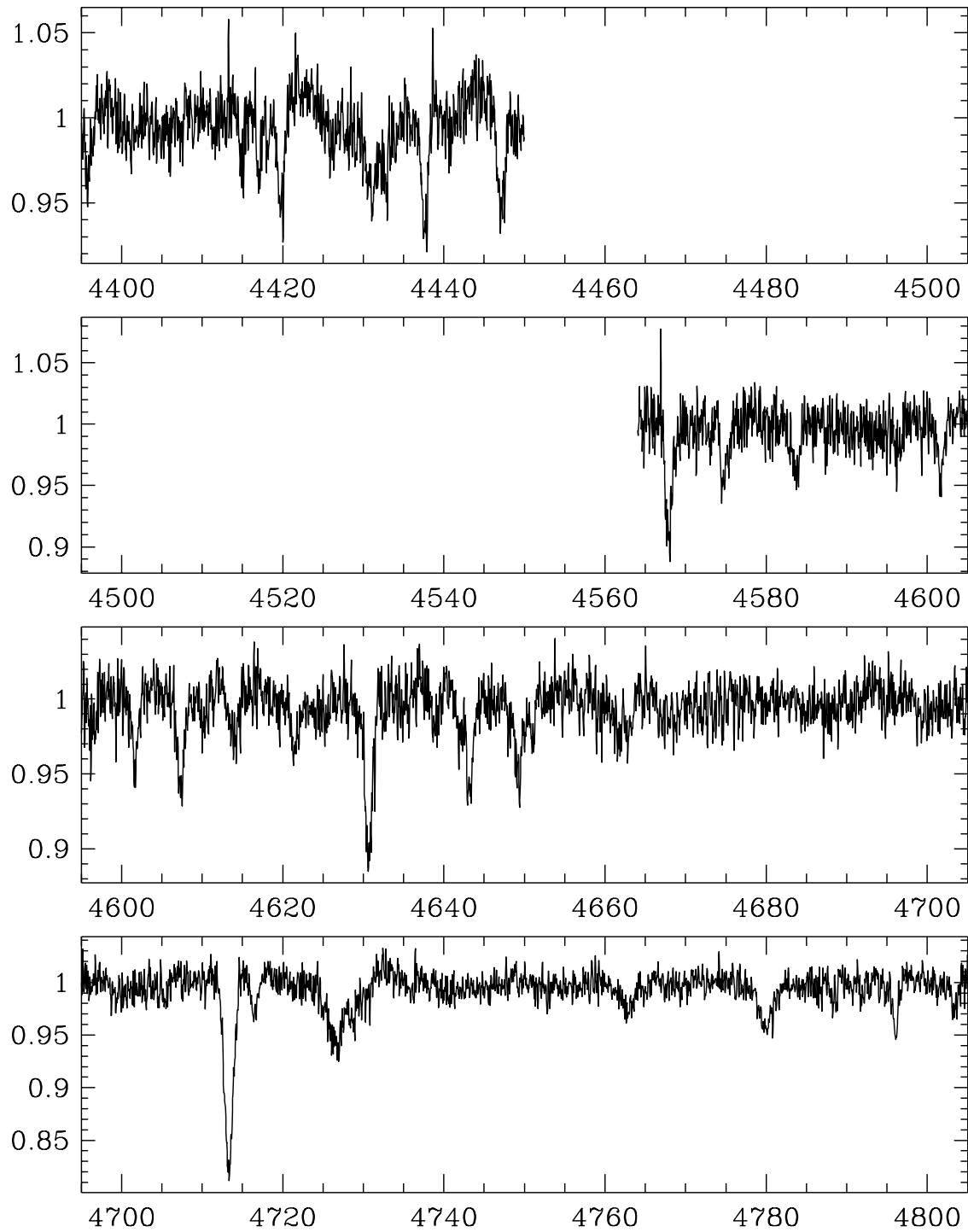
Figure A.27: Mean spectrum of HD 168625 from 4400−4800 Å; observed on Oct 4, 1995.
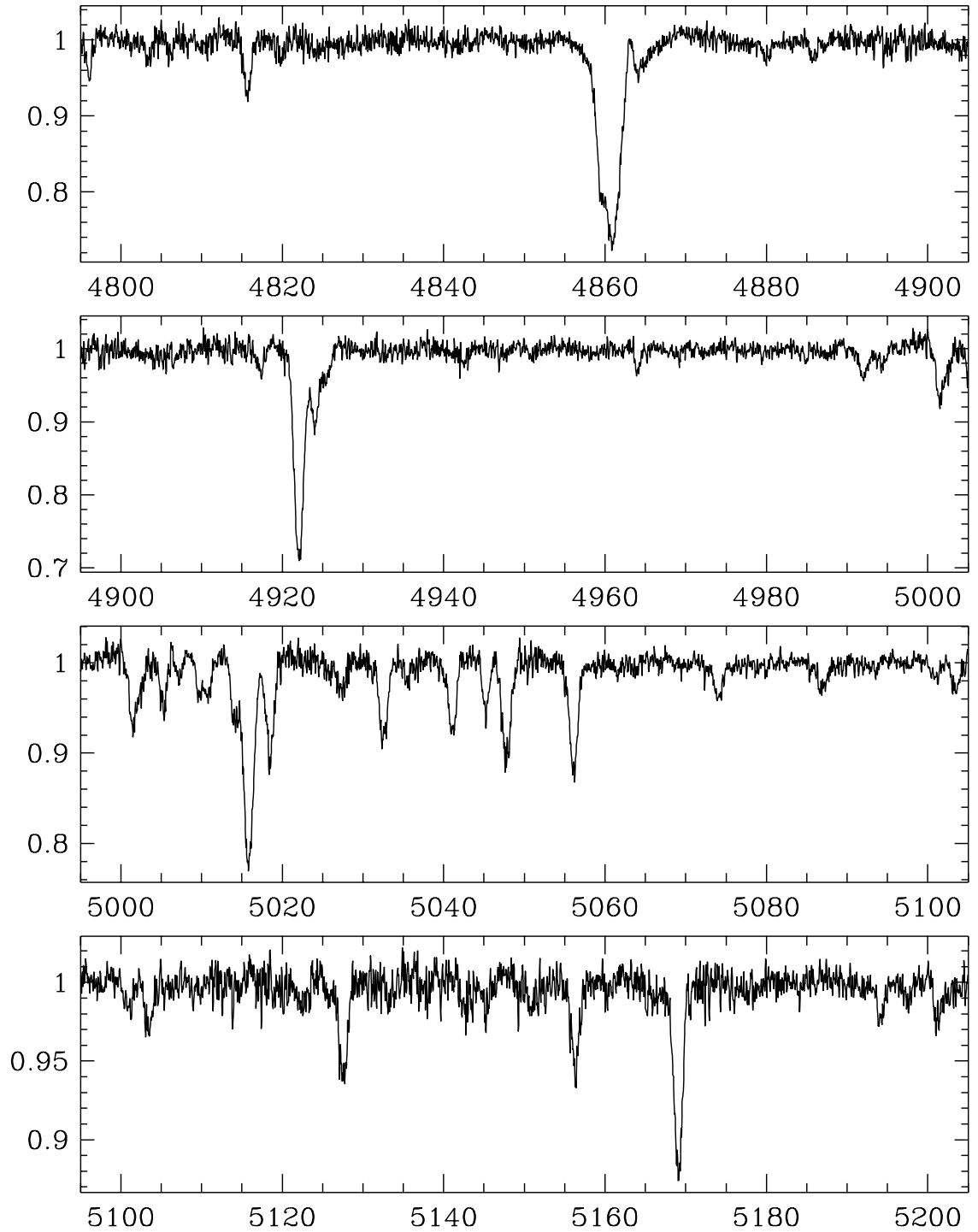
Figure A.28: Mean spectrum of HD 168625 from 4800–5200 Å; observed on Oct 4, 1995.
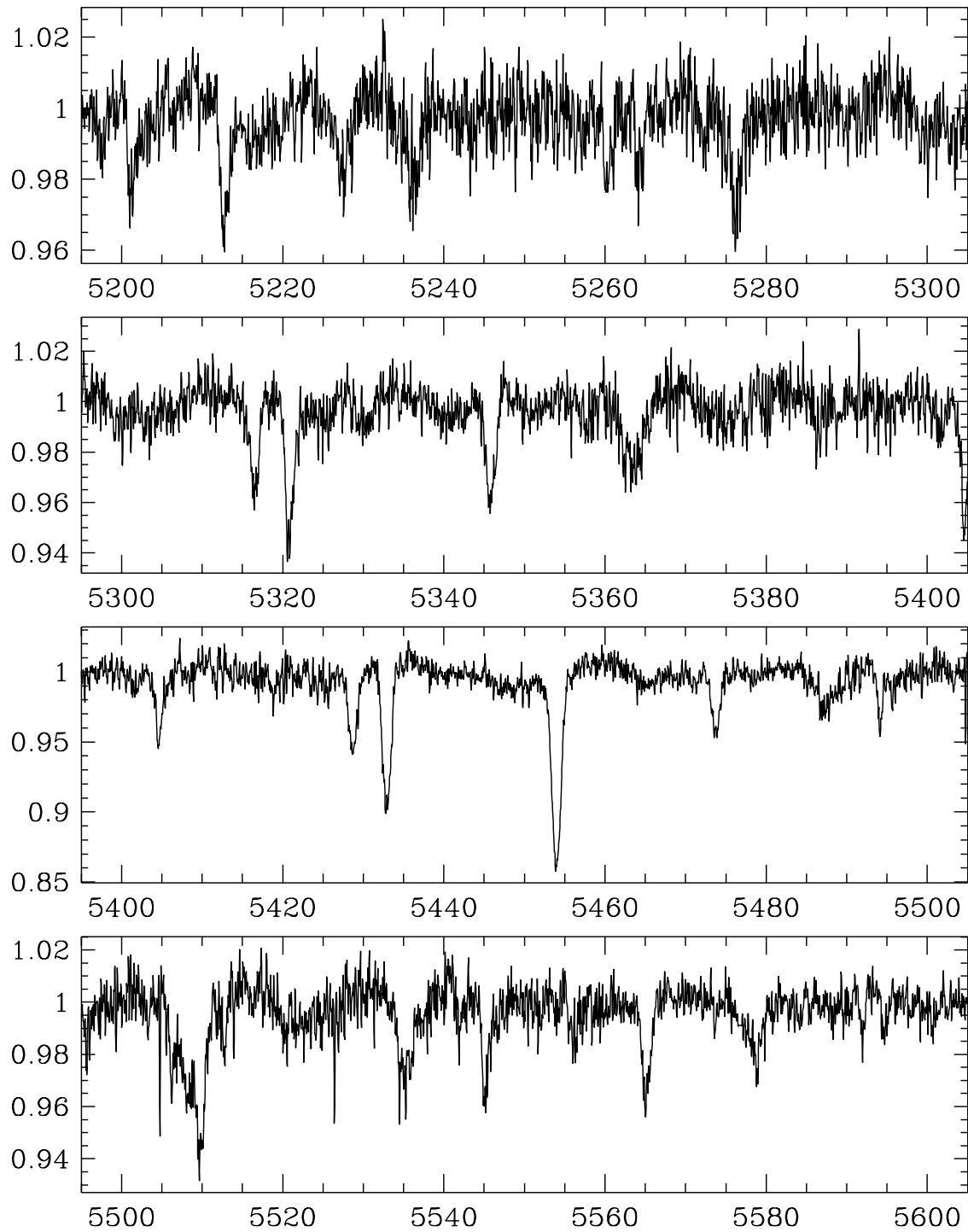
Figure A.29: Mean spectrum of HD 168625 from 5200−5600 Å; observed on Oct 4, 1995.
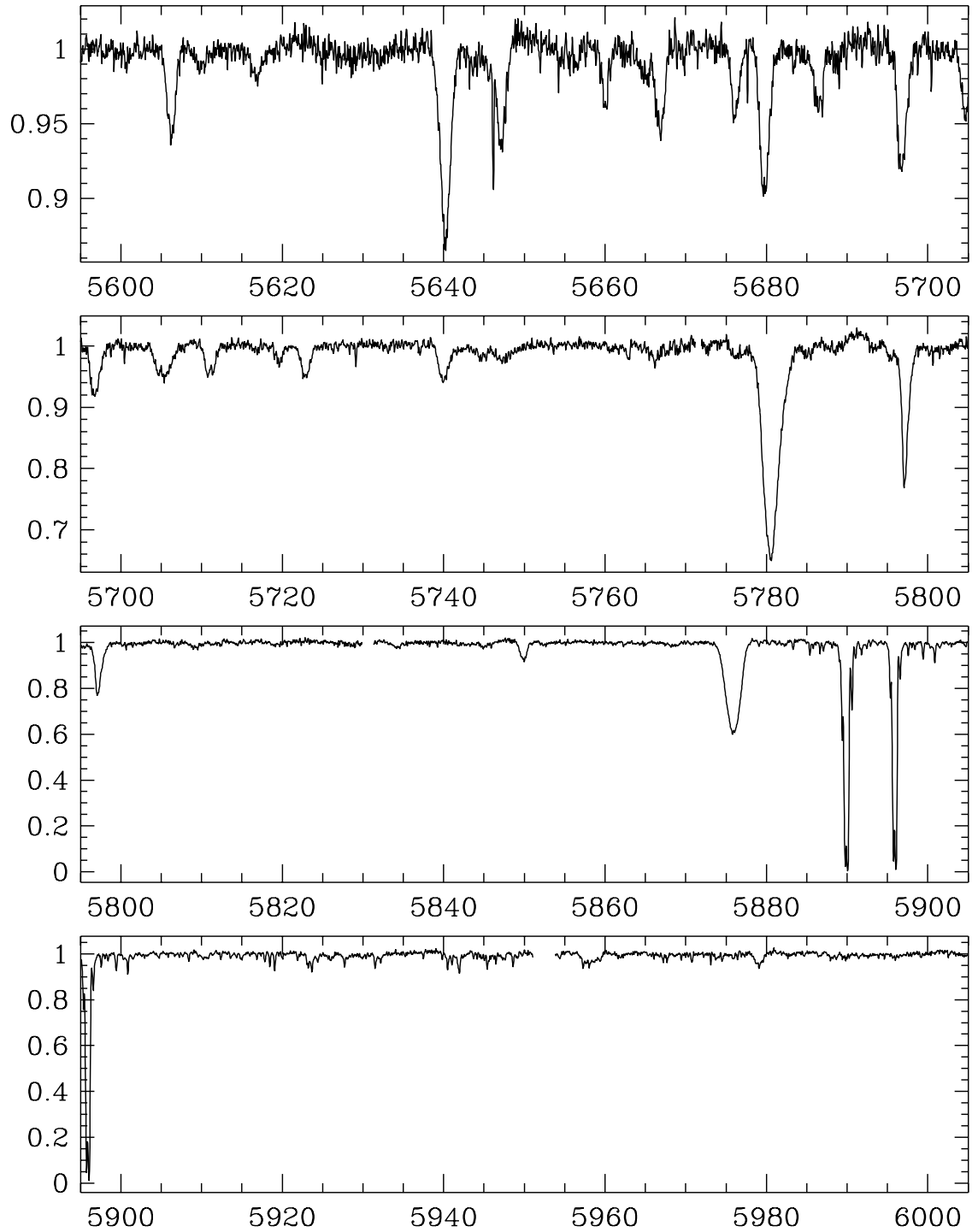
Figure A.30: Mean spectrum of HD 168625 from 5600 – 6000 Å; observed on Oct 4, 1995.
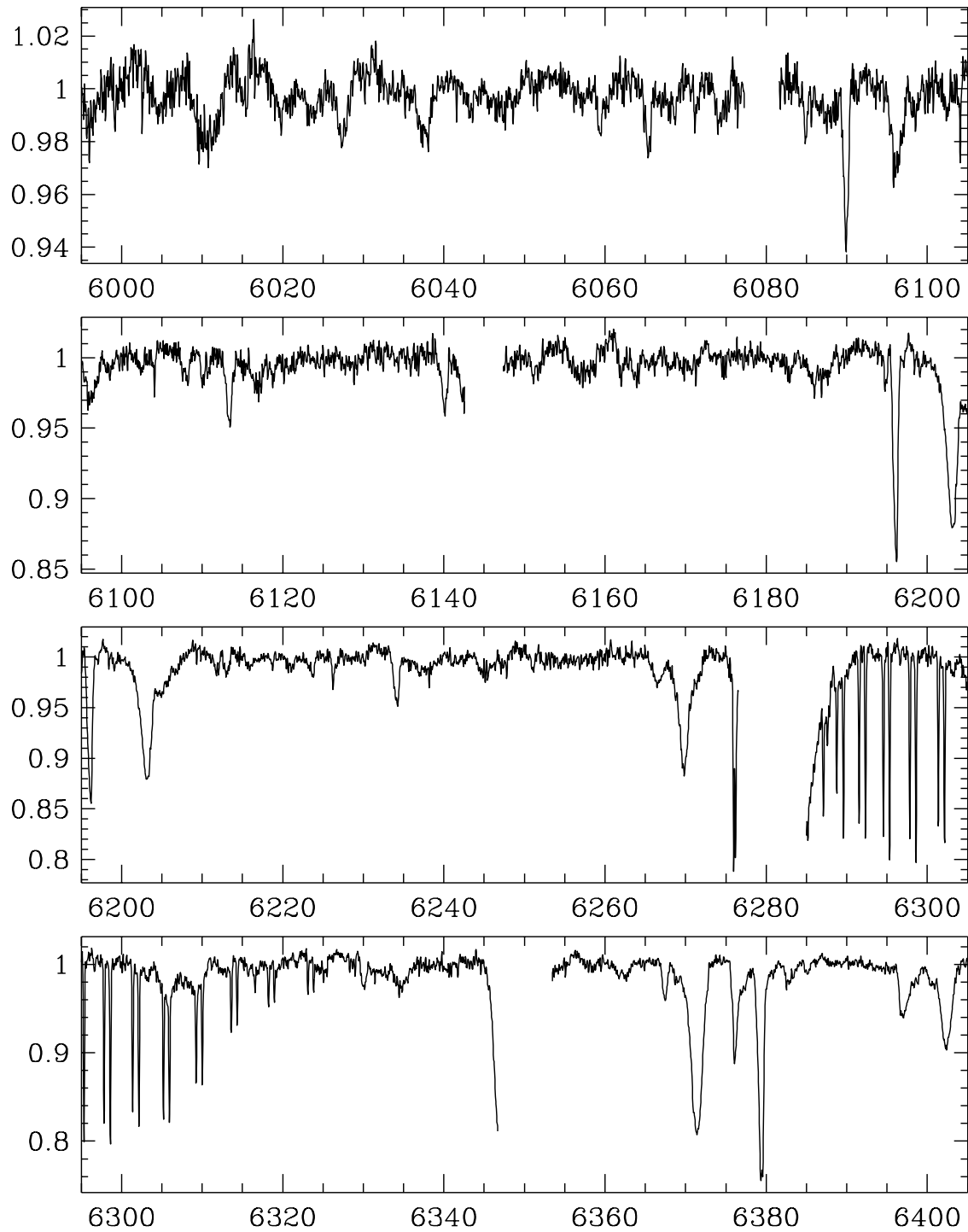
Figure A.31: Mean spectrum of HD 168625 from 6000 – 6400 Å; observed on Oct 4, 1995.
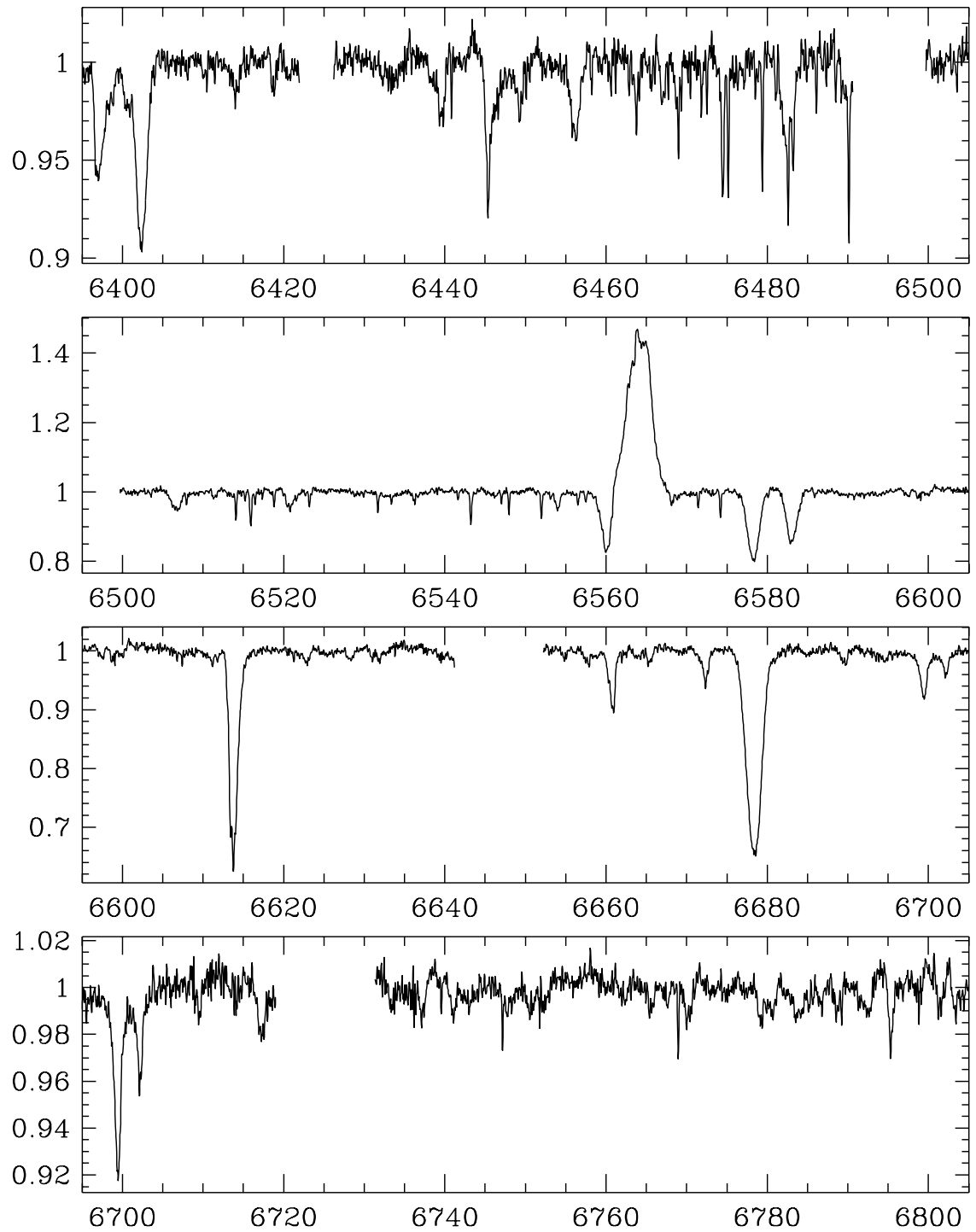
Figure A.32: Mean spectrum of HD 168625 from 6400 – 6800 Å; observed on Oct 4, 1995.

A.5   Mean Spectrum of HD 5980

- Observing instrument: UCLES/AAT

- Observing date: October 4, 1995

- Observed wavelength range: $3600-6800\,\text{Å}$

- Spectral resolution: 50 000

- S/N ratio at $6400\,\text{Å}$: 70
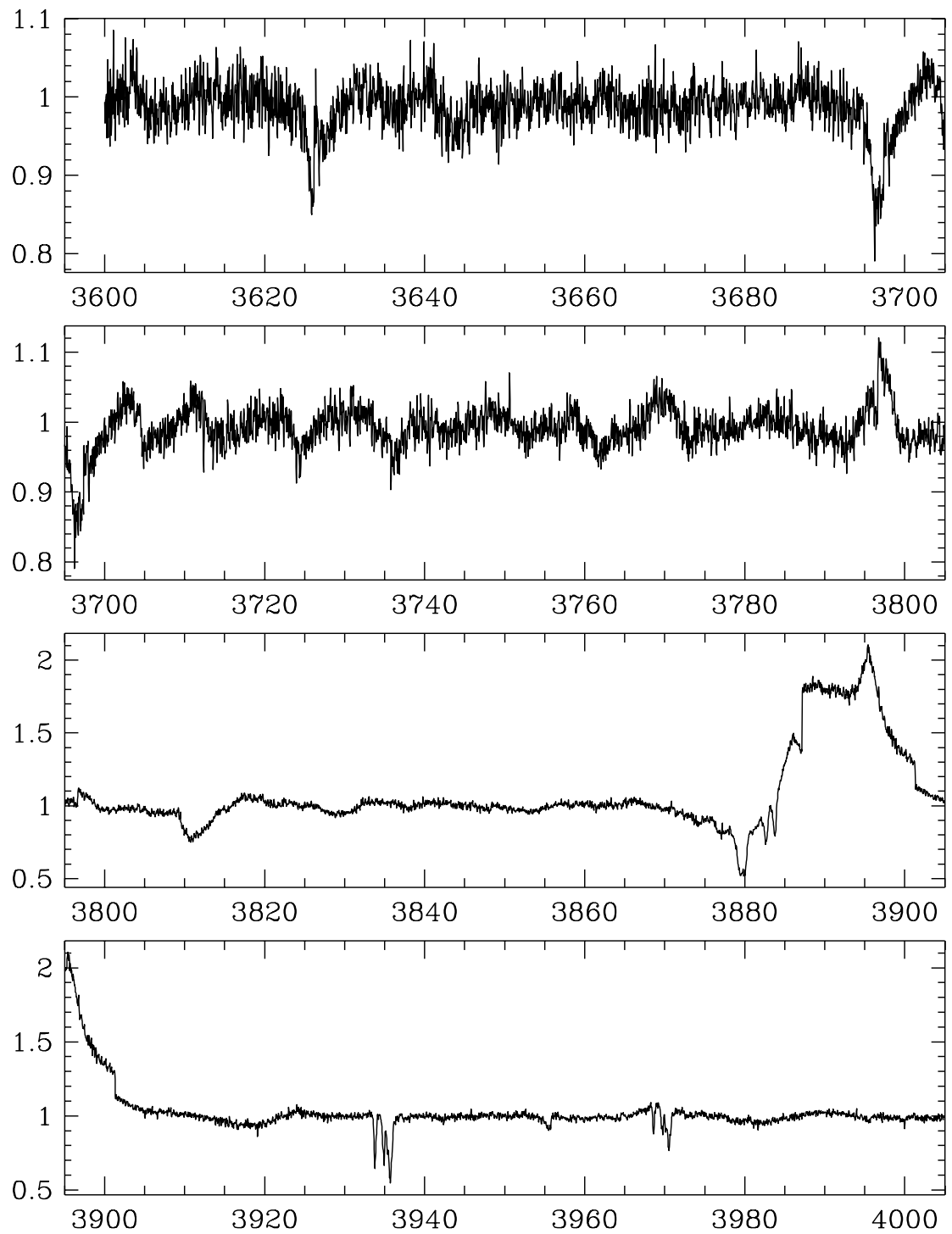
Figure A.33: Mean spectrum of HD 5980 from 3600−4000 Å; observed on Oct 4, 1995.
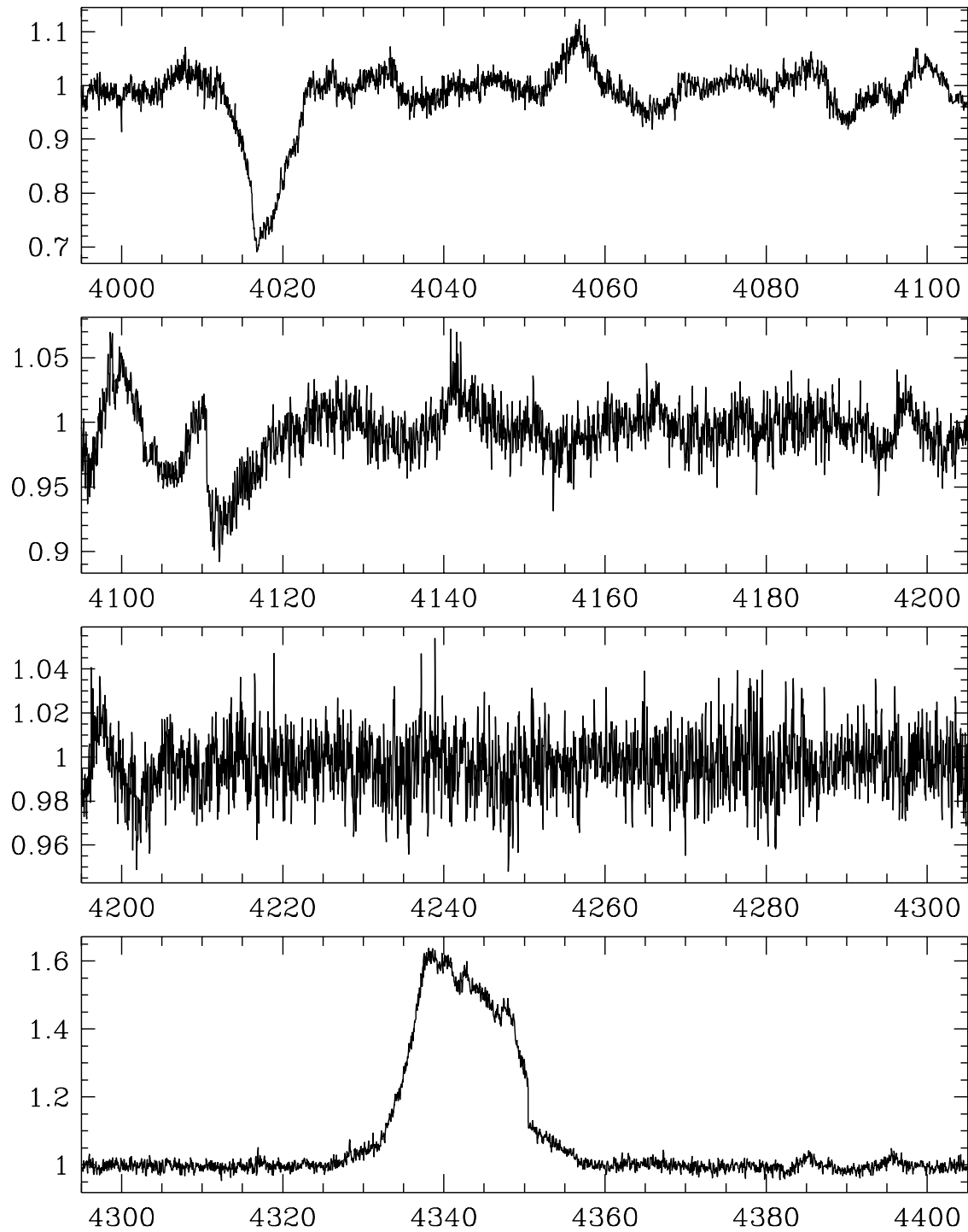
Figure A.34: Mean spectrum of HD 5980 from 4000 − 4400 Å; observed on Oct 4, 1995.
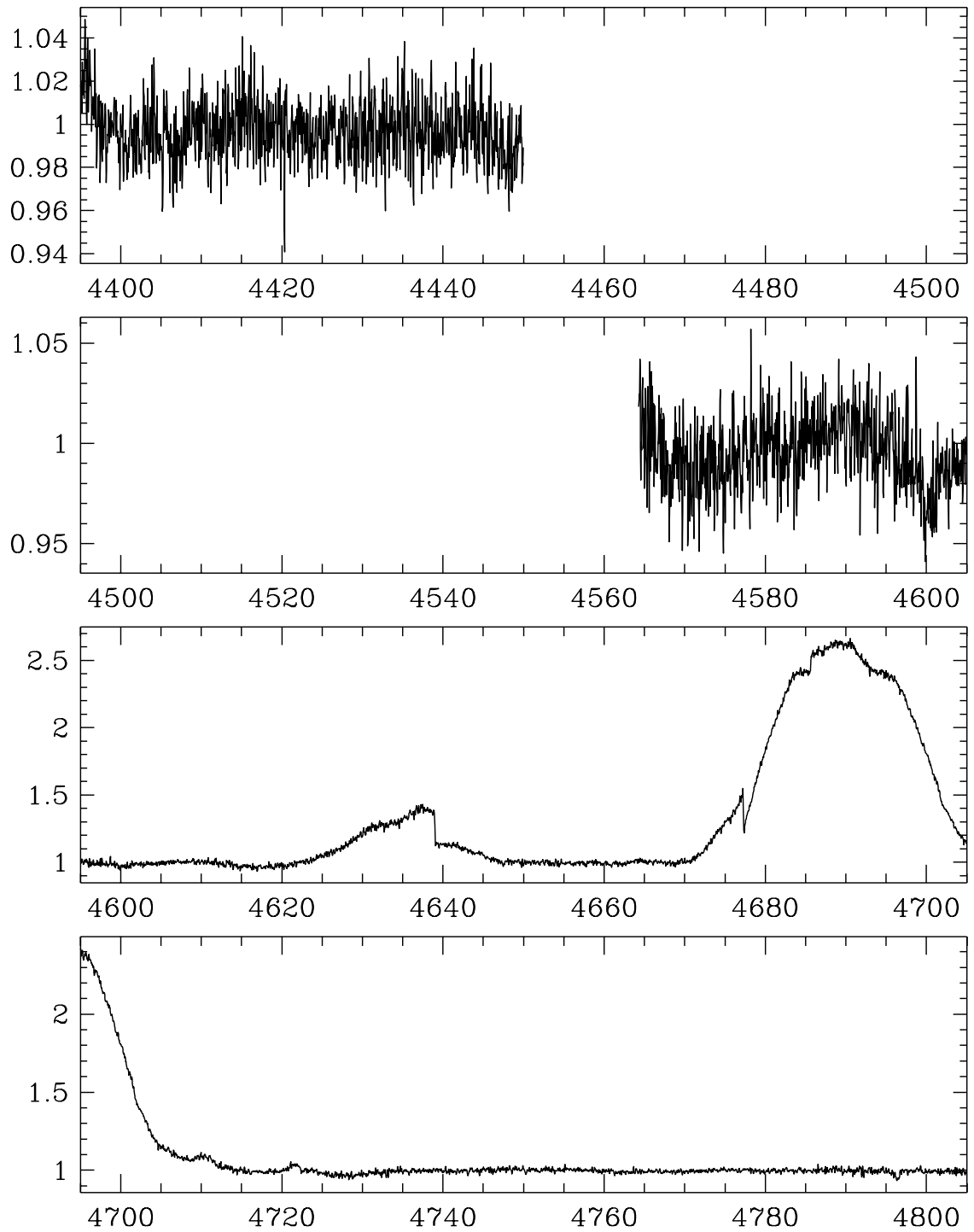
Figure A.35: Mean spectrum of HD 5980 from 4400 – 4800 Å; observed on Oct 4, 1995.
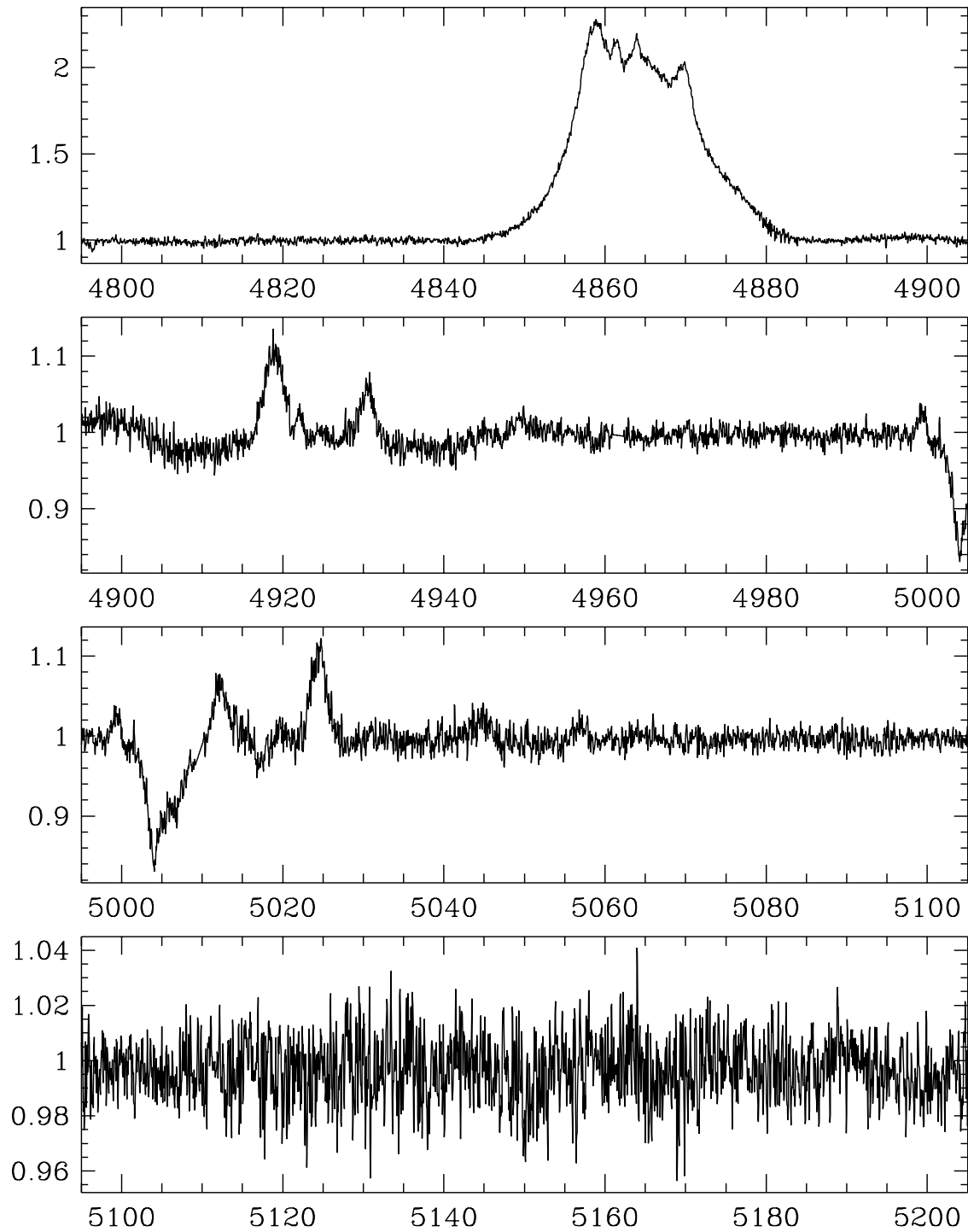
Figure A.36: Mean spectrum of HD 5980 from 4800 − 5200 Å; observed on Oct 4, 1995.
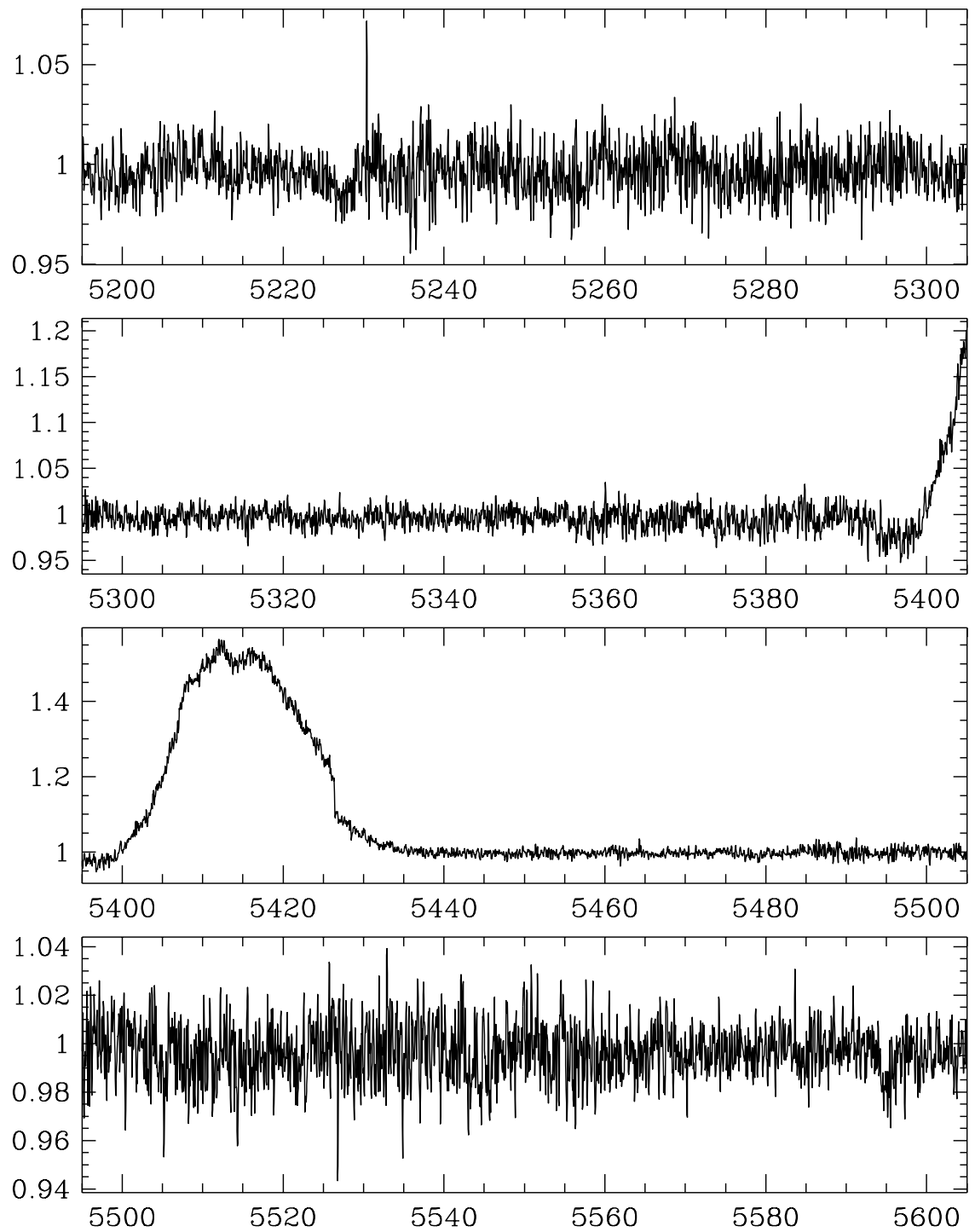
Figure A.37: Mean spectrum of HD 5980 from 5200 – 5600 Å; observed on Oct 4, 1995.
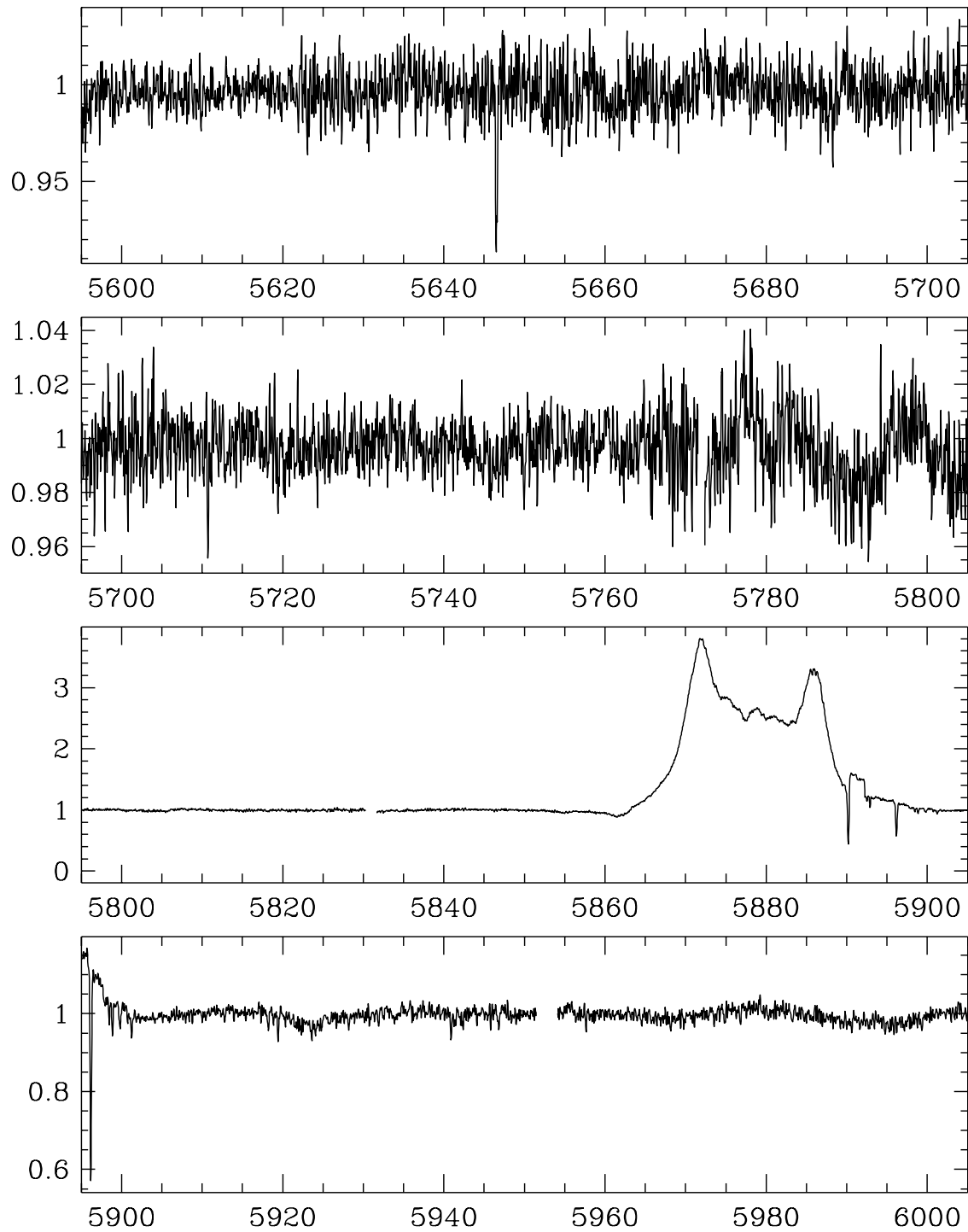
Figure A.38: Mean spectrum of HD 5980 from 5600 − 6000 Å; observed on Oct 4, 1995.
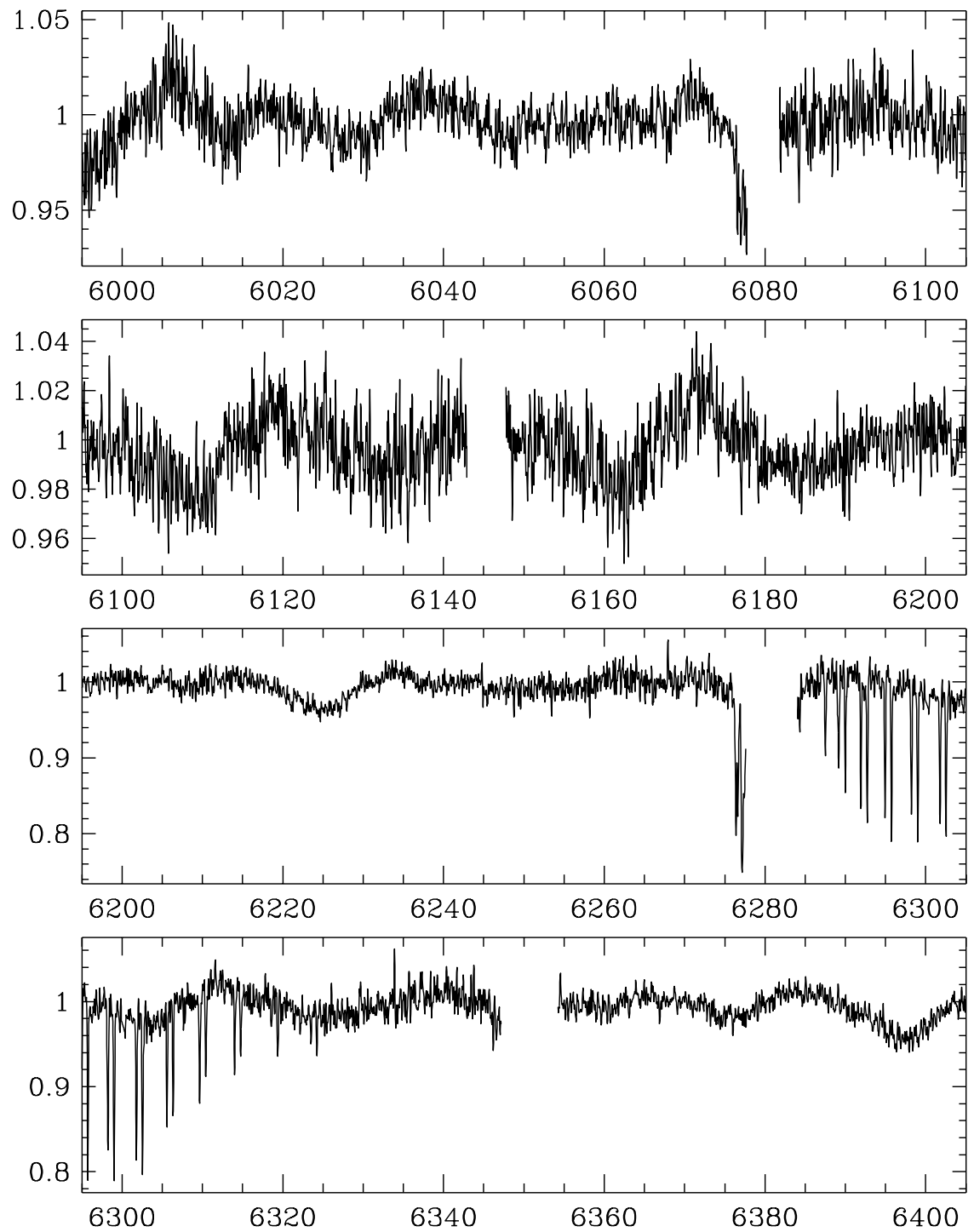
Figure A.39: Mean spectrum of HD 5980 from 6000 – 6400 Å; observed on Oct 4, 1995.
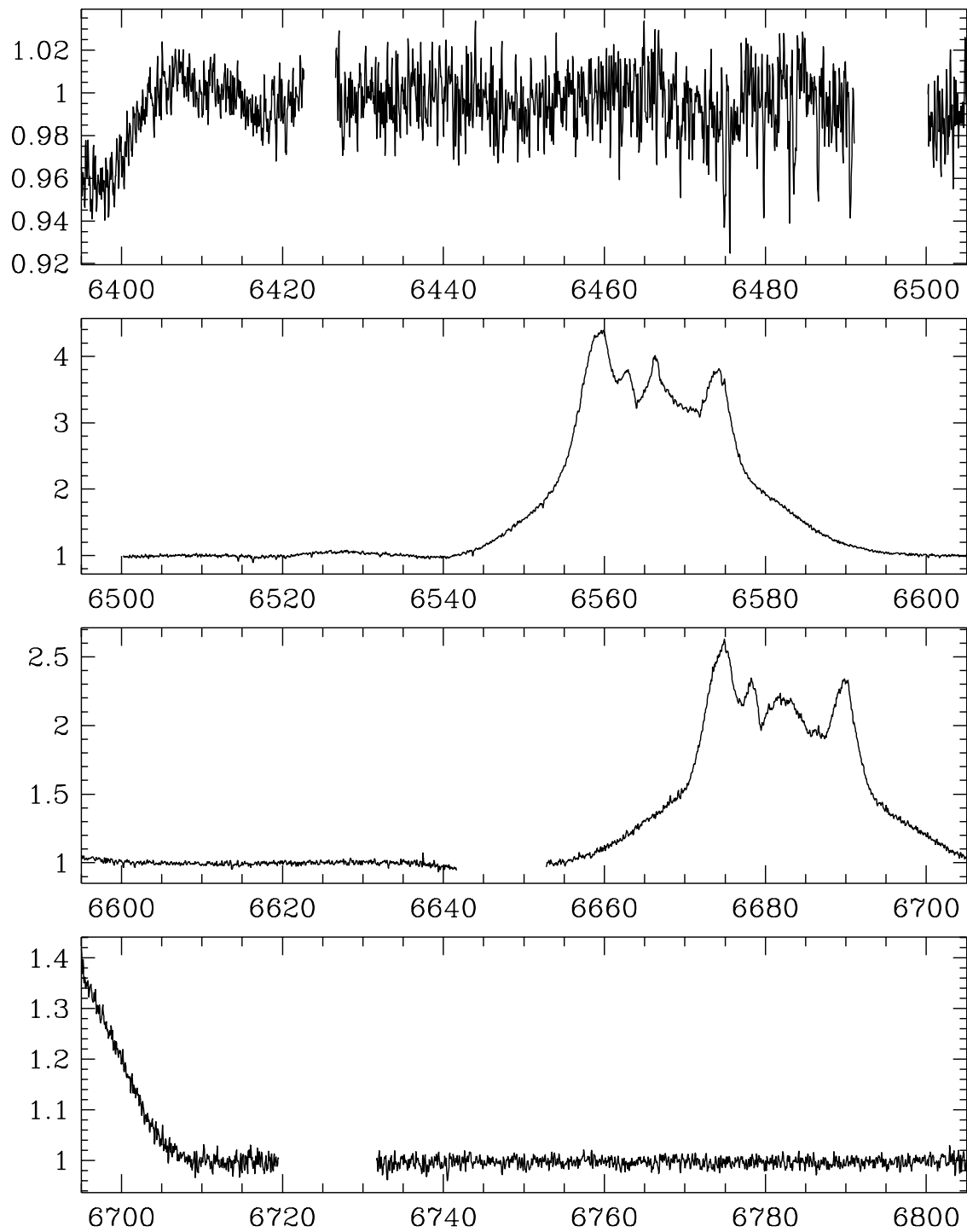
Figure A.40: Mean spectrum of HD 5980 from 6400 − 6800 Å; observed on Oct 4, 1995.

A.6   Mean Spectrum of S Dor

- Observing instrument: UCLES/AAT

- Observing date: October 4, 1995

- Observed wavelength range: $3600 - 6800$ Å

- Spectral resolution: 50 000

- S/N ratio at 6400 Å: 130
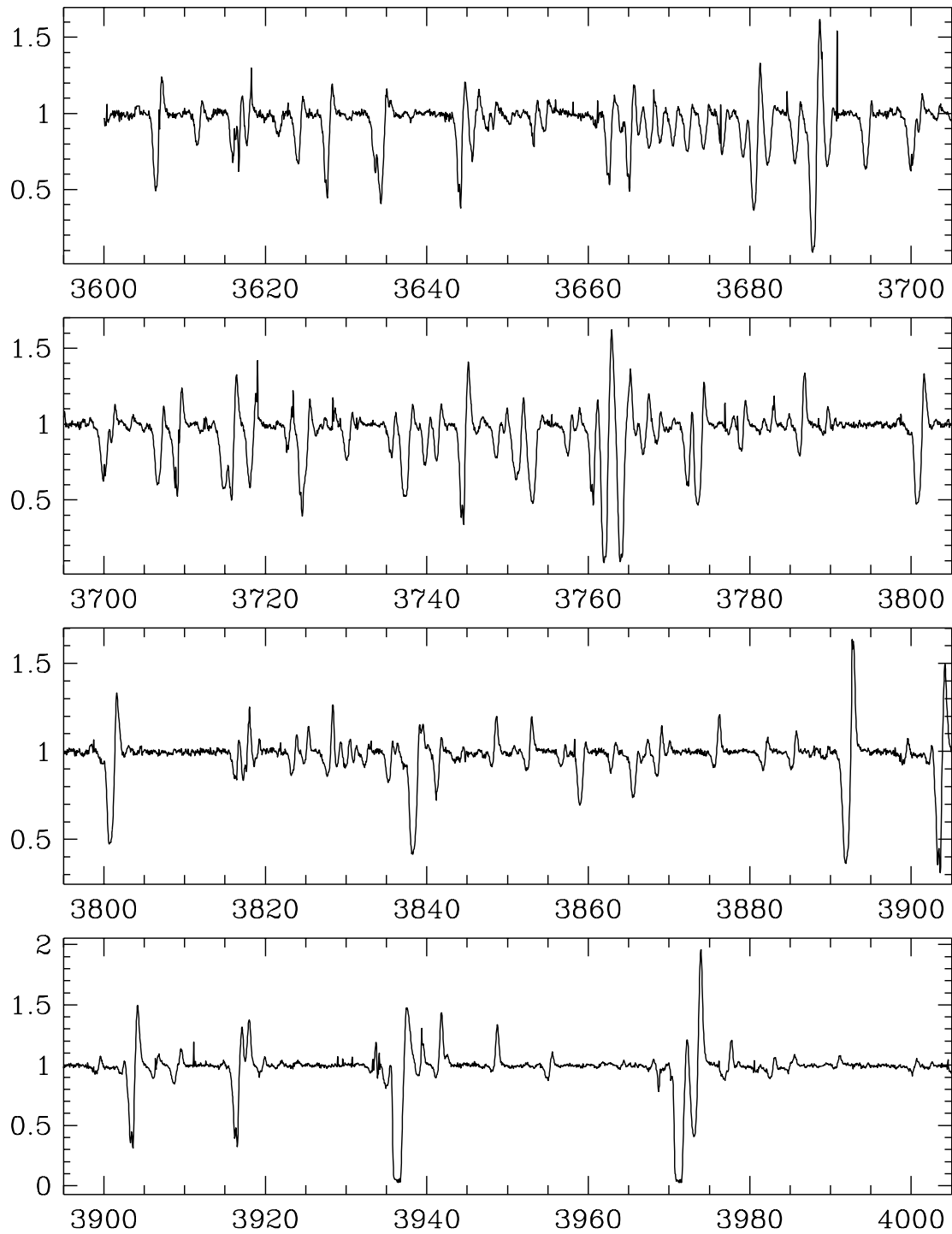
Figure A.41: Mean spectrum of S Dor from $3600-4000$ Å; observed on Oct 4, 1995.
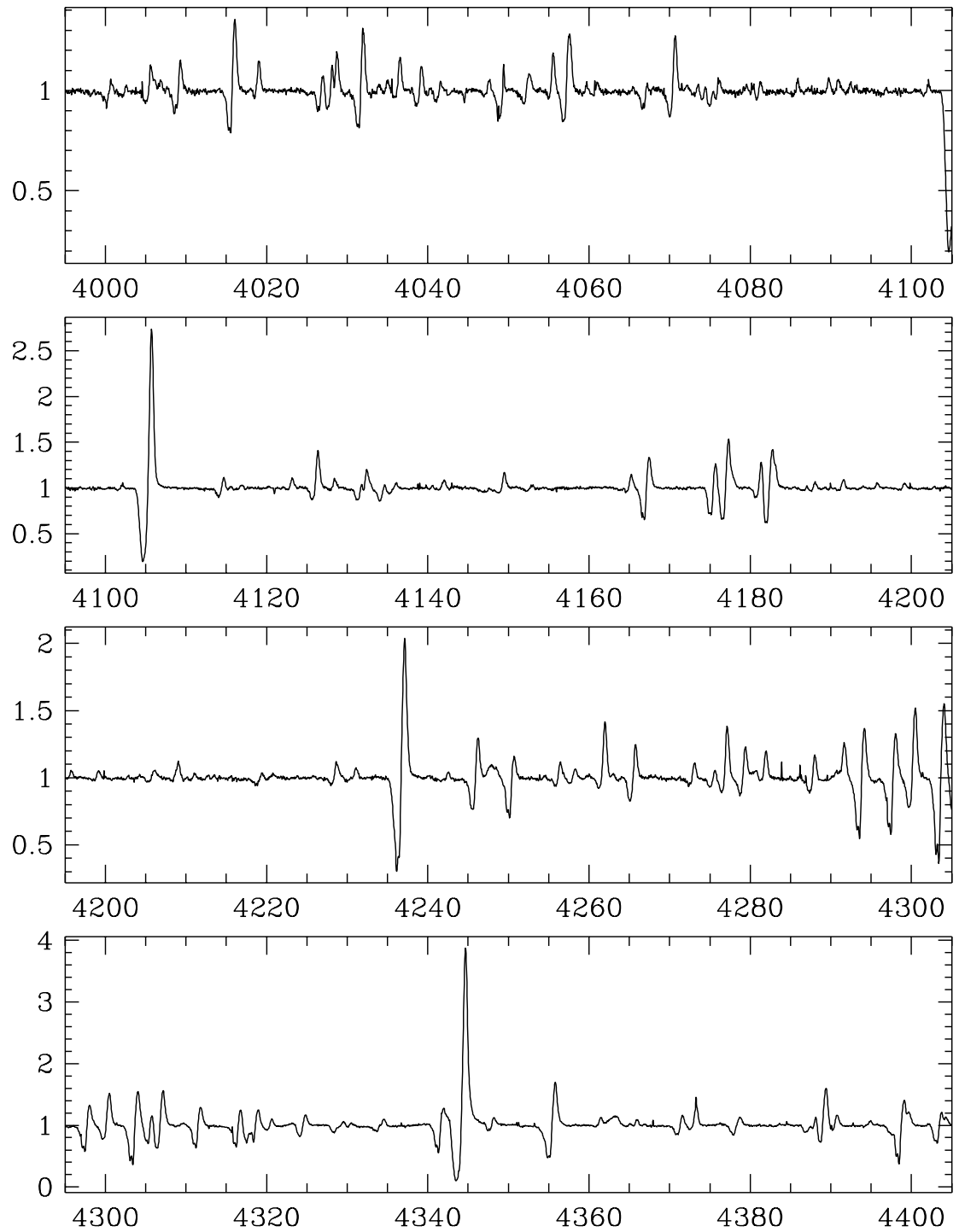
Figure A.42: Mean spectrum of S Dor from 4000−4400 Å; observed on Oct 4, 1995.
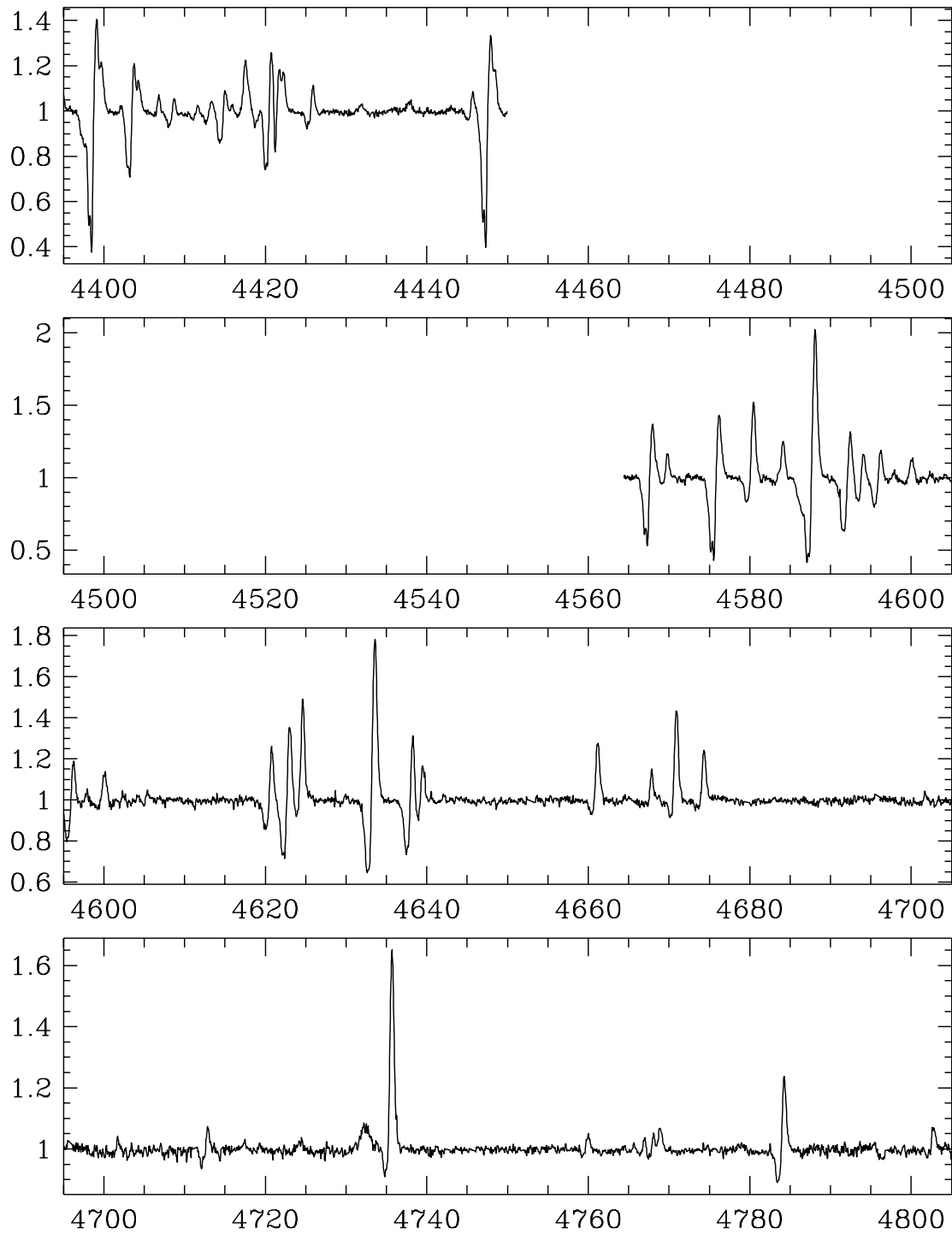
Figure A.43: Mean spectrum of S Dor from $4400-4800$ Å; observed on Oct 4, 1995.
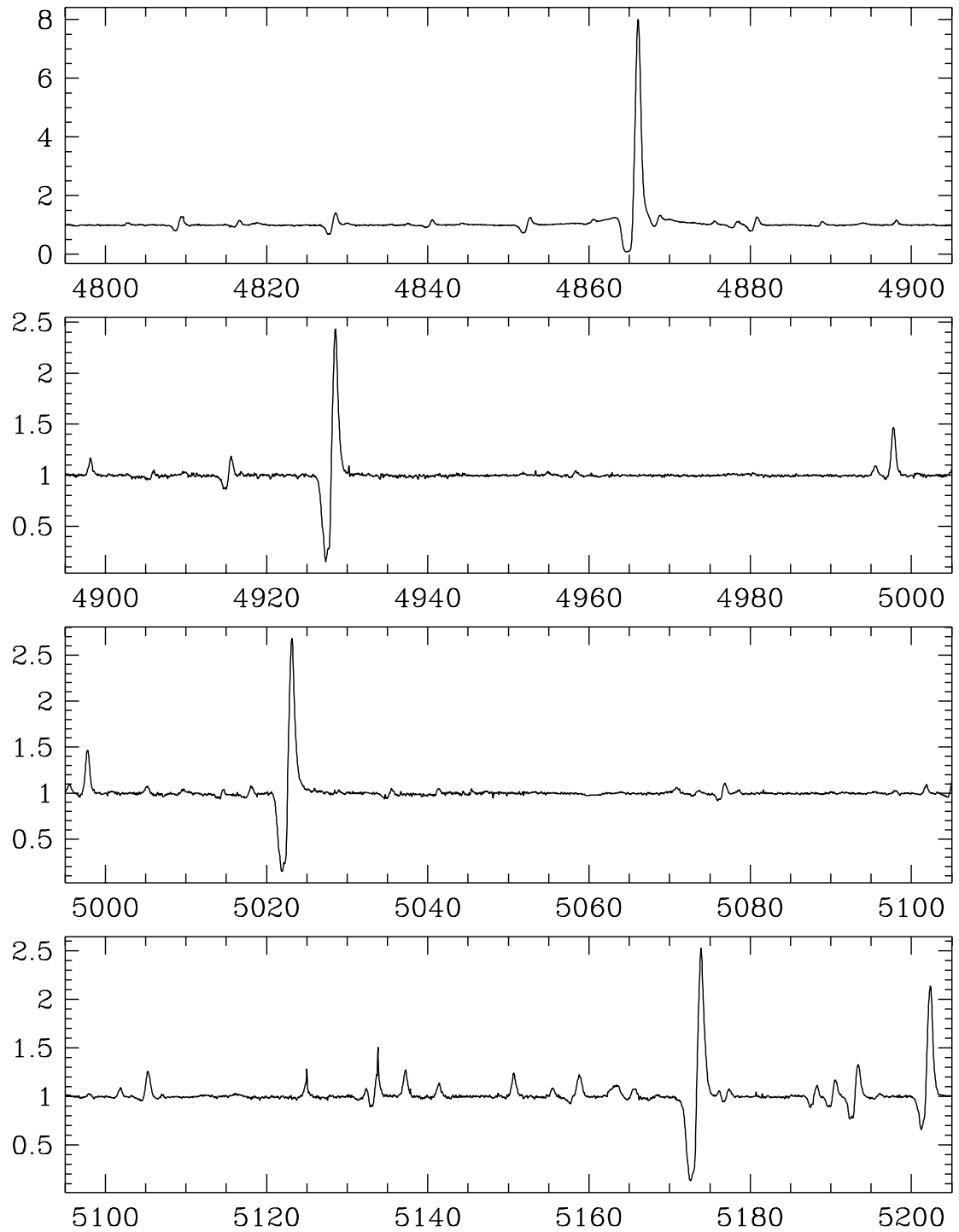
Figure A.44: Mean spectrum of S Dor from 4800−5200 Å; observed on Oct 4, 1995.
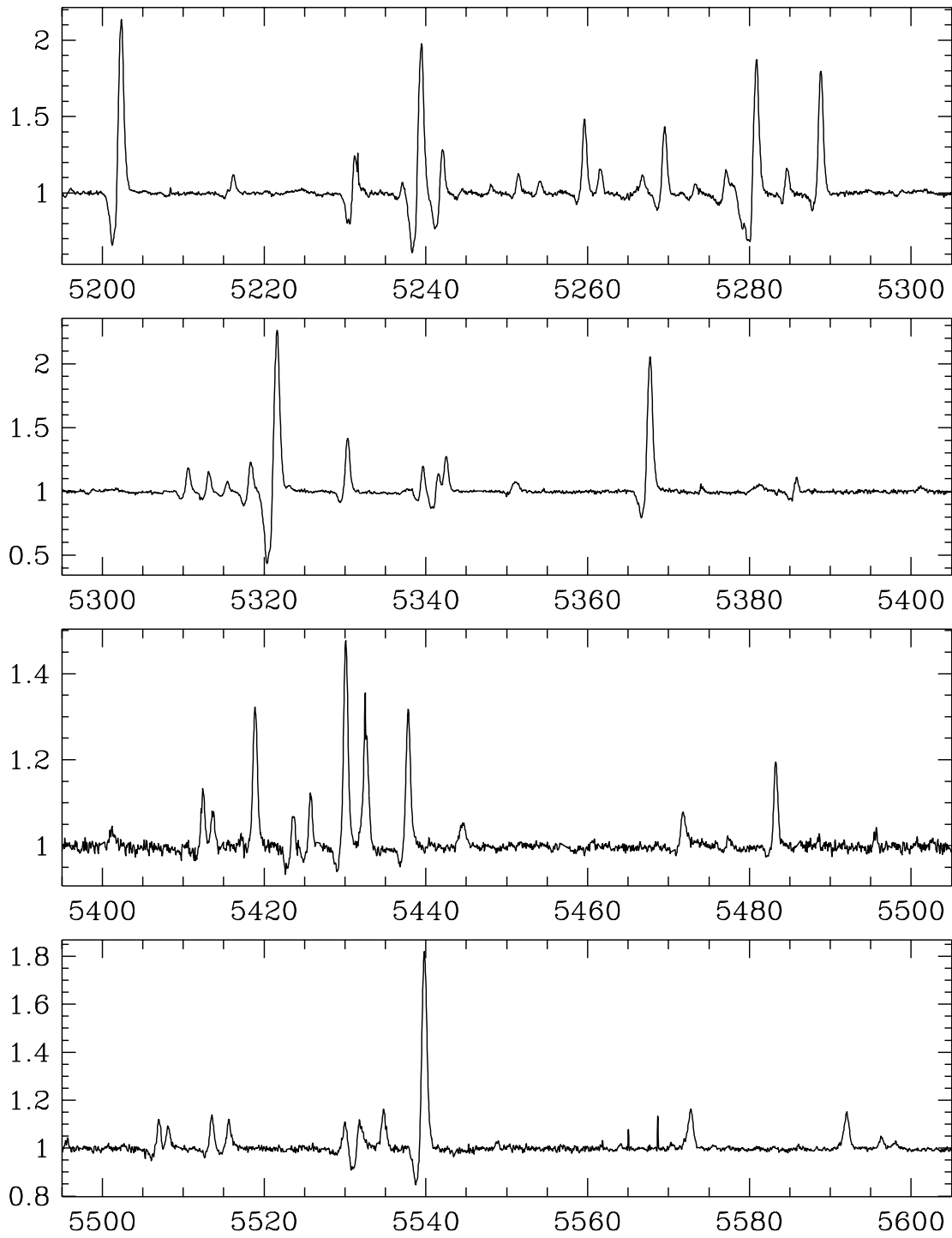
Figure A.45: Mean spectrum of S Dor from 5200−5600 Å; observed on Oct 4, 1995.
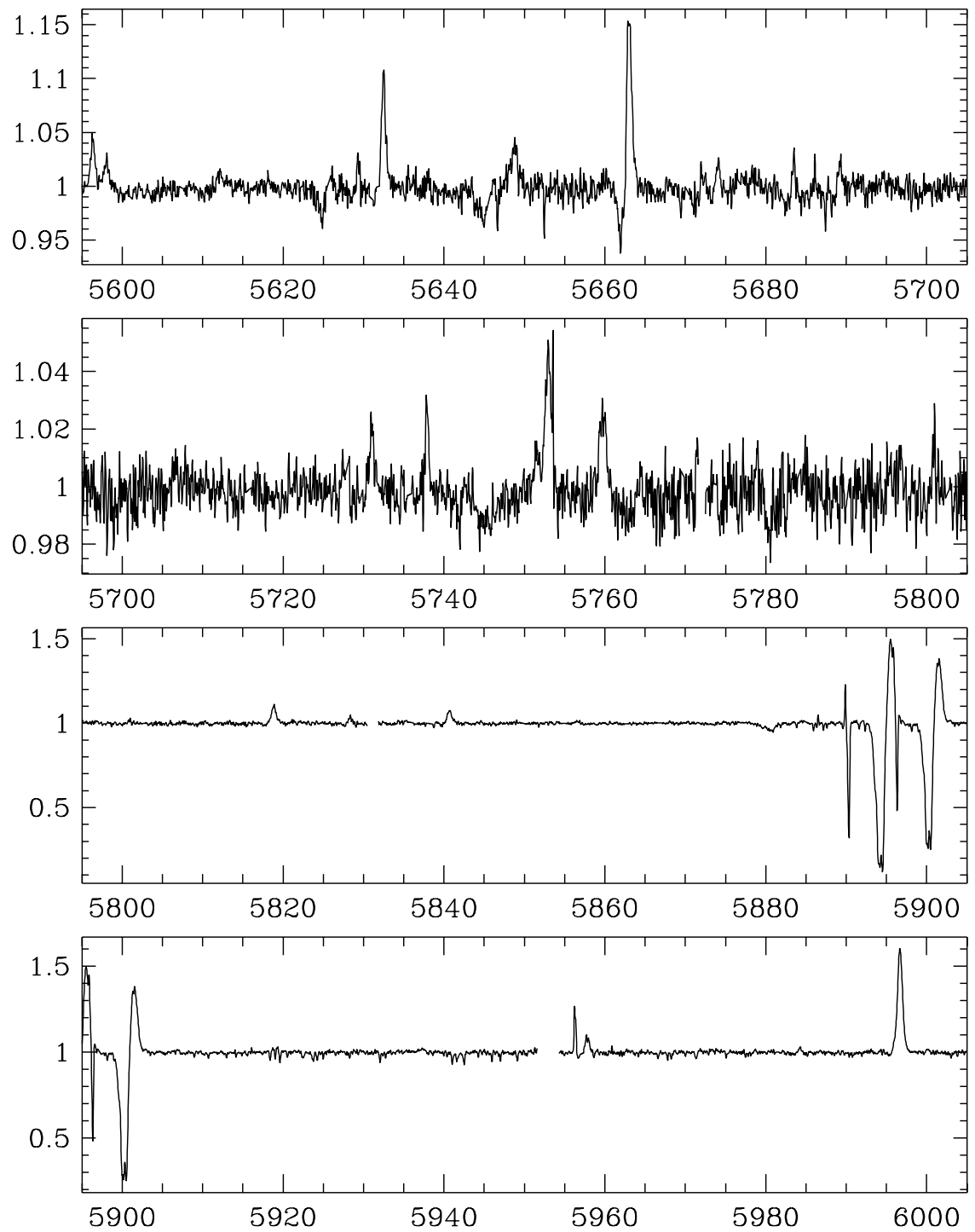
Figure A.46: Mean spectrum of S Dor from 5600 − 6000 Å; observed on Oct 4, 1995.
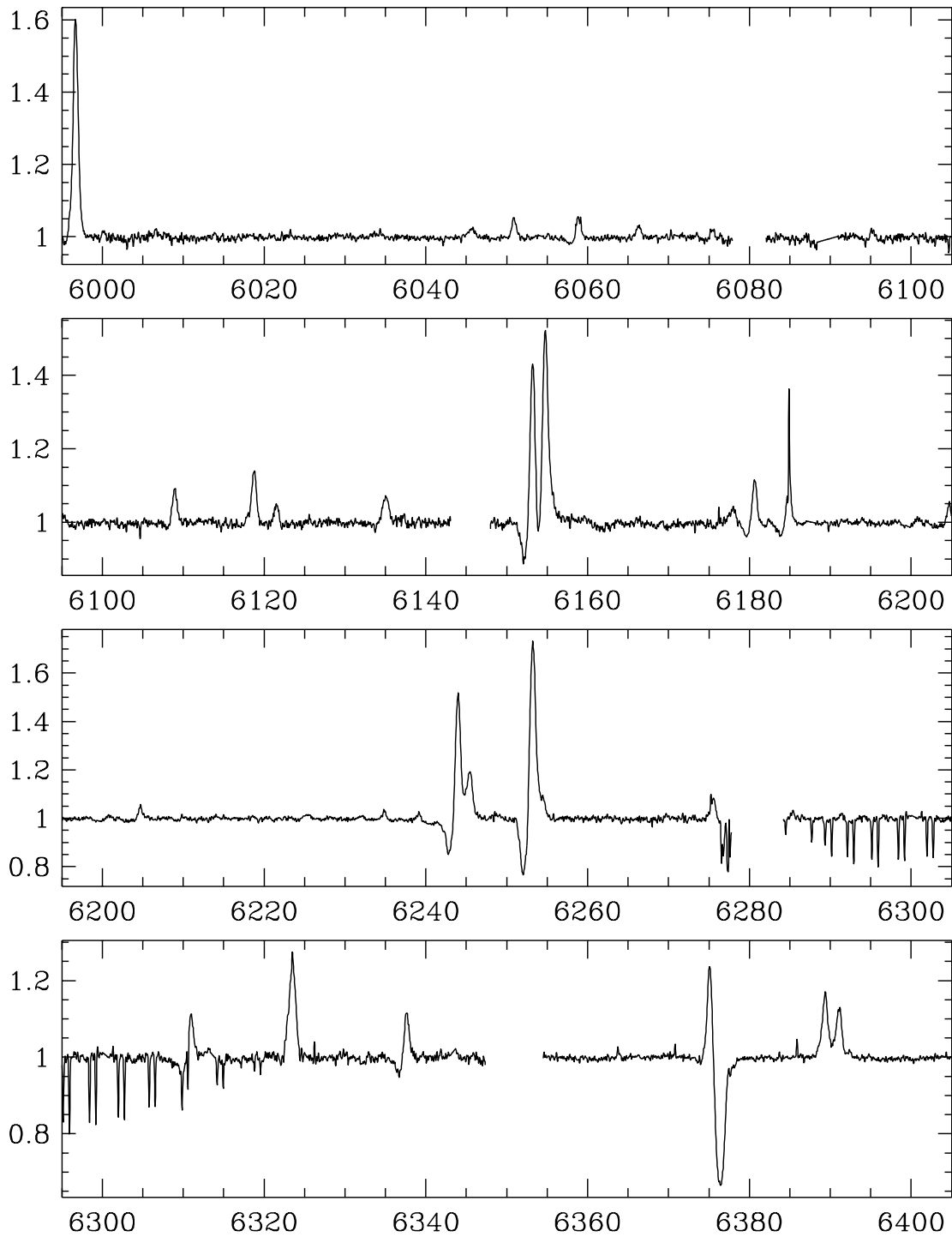
Figure A.47: Mean spectrum of S Dor from 6000−6400 Å; observed on Oct 4, 1995.
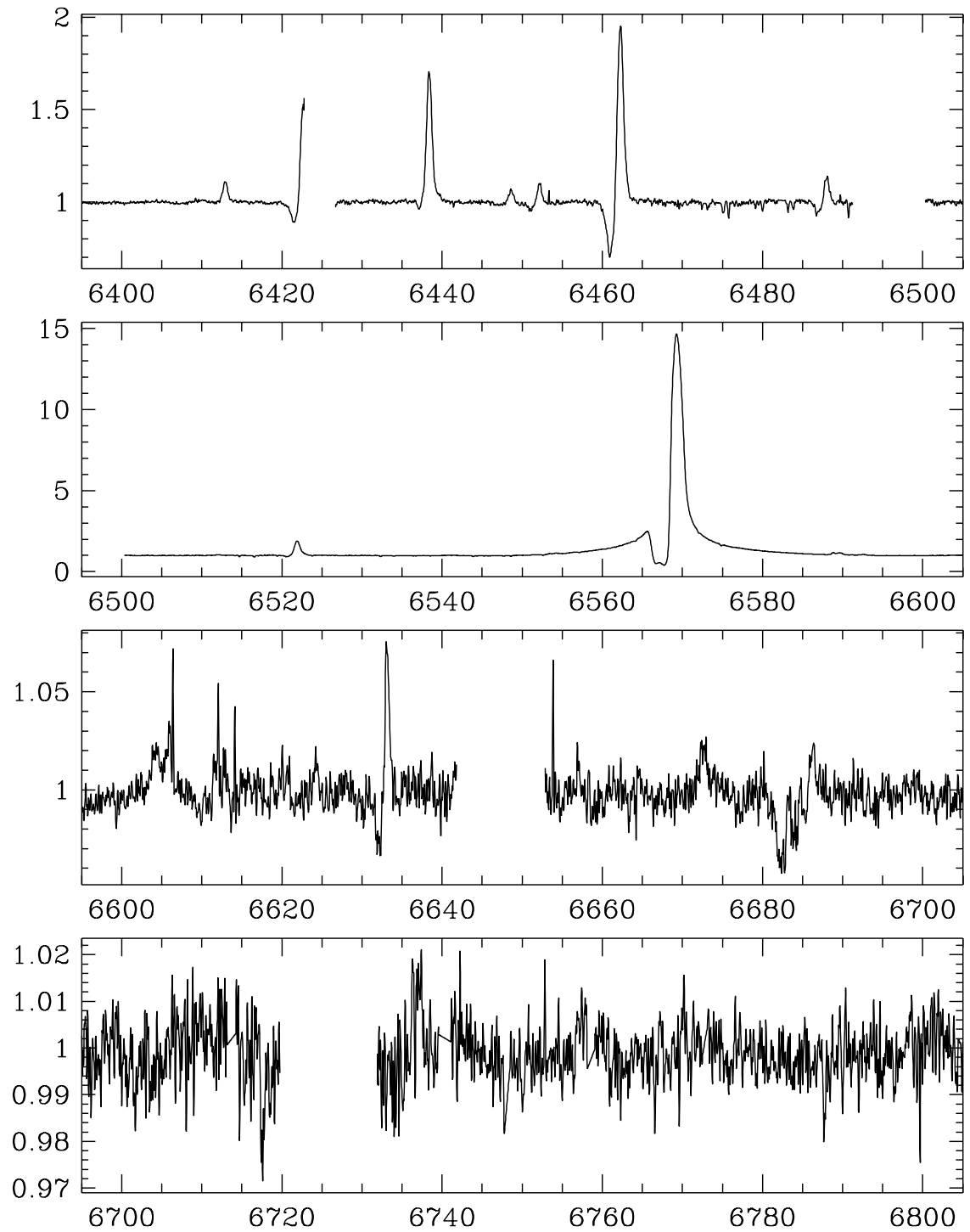
Figure A.48: Mean spectrum of S Dor from 6400 − 6800 Å; observed on Oct 4, 1995.

A.7   Mean Spectrum of R 40

- Observing instrument: UCLES/AAT

- Observing date: October 4, 1995

- Observed wavelength range: $3600 - 6800$ Å

- Spectral resolution: 50 000

- S/N ratio at 6400 Å: 140
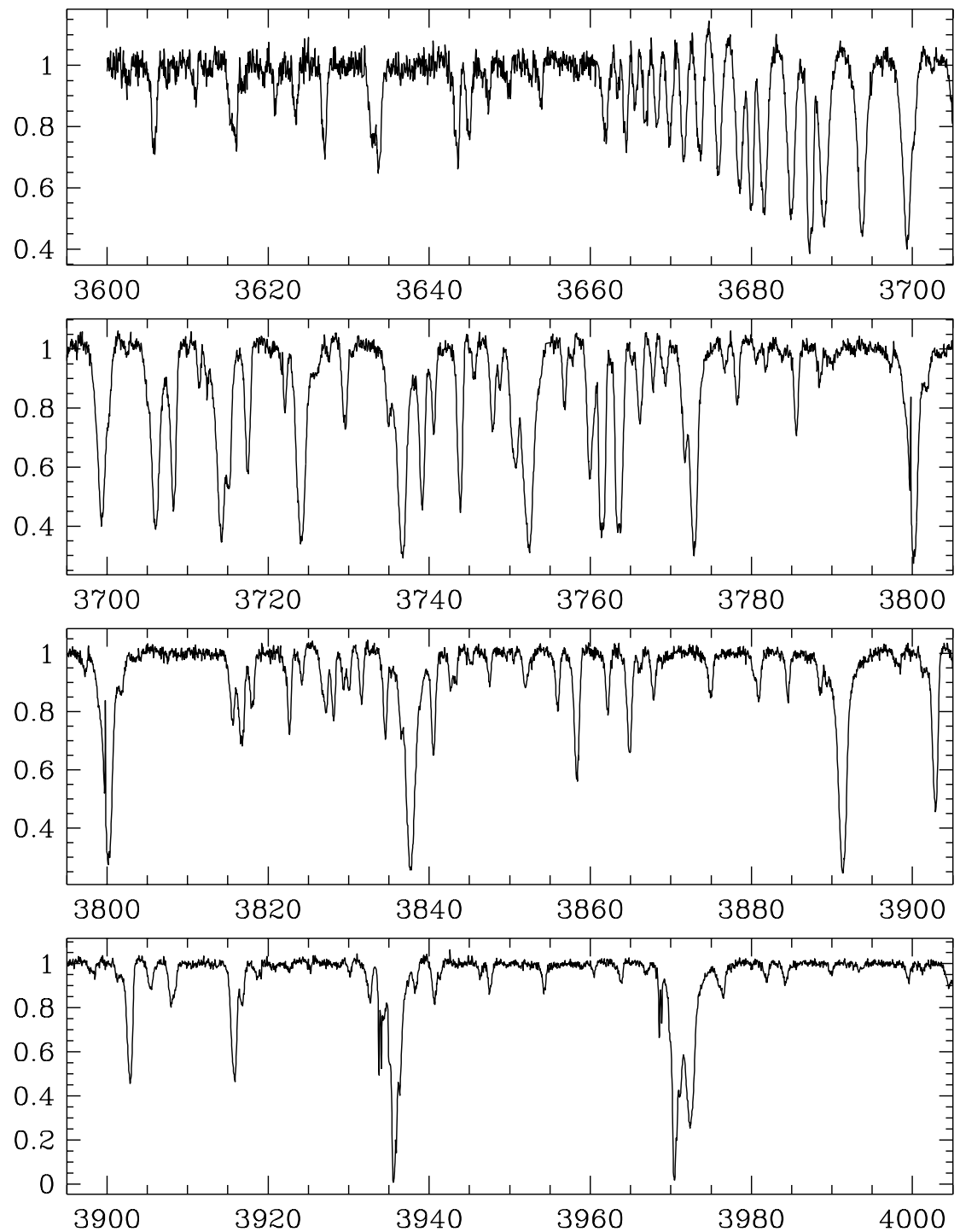
Figure A.49: Mean spectrum of R 40 from 3600−4000 Å; observed on Oct 4, 1995.
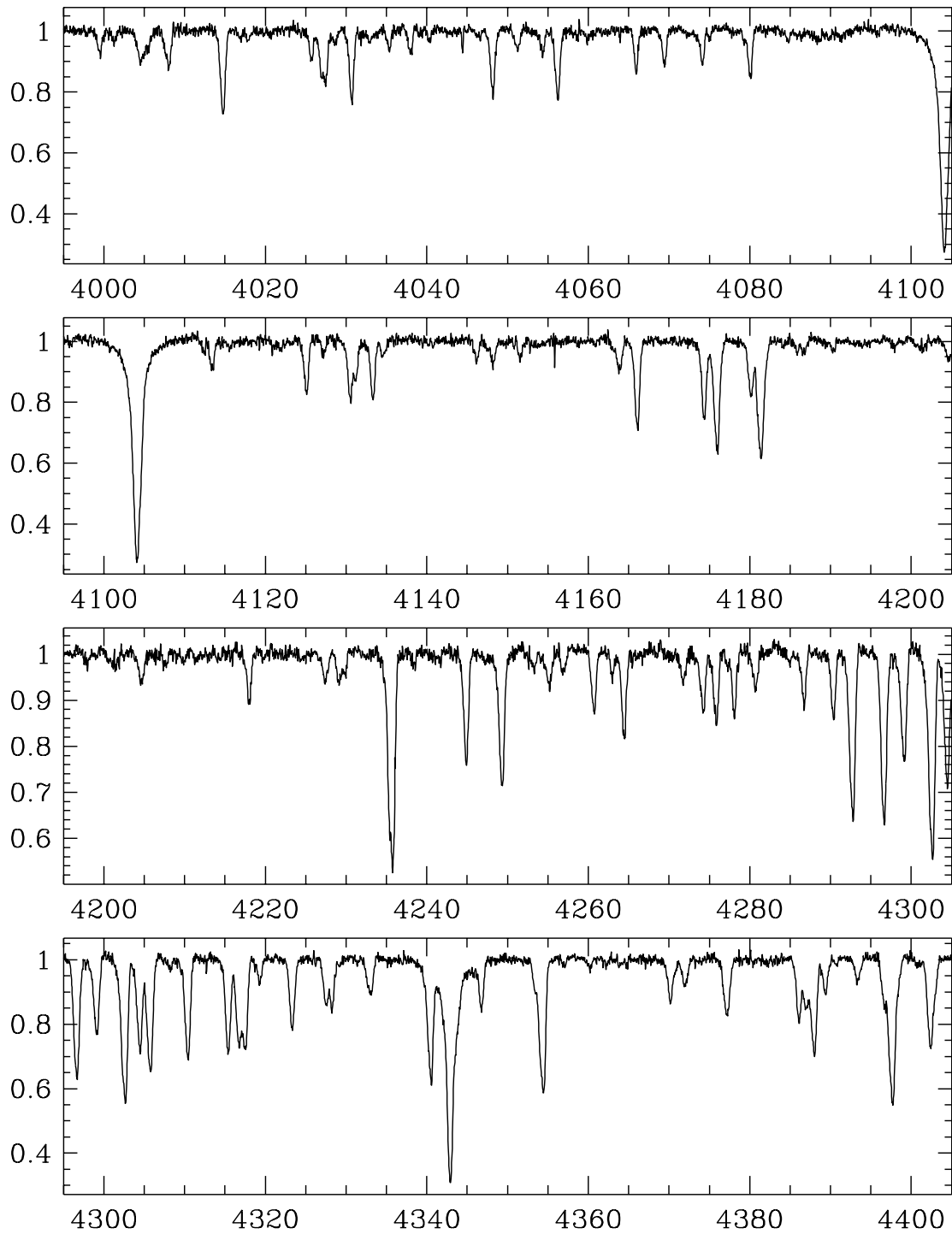
Figure A.50: Mean spectrum of R 40 from 4000 − 4400 Å; observed on Oct 4, 1995.
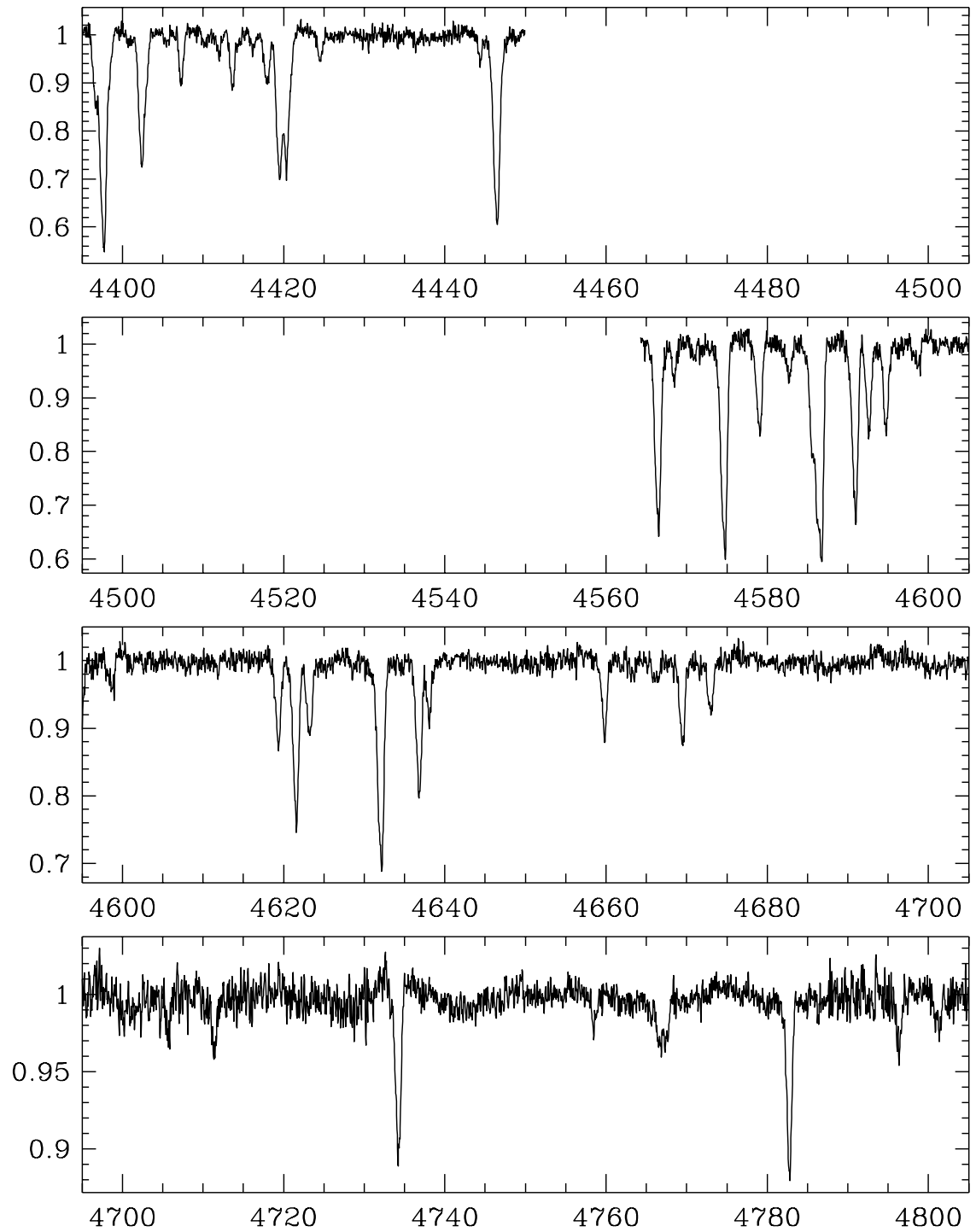
Figure A.51: Mean spectrum of R 40 from 4400 − 4800 Å; observed on Oct 4, 1995.
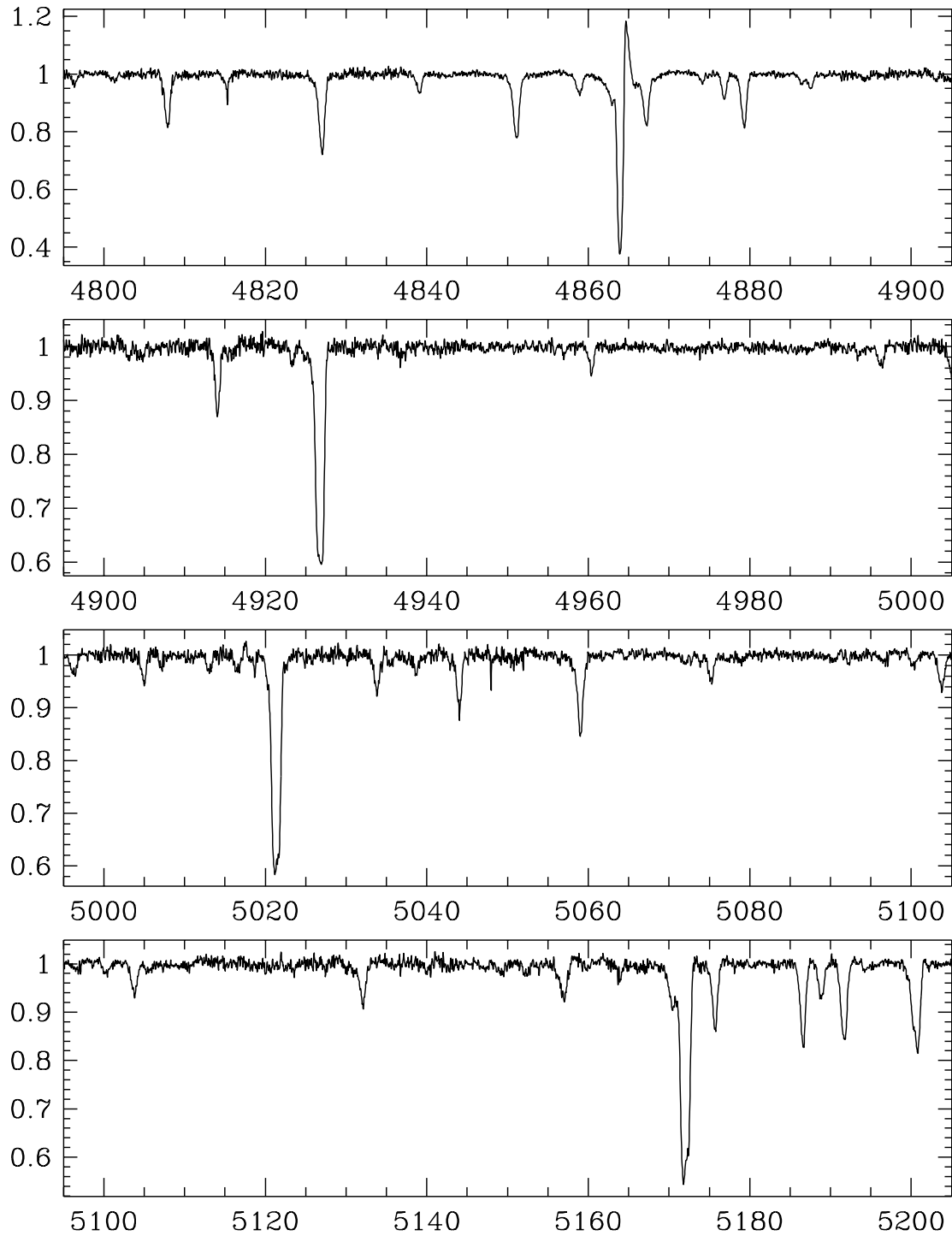
Figure A.52: Mean spectrum of R 40 from 4800 – 5200 Å; observed on Oct 4, 1995.
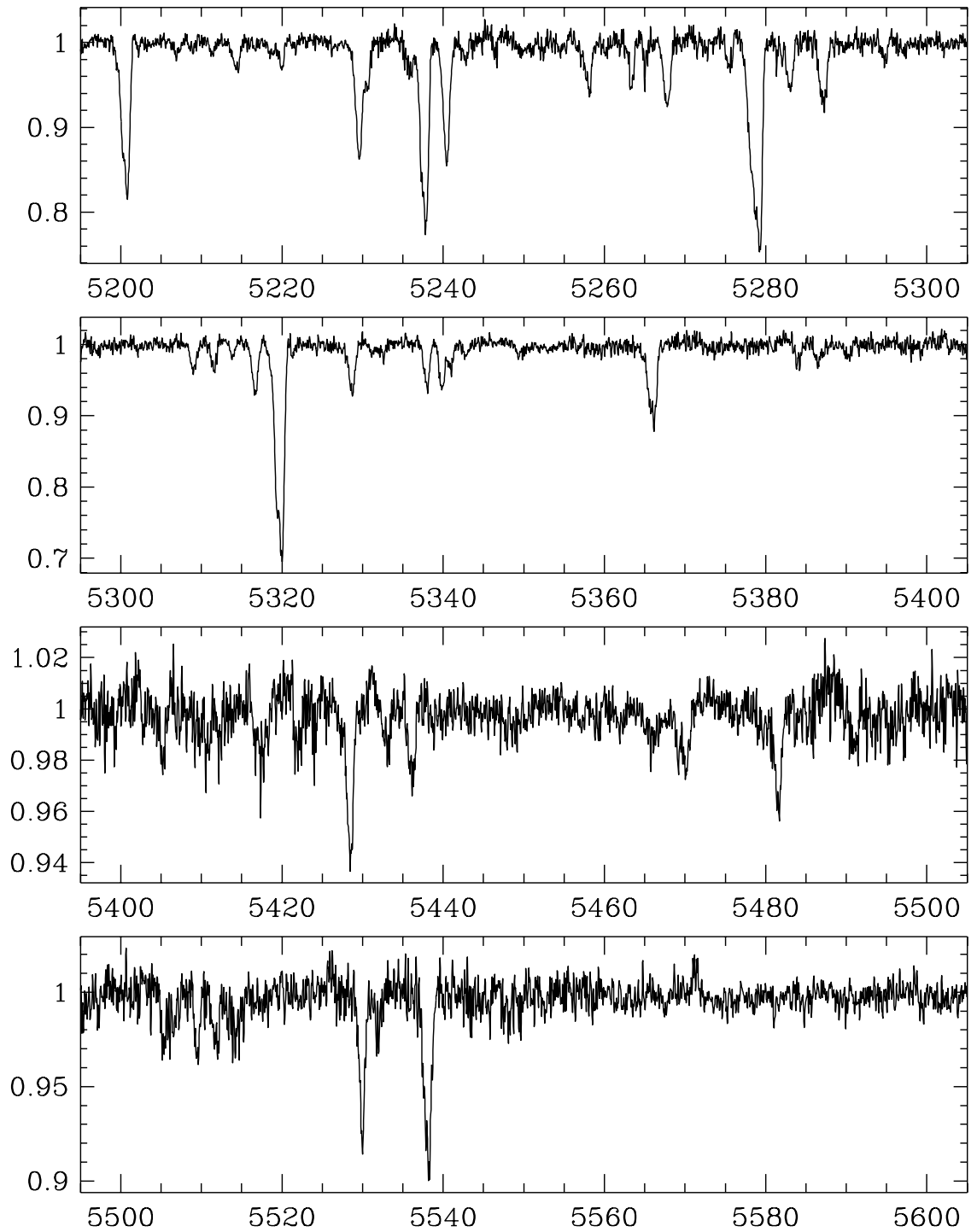
Figure A.53: Mean spectrum of R 40 from 5200 − 5600 Å; observed on Oct 4, 1995.
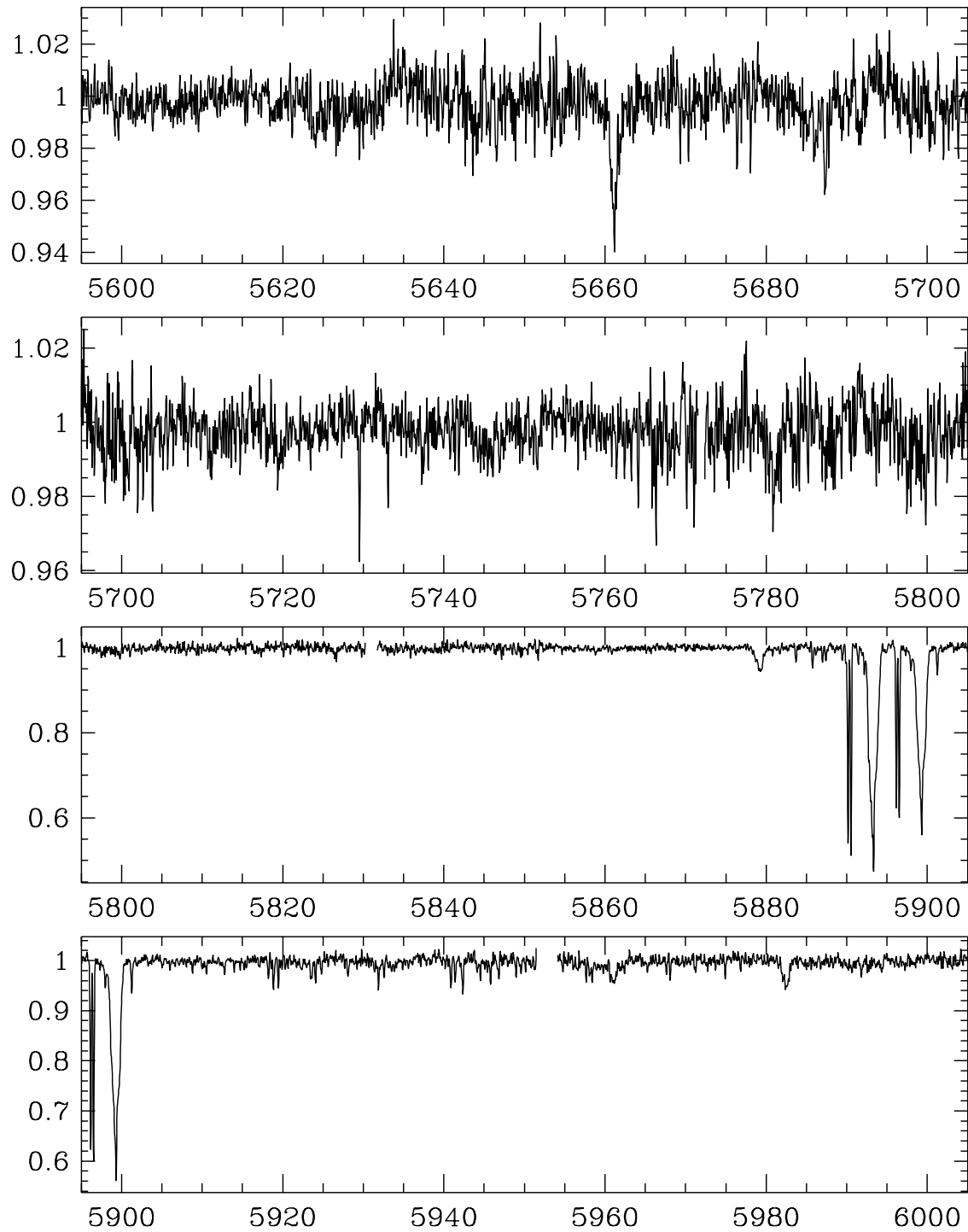
Figure A.54: Mean spectrum of R 40 from 5600−6000 Å; observed on Oct 4, 1995.
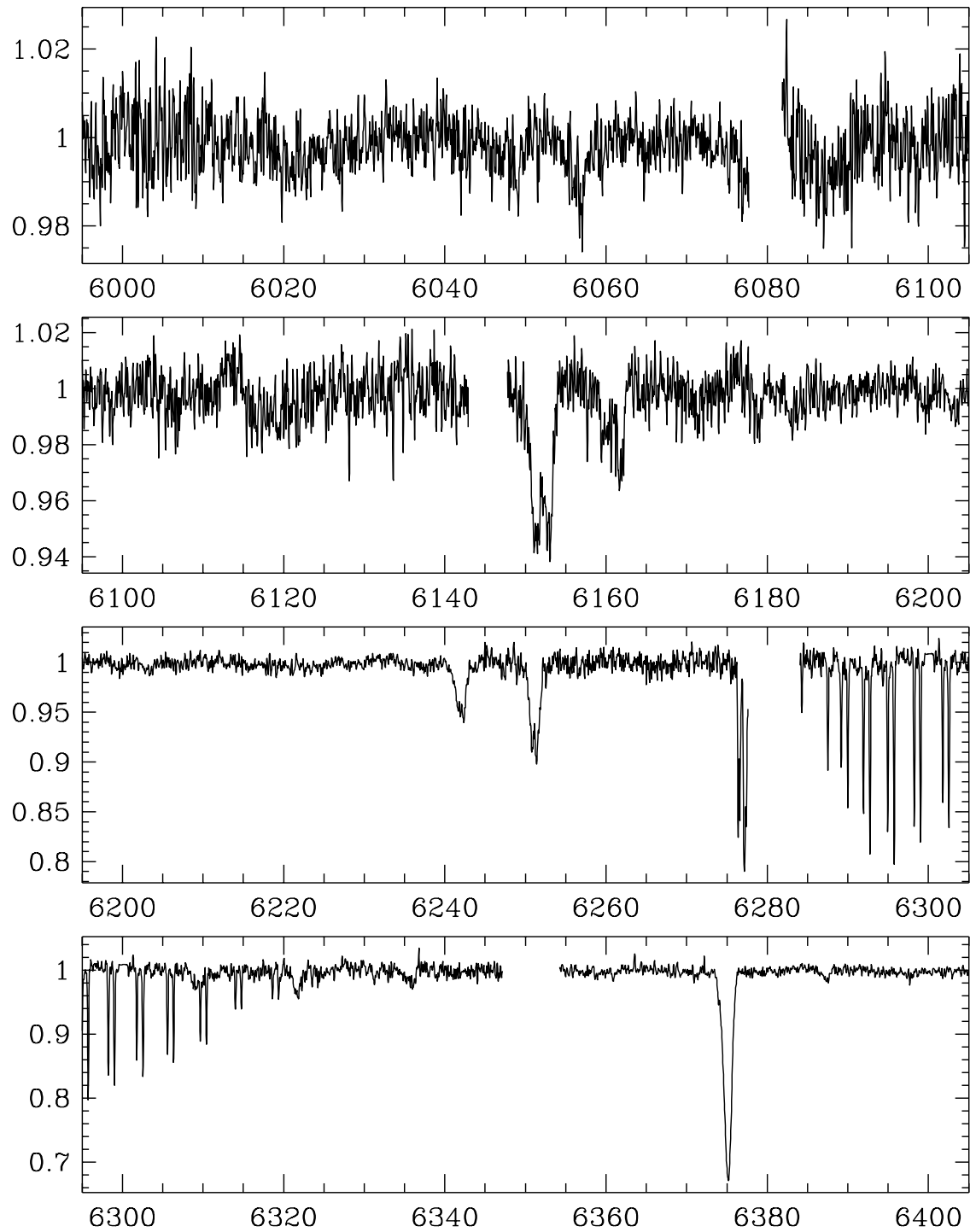
Figure A.55: Mean spectrum of R 40 from 6000−6400 Å; observed on Oct 4, 1995.
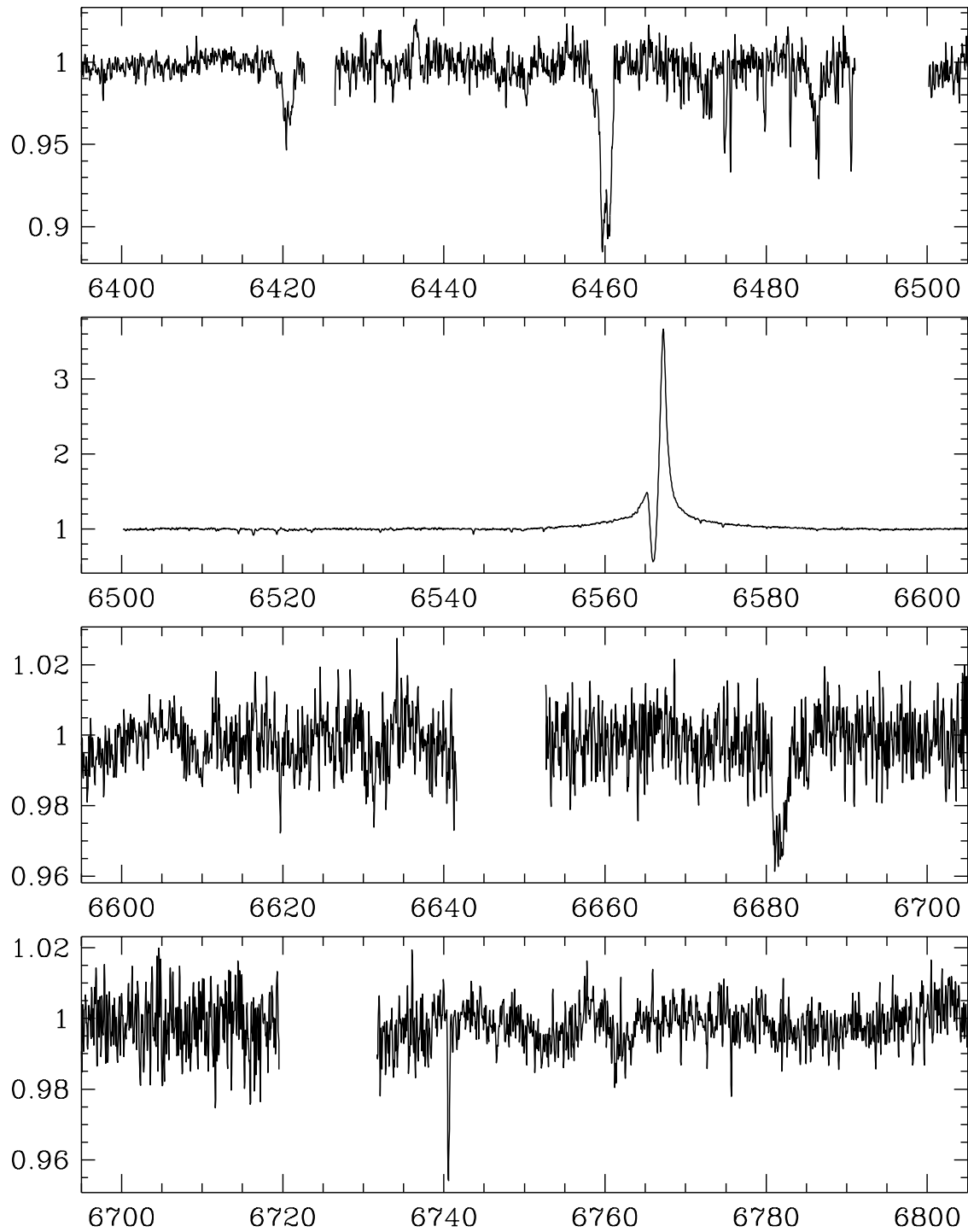
Figure A.56: Mean spectrum of R 40 from 6400–6800 Å; observed on Oct 4, 1995.

A.8   Mean Spectrum of R 71

- Observing instrument: UCLES/AAT

- Observing date: October 3, 1995

- Observed wavelength range: $3600 - 6800$ Å

- Spectral resolution: 50 000

- S/N ratio at 6400 Å: 50
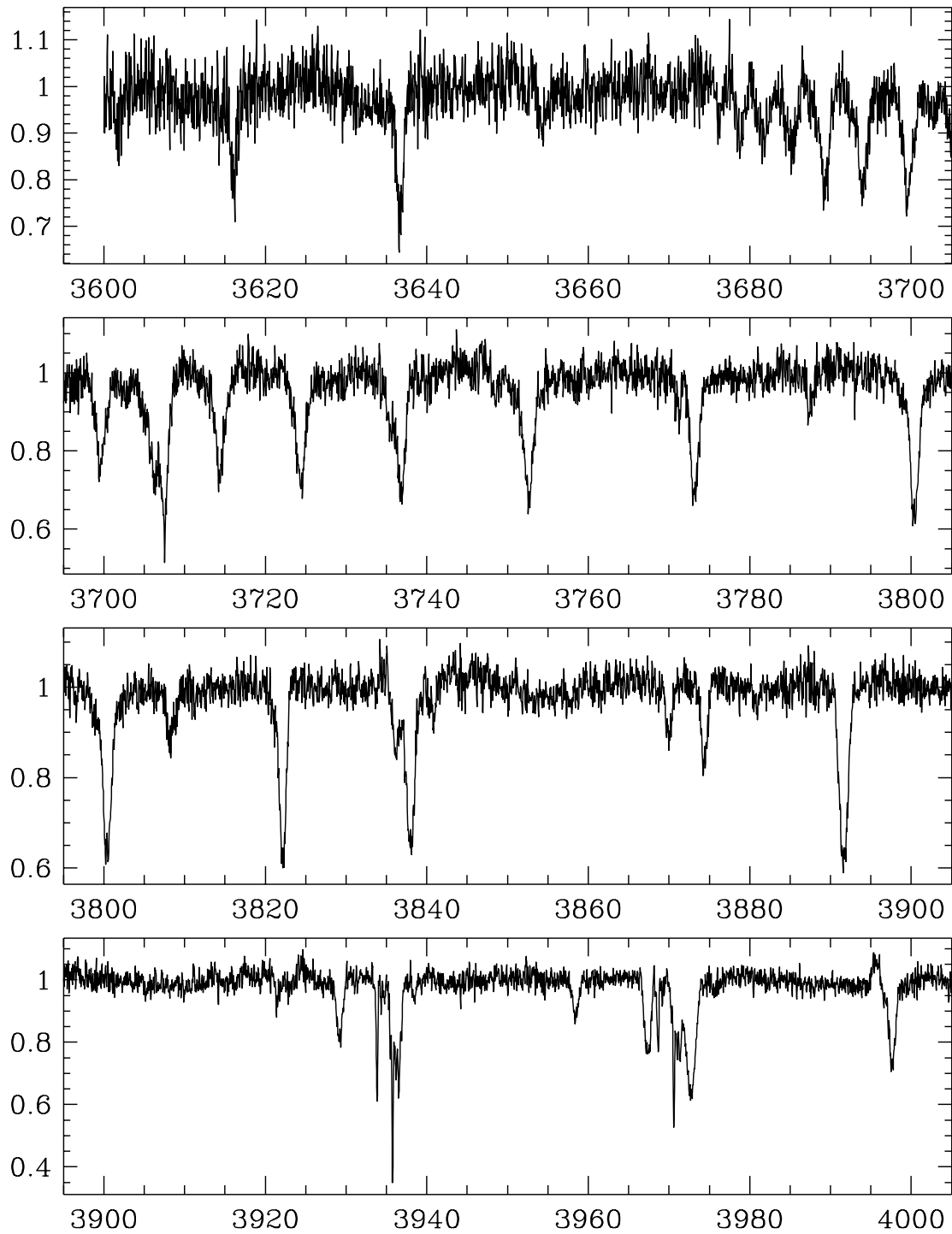
Figure A.57: Mean spectrum of R 71 from 3600−4000 Å; observed on Oct 3, 1995.
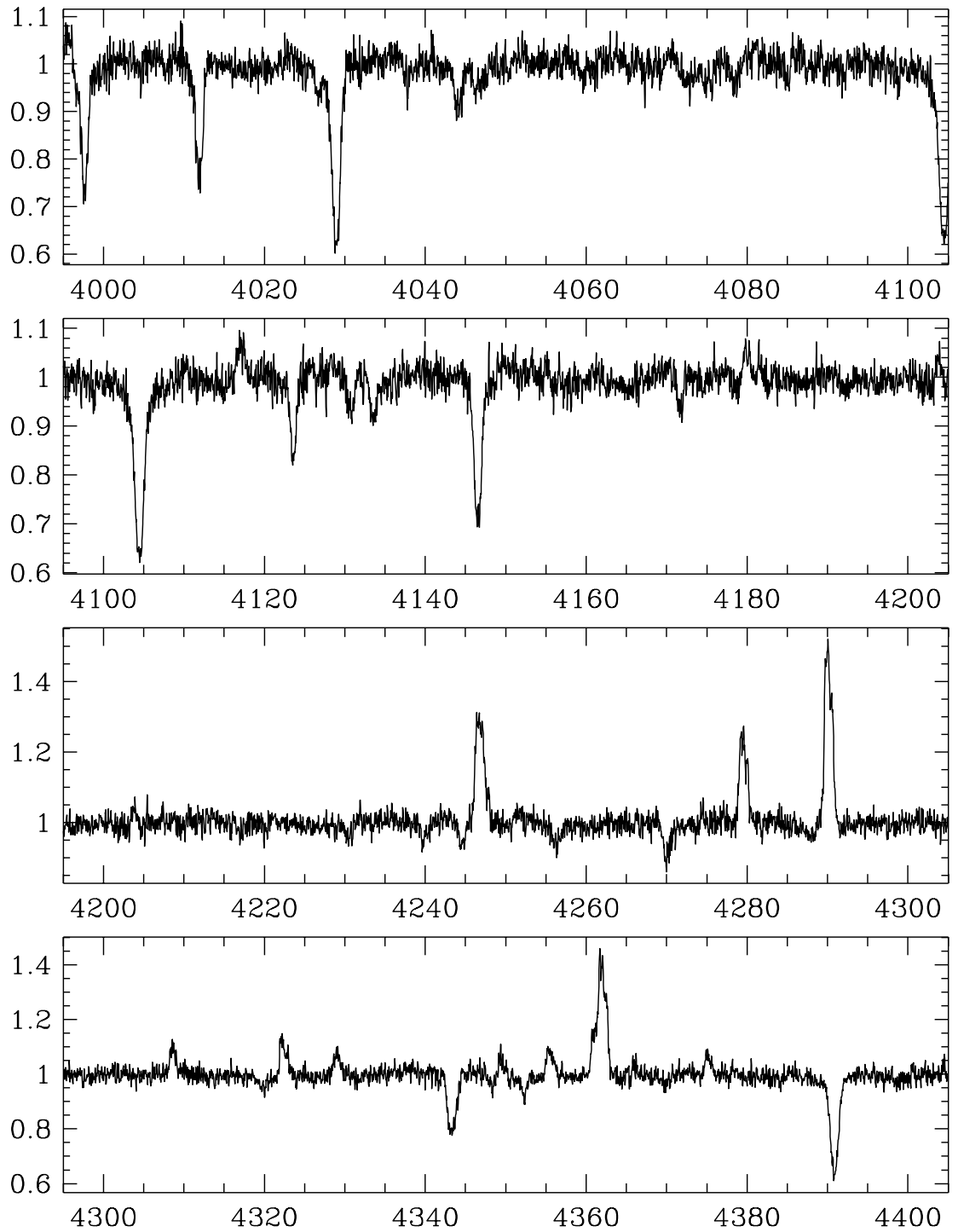
Figure A.58: Mean spectrum of R 71 from 4000 − 4400 Å; observed on Oct 3, 1995.
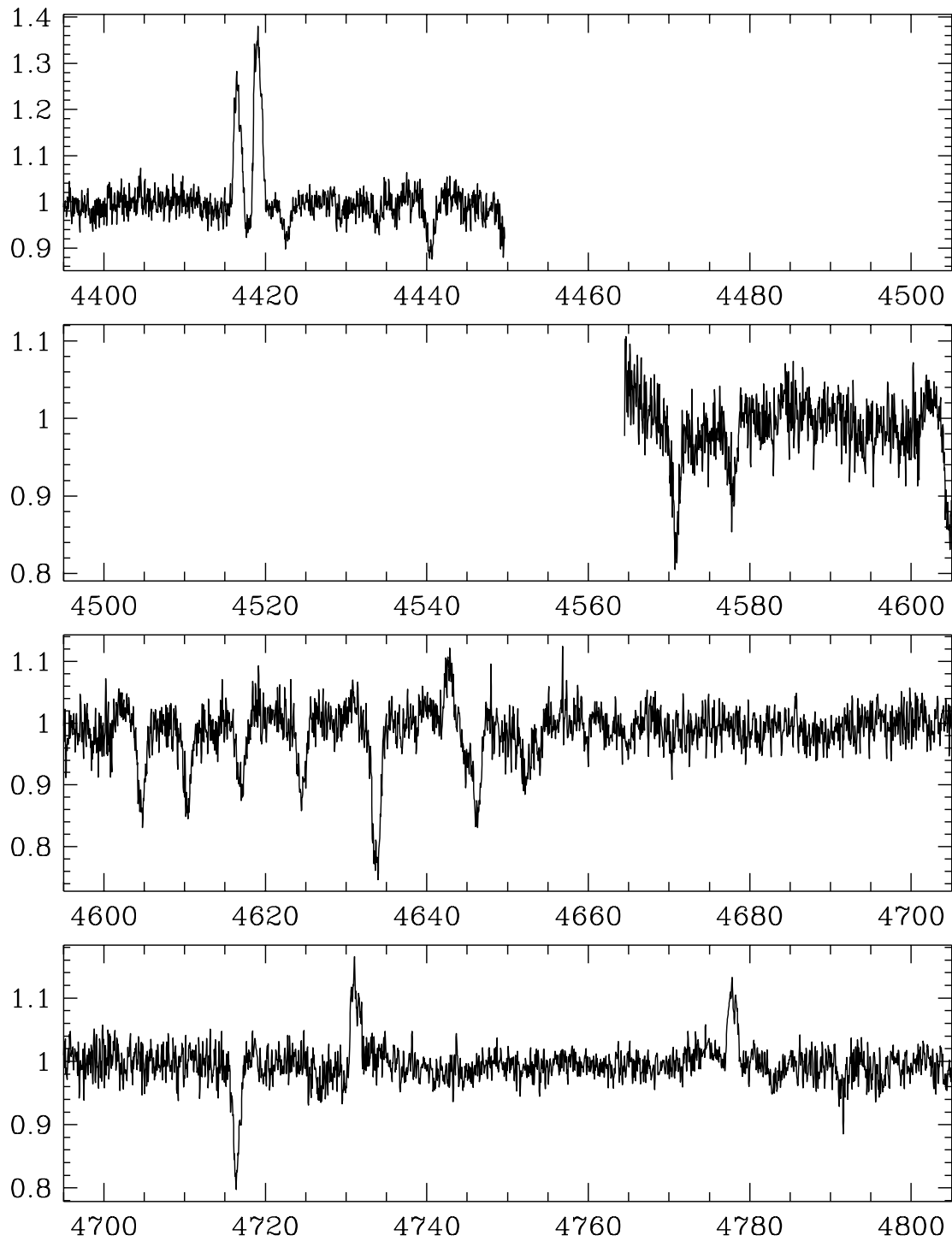
Figure A.59: Mean spectrum of R 71 from 4400 − 4800 Å; observed on Oct 3, 1995.
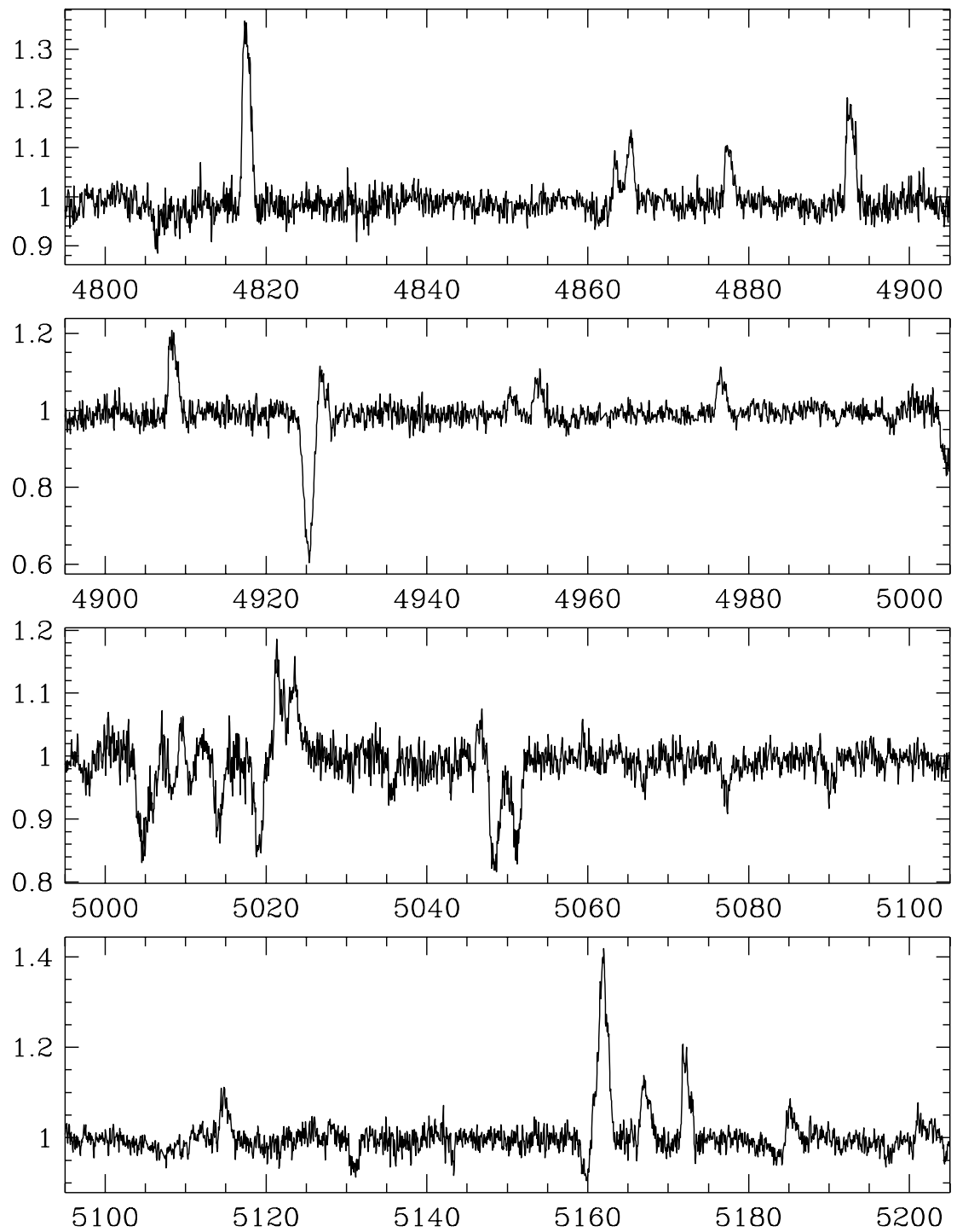
Figure A.60: Mean spectrum of R 71 from 4800−5200 Å; observed on Oct 3, 1995.
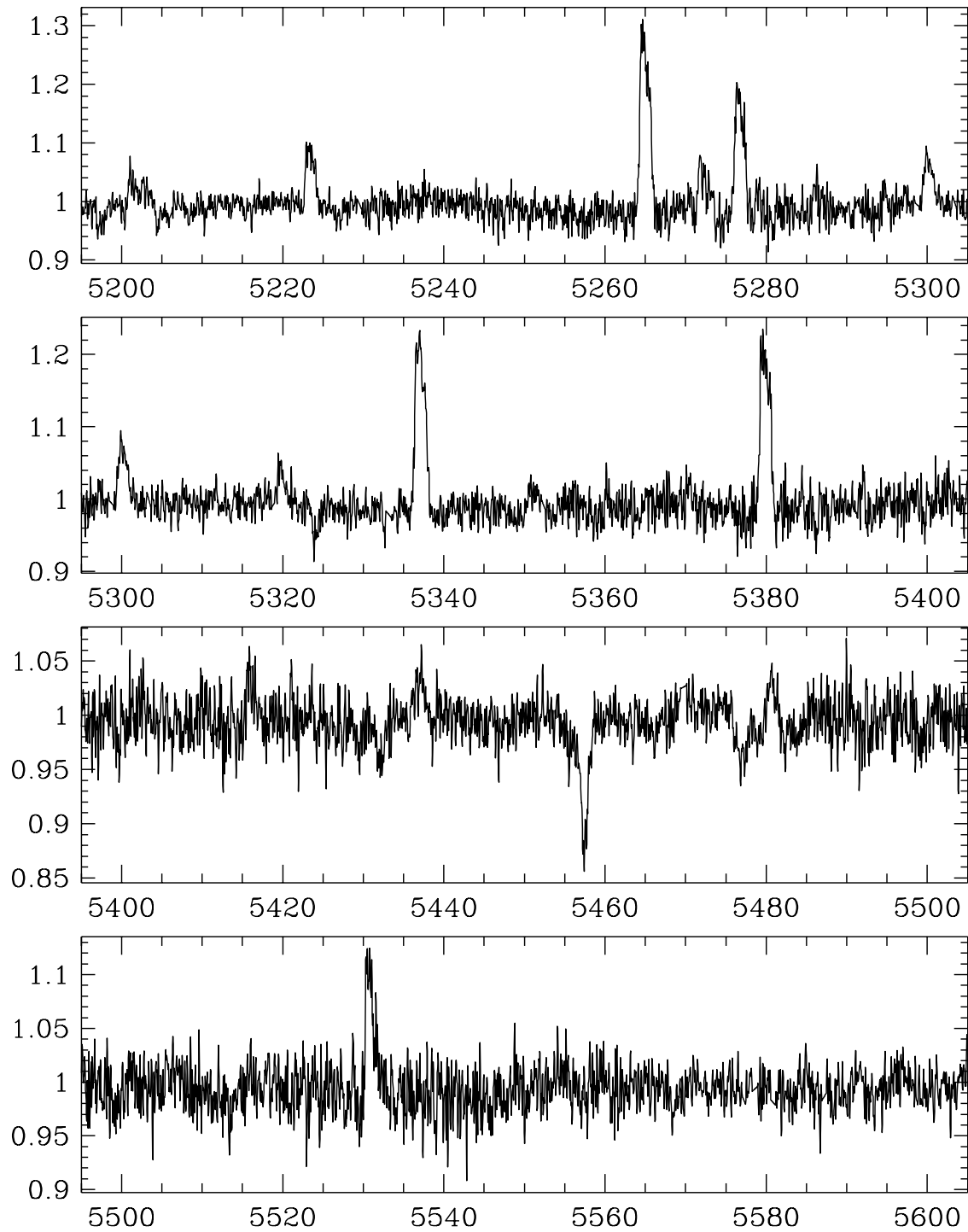
Figure A.61: Mean spectrum of R 71 from 5200 − 5600 Å; observed on Oct 3, 1995.
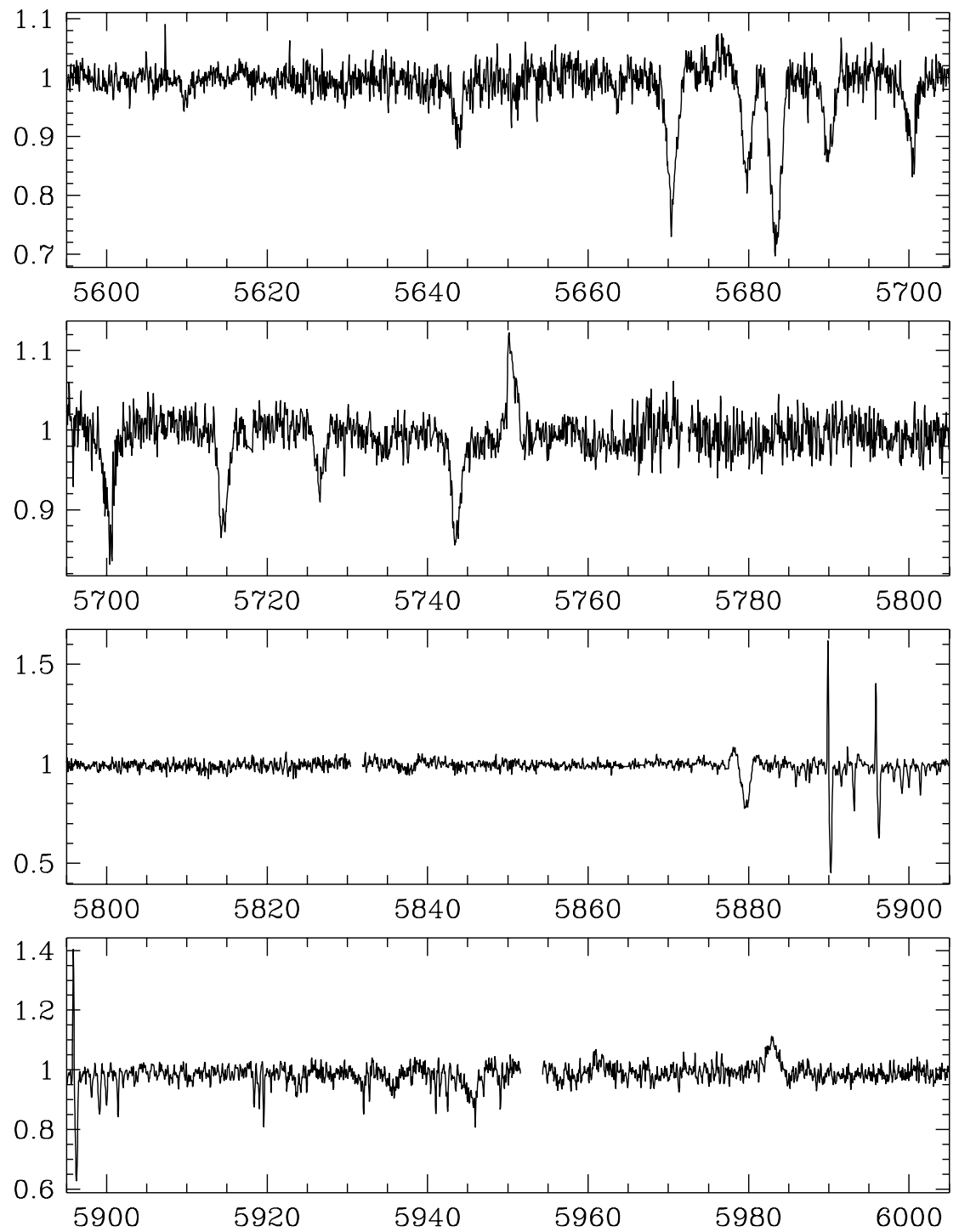
Figure A.62: Mean spectrum of R 71 from 5600 − 6000 Å; observed on Oct 3, 1995.
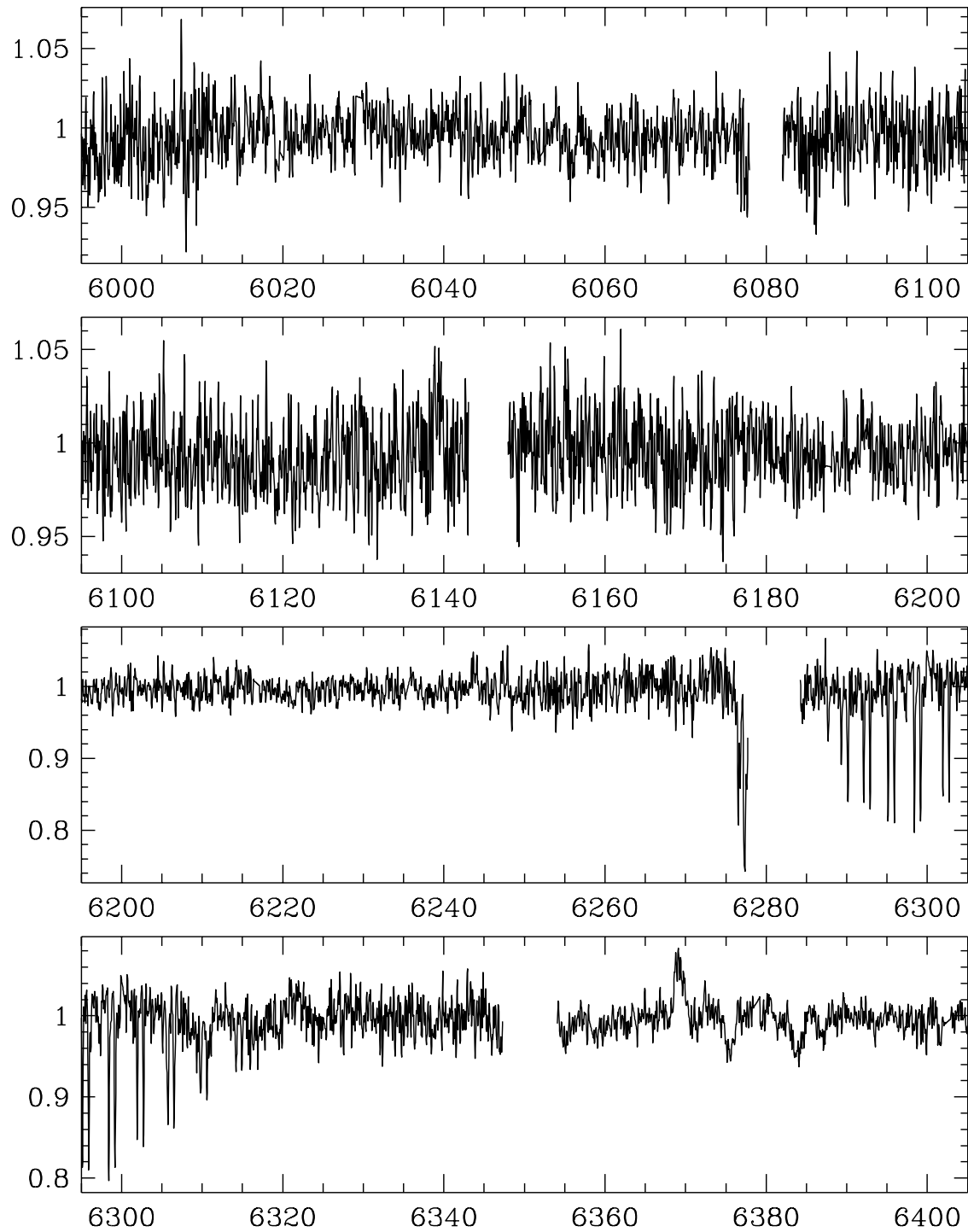
Figure A.63: Mean spectrum of R 71 from 6000–6400 Å; observed on Oct 3, 1995.
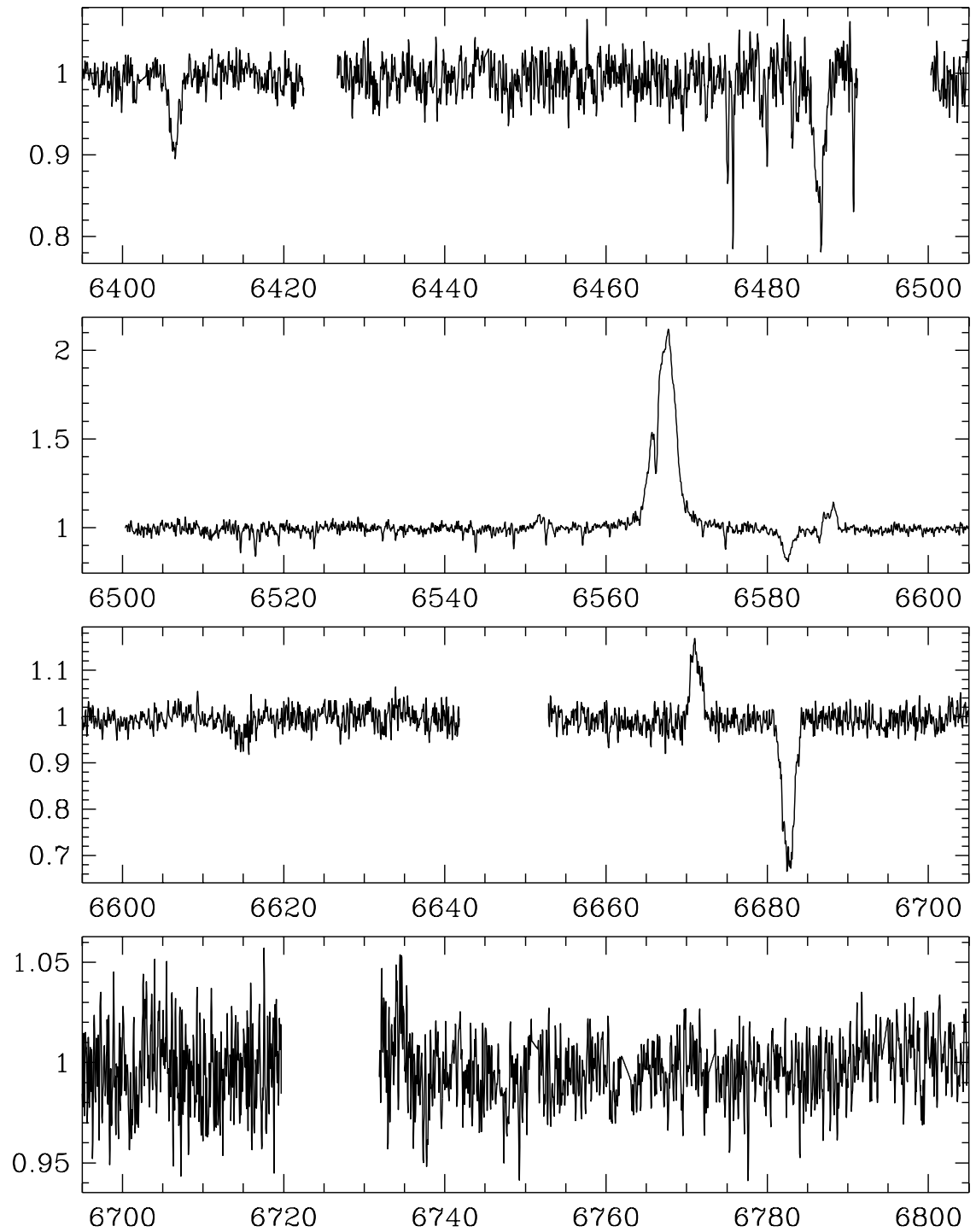
Figure A.64: Mean spectrum of R 71 from 6400 − 6800 Å; observed on Oct 3, 1995.

A.9   Mean Spectrum of R 81

- Observing instrument: UCLES/AAT

- Observing date: October 4, 1995

- Observed wavelength range: $3600 - 6800\,\text{Å}$

- Spectral resolution: 50 000

- S/N ratio at 6400 Å: 120
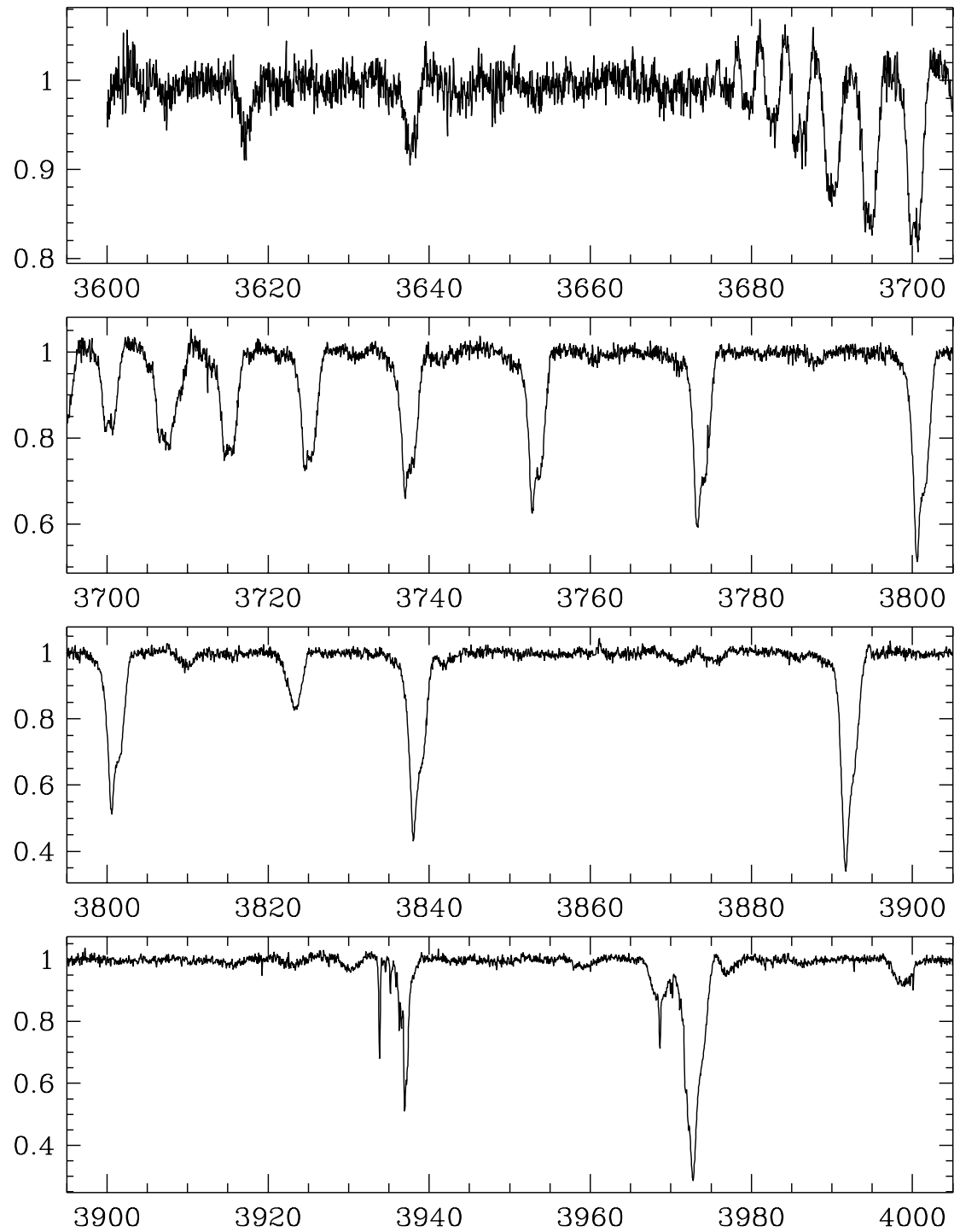
Figure A.65: Mean spectrum of R 81 from 3600−4000 Å; observed on Oct 4, 1995.
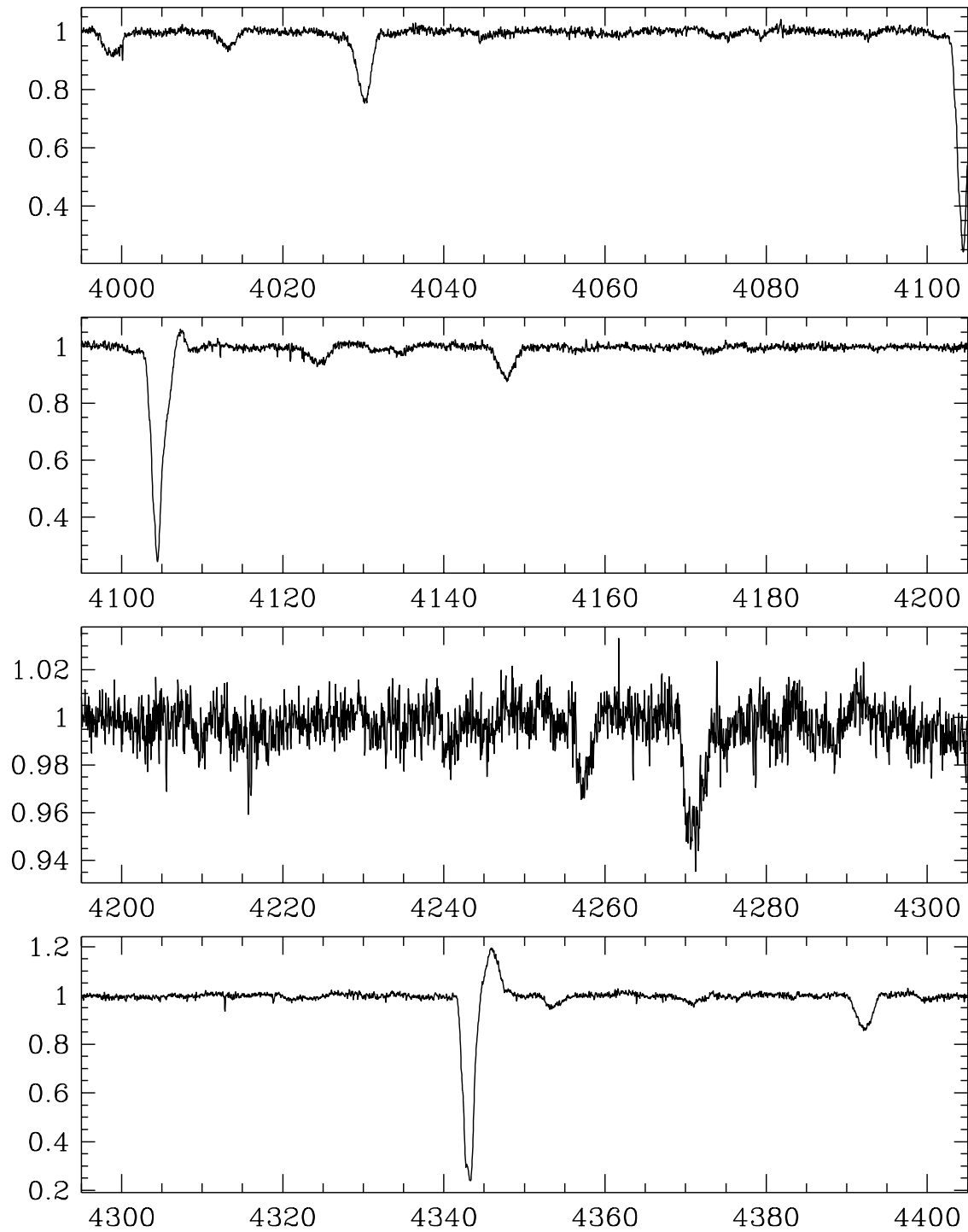
Figure A.66: Mean spectrum of R 81 from $4000-4400$ Å; observed on Oct 4, 1995.
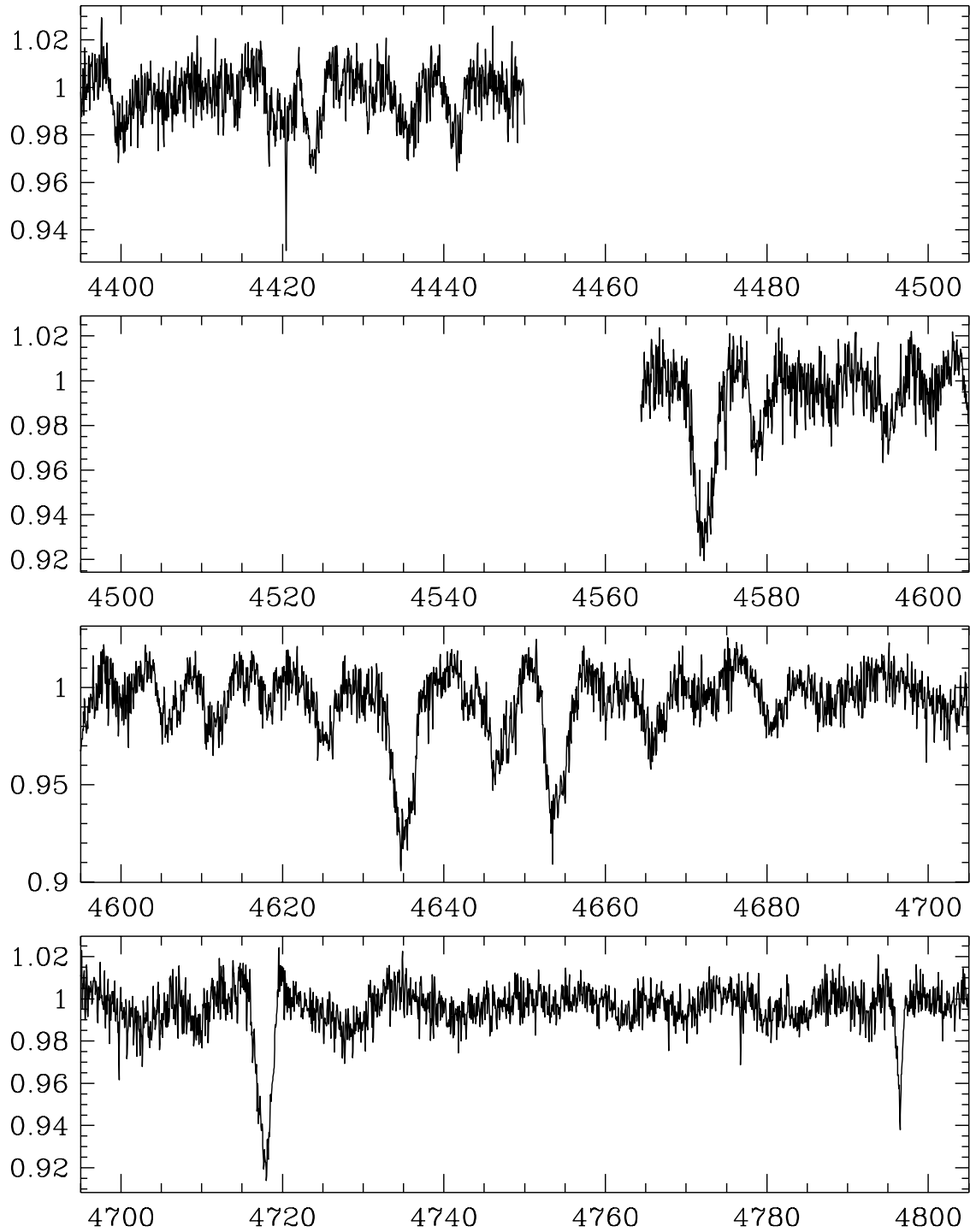
Figure A.67: Mean spectrum of R 81 from 4400−4800 Å; observed on Oct 4, 1995.
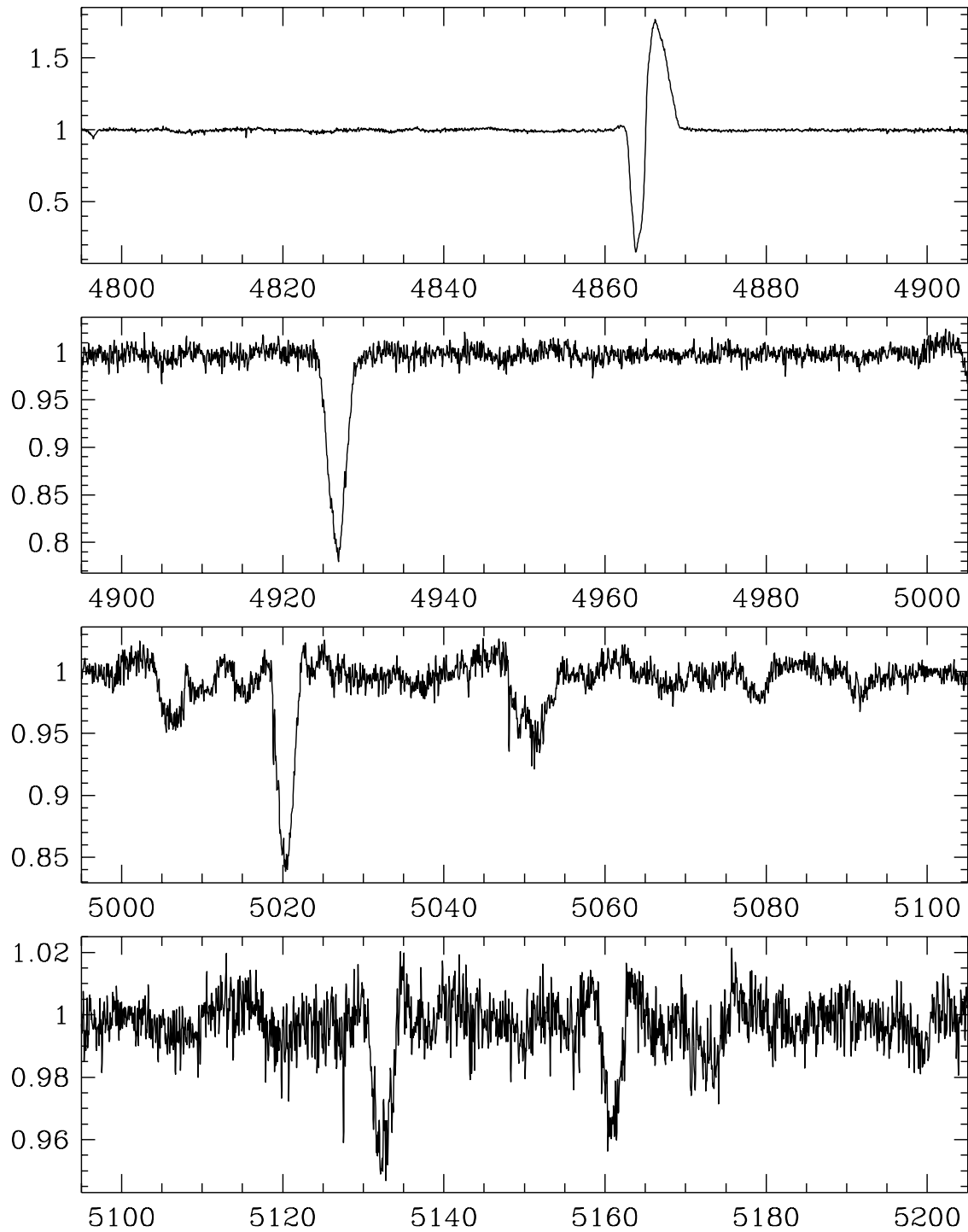
Figure A.68: Mean spectrum of R 81 from 4800−5200 Å; observed on Oct 4, 1995.
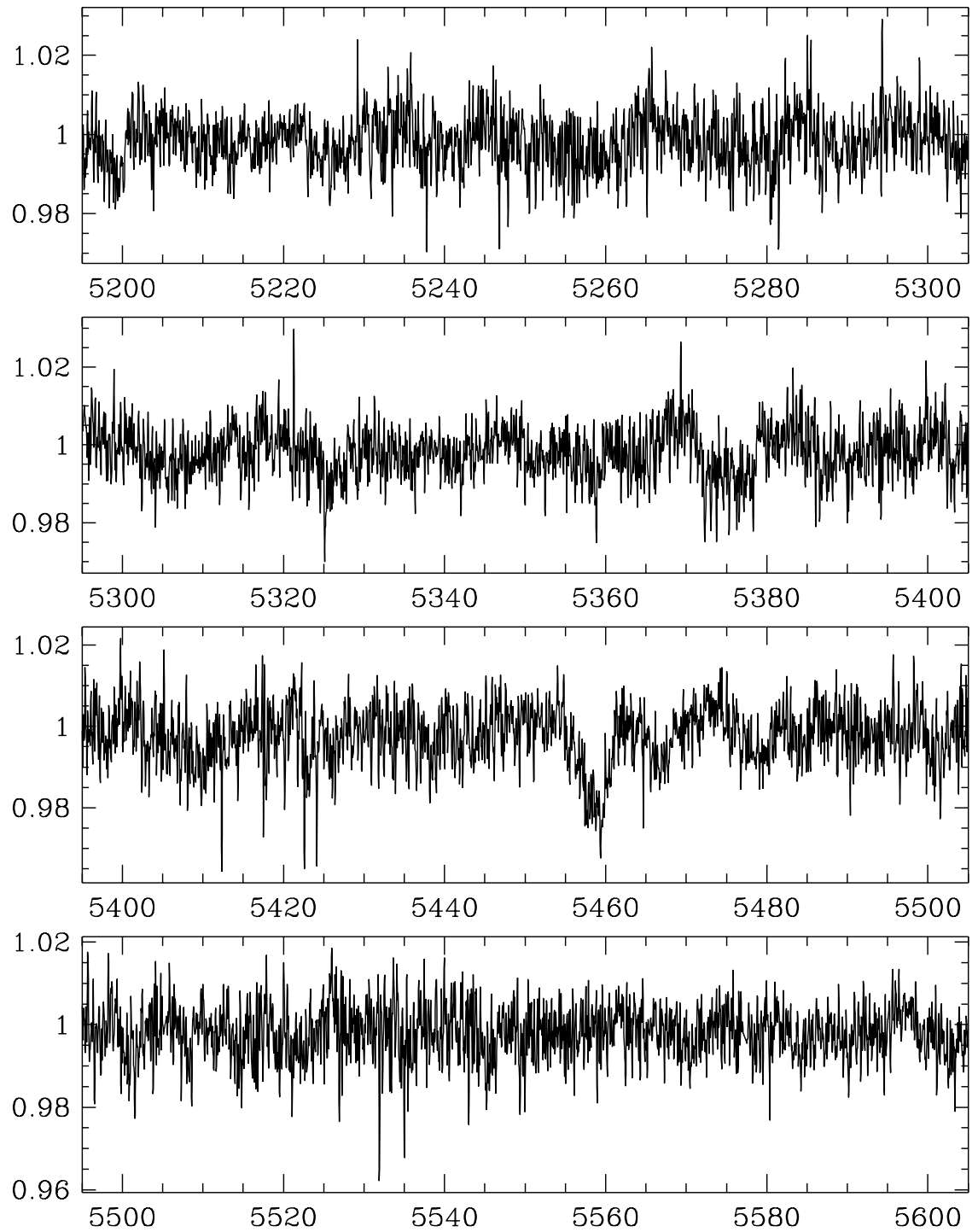
Figure A.69: Mean spectrum of R 81 from 5200 – 5600 Å; observed on Oct 4, 1995.
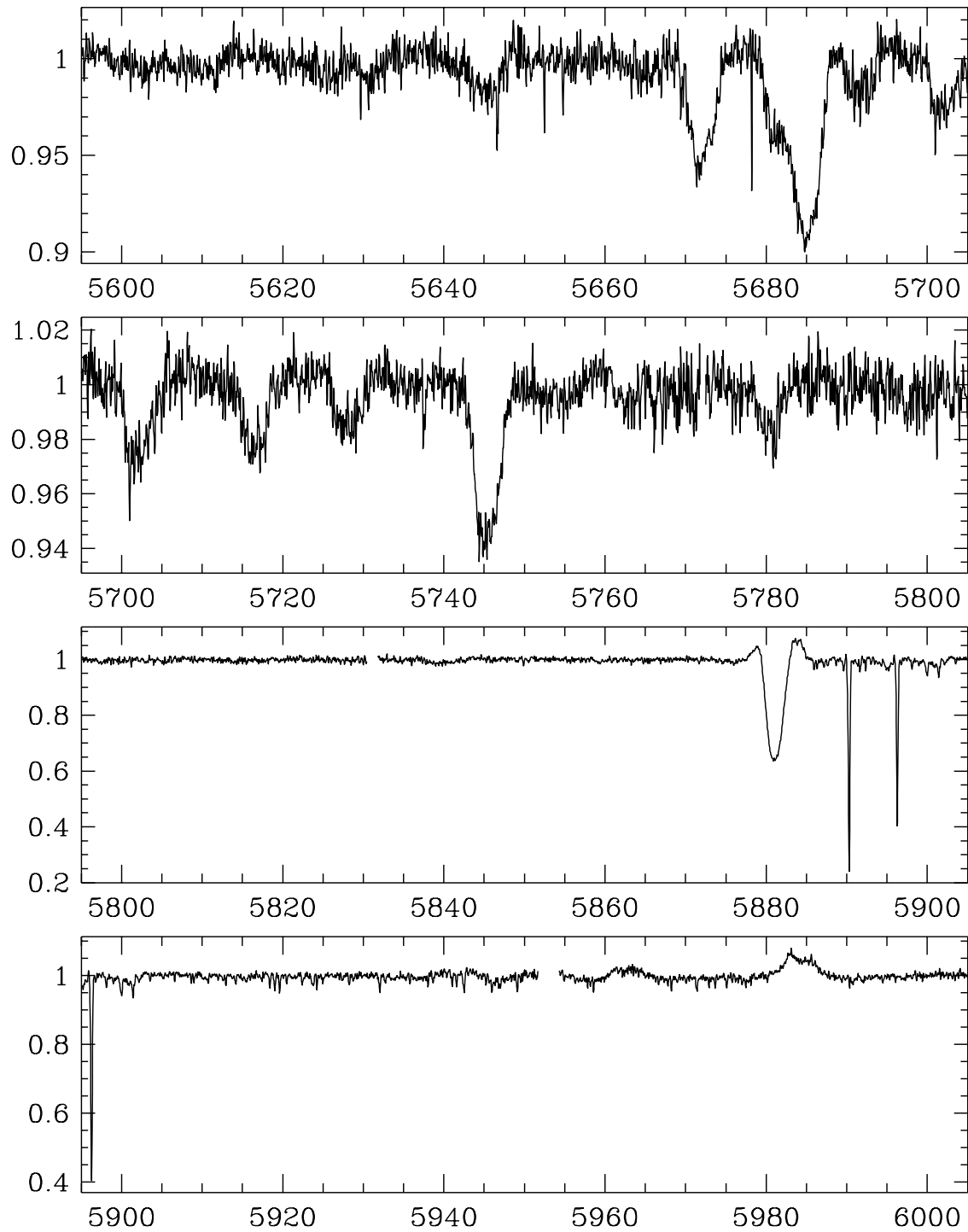
Figure A.70: Mean spectrum of R 81 from 5600−6000 Å; observed on Oct 4, 1995.
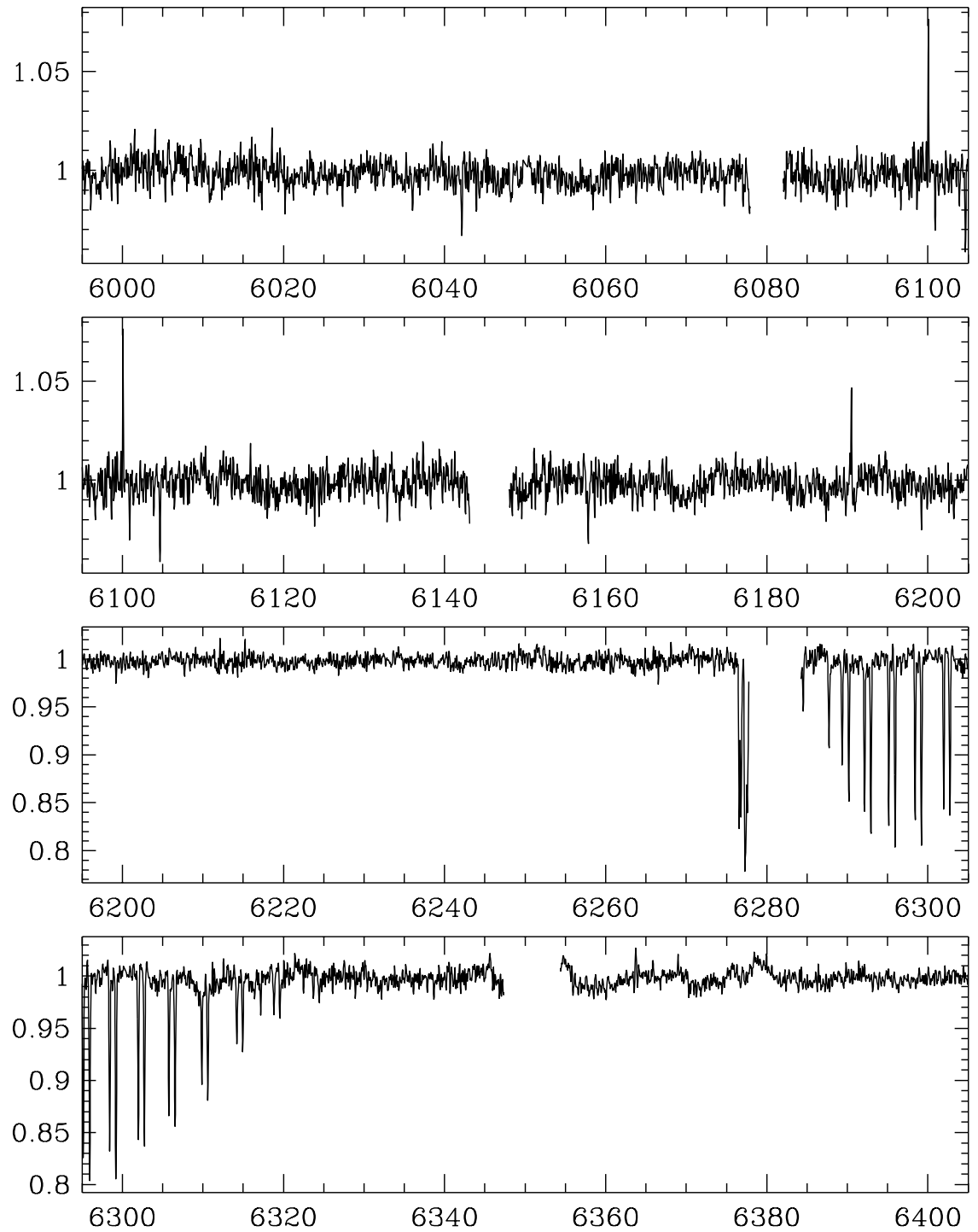
Figure A.71: Mean spectrum of R 81 from 6000−6400 Å; observed on Oct 4, 1995.
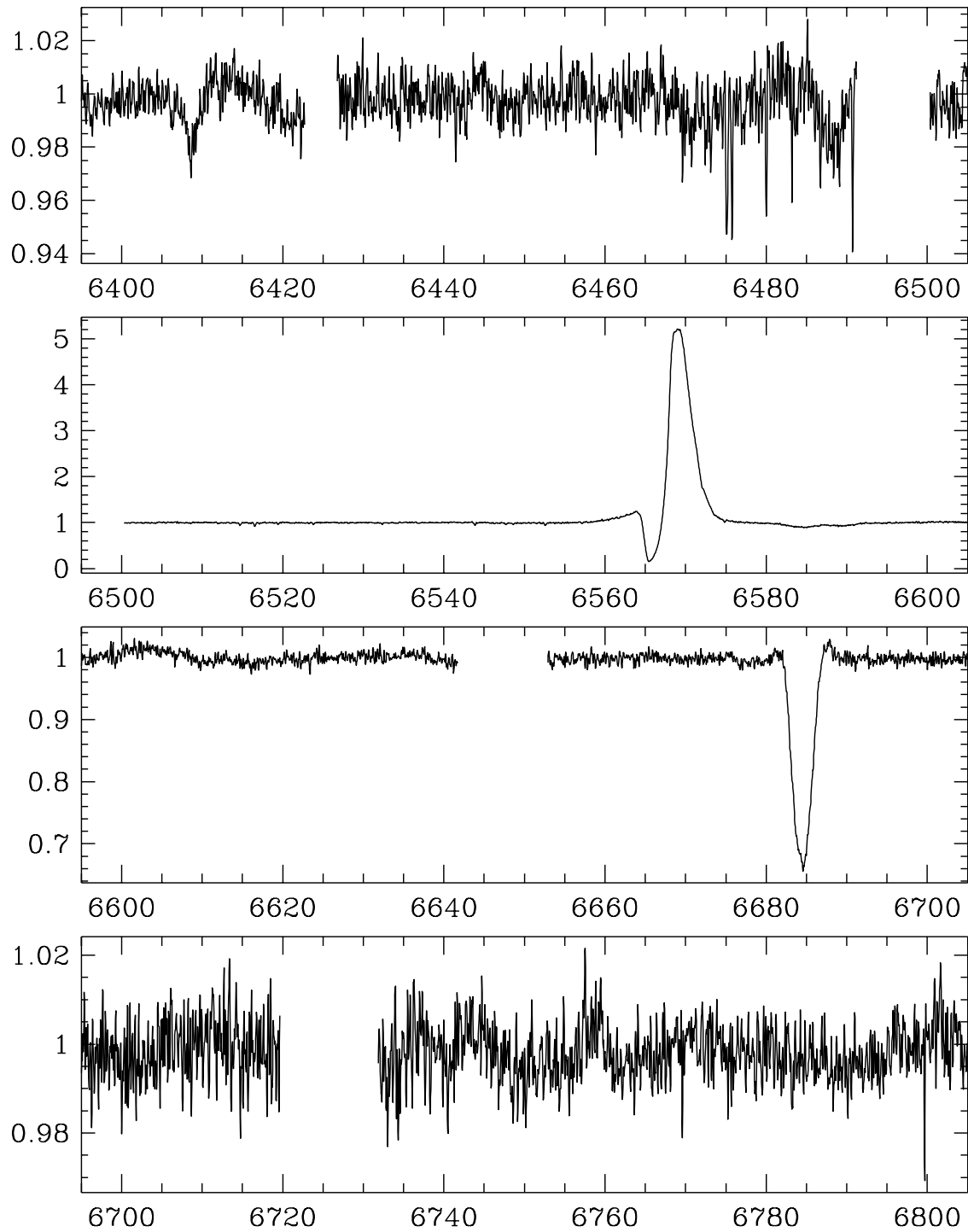
Figure A.72: Mean spectrum of R 81 from 6400−6800 Å; observed on Oct 4, 1995.

A.10 Mean Spectrum of η Car

- Observing instrument: CES/CAT

- Observing date: April 10 – 12, 1996

- Observed wavelength range: 4320 – 6602 Å

- Spectral resolution: 60 000

- S/N ratio at 6400 Å: 630
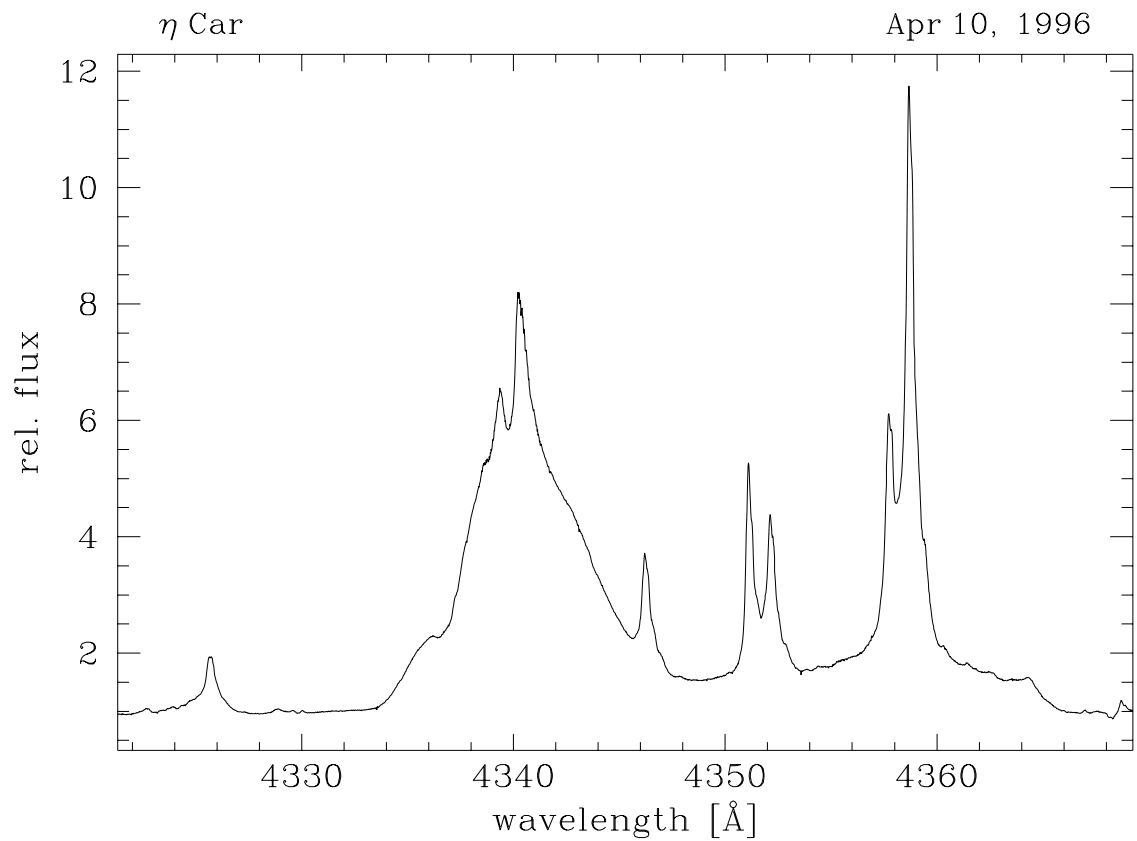
Figure A.73: Mean spectrum of η Car; observed in April 1996.
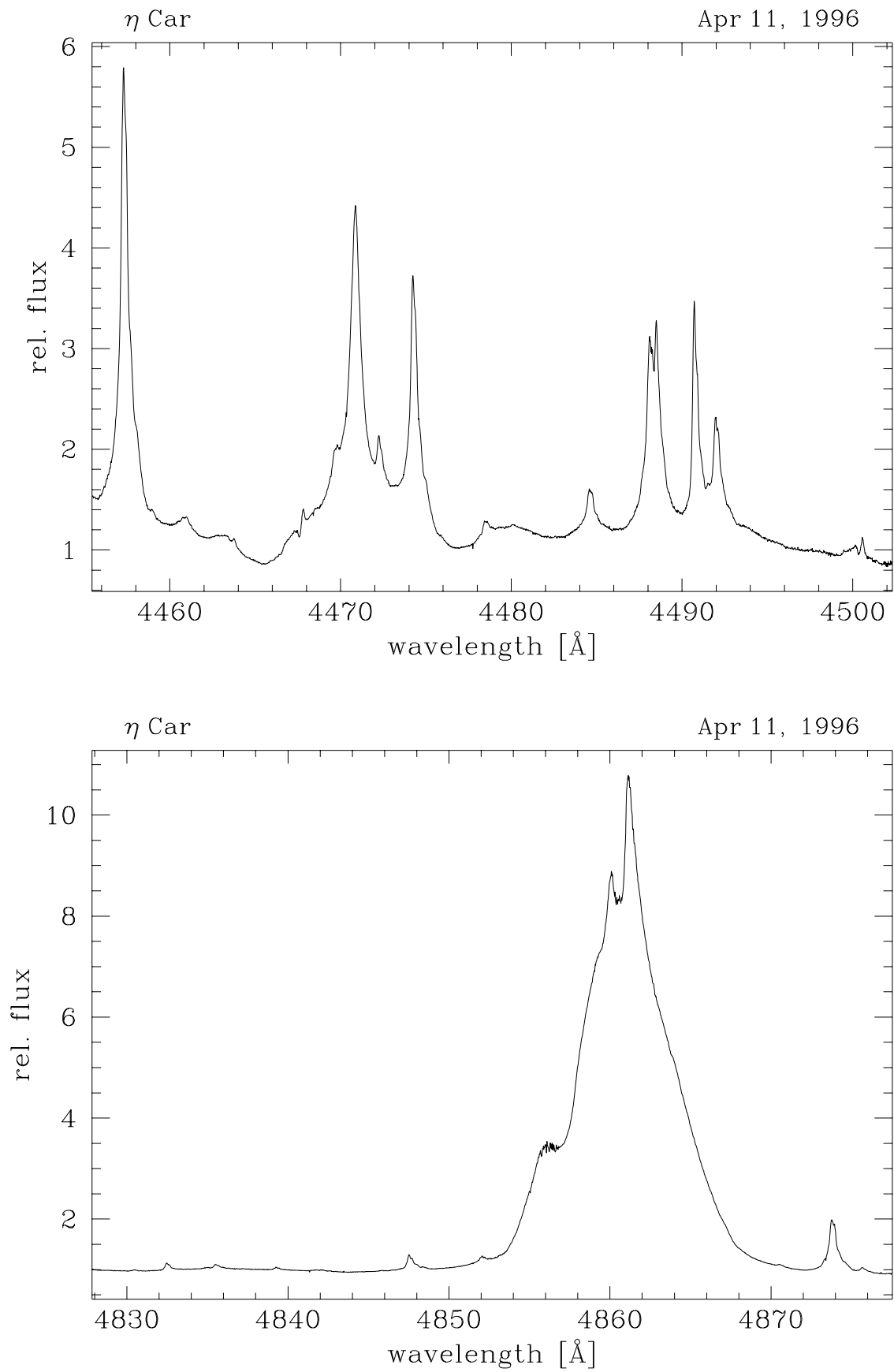
Figure A.74: Mean spectrum of η Car; observed in April 1996.
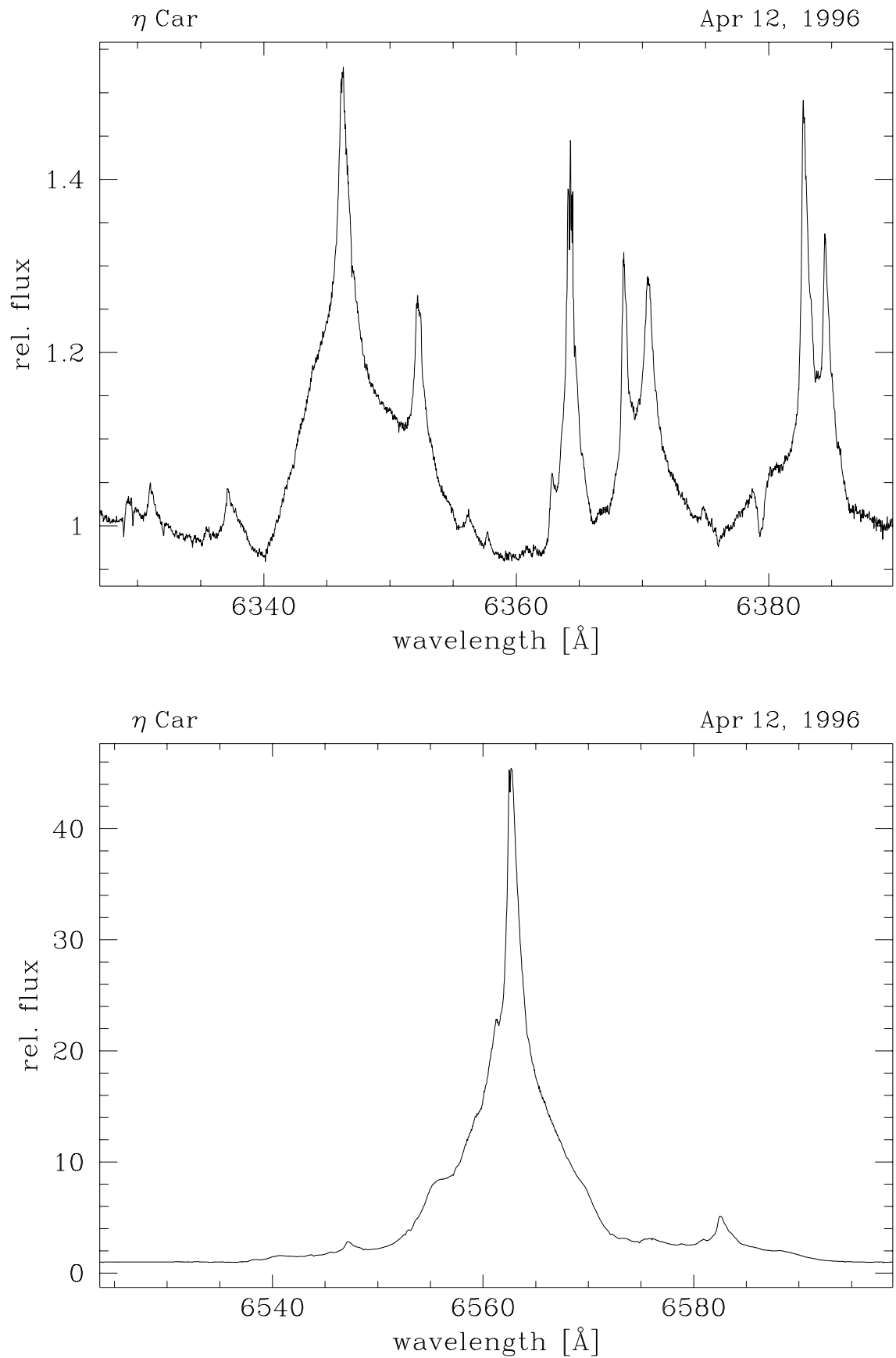
Figure A.75: Mean spectrum of η Car; observed in April 1996.

A.11 Mean Spectrum of AG Car

- Observing instrument: CES/CAT

- Observing date: April 5 − 9, 1996

- Observed wavelength range: 4320 − 6602 Å

- Spectral resolution: 60 000

- S/N ratio around 6400 Å: 240
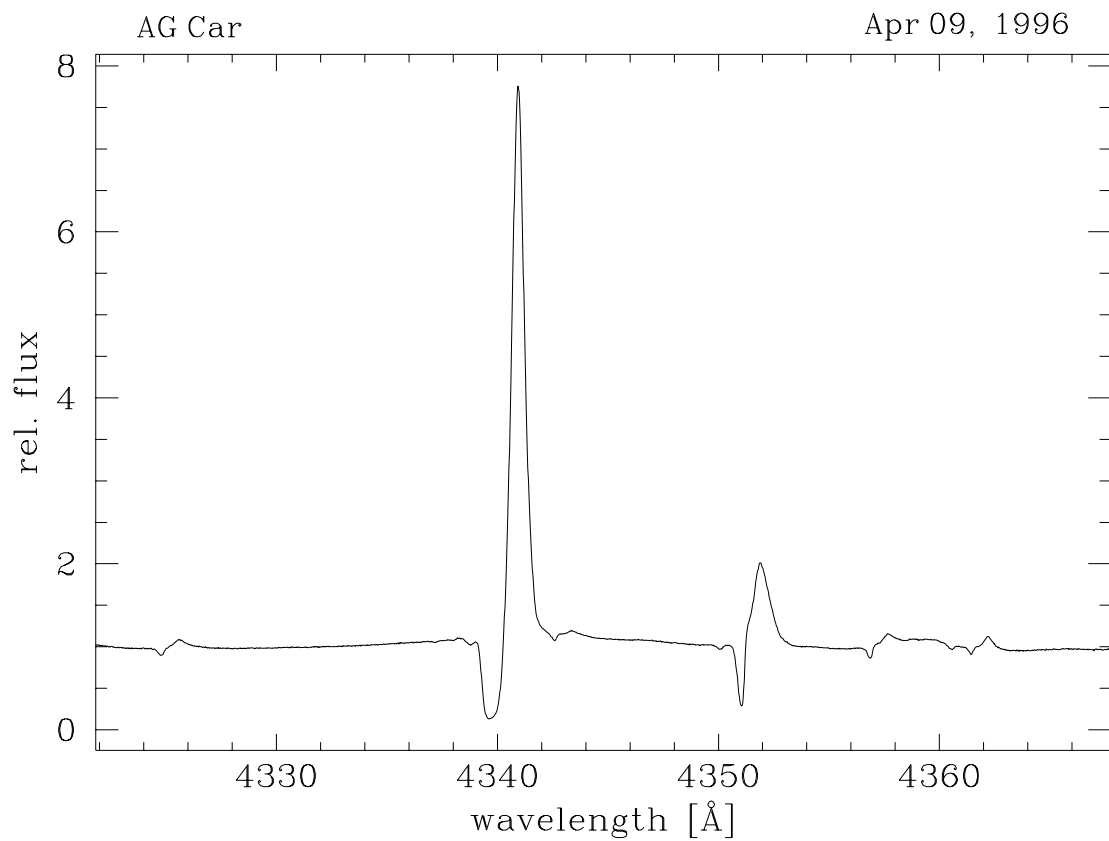
Figure A.76: Mean spectrum of AG Car; observed in April 1996.
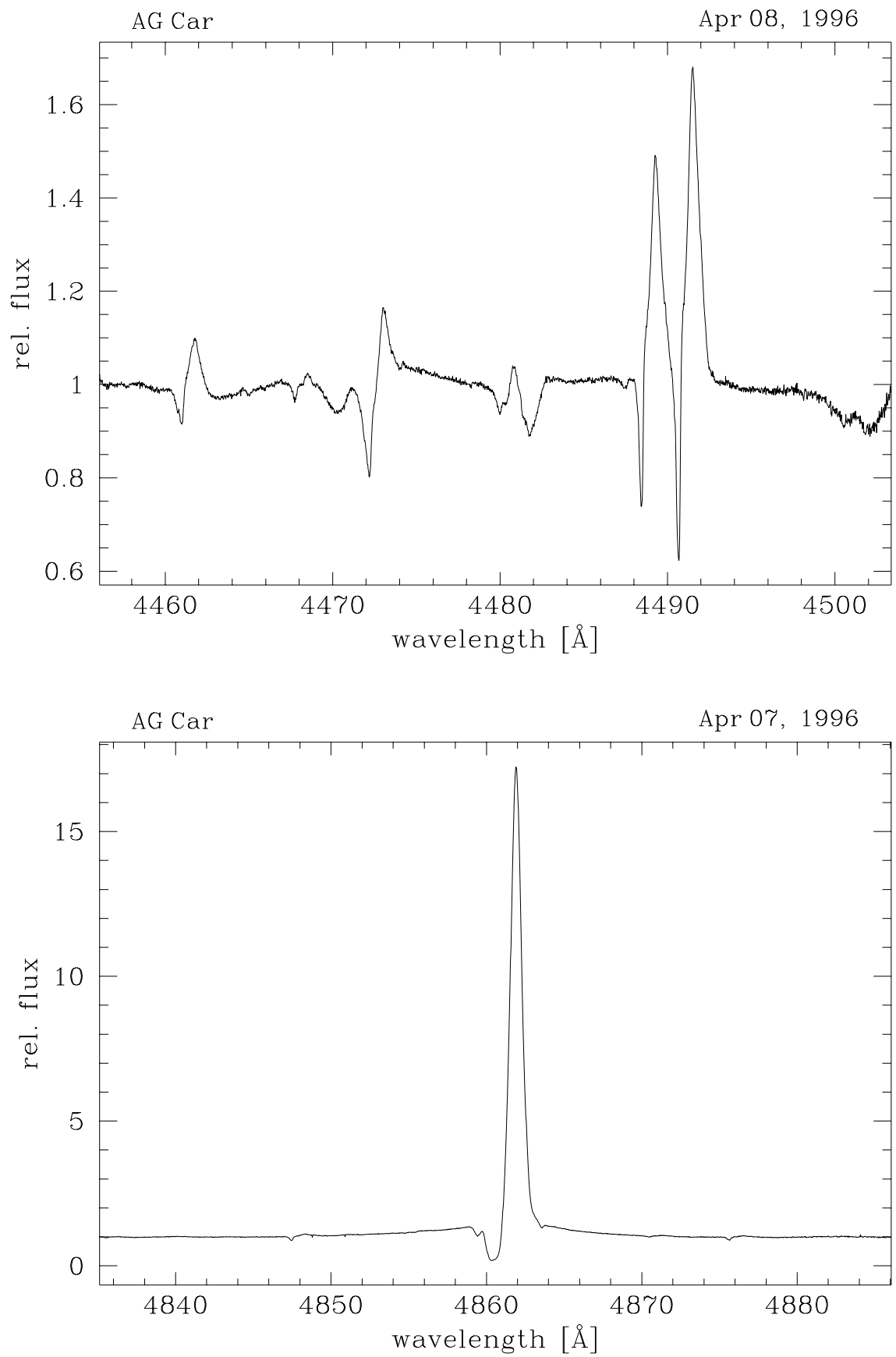
Figure A.77: Mean spectrum of AG Car; observed in April 1996.

AG Car   Apr 06, 1996

AG Car   Apr 05, 1996
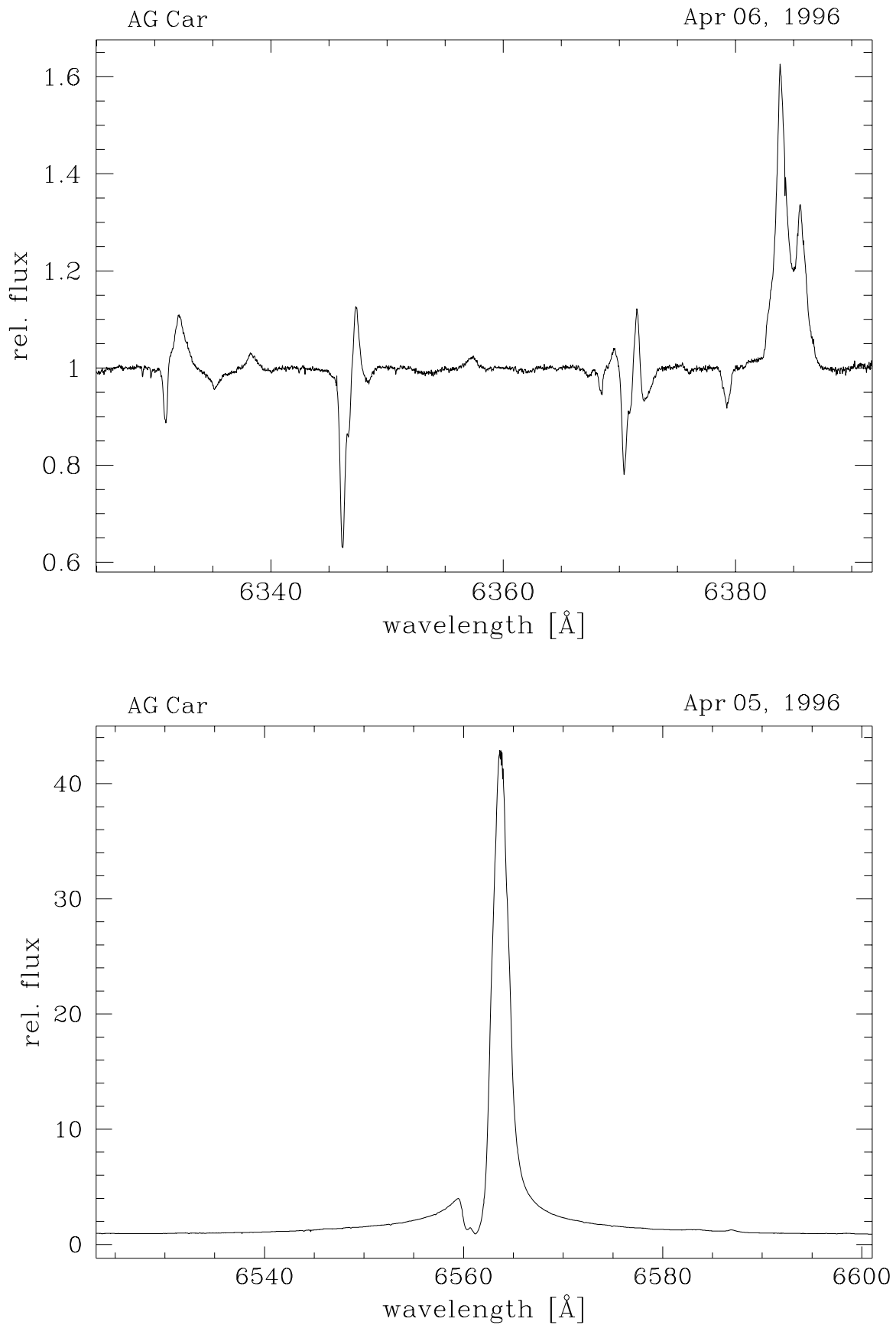
Figure A.78: Mean spectrum of AG Car; observed in April 1996.

A.12 Mean Spectrum of HR Car

- Observing instrument: CES/CAT

- Observing date: April 5 – 10, 1996

- Observed wavelength range: 4320 – 6602 Å

- Spectral resolution: 60 000

- S/N ratio at 6400 Å: 240
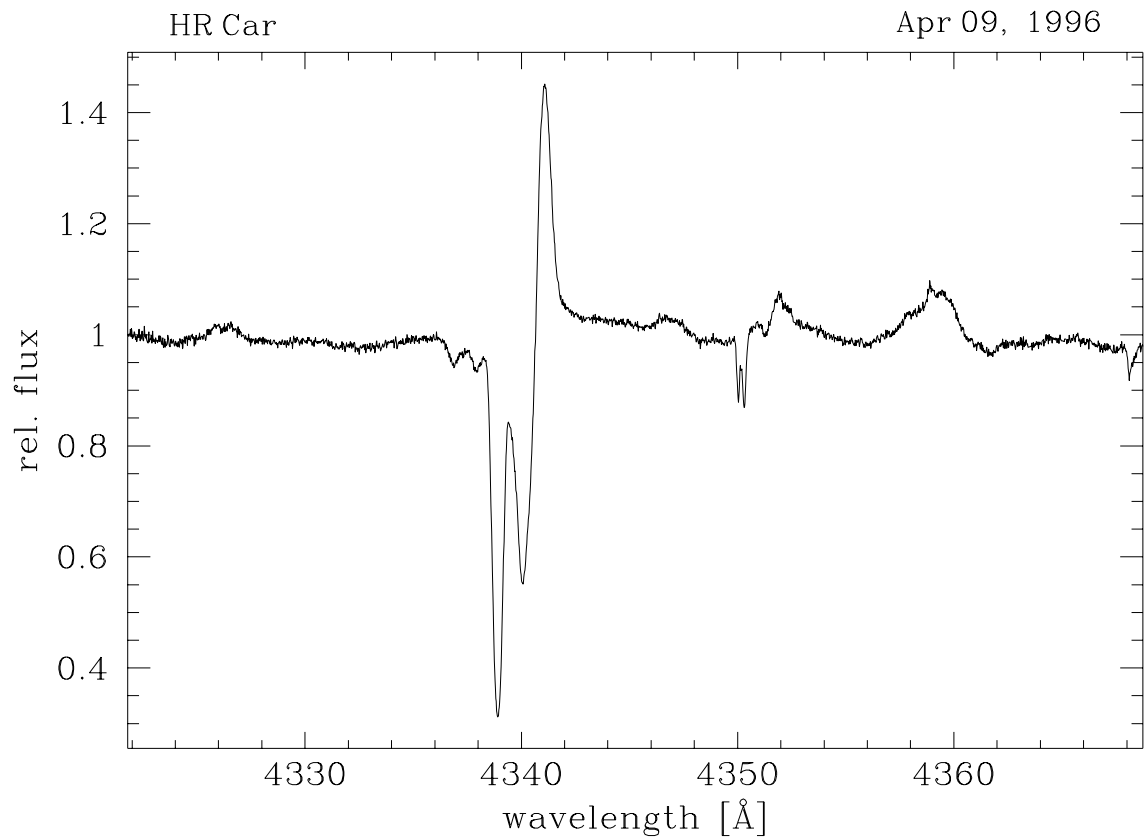
Figure A.79: Mean spectrum of HR Car; observed in April 1996.
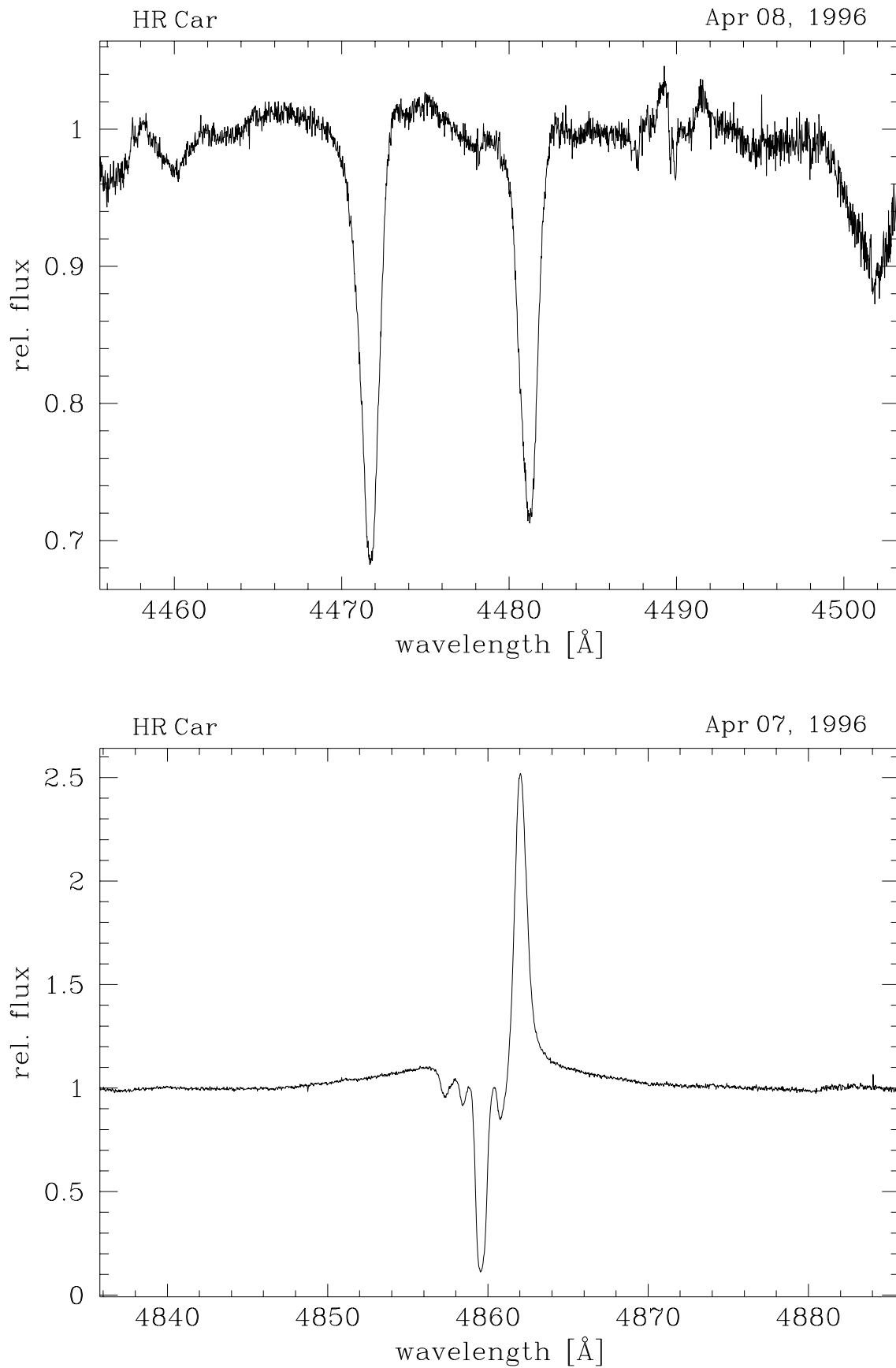
Figure A.80: Mean spectrum of HR Car; observed in April 1996.
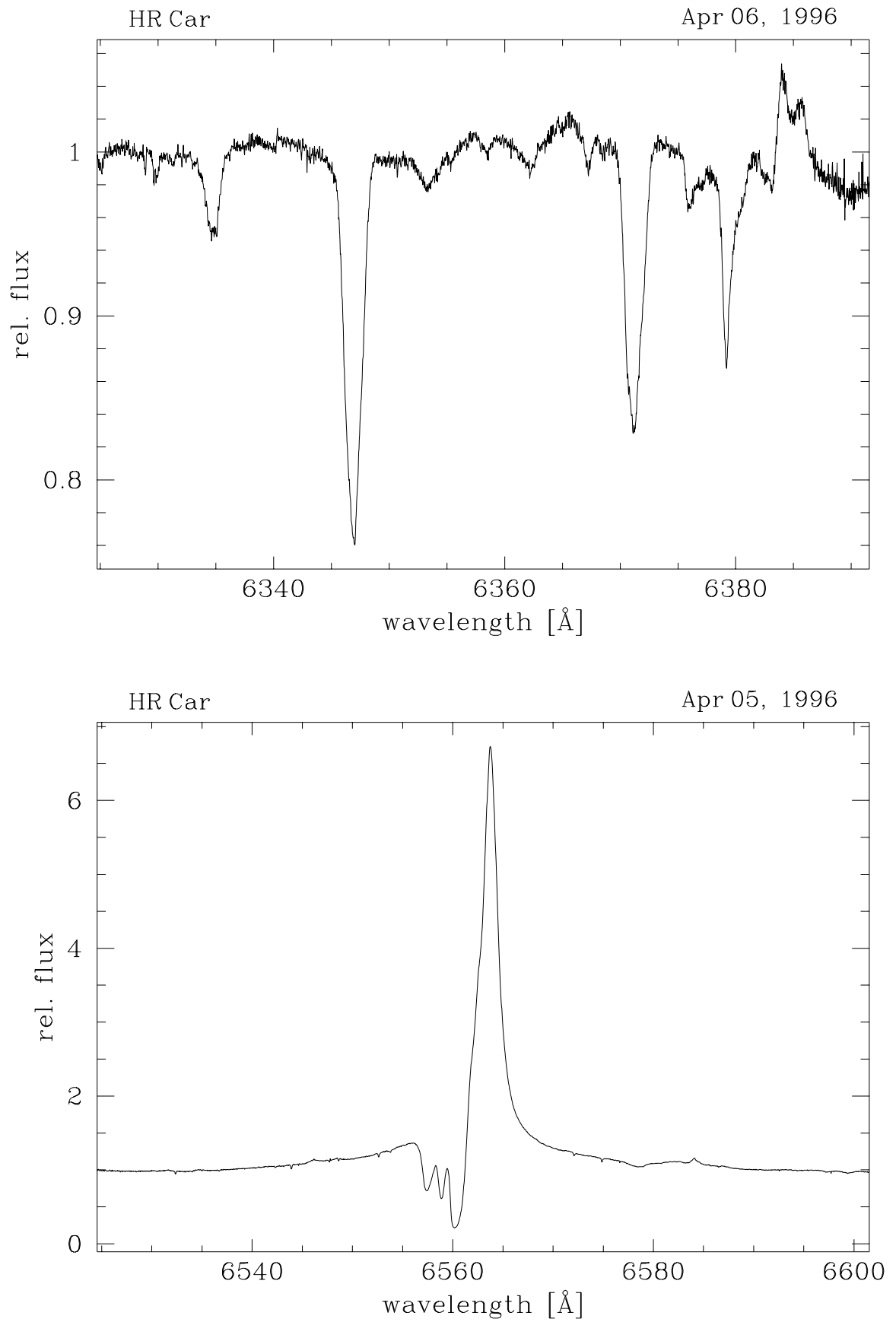
Figure A.81: Mean spectrum of HR Car; observed in April 1996.

A.13   Mean Spectrum of HD 169454

- Observing instrument: CES/CAT

- Observing date: April 5−9, 1996

- Observed wavelength range: 4320−6602 Å

- Spectral resolution: 60 000

- S/N ratio at 6400 Å: 230
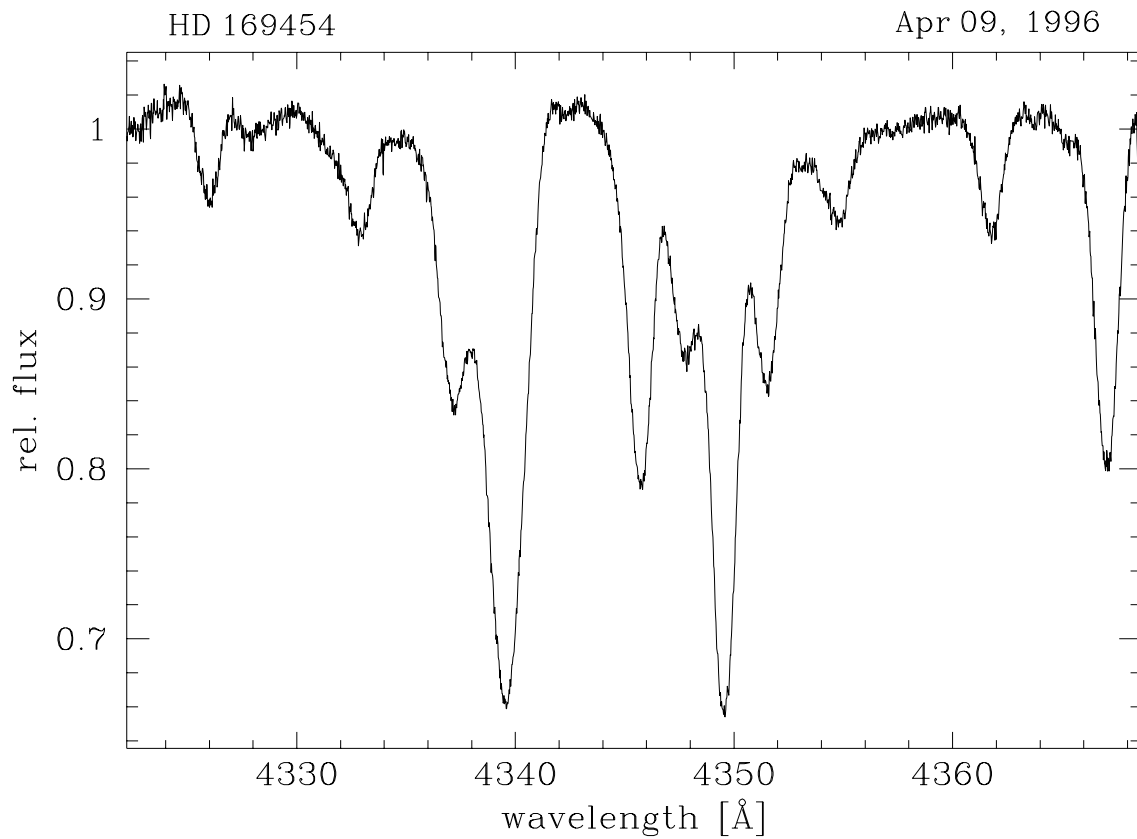
Figure A.82: Mean spectrum of HD 169454; observed in April 1996.
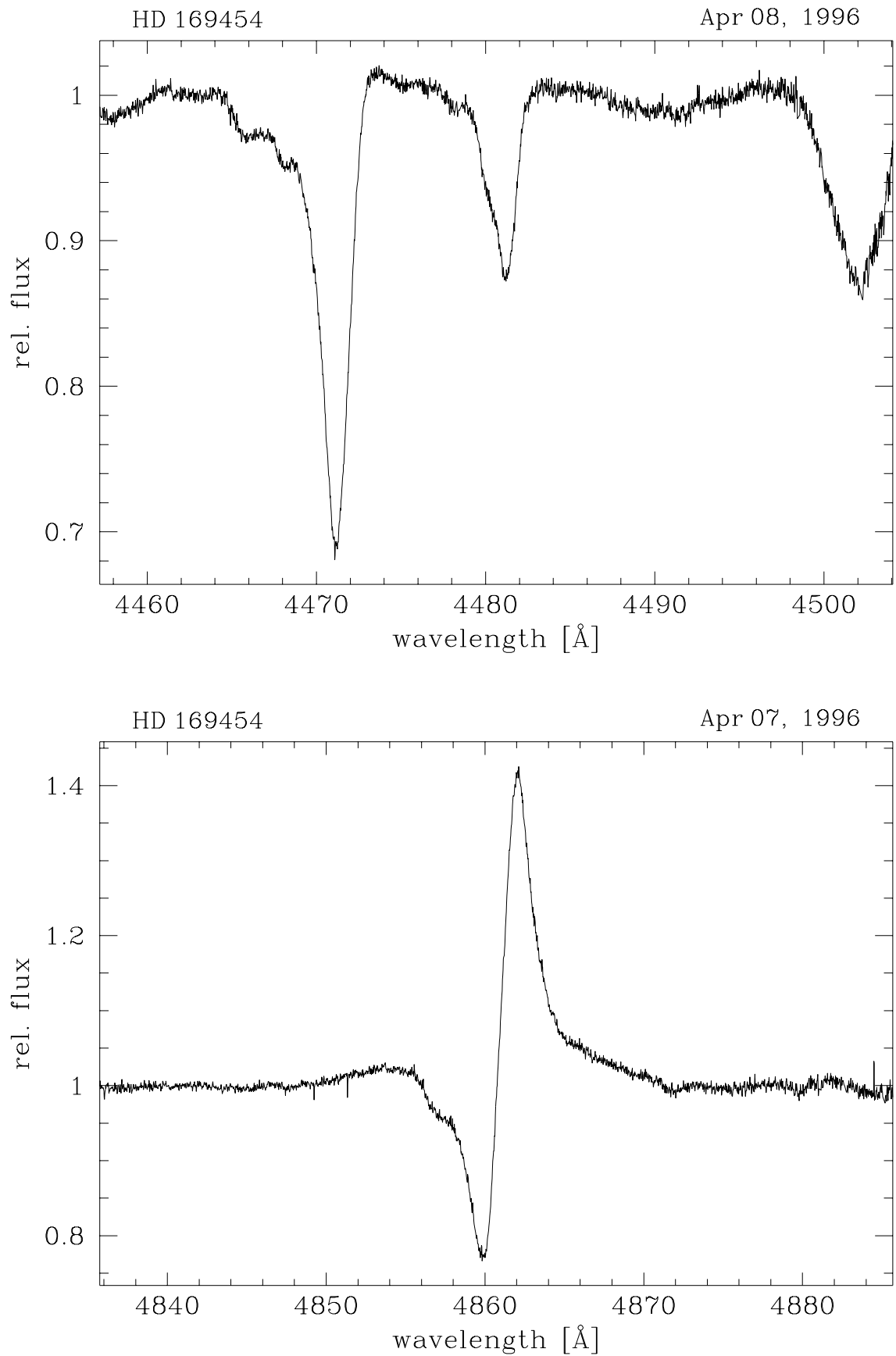
Figure A.83: Mean spectrum of HD 169454; observed in April 1996.
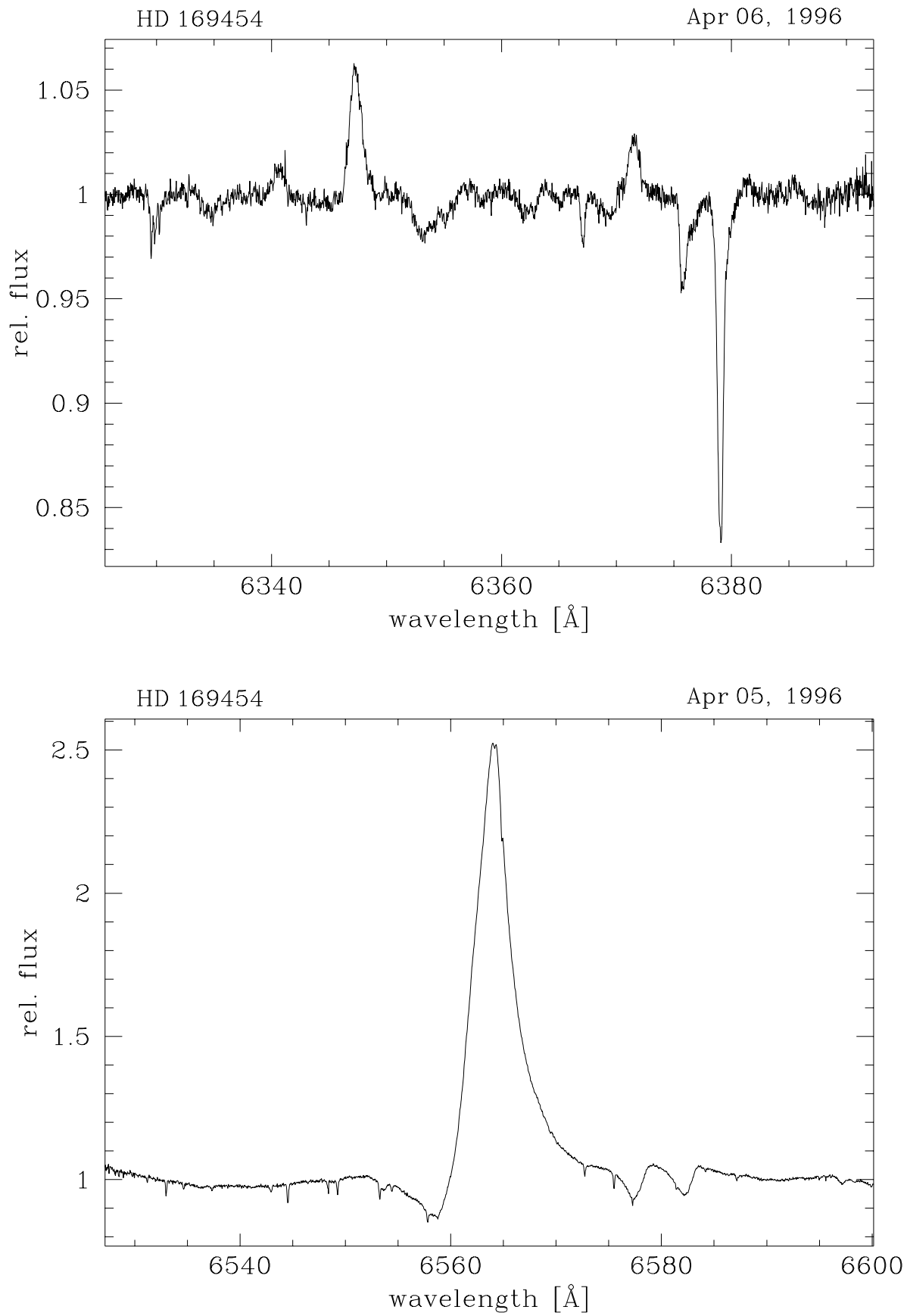
Figure A.84: Mean spectrum of HD 169454; observed in April 1996.

A.14   Mean Spectrum of HD 316285

- Observing instrument: CES/CAT

- Observing date: April 10 – 12, 1996

- Observed wavelength range: 4320 – 6602 Å

- Spectral resolution: 60 000

- S/N ratio at 6400 Å: 220
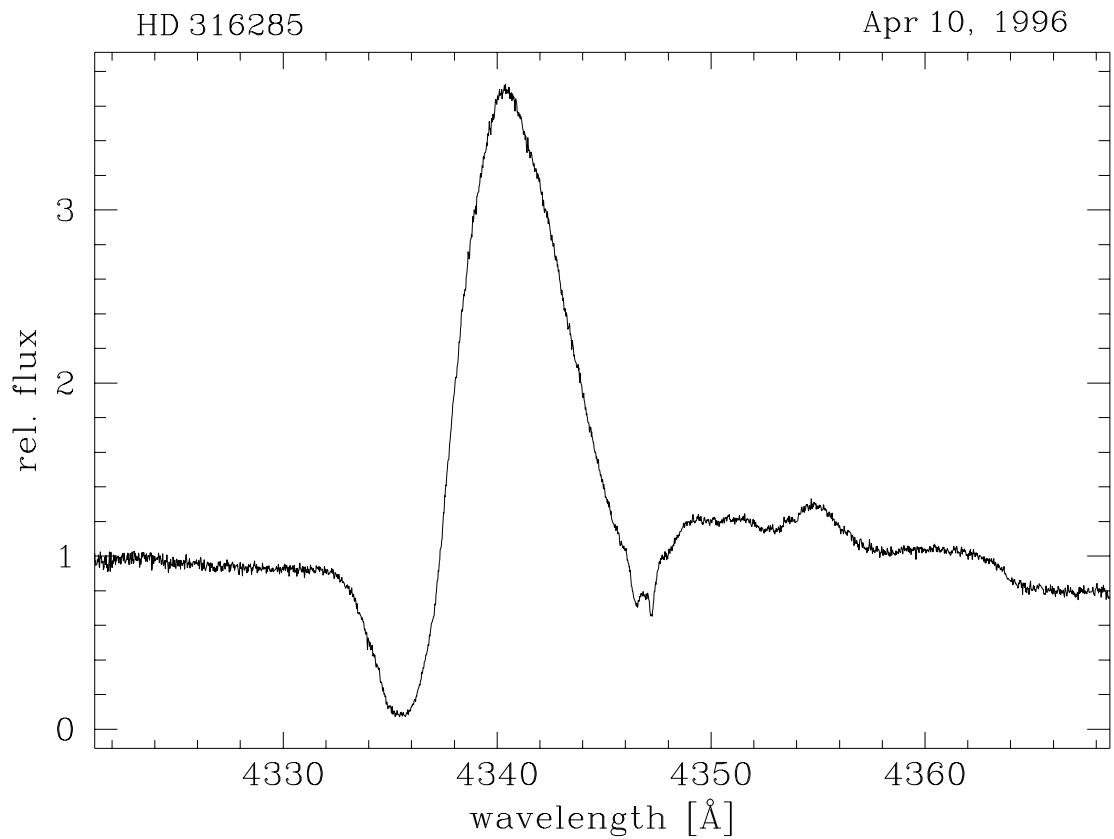
Figure A.85: Mean spectrum of HD 316285; observed in April 1996.
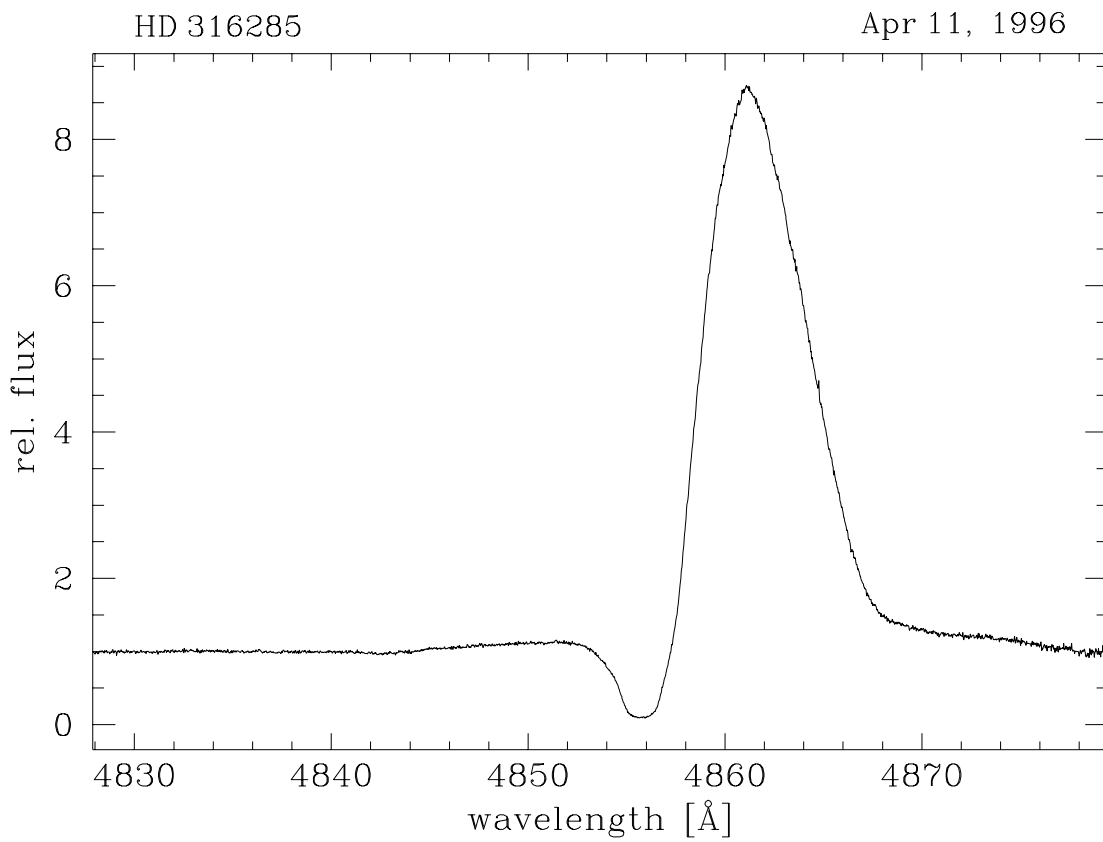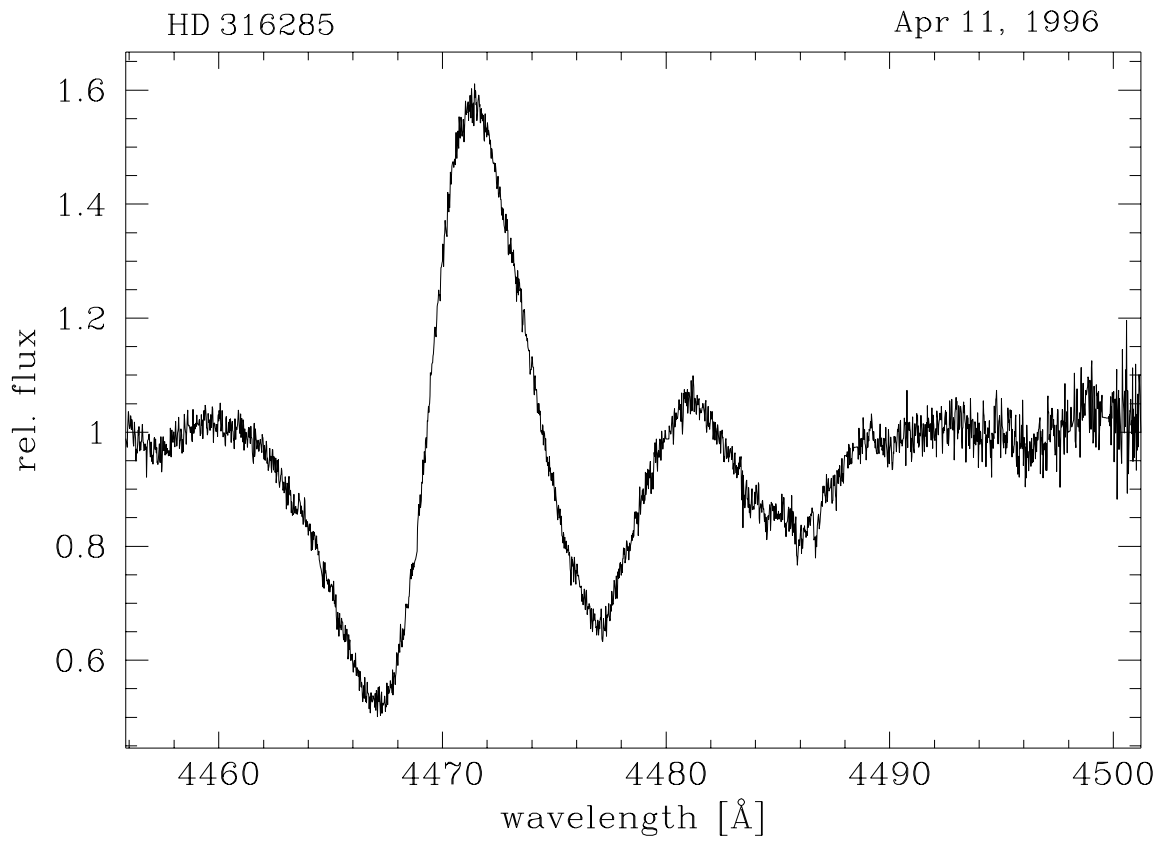
Figure A.86: Mean spectrum of HD 316285; observed in April 1996.
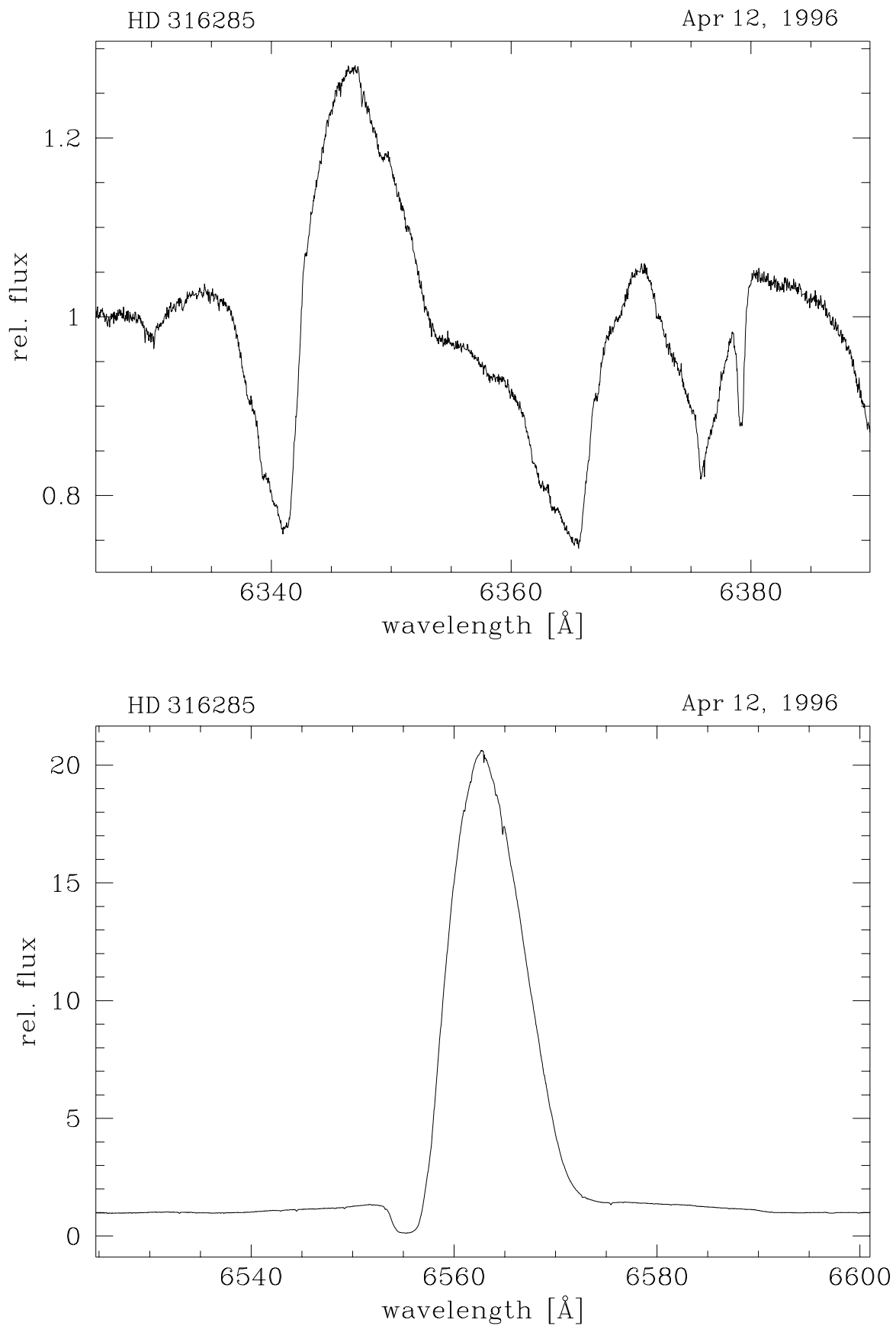
Figure A.87: Mean spectrum of HD 316285; observed in April 1996.

A.15   Mean Spectrum of HD 326823

- Observing instrument: CES/CAT

- Observing date: April 5 – 11, 1996

- Observed wavelength range: 4320 – 6602 Å

- Spectral resolution: 60 000

- S/N ratio at 6400 Å: 120
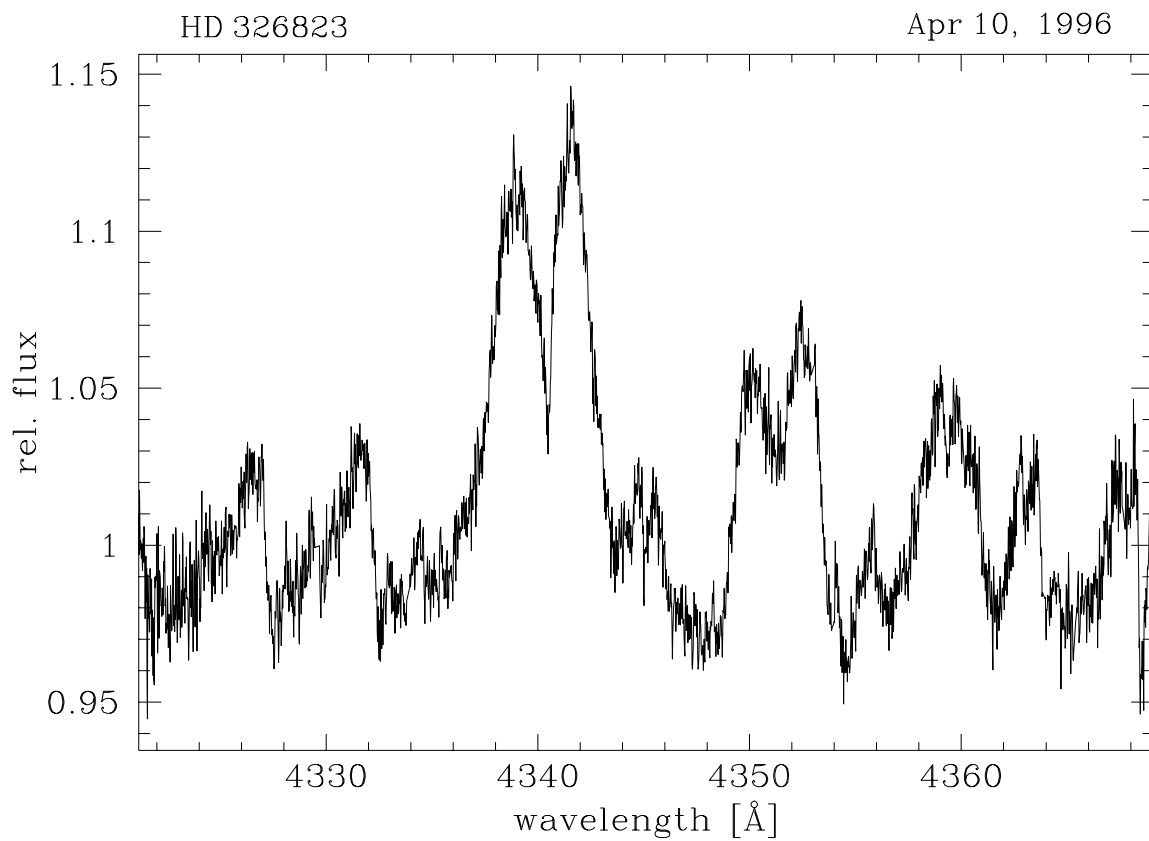
Figure A.88: Mean spectrum of HD 326823; observed in April 1996.
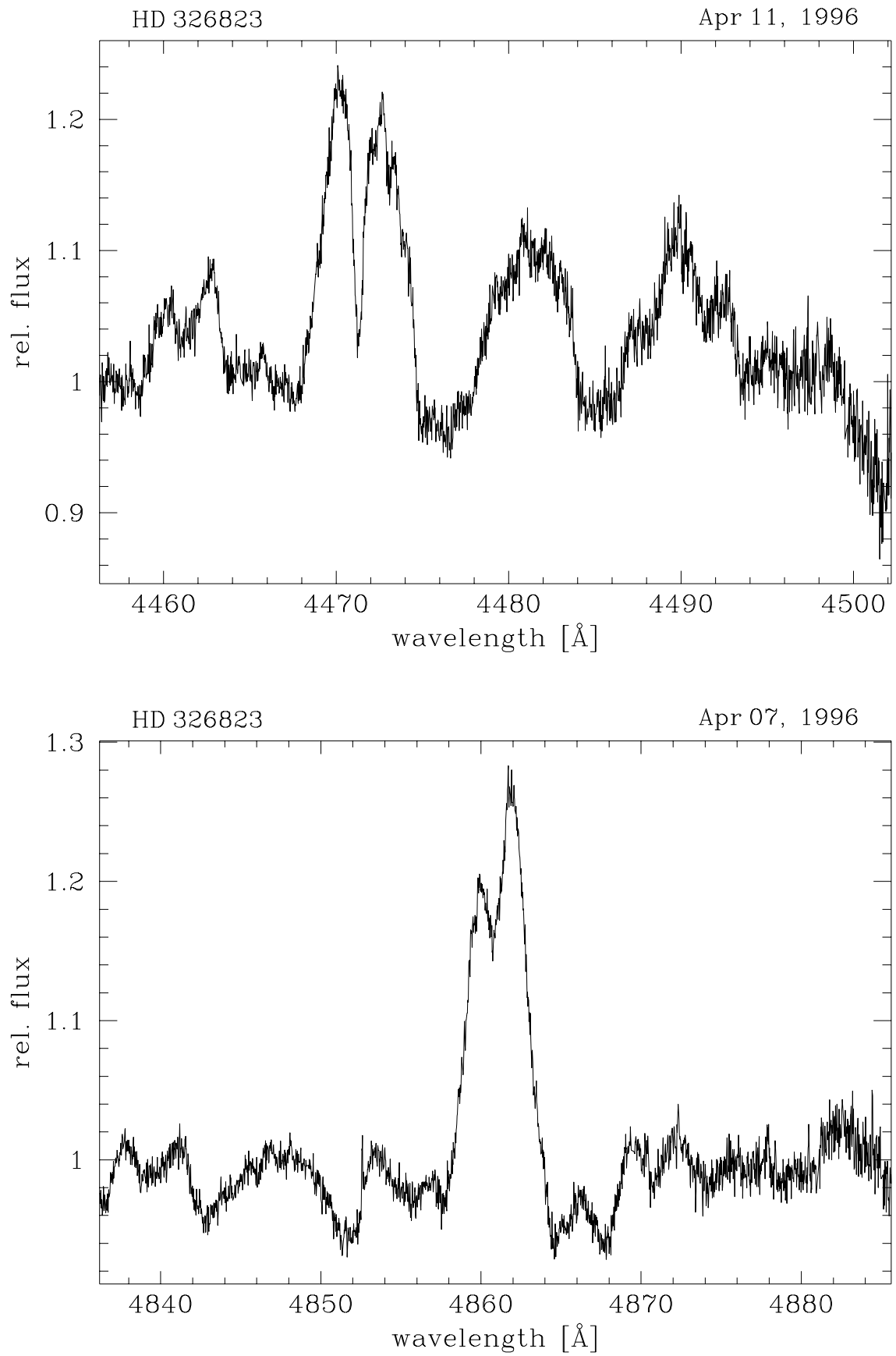
Figure A.89: Mean spectrum of HD 326823; observed in April 1996.
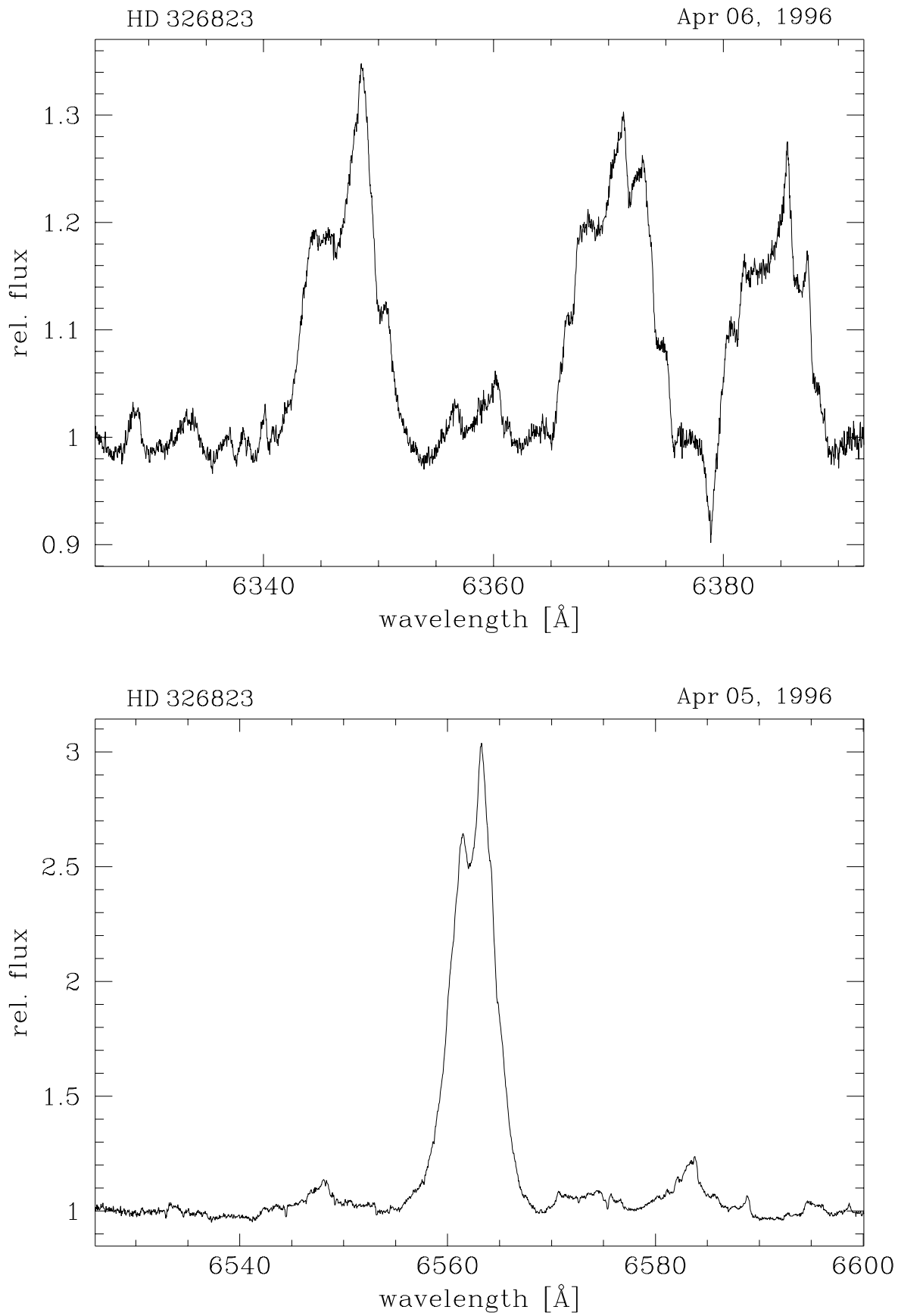
Figure A.90: Mean spectrum of HD 326823; observed in April 1996.

A.16 Mean Spectrum of HD 80077

- Observing instrument: CES/CAT

- Observing date: April 5 – 9, 1996

- Observed wavelength range: 4320 – 6602 Å

- Spectral resolution: 60 000

- S/N ratio at 6400 Å: 260
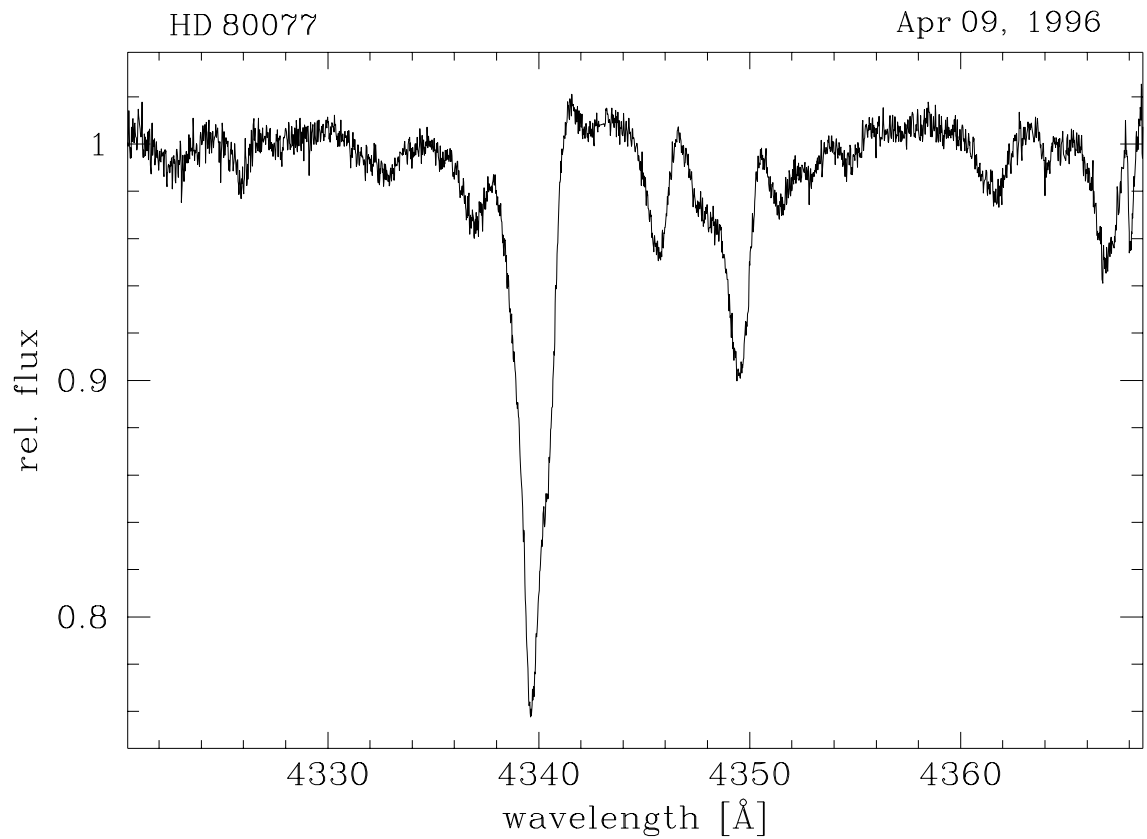
Figure A.91: Mean spectrum of HD 80077; observed in April 1996.
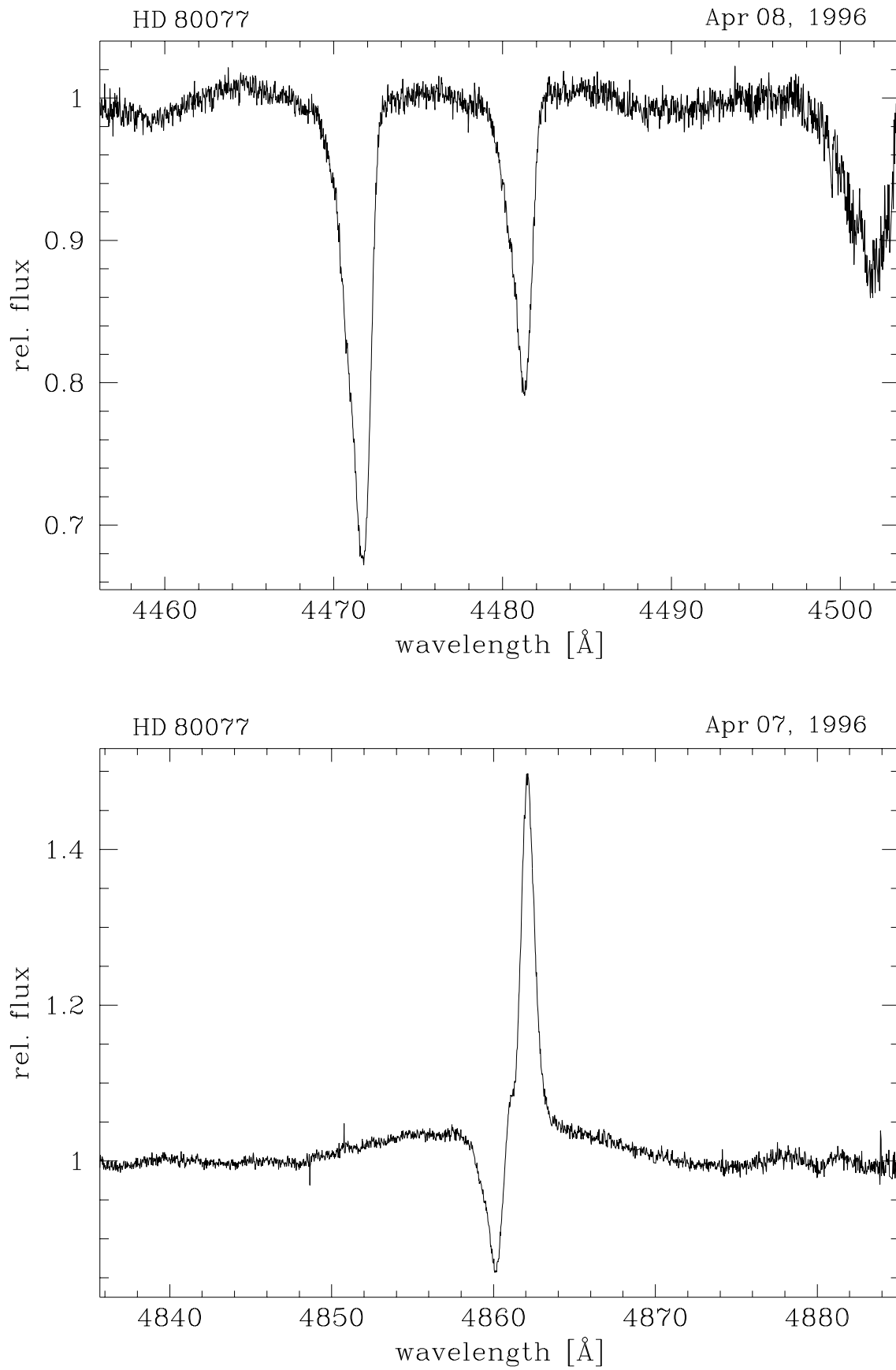
Figure A.92: Mean spectrum of HD 80077; observed in April 1996.
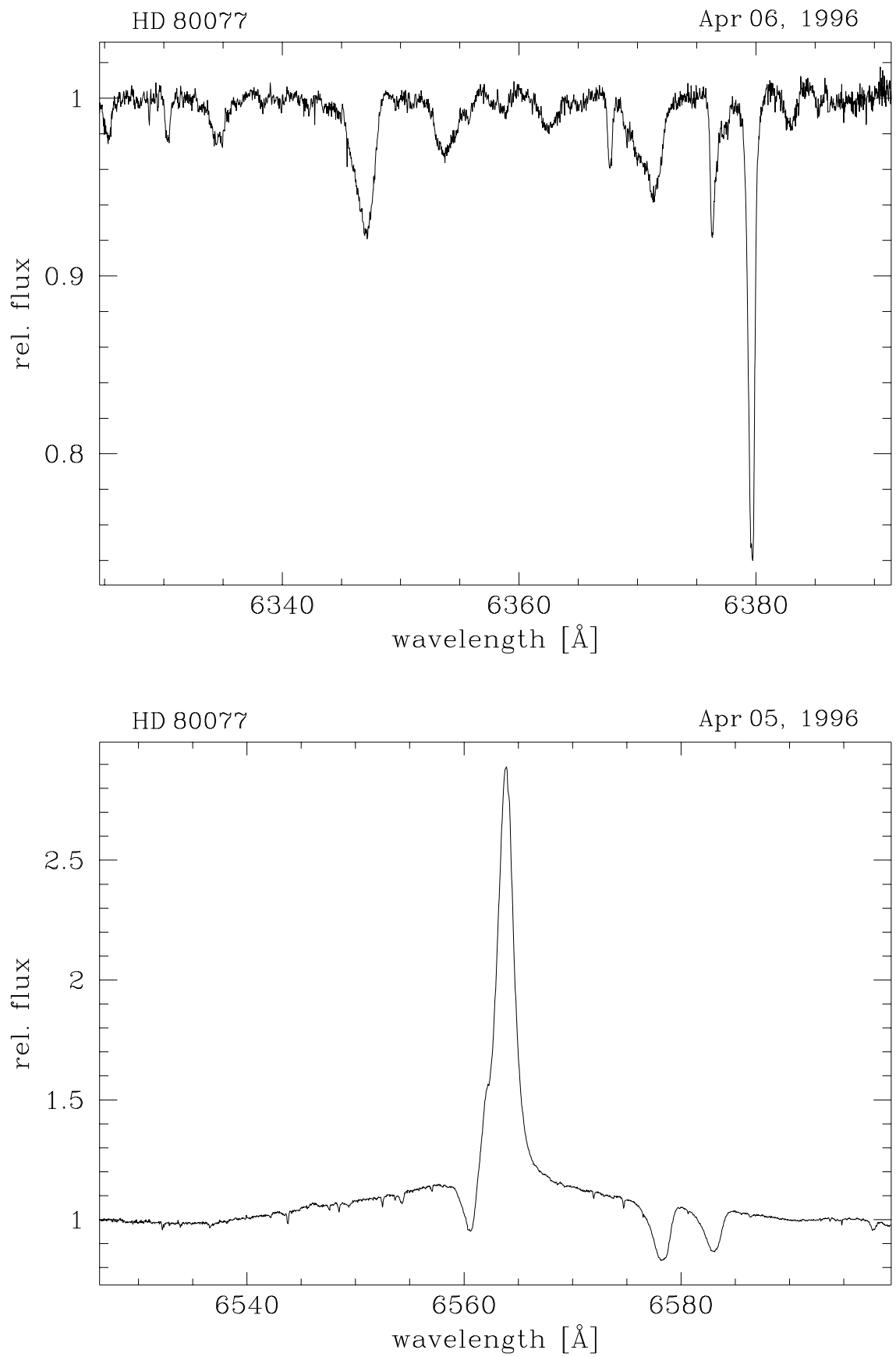
Figure A.93: Mean spectrum of HD 80077; observed in April 1996.